



Studies of new nonlinear crystals for infrared parametric generation with the broadest spectral bandwidth

Feng Guo

► To cite this version:

Feng Guo. Studies of new nonlinear crystals for infrared parametric generation with the broadest spectral bandwidth. Optics / Photonic. Université Grenoble Alpes, 2018. English. NNT: 2018GREAT047 . tel-01913330

HAL Id: tel-01913330

<https://theses.hal.science/tel-01913330>

Submitted on 6 Nov 2018

HAL is a multi-disciplinary open access archive for the deposit and dissemination of scientific research documents, whether they are published or not. The documents may come from teaching and research institutions in France or abroad, or from public or private research centers.

L'archive ouverte pluridisciplinaire **HAL**, est destinée au dépôt et à la diffusion de documents scientifiques de niveau recherche, publiés ou non, émanant des établissements d'enseignement et de recherche français ou étrangers, des laboratoires publics ou privés.

THÈSE

Pour obtenir le grade de

**DOCTEUR DE LA COMMUNAUTE UNIVERSITE
GRENOBLE ALPES**

Spécialité : OPTIQUE ET RADIOFREQUENCES

Arrêté ministériel : 25 mai 2016

Présentée par

Feng GUO

Thèse dirigée par **Patricia SEGONDS** et **Benoît BOULANGER**

préparée au sein de l'**Institut Néel**
dans l'**École Doctorale EEATS**

Etude de nouveaux cristaux non linéaires pour la génération paramétrique dans l'infrarouge

Thèse soutenue publiquement le **26 Juin 2018**,
devant le jury composé de :

Monsieur Guy VITRANT

Directeur de Recherche au CNRS, IMEP-LAHC, Président

Monsieur Fabien BRETENAKER

Directeur de Recherche au CNRS, Laboratoire Aimé Cotton, Rapporteur

Monsieur Frédéric DRUON

Directeur de Recherche au CNRS, Institut d'optique, Rapporteur

Monsieur Jean-Michel MELKONIAN

Ingénieur de Recherche à ONERA, Examineur

Madame Patricia SEGONDS

Professeure à l'Université Grenoble Alpes, Institut Néel, Directrice de
thèse

Monsieur Benoît BOULANGER

Professeur à l'Université Grenoble Alpes, Institut Néel, Directeur de thèse



Acknowledgements

I am very excited that four years of this thesis are completed. And in this most precious period of my life, I would like to express my gratitude to all those who have given me help.

I would first and foremost like to thank my two supervisors: Patricia Segonds and Benoît Boulanger, for their confidence and support with persistent enthusiasm during the four years. Despite their busy schedules, they spent a lot of time on my experiments and gave many instructive advices from the beginning to the end. I am deeply grateful of their help in the completion of this thesis.

I would like to thank all the members of the jury, Fabien BRETENAKER, Frédéric DRUON, Jean-Michel MELKONIAN and Guy VITRANT for agreeing to evaluate my work and for their precious time given to me.

This work cannot be done without the colleagues' assistance. I would like to express my heartfelt gratitude to David for the many hours spent in the optical lab with me to optimize the laser, also for his patience and sympathy. Thanks also to Jérôme, for the preparation of all these samples. And he also spent much time on training me in crystals and for discussions about the experiments.

I warmly thank Elodie, Cyril, Dazhi and Augustin, for the great moments spent together in the optical lab. Elodie and Cyril helped me a lot in how to use the laser and optical equipment.

I also thank Véronique, Corinne, Alexandra and Julien for their help in checking the laser and preparing the crystals.

Thanks to all members of building F and all the PhD students I have been able to meet during these four years, I spent a wonderful time in a very friendly environment.

Last my thanks would go to my beloved family for their loving considerations and great confidence in me all through these years.

Contents

Introduction.....	4
Chapter 1 Theoretical elements	6
1.1 Introduction	6
1.2 Linear optics	6
1.2.1 Linear induced polarization	6
1.2.2 Principal refractive indices	7
1.2.3 Propagation equation	8
1.2.4 Index surface.....	10
1.2.5 Spatial walk-off	12
1.2.6 Polarization states	15
1.3 Nonlinear optics.....	16
1.3.1 Nonlinear induced polarization	16
1.3.2 Propagation equation	18
1.3.3 Energy of the generated wave	19
1.3.4 Effective coefficient χ_{eff}	20
1.3.5 Birefringence phase-matching.....	20
1.3.6 Acceptances	22
1.3.7 Spatial walk-off and attenuation.....	23
1.3.8 Condition of supercontinuum generation	25
1.4 Summary.....	26
Chapter 2 Experimental methods	27
2.1 Introduction	27
2.2 Linear and nonlinear optics studies in slabs	28
2.2.1 Slabs shaping	28
2.2.2 Transmission spectra in polarized light.....	29
2.2.3 Optical damage threshold	30
2.2.4 Determination of nonlinear coefficients from phase-matched SHG	32
2.3 Linear and nonlinear optics studies in spheres or cylinders	35
2.3.1 Cylinders and spheres shaping	35
2.3.2 SPHERE method	37
2.3.3 Direct measurements and analysis.....	43
2.4 Summary.....	49
Chapter 3 Phase-matching directions and Sellmeier equations of GdCOB, LGN and Na ₃ O ₈	50
3.1 Introduction	50
3.2 GdCOB	51
3.2.1 State of the art.....	51
3.2.2 GdCOB sphere.....	56

3.2.3 Orientation of the dielectric frame as a function of wavelength	57
3.2.4 Recorded tuning curves	58
3.2.5 Refined Sellmeier equations of the three principal refractive indices...	64
3.2.6 Determination of SHG spectral and angular acceptances	68
3.2.7 Condition of supercontinuum generation	69
3.3 LGN.....	72
3.3.1 State of the art.....	72
3.3.2 Determination of the optical damage threshold.....	75
3.3.3 Recorded tuning curves	76
3.3.4 Refined Sellmeier equations of the two principal refractive indices.....	80
3.3.5 Determination of the nonlinear coefficient from phase-matched SHG.	82
3.3.6 Condition of supercontinuum generation	84
3.4 NaI308	85
3.4.1 State of the art.....	85
3.4.2 Determination of transmission spectra and optical damage threshold ..	87
3.4.3 Determination of the magnitude of a principal refractive index	88
3.4.4 Recorded tuning curves	92
3.4.5 First Sellmeier equations of the two principal refractive indices	96
3.4.6 Determination of the nonlinear coefficients from phase-matched SHG	98
3.4.7 Condition of supercontinuum generation	101
3.5 Comparison between studied crystals.....	102
3.6 Summary.....	105
Chapter 4 Magnitude and relative sign of nonlinear coefficients of BGSe	107
4.1 Introduction	107
4.2 State of the art.....	108
4.3 Magnitudes of the nonlinear coefficients d_{21} d_{22} and d_{33}	114
4.3.1 Maker fringes.....	114
4.3.2 Tunable fringes	116
4.4 Relative sign between nonlinear coefficients	122
4.4.1 Calculations	123
4.4.2 Measurement and analysis of data.....	125
4.4.3 Calculation out of the principal planes	127
4.5 Condition of supercontinuum generation	128
4.6 Summary.....	131
Conclusion.....	132
References.....	134



Introduction

Nowadays, there is still a real need in coherent sources which emission is able to cover the band II (3-5 μm) and band III (8-12 μm) of transmission of the atmosphere.

Compared with other coherent sources, solid state lasers have some advantages: they are compact, and they can cover a wide spectral range in band II with high output energies. Nevertheless, the discrete transitions of the rare earth elements used as dopants in the active medium limits the accessible wavelength ranges.

Optical parametric generators (OPG), which are based on frequency conversion in a nonlinear crystal from a second-order nonlinear process, can convert a monochromatic input beam into two output beams of higher wavelengths. Then they can generate a light over a very wide wavelength range from ultraviolet to far infrared, which overcomes the problem of solid state lasers. Furthermore, the OPG output energy can be optimized by using phase-matching conditions.

In this context, our interest is in high energy OPG emission with the broadest spectral bandwidth of the signal and idler generated beams covering bands II and band III. This so-called super-continuum condition of OPG emission is of prime importance for many applications in medical, commercial, and military technologies for example.

Although there are already many nonlinear crystals used in commercial OPG devices, they are not satisfactory. Then there is still a need for new crystals with more appropriate optical properties, such as: a very good optical quality and a wide transparency range, a high optical damage threshold and efficient nonlinear optical properties covering their transparency range.

We identified the three following crystals as a real alternative for a phase-matched OPG super-continuum emission covering band II: $\text{GdCa}_4\text{O}(\text{BO}_3)_3$ (GdCOB) belonging to the positive biaxial optical class, $\text{La}_3\text{Ga}_{5.5}\text{Nb}_{0.5}\text{O}_{14}$ (LGN) and NaI_3O_8 crystals from the positive and negative uniaxial optical class respectively. We also studied the BaGa_4Se_7 (BGSe) positive biaxial crystal for an emission covering band III. This PhD work is devoted to the study of their linear and nonlinear optical properties and this manuscript is based on 4 chapters following this introduction.

In the first chapter, main theoretical elements about linear and nonlinear optics are described. At first, linear optics defines the first-order polarization induced by the interaction between an electromagnetic wave and a crystal. The corresponding

propagation phenomena in polarized light are described taking into account the index surface and the spatial walk-off effect. In a second step, theoretical basics of nonlinear optics are reminded, in particular concerning the quadratic parametric processes. Finally, birefringence phase-matching conditions, the associated effective coefficients, acceptances and spatial walk-off angles are discussed.

The second chapter describes the experimental methods and the corresponding setups that we used to study linear and nonlinear optics in crystals. Techniques using oriented slabs are first reported. They are devoted to the linear optical properties and also phase-matched Second Harmonic Generation. The magnitude of the non-zero nonlinear coefficients and the associated spectral and angular acceptances are determined from the recorded data. Then comes the interest in crystals shaped as a sphere or a cylinder to study the angular distribution of their optical properties. The corresponding SPHERE method enables several direct measurements as a function of wavelength: spatial walk-off angles, dielectric frame orientation and phase-matching conditions. Finally, this chapter describes the analysis of data leading to the determination of the Sellmeier equations and to the relative signs of the non-zero coefficients of the second-order electric susceptibility tensor.

In the third chapter, we report the studies we performed in GdCOB, LGN and NaI₃O₈, the goal being to evaluate their potentiality for a phase-matched OPG super-continuum emission covering band II. The measurements deal with the transmission spectra, damage threshold, refractive indices and magnitude of the nonlinear coefficients. Then the phase-matching tuning curves, the associated conversion efficiencies, as well as the spectral and angular acceptances are recorded using the SPHERE method. All these experimental data are analysed using the theoretical elements of the first chapter to provide refined Sellmeier equations. Then come calculations for a phase-matched OPG super-continuum emission with the broadest spectral bandwidth.

The last chapter concerns the determination of the magnitude and relative sign of the nonlinear coefficients of BGSe from studying SHG conversion efficiencies. Since BGSe belongs to the point group *m* of the monoclinic system, six nonlinear non-zero and independent nonlinear coefficients were concerned under Kleinman assumption. All these results we obtained will provide reliable data for further experimental evaluations of OPG broadest spectral bandwidth covering band III.

The conclusion is followed by appendices including copies of three articles published in the framework of this PhD work.

Chapter 1 Theoretical elements

1.1 Introduction

In this chapter, we consider main theoretical elements about the interactions between light and crystals. We describe linear optics and nonlinear optics from quadratic parametric processes. These theoretical elements will be used to implement setups and analyze studies presented in the following chapters.

On the one hand, linear optics defines the first-order polarization induced by the interaction between an electromagnetic wave and crystals. The corresponding propagation phenomena in polarized light are described taking into account the index surface and walk-off effects.

On the other hand, theoretical basics of nonlinear optics are reminded, in particular the quadratic parametric processes. Finally, we discuss birefringence phase-matching conditions, the associated effective coefficients, the acceptances and walk-off effects.

1.2 Linear optics

1.2.1 Linear induced polarization

Electromagnetic waves consist of an electric field \vec{E} and a magnetic field \vec{H} which Fourier expansion leads at the position \vec{r} and angular frequency ω to the Fourier components $\vec{E}(\omega)$ and $\vec{H}(\omega)$. Both fields are perpendicular to each other and propagate along the wave propagation direction $\vec{k}(\omega)$.

The electric field of an electromagnetic wave interacts with the medium by inducing a dipole due to the displacement of the electrons density away from the equilibrium position. At the macroscopic scale, it gives rise to a polarization $\vec{P}(\omega)$ of the medium that is related to the applied electric field $\vec{E}(\omega)$ via the electric susceptibility tensor $\chi(\omega)$. When the power density of the electric field does not exceed about 1 MW/cm^2 , $\vec{P}(\omega)$ can be considered as varying linearly with the incident electric field of light $\vec{E}(\omega)$. This is written at the position \vec{r} and the angular frequency ω [1]:

$$\vec{P}(\omega) = \varepsilon_o \chi^{(1)}(\omega) \cdot \vec{E}(\omega) \quad (1.1)$$

$\omega = 2\pi c/\lambda$, λ is the wavelength and c is the velocity of light in vacuum; ε_o is the free space permittivity. $\chi^{(1)}(\omega)$ is the first-order electric susceptibility tensor. The symbol \cdot stands for a contracted product.

Equation (1.1) defines the linear constitutive relation of the light-matter interaction regarding the electric field. It shows that the linear polarization $\vec{P}(\omega)$ of matter and the exciting electric field $\vec{E}(\omega)$ from light oscillate at the same angular frequency ω but may have different orientations. In the following, this interaction is described in crystals.

The present work is limited to the transparency range of crystals, so that the imaginary part of all the elements of $\chi^{(1)}(\omega)$ can be neglected *i.e.* they are real numbers. Furthermore, there exists a frame in which the tensor $\chi^{(1)}(\omega)$ is diagonal. It is called the dielectric frame or the optical frame and labeled (x, y, z) in the following. The corresponding axes are called the principal axes, and define by pairs principal planes.

Then in the dielectric frame, the first-order electric susceptibility tensor $\chi^{(1)}(\omega)$ can be written at the position \vec{r} and the angular frequency ω as [1]:

$$\chi^{(1)}(\omega) = \begin{pmatrix} \chi_{xx}^{(1)}(\omega) & 0 & 0 \\ 0 & \chi_{yy}^{(1)}(\omega) & 0 \\ 0 & 0 & \chi_{zz}^{(1)}(\omega) \end{pmatrix} \quad (1.2)$$

Note that each Cartesian component of $\vec{P}(\omega)$ is linearly related to the corresponding component of $\vec{E}(\omega)$ according to Eq. (1.1) and (1.2).

1.2.2 Principal refractive indices

The electrical displacement vector $\vec{D}(\omega)$ is related to the electric field vector $\vec{E}(\omega)$ and to the induced polarization vector $\vec{P}(\omega)$. It is defined at the position \vec{r} and the angular frequency ω by [2]: $\vec{D}(\omega) = \varepsilon_o \vec{E}(\omega) + \vec{P}(\omega)$ and using Eq. (1.1), it becomes:

$$\vec{D}(\omega) = \varepsilon_o [1 + \chi^{(1)}(\omega)] \cdot \vec{E}(\omega) = \varepsilon_o \varepsilon_r(\omega) \cdot \vec{E}(\omega) \quad (1.3)$$

$\varepsilon_r(\omega)$ is the relative dielectric permittivity tensor of crystals written using Eq. (1.2):

$$\varepsilon_r(\omega) = \begin{pmatrix} \varepsilon_{rxx}(\omega) & 0 & 0 \\ 0 & \varepsilon_{ryy}(\omega) & 0 \\ 0 & 0 & \varepsilon_{rzz}(\omega) \end{pmatrix} = \begin{pmatrix} 1 + \chi_{xx}^{(1)}(\omega) & 0 & 0 \\ 0 & 1 + \chi_{yy}^{(1)}(\omega) & 0 \\ 0 & 0 & 1 + \chi_{zz}^{(1)}(\omega) \end{pmatrix} \quad (1.4)$$

$\varepsilon_{rxx}(\omega)$, $\varepsilon_{ryy}(\omega)$ and $\varepsilon_{rzz}(\omega)$ enable to define the three principal refractive indices $n_x(\omega)$, $n_y(\omega)$ and $n_z(\omega)$ from the relations:

$$\varepsilon_{rxx}(\omega) = n_x^2(\omega); \varepsilon_{ryy}(\omega) = n_y^2(\omega); \varepsilon_{rzz}(\omega) = n_z^2(\omega) \quad (1.5)$$

There are three optical classes according to the relative values of these principal indices:

1. The isotropic optical class defined by $n_x(\omega) = n_y(\omega) = n_z(\omega)$.
2. The anisotropic uniaxial optical class with $n_x(\omega) = n_y(\omega) \neq n_z(\omega)$.
3. The anisotropic biaxial optical class where $n_x(\omega) \neq n_y(\omega) \neq n_z(\omega)$.

For the isotropic optical class, the three principal refractive indices are equal to $n(\omega)$ so that the physical properties are identical along any direction of propagation. Crystals from the cubic system, as well as gas liquids and glasses, belong to the isotropic optical class.

Crystals of the tetragonal, hexagonal and trigonal systems belong to the uniaxial optical class. In that case, one defines the ordinary and extraordinary principal refractive indices, n_o and n_e respectively, as [1]: $n_x(\omega) = n_y(\omega) = n_o(\omega)$ and $n_z(\omega) = n_e(\omega)$. The uniaxial optical class is positive if $n_o(\omega) < n_e(\omega)$ and negative if $n_o(\omega) > n_e(\omega)$.

The triclinic, monoclinic and orthorhombic crystals belong to the biaxial optical class, which is either positive when $n_x(\omega) < n_y(\omega) < n_z(\omega)$, or negative when $n_x(\omega) > n_y(\omega) > n_z(\omega)$.

The variation of a principal refractive index with the angular frequency is well described by a Sellmeier equation in the transparency domain of crystals [3].

In the case of the so called “normal dispersion”, all the refractive indices increase with the angular frequency *i.e.* $n_i(\omega_1) < n_i(\omega_2)$ for $\omega_1 < \omega_2$, with $i = x, y$ or z . If ω_1 or ω_2 is near an absorption peak, even weak, we can have $n_i(\omega_1) > n_i(\omega_2)$, with $i = x, y$ or z , which corresponds to an “abnormal dispersion”.

1.2.3 Propagation equation

The wave propagation equation in a crystal is obtained from the constitutive relations of the medium and Maxwell’s equations. In the case of a non-conducting and non-

magnetic crystal, the wave propagation equation at the angular frequency ω is given at the position \vec{r} by the following equation [2]:

$$\vec{\nabla} \times \vec{\nabla} \times \vec{E}(\omega) = \frac{\omega^2}{c^2} \vec{E}(\omega) + \omega^2 \mu_o \vec{P}(\omega) \quad (1.6)$$

μ_o is the free-space permeability and the symbol \times stands for a vector product. By inserting Eq. (1.1) in Eq. (1.6) and using Eq. (1.3), we get:

$$\vec{\nabla} \times \vec{\nabla} \times \vec{E}(\omega) = \frac{\omega^2}{c^2} \epsilon_r(\omega) \cdot \vec{E}(\omega) \quad (1.7)$$

The plane wave is a solution of Eq. (1.7). At the angular frequency ω and position \vec{r} , the spatial component of the electric field propagating forward is then written:

$$\vec{E}(\omega, \vec{r}) = \vec{e}(\omega, \vec{r}) E(\omega, \vec{r}) e^{-i\vec{k}(\omega, \vec{r}) \cdot \vec{r}} \quad (1.8)$$

$\vec{e}(\omega, \vec{r})$ is the unit electric field vector, and $E(\omega, \vec{r})$ the scalar complex amplitude of the electric field verifying $E^*(\omega, \vec{r}) = E(-\omega, \vec{r})$. $\vec{k}(\omega, \vec{r})$ stands for the wave vector along the unit vector \vec{u} describing the direction of propagation.

We will use the angles of spherical coordinates (θ, φ) instead of the Cartesian coordinates (u_x, u_y, u_z) to describe the unit vector \vec{u} with $|\vec{u}| = 1$ in the dielectric frame. As shown in Figure 1.1, θ is the angle between \vec{u} and the z -axis, while φ is the angle between the orthogonal projection of \vec{u} in the x - y plane and the x -axis.

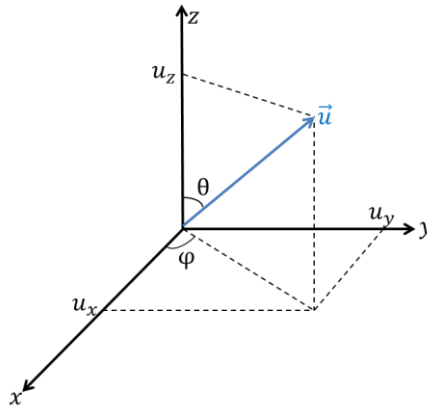


Figure 1.1: Cartesian (u_x, u_y, u_z) and spherical coordinates (θ, φ) of the unit vector \vec{u} in the dielectric frame (x, y, z) .

The Cartesian and spherical coordinates are linked by:

$$u_x = \cos\varphi \sin\theta, u_y = \sin\varphi \sin\theta, u_z = \cos\theta, \quad (1.9)$$

1.2.4 Index surface

In the transparency range of crystals, the projection of Eq. (1.7) on the three principal axes of the dielectric frame x , y and z , and the use of Eq. (1.9) allow to define Fresnel's equation [3]:

$$\frac{(\cos\varphi\sin\theta)^2}{n^{-2}(\omega,\theta,\varphi)-n_x^{-2}(\omega)} + \frac{(\sin\varphi\sin\theta)^2}{n^{-2}(\omega,\theta,\varphi)-n_y^{-2}(\omega)} + \frac{(\cos\theta)^2}{n^{-2}(\omega,\theta,\varphi)-n_z^{-2}(\omega)} = 0 \quad (1.10)$$

$n_x(\omega)$, $n_y(\omega)$ and $n_z(\omega)$ are the three principal refractive indices at the angular frequency ω defined by Eq. (1.5).

$n(\omega, \theta, \varphi)$ is the refractive index along the direction of propagation \vec{u} that can be found by solving Fresnel's equation. Since Eq. (1.10) is a quadratic equation, it has two solutions, $n^+(\omega, \theta, \varphi)$ and $n^-(\omega, \theta, \varphi)$. Taking into account the relation of order $n^+(\omega, \theta, \varphi) \geq n^-(\omega, \theta, \varphi)$ they are expressed as [3]:

$$\begin{cases} n^{\pm}(\omega, \theta, \varphi) = \left(\frac{2}{-B \mp (B^2 - 4C)^{1/2}} \right)^{1/2} \\ B = -u_x^2(b+c) - u_y^2(a+c) - u_z^2(a+b) \\ C = u_x^2bc + u_y^2ac + u_z^2ab \\ a = n_x^{-2}(\omega), b = n_y^{-2}(\omega), c = n_z^{-2}(\omega) \end{cases} \quad (1.11)$$

Equation (1.11) describes the double-sheeted three-dimensional index surface. It is shown in 1/8 of the dielectric frame in Figure 1.2 and Figure 1.3 for uniaxial and biaxial optical classes respectively. Along the direction of propagation $\vec{u}(\theta, \varphi)$, the distances between the origin of the dielectric frame and the external sheet (+) and the internal sheet (-) correspond to the index values $n^+(\omega, \theta, \varphi)$ and $n^-(\omega, \theta, \varphi)$ respectively. The quantity $n^+(\omega, \theta, \varphi) - n^-(\omega, \theta, \varphi)$ is called the birefringence of the crystal.

1.2.4.1 Uniaxial index surface

Figures 1.2(a) and 1.2(b) depict in 1/8 of the dielectric frame the index surface of the positive and negative uniaxial optical class respectively [3]. They show that the two sheets of the index surface do not depend on the spherical angle φ . They also highlight two umbilici corresponding to the z -axis regardless with the angular frequency ω , where $n^+(\omega, \theta) = n^-(\omega, \theta)$. The z -axis is called the optical axis (OA), which explains why this optical class is called uniaxial.

The index values are linked to the principal ordinary and extraordinary refractive indices $n_o(\omega)$ and $n_e(\omega)$ as follows: in the x - z and y - z principal planes, the ordinary

sheet is spherical with the index value $n_o(\omega)$ and the extraordinary sheet is ellipsoidal with the index value $n^e(\omega, \theta) = \left[\frac{\cos^2 \theta}{n_o^2(\omega)} + \frac{\sin^2 \theta}{n_e^2(\omega)} \right]^{-1/2}$.

For the positive uniaxial optical class,

$$n^+(\omega, \theta, \varphi) = n^+(\omega, \theta) = n^e(\omega, \theta) \text{ and } n^-(\omega, \theta, \varphi) = n_o(\omega).$$

For the negative uniaxial optical class,

$$n^+(\omega, \theta, \varphi) = n_o(\omega) \text{ and } n^-(\omega, \theta, \varphi) = n^e(\omega, \theta).$$

In the x - y principal plane, the two sheets are circular, the index value being $n_o(\omega)$ for one and $n_e(\omega)$ for the other one.

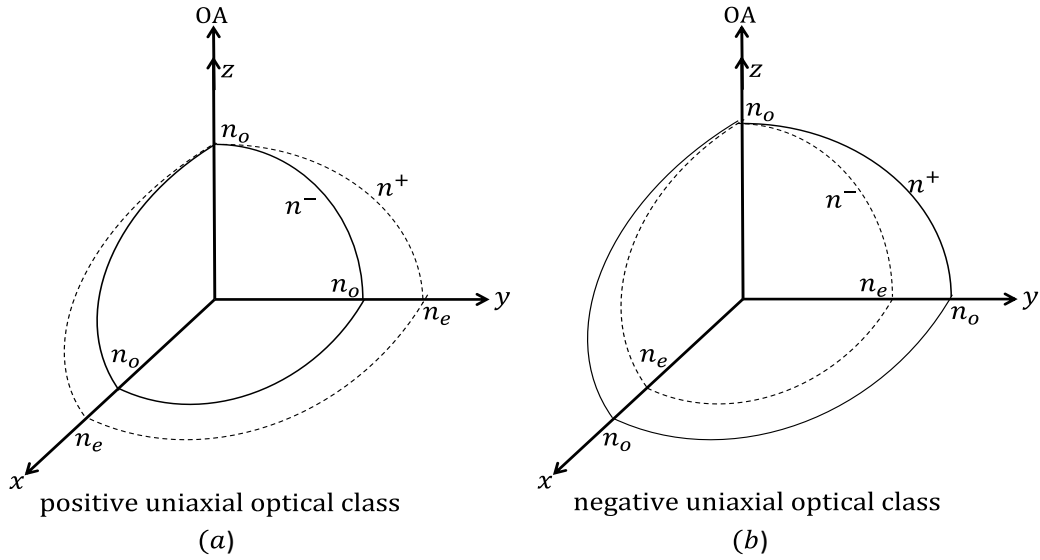


Figure 1.2: Index surface of the positive (a) and negative (b) uniaxial optical class at the angular frequency ω depicted in 1/8 of the dielectric frame. The solid line corresponds to an ordinary sheet and the dashed line to an extraordinary sheet. n^+ and n^- represent the indices values of the external and internal sheets respectively. OA stands for the optical axis.

1.2.4.2 Biaxial index surface

The index surfaces of the positive and negative biaxial optical class are depicted in 1/8 of the dielectric frame in Figure 1.3(a) and 1.3(b) respectively [3]. The refractive indices $n^+(\omega, \theta, \varphi)$ and $n^-(\omega, \theta, \varphi)$ are given by Eq. (1.11). They also correspond in the three principal planes to indices values of a circular sheet and an elliptic sheet. In the y - z principal plane where $\varphi = 90^\circ$ for example, we get for a positive biaxial crystal:

$$\begin{cases} n^+(\omega, \theta, \varphi) = \left[\frac{\cos^2(\theta)}{n_y^2(\omega)} + \frac{\sin^2(\theta)}{n_z^2(\omega)} \right]^{-1/2} \\ n^-(\omega, \theta, \varphi) = n_x(\omega) \end{cases} \quad (1.12)$$

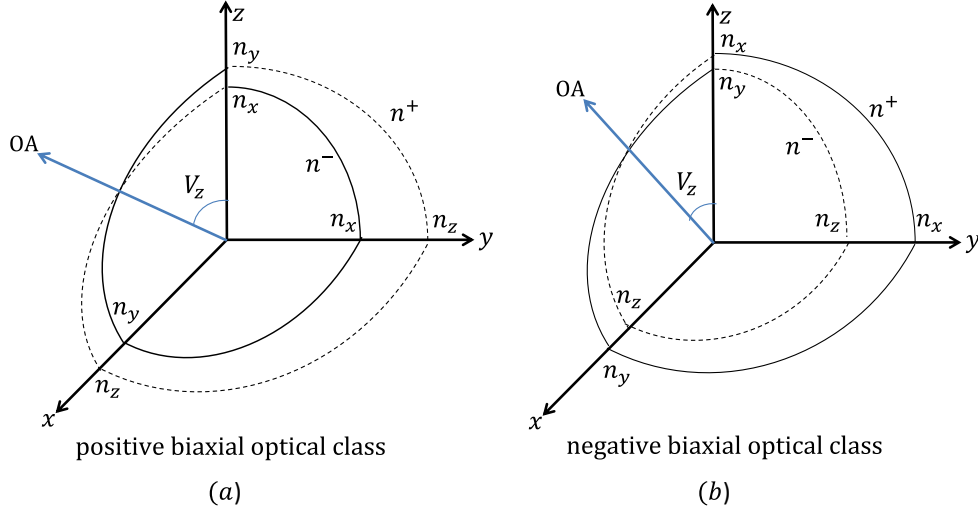


Figure 1.3: Index surface of the positive (a) and negative (b) biaxial optical class at the angular frequency ω depicted in 1/8 of the dielectric frame. The solid line corresponds to an ordinary sheet and the dashed line corresponds to an extraordinary sheet. n^+ and n^- stand for the indices values of the external and internal sheets respectively. V_z is the angle between the shown optical axis OA and z-axis.

The index surface of the biaxial optical class has four umbilici located in the x - z principal plane, which define by pair two optical axes (OA). It explains why this optical class is called biaxial. Along an optical axis, $n^+(\omega, \theta, \varphi) = n^-(\omega, \theta, \varphi)$ as shown in Figure 1.3. Using the Eq. (1.11), we can find that the angle between an optical axis and the z -axis named V_z varies with the angular frequency ω as follows:

$$\sin^2 V_z(\omega) = \frac{n_y^{-2}(\omega) - n_x^{-2}(\omega)}{n_z^{-2}(\omega) - n_x^{-2}(\omega)} \quad (1.13)$$

1.2.5 Spatial walk-off

When an electromagnetic wave at the angular frequency ω propagates in the direction of propagation \vec{u} of the dielectric frame, there are two possible electric field vectors $\vec{E}^+(\omega, \theta, \varphi)$ and $\vec{E}^-(\omega, \theta, \varphi)$. They correspond to the two unit electric field vectors $\vec{e}^+(\omega, \theta, \varphi)$ and $\vec{e}^-(\omega, \theta, \varphi)$ that define two polarization states of light.

There are also two possible magnetic field vectors $\vec{H}^+(\omega, \theta, \varphi)$ and $\vec{H}^-(\omega, \theta, \varphi)$ corresponding to the two unit vectors $\vec{h}^+(\omega, \theta, \varphi)$ and $\vec{h}^-(\omega, \theta, \varphi)$, and two possible electrical displacement vectors $\vec{D}^+(\omega, \theta, \varphi)$ and $\vec{D}^-(\omega, \theta, \varphi)$ corresponding to the unit vectors $\vec{d}^+(\omega, \theta, \varphi)$ and $\vec{d}^-(\omega, \theta, \varphi)$.

According to Eq. (1.3), the unit vectors $\vec{d}^\pm(\omega, \theta, \varphi)$ and $\vec{e}^\pm(\omega, \theta, \varphi)$ are in the same plane but non collinear to each other. Their directions make angles called the walk-off angles defined by [3]:

$$\rho^\pm(\omega, \theta, \varphi) = \arccos[\vec{e}^\pm(\omega, \theta, \varphi) \cdot \vec{d}^\pm(\omega, \theta, \varphi)] \quad (1.14)$$

where \bullet is a scalar product. Similarly, the energy flux is described by the two following Poynting vectors $\vec{S}^\pm(\omega, \theta, \varphi)$:

$$\vec{S}^\pm(\omega, \theta, \varphi) = \vec{E}^\pm(\omega, \theta, \varphi) \times \vec{H}^\pm(\omega, \theta, \varphi) \quad (1.15)$$

According to Eq. (1.15), the unit Poynting vectors $\vec{s}^\pm(\omega, \theta, \varphi)$ are perpendicular to both the unit vectors $\vec{e}^\pm(\omega, \theta, \varphi)$ and $\vec{h}^\pm(\omega, \theta, \varphi)$.

Furthermore the unit vectors, $\vec{s}^\pm(\omega, \theta, \varphi)$, $\vec{e}^\pm(\omega, \theta, \varphi)$ and $\vec{h}^\pm(\omega, \theta, \varphi)$ all propagate along the two possible wave vectors expressed as:

$$\vec{k}^\pm(\omega, \theta, \varphi) = \left(\frac{\omega}{c}\right)n^\pm(\omega, \theta, \varphi)\vec{u}(\theta, \varphi) \quad (1.16)$$

where $n^+(\omega, \theta, \varphi)$ and $n^-(\omega, \theta, \varphi)$ are the refractive indices given by Eq. (1.11). But according to Maxwell's equations, only $\vec{h}^\pm(\omega, \theta, \varphi)$ and $\vec{d}^\pm(\omega, \theta, \varphi)$ are perpendicular to $\vec{k}^\pm(\omega, \theta, \varphi)$.

Figure 1.4(a) shows their orientation for a direction of propagation \vec{u} of the dielectric frame. As an example it is detailed in Figure 1.4(b) in the x - z ($= y$ - z) principal plane of a positive uniaxial crystal, when taking into account the two sheets of the index surface.

As highlighted in Figure 1.4(b), the walk-off angles are also defined as follows [4]:

$$\rho^\pm(\omega, \theta, \varphi) = \arccos \left[\frac{\vec{s}^\pm(\omega, \theta, \varphi) \cdot \vec{k}^\pm(\omega, \theta, \varphi)}{\|\vec{s}^\pm(\omega, \theta, \varphi)\| \|\vec{k}^\pm(\omega, \theta, \varphi)\|} \right] \quad (1.17)$$

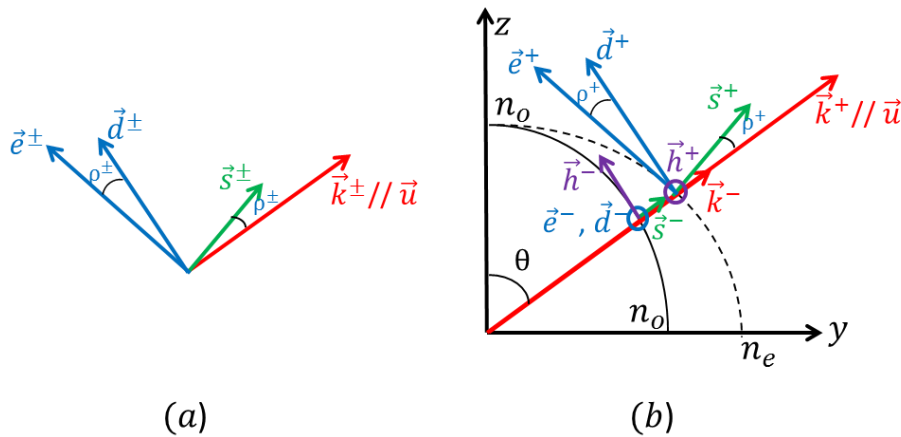


Figure 1.4: Orientation between the fields unit vectors and walk-off angles for a direction of propagation \vec{u} (a) of the dielectric frame and (b) of the y - z ($= x$ - z) plane of a positive uniaxial crystal.

The Poynting vector is always normal to the ordinary index sheet as is it the case for the wave vector (see for example Figure 1.4(b)) [3]. Then Eq. (1.17) shows that all spatial walk-off angles are equal to zero in the x - y principal plane of uniaxial crystals where both sheets of the index surface are circular *i.e.* $\rho^\pm(\omega, \varphi) = 0$. Only one spatial walk-off angle is equal to zero in the other principal planes of uniaxial crystals and in all principal planes of biaxial crystals where one sheet is circular.

Otherwise, the spatial walk-off angle is generally different from zero for the elliptical sheets (see for example Figure 1.4(b)). It reaches a maximal value when the direction of propagation is oriented at 45° from any principal axis but vanishes to zero along the three principal axes of the dielectric frame x , y or z .

For the elliptical sheet it can be written at the angular frequency ω as follows [3]:

$$\rho_{lm}(\omega, \alpha) = \arccos \left[\frac{[n_m^2(\omega)/n_l^2(\omega)]\cos^2\alpha + \sin^2\alpha}{[n_m^4(\omega)/n_l^4(\omega)]\cos^2\alpha + \sin^2\alpha} \right] \quad (1.18)$$

with $l, m = x, y$ or z and $\alpha = \theta$ or φ .

Then in the $(x-z) = (y-z)$ principal plane of a positive uniaxial crystal where $\alpha = \theta$, $\rho^+(\omega, \theta) = \rho_{oe}(\omega, \theta)$ and $\rho^-(\omega, \theta) = 0$; But $\rho^-(\omega, \theta) = \rho_{oe}(\omega, \theta)$ and $\rho^+(\omega, \theta) = 0$ for a negative uniaxial crystal.

Eq (1.18) can be used to describe $\rho^\pm(\omega, \theta, \varphi)$ in the three l - m principal planes of positive biaxial crystals and all possibilities are summarized in Table 1.1.

Note that Table 1.1 can also be applied to a negative biaxial crystal after exchanging all the signs (+) and (-).

According to the previous properties of the walk-off angle taking into account the index surface, $\rho^\pm(\omega, \theta, \varphi)$ also correspond to the angles between the unit Poynting vectors $\vec{s}^-(\omega, \theta, \varphi)$ and $\vec{s}^+(\omega, \theta, \varphi)$ in the principal planes of uniaxial or biaxial crystals where it is also defined by [3]:

$$\rho^\pm(\omega, \theta, \varphi) = \arccos[\vec{s}^-(\omega, \theta, \varphi) \cdot \vec{s}^+(\omega, \theta, \varphi)] \quad (1.19)$$

For example, it is $\rho^+(\omega, \theta) = \rho_{oe}(\omega, \theta)$ in Figure 1.4(b) describing a positive uniaxial crystal.

Principal plane $l-m$	\vec{e}^-	\vec{e}^+	$\pm \rho^\mp$
$x-y$	$e_x^o = -\sin[\varphi + \rho^-(\omega, \varphi)]$ $e_y^o = \cos[\varphi + \rho^-(\omega, \varphi)]$ $e_z^o = 0$	$e_x^e = 0$ $e_y^e = 0$ $e_z^e = 1$	$+\rho^-(\omega, \varphi) = \rho_{l=y, m=x}(\omega, \varphi)$ and $\rho^+(\omega, \varphi) = 0$
$y-z$	$e_x^o = -1$ $e_y^o = 0$ $e_z^o = 0$	$e_x^e = 0$ $e_y^e = -\cos[\theta - \rho^+(\omega, \theta)]$ $e_z^e = \sin[\theta - \rho^+(\omega, \theta)]$	$-\rho^+(\omega, \theta) = \rho_{l=y, m=z}(\omega, \theta)$ and $\rho^-(\omega, \theta) = 0$
$x-z$ ($0^\circ < \theta < V_z$)	$e_x^e = -\cos[\theta - \rho^-(\omega, \theta)]$ $e_y^e = 0$ $e_z^e = \sin[\theta - \rho^-(\omega, \theta)]$	$e_x^o = 0;$ $e_y^o = 1;$ $e_z^o = 0$	$-\rho^-(\omega, \theta) = \rho_{l=x, m=z}(\omega, \theta)$ and $\rho^+(\omega, \theta) = 0$
$x-z$ ($V_z < \theta < 90^\circ$)	$e_x^o = 0;$ $e_y^o = -1;$ $e_z^o = 0$	$e_x^e = -\cos[\theta - \rho^+(\omega, \theta)]$ $e_y^e = 0$ $e_z^e = \sin[\theta - \rho^+(\omega, \theta)]$	$-\rho^+(\omega, \theta) = \rho_{l=x, m=z}(\omega, \theta)$ and $\rho^-(\omega, \theta) = 0$

Table 1.1: Analytical expressions of the walk-off angles $\rho^\pm(\omega, \theta, \varphi)$ and the electric field unit vectors $\vec{e}^\pm(\omega, \theta, \varphi)$ in the three principal planes of a positive biaxial crystal. It can be used to describe a negative biaxial crystal after exchanging all the signs (+) and (-).

1.2.6 Polarization states

The components of the electric field unit vectors $\vec{e}^+(\omega, \theta, \varphi)$ and $\vec{e}^-(\omega, \theta, \varphi)$ can be determined along the direction of propagation $\vec{u}(\theta, \varphi)$ by projecting the propagation equation (1.7) along the three principal axes of the optical frame, with the relation $(e_x^\pm)^2 + (e_y^\pm)^2 + (e_z^\pm)^2 = 1$. Three equations related to (e_x, e_y, e_z) and (u_x, u_y, u_z) are then obtained as a function of the angles of spherical coordinates. They write [3]:

$$(n^\pm(\omega, \theta, \varphi))^2 (e_p^\pm - u_p(\theta, \varphi) [u_x(\theta, \varphi) e_x^\pm + u_y(\theta, \varphi) e_y^\pm + u_z(\theta, \varphi) e_z^\pm]) = (n_p(\omega))^2 e_p^\pm \quad (1.20)$$

where $p = x, y$ or z and u_x, u_y, u_z are given by Eq. (1.9). The refractive indices $n^\pm(\omega, \theta, \varphi)$ can be calculated in the direction of propagation $\vec{u}(\theta, \varphi)$ by using Eq. (1.11) and knowing the principal refractive indices $n_p(\omega)$.

In the case of a uniaxial crystal, the two electric field unit vectors $\vec{e}^-(\omega, \theta, \varphi)$ and $\vec{e}^+(\omega, \theta, \varphi)$ correspond to the ordinary or extraordinary electric field unit vectors $\vec{e}^o(\omega, \theta, \varphi)$ and $\vec{e}^e(\omega, \theta, \varphi)$ defined by the following analytical expressions [3]:

$$\vec{e}^o = \begin{pmatrix} -\sin\varphi \\ +\cos\varphi \\ 0 \end{pmatrix} \quad (1.21)$$

$$\vec{e}^e = \begin{pmatrix} -\cos[\theta \pm \rho^\mp(\omega, \theta)] \cdot \cos\varphi \\ -\cos[\theta \pm \rho^\mp(\omega, \theta)] \cdot \sin\varphi \\ \sin[\theta \pm \rho^\mp(\omega, \theta)] \end{pmatrix} \quad (1.22)$$

According to Eq. (1.21) and (1.22), the two polarization states of light are linear in a crystal

from the uniaxial optical class. For the positive uniaxial optical class, $\vec{e}^- = \vec{e}^o$, $\vec{e}^+ = \vec{e}^e$ and $\pm \rho^\mp(\omega, \theta) = -\rho^+(\omega, \theta)$; But for the negative uniaxial optical class, $\vec{e}^- = \vec{e}^e$, $\vec{e}^+ = \vec{e}^o$ and $\pm \rho^\mp(\omega, \theta) = +\rho^-(\omega, \theta)$, $\rho^\pm(\omega, \theta)$ standing for the optical walk-off angles detailed in part 1.2.5.

In the principal planes of a biaxial crystal, the two electric field unit vectors $\vec{e}^-(\omega, \theta, \varphi)$ and $\vec{e}^+(\omega, \theta, \varphi)$ are as a function of the ordinary or extraordinary unit electric field vectors, according to the analytical expressions summarized in Table 1.1.

Finally, in any direction of a uniaxial crystal, and in the principal planes of a biaxial crystal, Eq (1.21), Eq.(1.22) and Table 1.1 show that the electric field unit vectors $\vec{e}^+(\omega, \theta, \varphi)$ and $\vec{e}^-(\omega, \theta, \varphi)$ remain always tangent to the index sheet (+) and (-) respectively. Furthermore, $\vec{e}^+(\omega, \theta, \varphi)$ is always orthogonal to $\vec{e}^-(\omega, \theta, \varphi)$.

Out of the principal planes of a biaxial crystal, $\vec{e}^+(\omega, \theta, \varphi) \bullet \vec{e}^-(\omega, \theta, \varphi) = 0$ is not fulfilled and the expressions of the two electric field unit vectors that are solutions of Eq. (1.20) become numerical.

1.3 Nonlinear optics

1.3.1 Nonlinear induced polarization

With the advent of lasers, the available power density is much higher than what could be produced by any conventional source. When the power density of the exciting electric field is greater than about 1 MW/cm^2 , it is possible to detect with current detectors the nonlinear optical phenomena, leading to a great variety of applications. Provided the power density remains lower than the TW/cm^2 , each Fourier component of the induced polarization \vec{P} of the medium can be developed in a Taylor power series of the applied electric field \vec{E} at the position \vec{r} as follows [3]:

$$\begin{aligned} \vec{P}(\omega) = & \varepsilon_o \chi^{(1)}(\omega) \cdot \vec{E}(\omega) + \varepsilon_o \chi^{(2)}(\omega = \omega_1 \pm \omega_2) : \vec{E}(\omega_1) \otimes \vec{E}(\pm \omega_2) \\ & + \varepsilon_o \chi^{(3)}(\omega = \omega_1 \pm \omega_2 \pm \omega_3) : \vec{E}(\omega_1) \otimes \vec{E}(\pm \omega_2) \otimes \vec{E}(\pm \omega_3) + \dots \end{aligned} \quad (1.23)$$

$\chi^{(2)}$ and $\chi^{(3)}$ are the second- and third-order electric susceptibilities that are third- and fourth-rank tensors, respectively. The dots ($\cdot, :, \cdot$) stand for contracted products, while \otimes are tensor products. The first term in Eq. (1.23) corresponds to the polarization governing linear optics, and the two other terms govern the nonlinear second- and third-order optical properties respectively.

In this work, only the second-order nonlinear optics is considered. It corresponds to the interaction between three electromagnetic waves at the angular frequencies ω_1 , ω_2 , and ω_3 , with the energy conservation relation and the following relation of order:

$$\begin{cases} \hbar\omega_1 + \hbar\omega_2 = \hbar\omega_3 \\ (\omega_1 \leq \omega_2 < \omega_3) \end{cases} \quad (1.24)$$

The second-order induced polarization at each angular frequency is then expressed at the position \vec{r} as:

$$\begin{cases} \vec{P}^{(2)}(\omega_1) = \epsilon_o \chi^{(2)}(\omega_1 = \omega_3 - \omega_2) : \vec{E}(\omega_3) \otimes \vec{E}^*(\omega_2) \\ \vec{P}^{(2)}(\omega_2) = \epsilon_o \chi^{(2)}(\omega_2 = \omega_3 - \omega_1) : \vec{E}(\omega_3) \otimes \vec{E}^*(\omega_1) \\ \vec{P}^{(2)}(\omega_3) = \epsilon_o \chi^{(2)}(\omega_3 = \omega_1 + \omega_2) : \vec{E}(\omega_1) \otimes \vec{E}(\omega_2) \end{cases} \quad (1.25)$$

where $\vec{E}^*(\omega_i) = \vec{E}(-\omega_i)$ and $i = 1, 2, 3$. Eq. (1.25) shows 3 possible frequency conversion processes allowed in a nonlinear crystal, *i.e.* from top to down:

Difference-frequency generation between ω_3 and ω_2 , written DFG ($\omega_1 = \omega_3 - \omega_2$);

Difference-frequency generation between ω_3 and ω_1 written DFG ($\omega_2 = \omega_3 - \omega_1$);

Sum-frequency generation between ω_1 and ω_2 written SFG ($\omega_3 = \omega_1 + \omega_2$).

For example, Figure 1.5(a) and Figure 1.5(b) give the schemes of DFG ($\omega_1 = \omega_3 - \omega_2$) and SFG ($\omega_3 = \omega_1 + \omega_2$) respectively, in a crystal cut at the phase-matching (PM) angle ($\theta_{PM}, \varphi_{PM}$). The degenerate case of sum-frequency generation, for which $\omega_2 = \omega_1 = \omega$ and $\omega_3 = 2\omega$, is called second-harmonic generation, SFG, is written SHG ($2\omega = \omega + \omega$).

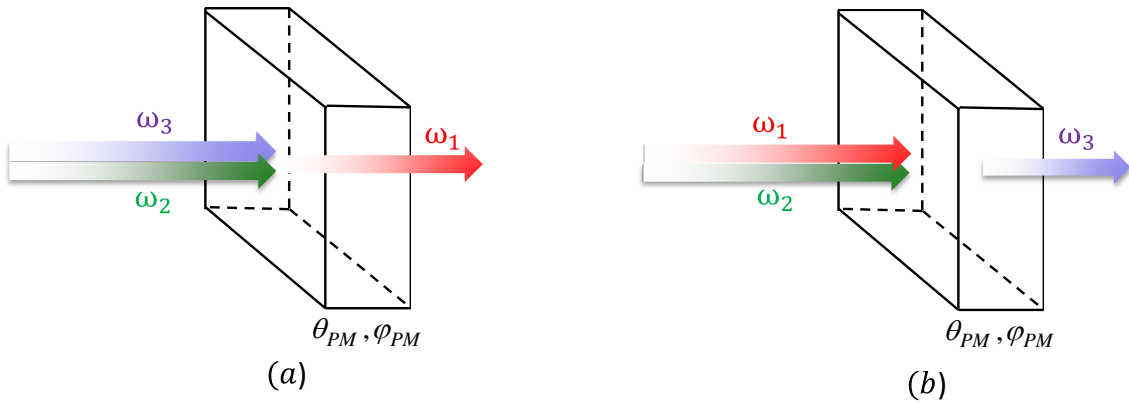


Figure 1.5: DFG ($\omega_1 = \omega_3 - \omega_2$) (a) and SFG ($\omega_3 = \omega_1 + \omega_2$) (b). θ_{PM} and φ_{PM} represent the corresponding phase-matching angles.

The second-order electric susceptibility tensor $\chi^{(2)}(\omega_i)$ has 27 independent elements in the general case [3]. Neumann principle allows some elements to equal to zero and the others which magnitudes to be equal or of opposite sign. Furthermore, in the case of low absorption and low dispersion at the considered angular frequencies, Kleinman's conditions reduce more the number of independent non-zero elements [4]. The tensor $\chi^{(2)}(\omega_i)$ of the crystals studied in present work will be detailed in chapters 3 and 4.

The electric second-order susceptibility tensor also depends on the angular frequency, which is well described by Miller's rule arising from the Lorentz model, *i.e.* [5]:

$$\chi_{ijk}^{(2)}(\omega = \omega_1 \pm \omega_2) = \delta_{ijk} \chi_{ii}^{(1)}(\omega = \omega_1 \pm \omega_2) \chi_{jj}^{(1)}(\omega_1) \chi_{kk}^{(1)}(\pm \omega_2) \quad (1.26)$$

δ_{ijk} is called the Miller index, which does not depend on the angular frequency. From Eq. (1.26), it is possible to calculate the value of any $\chi_{ijk}^{(2)}$ coefficient at any angular frequency $\omega_A = \omega_{A1} \pm \omega_{A2}$ knowing the value of this coefficient at a given angular frequency $\omega_B = \omega_{B1} \pm \omega_{B2}$ as well as the values of the principal refractive indices at all the angular frequencies that are concerned. $\chi_{ijk}^{(2)}$ and $\chi_{ijk}^{(2)}$ are related by the relation [5]:

$$\chi_{ijk}^{(2)}(\omega_A = \omega_{A1} \pm \omega_{A2}) = \chi_{ijk}^{(2)}(\omega_B = \omega_{B1} \pm \omega_{B2}) \cdot \frac{\chi_{ii}^{(1)}(\omega_A) \chi_{jj}^{(1)}(\omega_{A1}) \chi_{kk}^{(1)}(\pm \omega_{A2})}{\chi_{ii}^{(1)}(\omega_B) \chi_{jj}^{(1)}(\omega_{B1}) \chi_{kk}^{(1)}(\pm \omega_{B2})} \quad (1.27)$$

Where $\chi_{aa}^{(1)}(\omega) = n_a^2(\omega) - 1$ ($a = i, j$ and k).

1.3.2 Propagation equation

According to Eqs. (1.6), (1.23) and (1.25), the propagation equation of each interacting wave is written at the position \vec{r} and the angular frequency ω_i as [4]:

$$\vec{\nabla} \times \vec{\nabla} \times \vec{E}(\omega_i) = \frac{\omega_i^2}{c^2} \epsilon_r(\omega_i) \cdot \vec{E}(\omega_i) + \omega_i^2 \mu_o \vec{P}^{(2)}(\omega_i) \quad (1.28)$$

with $i = 1, 2$ or 3 and the symbols \cdot and \times standing for contracted and vector products respectively. Then three propagation equations are coupled by the Fourier components of the nonlinear polarization $\vec{P}^{(2)}(\omega_1)$, $\vec{P}^{(2)}(\omega_2)$ and $\vec{P}^{(2)}(\omega_3)$ given by Eq. (1.25).

When studying a collinear interaction between the three interacting waves, it leads to the variation of three complex amplitudes $\vec{E}(\omega_i)$ along the same spatial coordinate Z -

axis that is collinear to the direction of propagation unit vector $\vec{u}(\theta, \varphi)$. Note that Z-axis is from the laboratory frame (X, Y, Z) that is different from the dielectric frame (x, y, z).

In the slowly varying envelope approximation, which corresponds to a small variation of the wave amplitudes over one wavelength, it is possible to get the three following coupled equations:

$$\begin{cases} \frac{\partial E(\omega_1, Z)}{\partial Z} = j\kappa_1 \chi_{eff} E(\omega_3, Z) E^*(\omega_2, Z) \exp(j\Delta k Z) \\ \frac{\partial E(\omega_2, Z)}{\partial Z} = j\kappa_2 \chi_{eff} E(\omega_3, Z) E^*(\omega_1, Z) \exp(j\Delta k Z) \\ \frac{\partial E(\omega_3, Z)}{\partial Z} = j\kappa_3 \chi_{eff} E(\omega_1, Z) E(\omega_2, Z) \exp(-j\Delta k Z) \end{cases} \quad (1.29)$$

With $\kappa_i = \frac{\omega_i}{2c\epsilon_0 n(\omega_i, \theta, \varphi) \cos^2 \rho(\omega_i, \theta, \varphi)}$, χ_{eff} is the effective coefficient.

The product $\Delta k Z$ is the phase-mismatch between the nonlinear polarization, $\vec{P}^{(2)}(\omega_i)$, and the electric field, $\vec{E}(\omega_i)$, radiated by the nonlinear polarization it-self. Since studying a collinear interaction, $\Delta k = k^\pm(\omega_3, \theta, \varphi) - k^\pm(\omega_1, \theta, \varphi) - k^\pm(\omega_2, \theta, \varphi)$ with $k^\pm(\omega_i, \theta, \varphi)$ defined by Eq. (1.16).

1.3.3 Energy of the generated wave

We consider here the example of the energy generated by SFG ($\omega_3 = \omega_1 + \omega_2$) under the undepleted pump approximation. It means that the variation of the amplitude of the electric fields at the angular frequencies ω_1 and ω_2 is negligible along the propagation direction Z. Then $E(\omega_1, Z) \simeq E(\omega_1, 0)$ and $E(\omega_2, Z) \simeq E(\omega_2, 0)$, and the energy of the generated wave at the angular frequency ω_3 is given by:

$$\varepsilon(\omega_3, Z) = \beta \frac{A}{\lambda_1 \lambda_2} G(Z, w_o, \rho) \chi_{eff}^2 \varepsilon(\omega_1, 0) \varepsilon(\omega_2, 0) Z^2 \text{sinc}^2\left(\frac{\Delta k Z}{2}\right) \quad (1.30)$$

with
$$A = \frac{T^\pm(\omega_3, \theta, \varphi) T^\pm(\omega_1, \theta, \varphi) T^\pm(\omega_2, \theta, \varphi)}{n^\pm(\omega_3, \theta, \varphi) n^\pm(\omega_1, \theta, \varphi) n^\pm(\omega_2, \theta, \varphi)} \quad (1.31)$$

β is the coefficient related with the geometry and cross-section of all the beams, and $\lambda_i = 2\pi c / \omega_i$ ($i = 1, 2$ or 3) is the wavelength of the input beams. $T^\pm(\omega_i, \theta, \varphi) = 4n^\pm(\omega_i, \theta, \varphi) / (n^\pm(\omega_i, \theta, \varphi) + 1)^2$ stands for the transmission coefficient. $n^\pm(\omega_i, \theta, \varphi)$ are the refractive indices expressed by Eq. (1.11). G is the spatial walk-off attenuation that will be defined in detail in part 1.3.7.

1.3.4 Effective coefficient χ_{eff}

Eq. (1.30) shows that the effective coefficient χ_{eff} is a very important parameter in the expression of the energy of the generated wave. The effective coefficient depends both on the polarization modes of the three interacting waves and on the second-order electric susceptibility of the crystal. For example, it comes for SFG [6]:

$$\chi_{eff}(\omega_3, \omega_1, \omega_2, \theta, \varphi) = \vec{e}^\pm(\omega_3, \theta, \varphi) \cdot [\chi^{(2)}(\omega_3 = \omega_1 + \omega_2) : \vec{e}^\pm(\omega_1, \theta, \varphi) \otimes \vec{e}^\pm(\omega_2, \theta, \varphi)] \quad (1.32)$$

The dots \cdot and $:$ stand for contracted products, and \otimes is the tensor product. The vectors $\vec{e}^\pm(\omega_i, \theta, \varphi)$ with $i = 1, 2$ or 3 correspond to the unit electric field vectors of the interacting waves given in part 1.2.6. Then, Eq. (1.32) can be also written:

$$\chi_{eff}(\omega_3, \omega_1, \omega_2, \theta, \varphi) = \sum_{ijk} \vec{e}_i^\pm(\omega_3, \theta, \varphi) \chi_{ijk}^{(2)}(\omega_3 = \omega_1 + \omega_2) \vec{e}_j^\pm(\omega_1, \theta, \varphi) \vec{e}_k^\pm(\omega_2, \theta, \varphi) \quad (1.33)$$

The indices i, j and k correspond to the Cartesian indices x, y or z . e_i^\pm, e_j^\pm and e_k^\pm are the Cartesian coordinates of the unit electric field vectors of the three interacting waves. Then for SFG, the effective coefficient is related to the polarization configuration and also to the non-zero elements of the tensor $\chi^{(2)}$ at the generated angular frequency ω_3 . The notation $d_{eff} = \chi_{eff}/2$ will be also used in the following chapters.

Note that the polarization state of the three interacting waves, can be described by a field tensor defined as [6]:

$$F^{(2)}(\omega_3, \omega_1, \omega_2, \theta, \varphi) = \vec{e}^\pm(\omega_3, \theta, \varphi) \otimes \vec{e}^\pm(\omega_1, \theta, \varphi) \otimes \vec{e}^\pm(\omega_2, \theta, \varphi) \quad (1.34)$$

$F^{(2)}$ is also a second-order tensor with 27 elements and can be also written:

$$F_{ijk}^{(2)}(\omega_3, \omega_1, \omega_2, \theta, \varphi) = \vec{e}_i^\pm(\omega_3, \theta, \varphi) \vec{e}_j^\pm(\omega_1, \theta, \varphi) \vec{e}_k^\pm(\omega_2, \theta, \varphi) \quad (1.35)$$

Then, according to Eq. (1.33), (1.34) and (1.35), the effective coefficient becomes:

$$\chi_{eff}(\omega_3 = \omega_1 + \omega_2, \theta, \varphi) = \chi^{(2)}(\omega_3) \cdot F^{(2)}(\omega_3, \omega_1, \omega_2, \theta, \varphi) = \sum_{ijk} \chi_{ijk}^{(2)}(\omega_3) F_{ijk}^{(2)}(\omega_3, \omega_1, \omega_2, \theta, \varphi) \quad (1.36)$$

1.3.5 Birefringence phase-matching

According Eq. (1.30), the generated energy at the angular frequency ω_3 is shown in Figure 1.6 as a function of the interactive length Z , in the cases of $\Delta k = 0$ and $\Delta k \neq 0$. When $\Delta k \neq 0$, there is a reversal of the energy flow among the interactive waves with a spatial period $L_c = \pi/\Delta k$ defined as the coherent length. This is out of phase-matching condition and it is not interesting for applications.

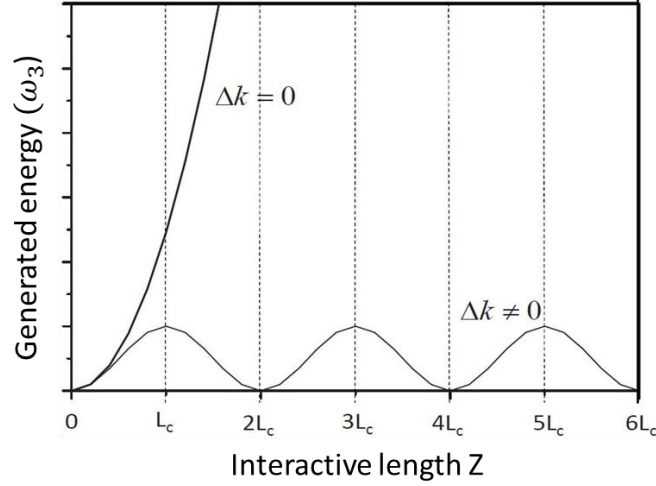


Figure 1.6: The generated energy at the angular frequency ω_3 as a function of the interactive length Z out of phase-matching ($\Delta k \neq 0$) and under phase-matching ($\Delta k = 0$) conditions. L_c is the coherent length.

When $\Delta k = 0$, the energy flow between the interactive waves does not alternate in sign, so that the generated energy grows continuously as the square of the interacting length Z . It is of special interest for applications and $\Delta k = 0$ is called phase-matching condition.

Phase-matching condition, from the classical point of view, corresponds to the interference between the nonlinear polarization and the field that it radiates is constructive. From the quantum point of view, it corresponds to the momentum conservation.

In anisotropic crystals with a collinear three waves interaction, the phase-matching condition can be written as follows:

$$\Delta k = k^\pm(\omega_3, \theta_{PM}, \varphi_{PM}) - k^\pm(\omega_1, \theta_{PM}, \varphi_{PM}) - k^\pm(\omega_2, \theta_{PM}, \varphi_{PM}) = 0 \quad (1.37)$$

Where PM stands for phase-matching and $(\theta_{PM}, \varphi_{PM})$ are the phase-matching angles. By using Eq. (1.16), the phase-matching condition can be also expressed as a function of the refractive indices along the phase-matching direction $\vec{u}_{PM}(\theta_{PM}, \varphi_{PM})$ as:

$$\omega_3 n^\pm(\omega_3, \theta_{PM}, \varphi_{PM}) - \omega_1 n^\pm(\omega_1, \theta_{PM}, \varphi_{PM}) - \omega_2 n^\pm(\omega_2, \theta_{PM}, \varphi_{PM}) = 0 \quad (1.38)$$

In uniaxial or biaxial crystals, each refractive index can exhibit two possible values as described in part 1.2.4, so that the birefringence can be used to compensate the dispersion, which is called “birefringence phase-matching”. As a result, there are 2^3 different possible relations from Eq. (1.38) to satisfy the birefringence phase-matching condition. According to part 1.2.6, they correspond to 8 possible configurations of polarization of the three interacting waves.

Among them, just 3 relations are compatible with the combination of the momentum

conservation, the energy conservation, and the normal dispersion [6]. They are called interaction type and labeled type I, type II and type III. They are defined in Table 1.2:

Birefringence phase-matching relation	Interaction type		
	SFG (ω_3)	DFG(ω_1)	DFG(ω_2)
$\omega_3 n_3^- - \omega_1 n_1^+ - \omega_2 n_2^+ = 0$	I	II	III
$\omega_3 n_3^- - \omega_1 n_1^- - \omega_2 n_2^+ = 0$	II	III	I
$\omega_3 n_3^- - \omega_1 n_1^+ - \omega_2 n_2^- = 0$	III	I	II

Table 1.2: Definition of the interaction type *versus* the birefringence phase-matching relation according to sum-frequency generation (SFG) and difference-frequency generation (DFG). $n_i^\pm = n^\pm(\omega_i, \theta_{PM}, \varphi_{PM})$ with $i = 1, 2, 3$.

The interaction type is valid for SFG (ω_3), DFG(ω_1) and DFG(ω_2). For type I the two input waves have the same polarization, but they are different for types II and III. Obviously, for SHG corresponding to SFG ($\omega_1 = \omega_2 = \omega, \omega_3 = 2\omega$), types II and III are equivalent.

1.3.6 Acceptances

We consider here a collinear birefringence phase-matching condition at room temperature in a crystal of length L . It is achieved along a phase-matching direction $(\theta_{PM}, \varphi_{PM})$ and at a given set of angular frequencies $(\omega_1, \omega_2, \omega_3)$ corresponding to wavelengths $(\lambda_1, \lambda_2, \lambda_3)$. PM stands for phase-matching.

We are interested in the effect of a variation of the generated energy from a phase-matching condition *i.e.* from $\Delta k = 0$ for which this energy is maximal. It is due to variations of ξ from ξ_{PM} *i.e.* $\xi_{PM} \pm d\xi$ which stands for the variation of any wavelength $\lambda_i^{PM} \pm d\lambda_i$ with $i = (1, 2, 3)$ or angle $\theta_{PM} \pm d\theta$ or $\varphi_{PM} \pm d$. The normalized generated energy as a function of $\xi = \theta, \varphi, \lambda$, can be calculated by using Eq. (1.30) and Eq. (1.37).

It is plot in Figure 1.7 showing a bandwidth $\delta\xi$ that corresponds to the full width of the normalized generated energy curve plotted as a function of $\xi = \theta, \varphi, \lambda$, at 0.405 of the maximum. $\delta\xi$ is also the bandwidth between the origin and the first zero value of the normalized generated energy.

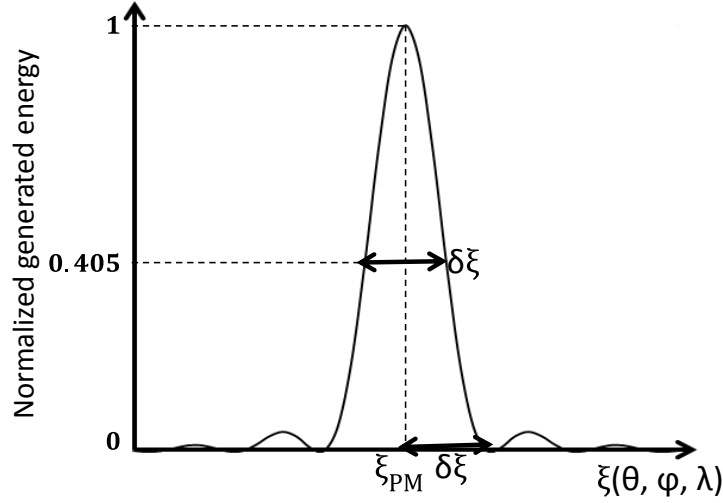


Figure 1.7: Normalized generated energy evolution as a function of ξ for a given crystal length L . ξ_{PM} represents the parameter allowing phase-matching condition; ξ is the angle (θ or φ) or the wavelength (λ). $\delta\xi$ is the full-width of the curve at 0.405 of the maximum, corresponding to a phase-mismatch $\Delta k = \pm 2\pi/L$ [3].

The acceptance is $L\delta\xi$ ($\xi = \theta, \varphi, \lambda$). It is also defined as the deviation from the phase-matching value ξ_{PM} leading to a phase-mismatch variation Δk from 0 to $\pm 2\pi/L$, where L is the crystal length [3]. When $\xi = (\theta, \varphi)$ the acceptances $L\delta\theta$ and $L\delta\varphi$ correspond to the angular acceptances; when $\xi = \lambda$, $L\delta\lambda$ is the spectral acceptance.

The acceptance $L\delta\xi$ can be calculated by expanding Δk in a Taylor series about ξ_{PM} :

$$\Delta k(\xi_{PM}) = \frac{2\pi}{L} = \delta\xi \left. \frac{\partial \Delta k}{\partial \xi} \right|_{\xi=\xi_{PM}} + \frac{1}{2} (\delta\xi)^2 \left. \frac{\partial^2 \Delta k}{\partial \xi^2} \right|_{\xi=\xi_{PM}} + \dots \quad (1.39)$$

When the second- and higher-order differential terms in Eq. (1.39) are negligible, it is called critical phase-matching (CPM), and the corresponding acceptance is written as:

$$L\delta\xi = \frac{2\pi}{\left. \frac{\partial \Delta k}{\partial \xi} \right|_{\xi=\xi_{PM}}} \quad (1.40)$$

When $\partial(\Delta k)/\partial \xi|_{\xi_{PM}} = 0$, which is called non-critical phase-matching (NCPM), we need to consider the second-order differential term. The corresponding acceptance is then written as:

$$L\delta\xi = \sqrt{\frac{4\pi L}{\left. \frac{\partial^2 \Delta k}{\partial \xi^2} \right|_{\xi=\xi_{PM}}}} \quad (1.41)$$

1.3.7 Spatial walk-off and attenuation

In uniaxial and biaxial crystals, the angular non-critical phase-matching (ANCPM) can

be accessible only along the principal axes of the dielectric frame. It is also the case in the x - y principal plane of a uniaxial crystal. As discussed in part 1.2.5, along all these directions of propagation, the spatial walk-off angles are equal to zero. Then no spatial walk-off attenuation is expected and the overlap between the beams of the three interacting is complete inside the crystal length L .

According to Eq. (1.30), it means no attenuation effect of the spatial walk-off angles on the conversion efficiency defined at the output of the crystal by $\eta = \frac{\varepsilon(\omega_3, L)}{\varepsilon(\omega_1, 0) + \varepsilon(\omega_2, 0)}$ for ANCPM directions. This effect takes place through $G(L, \omega_o, \rho)$ that is equal to 1.

For all other directions where the phase-matching is critical angularly (ACPM), the three interacting waves propagate with different spatial walk-off angles. Then their beams are separated after an interactive length that can be smaller than the crystal length L . In that case, it is necessary to consider the effect of the spatial walk-off angles leading to an attenuation of the conversion efficiency η defined above that is evaluated by the factor $G(L, \omega_o, \rho)$ of Eq. (1.30).

To evaluate this factor G , we propose to consider as an example ACPM type I and type II SHG occurring out of the x - y principal plane of a positive uniaxial nonlinear crystal, or in y - z plane of a positive biaxial crystal. The beams of the three interacting waves are depicted in Figure 1.8(a) and 1.8(b) for type I and type II SHG respectively, according to Table 1.2. The parameters r and u are the Cartesian coordinates in the plane, where u is collinear with the three wave vectors.

Figure 1.8 show two fundamental beams and the harmonic beams propagating respectively with the collinear wave vectors $\vec{k}^{-,o}(\omega, \theta_{PM}, \varphi_{PM})$, $\vec{k}^{+,e}(\omega, \theta_{PM}, \varphi_{PM})$ and $\vec{k}^{-,o}(2\omega, \theta_{PM}, \varphi_{PM})$; However there is a spatial walk-off angle limiting the interacting length inside the crystal length L . It is given by Eq. (1.19).

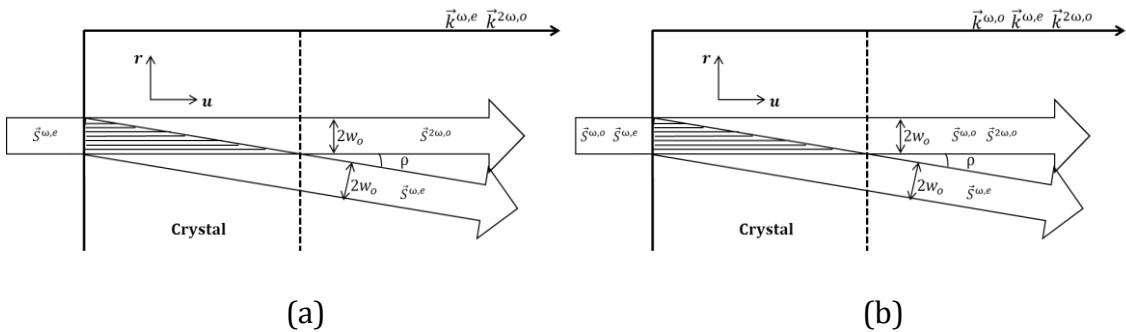


Figure 1.8: Beam separation in the case of type I(a) and II(b) ACPM SHG. $\vec{k}^{-,o}(\omega, \theta_{PM}, \varphi_{PM})$, $\vec{k}^{+,e}(\omega, \theta_{PM}, \varphi_{PM})$ and $\vec{k}^{-,o}(2\omega, \theta_{PM}, \varphi_{PM})$ are the three associated wave-vectors; $\vec{S}^{-,o}(\omega, \theta_{PM}, \varphi_{PM})$, $\vec{S}^{+,e}(\omega, \theta_{PM}, \varphi_{PM})$ and $\vec{S}^{-,o}(2\omega, \theta_{PM}, \varphi_{PM})$ are the two fundamental and the harmonic Poynting vectors. W_o is the fundamental beam radius and ρ is the spatial walk-off angle.

For type I, the Poynting vector is $\vec{S}^{+,e}(\omega, \theta_{PM}, \varphi_{PM})$ for the two fundamental beams and it is oriented at the spatial walk-off angle from the Poynting vector of the harmonic beam $\vec{S}^{-,o}(2\omega, \theta_{PM}, \varphi_{PM})$. Then the corresponding $G_I(L, \omega_o, \rho)$ factor in Eq. (1.30) is expressed as [7]:

$$G_I(t) = \left(\frac{\sqrt{\pi}}{t}\right) \text{erf}(t) - \left(\frac{1}{t^2}\right)[1 - \exp(-t^2)]$$

$$\text{with } t = \left(\frac{\rho L}{w_o}\right) \text{ and } \text{erf}(x) = \left(\frac{2}{\sqrt{\pi}}\right) \int_0^x \exp(-t^2) dt \quad (1.42)$$

For type II, the Poynting vectors of one fundamental beam and of the harmonic beam, $\vec{S}^{+,o}(\omega, \theta_{PM}, \varphi_{PM})$ and $\vec{S}^{+,o}(2\omega, \theta_{PM}, \varphi_{PM})$, are collinear. But they are oriented at a spatial walk-off angle from the Poynting vector of the other fundamental beam $\vec{S}^{-,e}(\omega, \theta_{PM}, \varphi_{PM})$. The $G_{II}(L, \omega_o, \rho)$ is [7]:

$$G_{II}(t) = \left(\frac{2}{\sqrt{\pi}}\right) \int_{-\infty}^{+\infty} F^2(a, t) da$$

$$\text{with } F(a, t) = \left(\frac{1}{t}\right) \exp(-a^2) \int_0^t \exp[-(a + \tau)^2] d\tau \quad (1.43)$$

$$a = \frac{r}{w_o}, \tau = \frac{\rho u}{w_o}, t = \frac{\rho L}{w_o}$$

1.3.8 Condition of supercontinuum generation

There is a great interest for generating beams with a very broad bandwidth by Optical Parametric Generation (OPG) under phase-matching condition. In such a quadratic process, an incident pump beam at the angular frequency ω_3 generates in a nonlinear crystal a signal beam with angular frequency ω_2 and an idler beam with angular frequency ω_1 . The set of angular frequencies $(\omega_1, \omega_2, \omega_3)$ fulfill Eq. (1.24) and correspond to the set of wavelengths $(\lambda_1, \lambda_2, \lambda_3)$. The nonlinear crystal is cut at the corresponding birefringence phase-matching (BPM) direction $(\theta_{PM}, \varphi_{PM})$ given by Eq. (1.37).

Under BPM conditions, the spectral acceptance for type II OPG is greater than for type I and type III [8]. Then for type II OPG, there is a “magical” pump angular frequency ω_3^* (or wavelength λ_3^*) leading to the broadest spectral bandwidth of the signal and Idler generated beams over the transparency range of the nonlinear crystal. Such broadest spectral bandwidth generation is called condition of supercontinuum generation.

According to Table 1.2, Type II OPG corresponds to the following birefringence phase-matching relation:

$$\omega_3 n^-(\omega_3^*, \theta_{PM}, \varphi_{PM}) - \omega_1 n^+(\omega_1, \theta_{PM}, \varphi_{PM}) - \omega_2 n^+(\omega_2, \theta_{PM}, \varphi_{PM}) = 0 \quad (1.44)$$

At the angular frequency $\omega_3^*/2$ (the wavelength $2\lambda_3^*$), the dispersion of the external index n^+ of the nonlinear crystal has an inflection point [8]. Then it can be calculated by using Eq (1.11) with the Sellmeier equations describing the three principal refractive indices of the nonlinear crystal, and by solving the following equation [8]:

$$\left. \frac{d^2 n^+(\lambda, \theta, \varphi)}{d\lambda^2} \right|_{2\lambda_3^*} = 0 \quad (1.45)$$

1.4 Summary

The theoretical elements given in this chapter are of prime importance for understanding the experimental setup implemented for the study of new crystals that are presented in the next chapters and for the analysis of recorded data.

This chapter reminded the main parameters to describe linear optics and the energy generated from quadratic processes, for angular frequencies located in the transparency range of nonlinear crystals. It mainly deals with the heart of this thesis: the index surface, the polarization states and spatial walk-off angles that govern crystal optics; The second-order susceptibility tensor and phase-matching condition that are two important parameters to consider for maximal conversion efficiencies.

We are interested in birefringence phase-matching condition in uniaxial and biaxial nonlinear crystals from the compensation of the wavelength dispersion of their principal refractive indices by their birefringence. We discussed the associated spatial walk-off attenuation on the generated energies from frequency conversion and the condition of supercontinuum generation.

Chapter 2 Experimental methods

2.1 Introduction

This chapter describes the experimental methods and the corresponding setups used at Néel Institute to study linear and nonlinear optics in crystals. We also implemented two new methods for the present work that will be described in chapters 3 and 4. All allow to perform studies with a very high accuracy in samples shaped either as slabs or as spheres or cylinders. The used faces are oriented in the dielectric frame, polished to optical quality but uncoated. Shaping is a crucial step that relies on original homemade techniques available at Néel Institute.

Methods for Linear optics studies in oriented slabs are first reported. They concern the transmission spectra recorded under polarized light and the optical damage threshold determined using a homemade setup. We also implemented a new method described in chapter 3, in order to measure the magnitude of principal refractive indices of crystals at one wavelength. Second Harmonic Generation (SHG) under angular critical phase-matching (ACPM) conditions is also studied in slabs. From the recorded data we determine, the magnitude of non-zero elements of the second-order electric susceptibility, also called nonlinear coefficients as well as the associated spectral and angular acceptances. We also implemented another method for the determination of the magnitude of nonlinear coefficients out of phase-matching condition (see chapter 4).

Then this chapter presents spheres and cylinders that are unique shapes for a direct study of the angular distribution of all optical properties. In the following the SPHERE method dealing with these samples is described [9]. It was proposed in 1989 by B. Boulanger. It is implemented in this work with specific incoming beams, optical elements and detectors according to the requested spectral ranges. It allows direct measurements as a function of wavelength of the spatial walk-off angles, the dielectric frame orientation and phase-matching condition: directions, associated conversion efficiencies, spectral and angular acceptances.

Finally, this chapter focuses on the determination of the main parameters for frequency conversion detailed in chapter 1, from the recorded previous data. There will be a special interest for the Sellmeier equations describing the dispersion of the principal refractive indices as a function of wavelength, and the magnitude and relative sign of the non-zero elements of the second-order electric susceptibility.

2.2 Linear and nonlinear optics studies in slabs

2.2.1 Slabs shaping

The most current shape of crystals used to study their optical properties, is the slab with at least two parallel faces polished to optical quality. Note that no face is coated in the present work. Dealing with crystals from anisotropic optical classes (uniaxial and biaxial) the used faces must be cut oriented perpendicular to a direction of propagation from the dielectric frame (x, y, z) with the best precision. The reason is that all optical properties are studied in this frame (see chapter 1). For linear optics, the unit vector of this direction of propagation \vec{u} is given by any the spherical angle (θ, φ) and it usually corresponds to a phase-matching (PM) angle $(\theta_{PM}, \varphi_{PM})$ for nonlinear optics.

At first, a volume of an undefected crystal is selected by using a strioscopy and an ombroscopy method available at Néel Institute [10]. It is a crucial step for further successful optics studies. For example, there can be an effect of defects or crack, impurities or bubbles, on the optical damage threshold and the energy generated by frequency conversion.

The best precision for cutting a crystal oriented in the dielectric frame (x, y, z) is first to mark the coordinates of the selected direction in the crystallographic frame (a, b, c) and to cut the slab oriented in this last frame. Such a change of frame is easy in uniaxial crystals and biaxial crystals belonging to the orthorhombic system [1]. For biaxial crystals belonging to the monoclinic system, it is much more complicated since the dielectric frame can rotate as a function of wavelength and unique methods implemented at Néel Institute as the one described in part 2.3.3 must be used [11].

The selected volume of crystal is cut oriented in the crystallographic frame thanks to a diamond wire saw and the polychromatic X-rays diffraction in backscattered Laue geometry with an accuracy of less than $\pm 0.5^\circ$. Thus the first face of the slab oriented in the aimed direction is obtained. It will be used as a reference in further operations. It is glued to a polishing head but the polishing of a second face parallel to the reference one is carried out first, using an automatic polishing machine PM5 (Logitech) [12]. Different trays are used and also abrasives with particles size reduced successively from a few tens to a few tenths of a millimeter. In this way, a so-called "optical" polish with a roughness less than $\lambda/10$ is achieved. Then the reference first face is polished in turn. After that the oriented and polished slab is ready to be used. An example is shown in Figure 2.1(a) giving the orientation of all the faces in the crystallographic frame and in the dielectric frame.

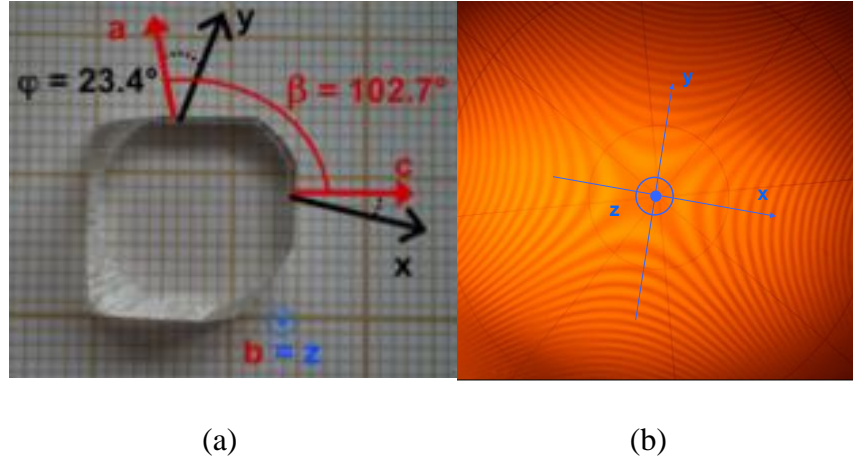


Figure 2.1: (a) Picture of a crystal slab cut perpendicular to the z-axis of the dielectric frame as an example; The two parallel faces polished to optical quality are oriented in the crystallographic and dielectric frames. (b) Conoscopy transmission picture through the polished faces of the slab shown in (a).

A conoscopy transmission picture can control a slab cut with two polished faces perpendicular to a principal x-, y- or z- axis of the dielectric frame. The device available at Néel Institute, is a microscope equipped with a Bertrand lens [13]. It is coupled to a monochromatic light (Sodium lamp or He-Ne laser) source emitting a wavelength λ_0 and polarized linearly. An example of a conoscopy transmission picture through a slab with two polished faces cut perpendicularly to the z-axis is shown in Figure 2.1(b).

The conoscopy transmission picture gives access to interference patterns whose axes of symmetry correspond to the three axes of the dielectric frame. Thus the dielectric frame orientation is determined with the accuracy of the order of 1° [14]. For example in Figure 2.1(b) (x, y) axes correspond to the neutral lines since they are associated with two linear polarization states perpendicular one to each other; The third principal axis (z-axis) is the symmetry axis perpendicular to the intersection of two previous neutral lines. The assignment between the three symmetry axes and (x, y, z) axes is easy in uniaxial crystals but much more complicated in biaxial crystals [14]. It will be specified in the following chapters for each studied crystal.

The slab ready for a use is stuck on a HUBER goniometer head with two perpendicular translations adjusting the center of the slab rotation axis, and two perpendicular rotating cradles providing small orientation adjustments of the slab.

2.2.2 Transmission spectra in polarized light

Transmission spectra in polarized light are the first data to record in nonlinear crystals since they give the transparency range over which the three angular frequencies ($\omega_1, \omega_2, \omega_3$) can be selected for nonlinear optics. The transmission spectra are

recorded as a function of the wavelength through oriented slabs using first a commercial Perkin-Elmer Lambda (PEL) 900 spectrometer between 0.175 and 3.300 μm and then a commercial Bruker FT-IR between 3.300 μm and 40 μm .

We use a slab with two parallel polished faces cut perpendicular to a principal axis of the dielectric frame, for example z-axis. In the PEL spectrometer, it is inserted between two Glan-Taylor Polarizers with an extinction ratio of 10^{-3} . Firstly, by orienting the two polarizers perpendicular, the two other principal dielectric axes are located in the plane of the two parallel faces, *i.e.* x- and y-axis in this example. Then with the two polarizers parallel to x- and y- axis successively, two transmission spectra are recorded in polarized light. Note that one slab is enough for uniaxial crystals but two are necessary for biaxial crystals in order to record the third transmission spectra with polarized light parallel to z-axis. Wire-grid polarizers are necessary in the Bruker spectrometer.

An important point is that all transmission spectra in polarized light depicted in the present work are not corrected from the Fresnel losses.

2.2.3 Optical damage threshold

The optical damage threshold determines the maximum energy of the incident laser beam that can be sent on a crystal without damaging its surface or volume. It is independent of the direction of propagation in the crystal but remains quite a variable data according to the wavelength, pulse duration and repetition rate of the laser [15, 16].

In the present work the optical damage threshold is determined at the surface of the input face of a slab polished to optical quality and cut perpendicular to a principal axis of the dielectric frame. A scheme of our experimental setup is shown in Figure 2.2.

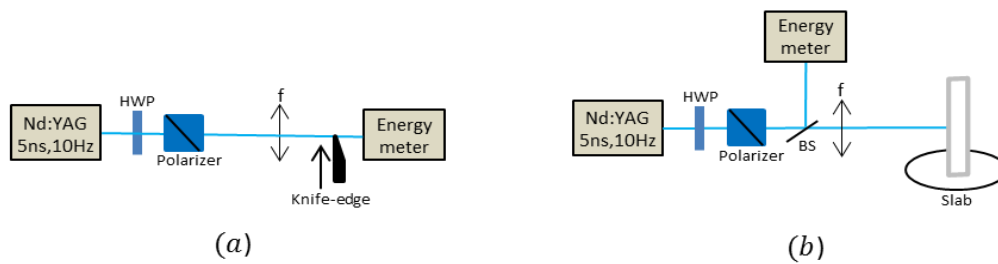


Figure 2.2: Scheme of the optical damage threshold experimental setup with the knife-edge (a), slab (b).

A pulsed laser beam, with a very high spatial quality and a very small beam waist size, is provided by a Nd:YAG laser from Continuum company. The emitted wavelength is 1.064 μm , the pulse width at Full-Width-of-Half-Maximum (FWHM) is 5-ns; It is 10-Hz repetition rate and linearly polarized. The maximum emission energy is 14 mJ but it

can be decreased continuously down to 0 mJ by rotating a 1.064 μm -half-wave plate inserted in front of a Glan-Taylor polarizer as shown in Figure 2.2.

By using a $f=140\text{-mm}$ -focal BK_7 lens, the laser beam is directly focused at the surface of the input face of the slab which distance from the lens remains fixed. Before inserting the crystal, the beam radius W was determined with an accuracy of $\pm 5 \mu\text{m}$. For that purpose, the energy per pulse was measured with an Ophir P50 energy-meter while using the knife-edge method, i.e. while hiding the laser beam continuously by a razor blade mounted on a vertical translation holder as shown in Figure 2.2(a) [17]. The holder was placed at several distances Z from the lens, in the range located from each side of the beam-waist radius W_0 . The corresponding values of $W(Z)$ and W_0 are shown in Figure 2.3.

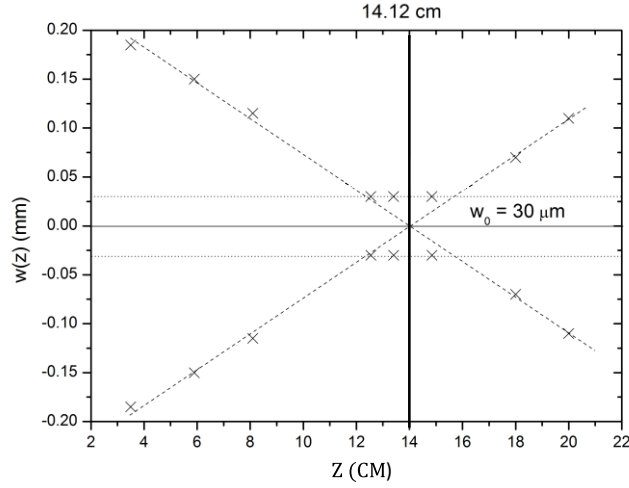


Figure 2.3: The beam radius value recorded as a function of the distance between the lens and the razor blade vertical translation axis, Z . W_0 is the beam-waist radius.

The beam-waist radius W_0 is determined by fitting $W(Z)$ shown in Figure 2.3 by the following equation [18]:

$$W(Z) = W_0 \left[1 + \left(\frac{Z}{Z_R} \right)^2 \right]^{1/2} \quad (2.1)$$

where $Z_R = \frac{\pi W_0^2}{\lambda M^2}$ is the Rayleigh length over which $W(Z)$ remains equal to W_0 ; M^2 is the M-square parameter defined in [18].

We found that $W_0 = 30 \mu\text{m}$ and $M^2 = 1$ leading to a Rayleigh parameter $Z_R = 2.66 \text{ mm}$. These data are in agreement with the specifications of the delivered Nd:YAG laser.

The optical damage threshold is determined from the observation of the early stage damage at the same location of the input surface of the slab that remains fixed. The laser

energy per pulse is incremented from 0 mJ by 0.25 mJ between two successive one-minute shootings and measured using an Ophir P50 energy-meter. Actually, the optical damage threshold is reported at $1.064 \mu\text{m}$ from the value of the energy per pulse and the corresponding peak power density for which the damage is observed. It is described in chapter 3 in each studied nonlinear crystal and in KTiOPO_4 (KTP) crystal for comparison. For that purpose, a x-cut KTP slab polished to optical quality is studied in the same condition.

2.2.4 Determination of nonlinear coefficients from phase-matched SHG

Second Harmonic Generation (SHG) is studied under angular critical phase-matching (ACPM) conditions located in the principal planes of nonlinear crystals, to determine their nonlinear coefficients. For all of them, it will be shown in chapter 3 that the corresponding fundamental phase-matching wavelength is ranging below $2.4 \mu\text{m}$. Then a pulsed optical parametric oscillator (OPO) delivering high-energy pulses is used. Note that OPO combines phase-matched difference frequency generation (DFG) and spontaneous down-conversion (SPDC) from quadratic processes, in a commercial nonlinear crystal inserted in an optical cavity.

2.2.4.1 OPO in the nanosecond regime

A scheme of the different stages of the OPO from Continuum Company is shown in Figure 2.4. The pump beam is a Nd:YAG laser with a pulse width of 5-ns FWHM, and 10-Hz repetition rate. The emission wavelength is $1.064 \mu\text{m}$ with an energy per pulse of 450 mJ. After a phase-matched SHG in a KD_2PO_4 (KDP) nonlinear crystal, 200 mJ is generated at $0.532 \mu\text{m}$. The two previous beams are then collinearly sent in another KDP crystal in order to generate a new beam at $0.355 \mu\text{m}$ from phase-matched Sum Frequency Generation (SFG). The generated energy per pulse of the $0.355 \mu\text{m}$ beam is 100 mJ and it is pumping the OPO based on a rotating $\beta\text{-BaB}_2\text{O}_4$ ($\beta\text{-BBO}$) nonlinear crystal. It leads to a phase-matching emission continuously tunable over the full transparency range of the $\beta\text{-BBO}$ crystal. It is based on a signal beam emission between $0.4 \mu\text{m}$ and $0.71 \mu\text{m}$, and an idler emission between $0.71 \mu\text{m}$ and $2.4 \mu\text{m}$ [12].

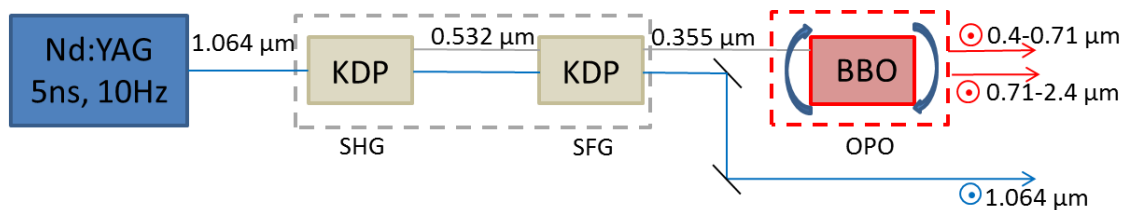


Figure 2.4: Scheme of the optical parametric oscillator (OPO) in the nanosecond regime.

The OPO generated beams that we used, are all linearly polarized as shown in Figure 2.4. The maximal value of their energy per pulse is around 15 mJ in the visible and decreases when the wavelength increases.

2.2.4.2 Experimental setup

For SHG, one OPO beam (Signal or Idler) is sent as one incoming beam on the experimental setup shown in Figure 2.5. It is collinear with a He-Ne laser emitting the wavelength of $0.633 \mu\text{m}$ that is used for a safe alignment of the experimental setup with the incoming beam (it is not shown in Figure 2.5). The energy of the OPO beam is controlled independently by rotating a half-wave plate inserted in front of a Glan-Taylor polarizer. Then a second half-wave plate inserted on the beam, controls the orientation of the incoming linear polarization state for type I- and type II- SHG phase-matching condition (see part 1.3.5 of chapter 1). The half-wave plates are achromatic over $1 \mu\text{m}$ according to the selected spectral range of the OPO beam.

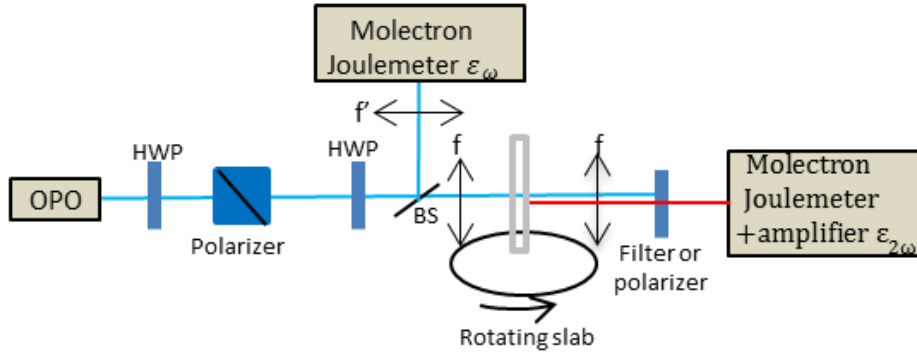


Figure 2.5: Scheme of the experimental setup used to determine a nonlinear coefficient under phase-matched SHG condition.

The OPO wavelengths λ_ω are directly measured between 0.2 and $1.1 \mu\text{m}$ with accuracy of 0.2 nm using the HR4000 spectrometer, and between 0.9 and $1.7 \mu\text{m}$ with accuracy of 3 nm using the NIRQuest spectrometer. For OPO wavelengths λ_ω ranging above $1.7 \mu\text{m}$, the wavelength $\lambda_{2\omega} = \lambda_\omega / 2$ that is generated in the slab by phase-matched SHG, is measured using the previous spectrometers.

The incoming beam energy in front of the slab is measured using the J4-09 Molelectron pyroelectric joulemeter with a constant spectral response between $0.2 \mu\text{m}$ and $100 \mu\text{m}$. This detector is located after a beam splitter (BS) and a CaF_2 lens with a focal length of $f'=50 \text{ mm}$ as shown in Figure 2.5. It has the advantage of an access to $H\epsilon_\omega(0)$ where $\epsilon_\omega(0)$ is the fundamental energy per pulse incoming on the slab and H is the setup transfert function. H depends on the transmission and/or reflexion coefficients of all the optical elements inserted in front of the Joulemeter and the slab, as well as the OPO

wavelength and polarization.

For all our studies, $\varepsilon_\omega(0)$ is set around 20 μJ at the entrance of the slab, in order to avoid any optical damage of the sample and to remain in the undepleted pump approximation described in part 1.3.3 of chapter 1.

The slab polished to optical quality is cut at the ACPM SHG phase-matching direction $(\theta_{PM}, \varphi_{PM})$ located in a principal plane. This direction is determined from the associated tuning curve previously recorded using the SPHERE method as described in the following part 2.3.3. The incoming tunable wavelength is first set at the corresponding fundamental phase-matching wavelength λ_ω^{PM} . The slab is stuck on the commercial HUBER goniometer head in auto-collimation with the incoming beam for its propagation along the phase-matching direction $(\theta_{PM}, \varphi_{PM})$.

As shown in Figure 2.5, the incoming OPO beam is focused in the slab with a $f=100$ -mm-focal BK₇ lens. The focal value is selected in order to provide a beam waist diameter $W_0=120$ μm at the input surface of the slab. Thus the slab thickness L is much smaller than twice the Rayleigh length $Z_R=30$ mm in our setup. Such a condition leads to a spatial walk-off attenuation $G(L, W_0, \rho)$ negligible in Eq. (1.30), where ρ is the spatial walk-off angle. It also ensures the parallel beam approximation used of chapter 1. The HUBER goniometric head is placed at the center on a rotation stage controlling the slab angular orientation.

2.2.4.3 Measurements and analysis

The energy generated by ACPM SHG, $\varepsilon_{2\omega}(\theta_{PM}, \varphi_{PM}, L)$ at the output of the L -thickness slab is detected after another $f=100$ mm-focal BK₇ lens followed by a Glan Taylor polarizer and/or a filter removing the input beam after the slab (see Fig. 2.5). A J3-05 Molelectron joulemeter with a spectral response constant between 0.2 μm and 100 μm combined with a PEM531 amplifier is used.

An ACPM SHG direction is detected when the conversion efficiency reaches a maximal value. According to Eq. 1.30, it is defined at the output of the slab by:

$$\eta_{SHG}(2\omega, \theta_{PM}, \varphi_{PM}, L) = \frac{\varepsilon_{2\omega}(\theta_{PM}, \varphi_{PM}, L)}{\varepsilon_\omega(0) + \varepsilon_\omega(0)} \quad (2.2)$$

The phase-matching condition is confirmed if η_{SHG} shows the theoretical behavior of Fig. 1.7. Two studies are possible: η_{SHG} is recorded a function of λ by tuning the OPO wavelength around λ_ω^{PM} in the sample fixed in the direction $(\theta_{PM}, \varphi_{PM})$; η_{SHG} is recorded as a function of θ or φ by rotating the slab around $(\theta_{PM}, \varphi_{PM})$ while the OPO wavelength is fixed at λ_ω^{PM} . They respectively give access to the spectral and angular

acceptances defined in part 1.3.6 of chapter 1. These two kinds of measurements will be shown in Chapter 3 for the studied nonlinear crystals.

According to Eq. (1.30), the maximal value of the conversion efficiency is proportional to the magnitude of the involved nonlinear coefficients. This magnitude will be determined under ACPM SHG studies in a principal plane using the same experimental setup for all the studied nonlinear crystals and also for a KTP crystal. Thus the well-known associated nonlinear coefficient of KTP is used as a reference [19]. The same fundamental phase-matching wavelength λ_{ω}^{PM} of the incoming beam will be selected. One difficulty is that it implies that the ACPM SHG tuning curves of all the new studied nonlinear crystals have phase-matching angles $(\theta_{PM}, \varphi_{PM})$ at the same λ_{ω}^{PM} as KTP crystal. But it has the advantage that the data analysis gets rid of the spectral response of the experimental setup.

The analysis of all recorded data will be detailed in Chapter 3. Phase-matched SHG has the advantage of a much higher generated energy compared with out-of phase-matching SHG, according to Eq. (1.30). However, in the biaxial crystal from the monoclinic system studied in chapter 4, some non-zero and independent elements of the second-order susceptibility cannot be determined from phase-matched SHG in the principal planes. In this case, out of SHG phase-matching conditions will be studied.

2.3 Linear and nonlinear optics studies in spheres or cylinders

2.3.1 Cylinders and spheres shaping

The homemade methods shaping spheres and cylinders at Neel Institute are very mature.

Details were recently published in [20]. The first requirement for shaping a cylinder is to realize two faces cut oriented perpendicular to an axis that will be the revolution axis of the cylinder. This axis is always a principal axis of the dielectric frame corresponding to a principal crystallographic axis. Then X-ray diffraction enables the orientation of the faces with an accuracy of $\pm 0.01^\circ$. Such an orientation is confirmed by conoscopy.

The cylindrical shape is achieved using our homemade shaping apparatus, after the previous sample is sandwiched between two 1-mm-thick glass slabs stuck on its parallel faces. This mounting stiffens very thin samples ($<1\text{mm}$), strengthens those with poor mechanical properties, lessens the effects of hardness anisotropy, which may lead to elliptical shapes, and limits edge bevelling on the final cylinder. The shaping technique produces cylinders with a revolution axis normal to the reference face within 0.1° , an acylindricity relative to the diameter below 0.1%, and a rim polished to a roughness of

about 10 nm r.m.s. (root mean square). Several crystals shaped as cylinders using this technique, are shown in Fig. 2.6.

The polished cylinder stuck on a HUBER goniometer head can rotate perpendicular to the revolution axis corresponding to a principal axis of the dielectric frame. Thus it gives access to the full principal plane perpendicular to this axis.

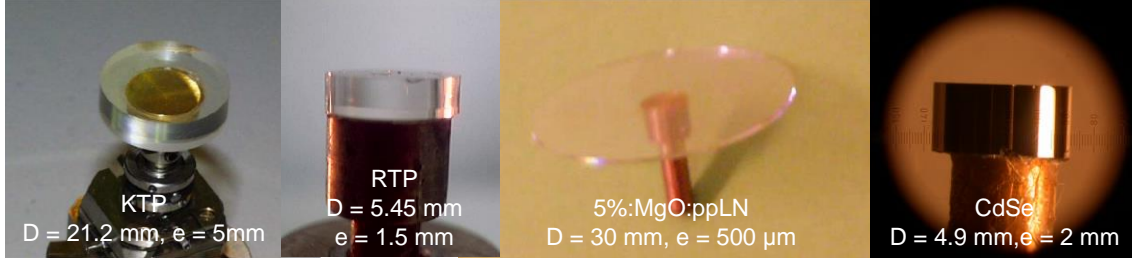


Figure 2.6: Examples of polished cylinders

The sphere is shaped from the progressive abrading of a rotating starting sample following the five main steps that are illustrated in Fig. 2.7. The first step consists in shaping the starting sample as a cube as shown in Fig. 2.7(a), with 6 faces perpendicular to each other and of same size. It makes the centring of the object on the successive rotation axes easier and controls the isotropic removal of material toward the spherical shape. There is not need to cut the cube oriented.

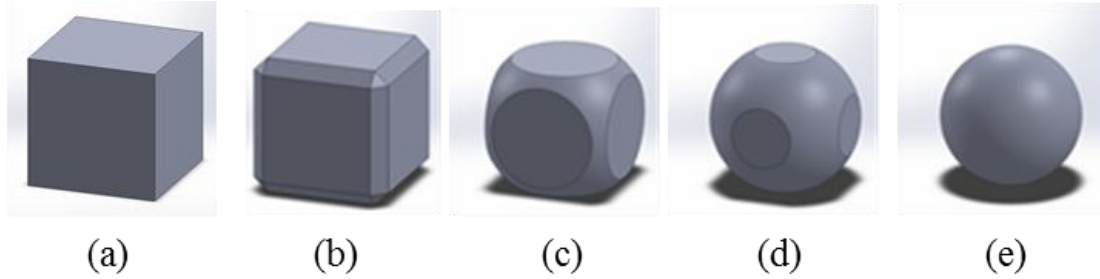


Figure 2.7: Successive five steps for shaping and polishing a sphere from a cube.

The cube is stuck on a pin on one face, after bevelling all the edges with a template as shown in Fig. 2.7(b). Then it is mounted on a motorized rotation axis with two crossed translations in order to be centred and slowly rotated with a speed between 10 and 20 rotations per minute (rpm). From this step the linear edges are removed, as shown Fig. 2.7(c) and 2.7(d). Concave hemispherical templates covered with abrasive suspension are manually put in contact with the rotating sample. The size of the hemisphere template is gradually reduced, so that the shape of the sample is changed from the cube to the final sphere diameter, the corresponding abrasive particle size being reduced progressively.

To converge toward a spherical shape, the sample has to be rotated around many different directions, the pin being unstuck and stuck again many times. Once all facets have vanished, the spherical shape with a diameter D is achieved with a typical asphericity $\Delta D/D$ below 1% as shown in Fig. 2.7(e). The sphere is then polished with stretched cloths and abrasive of small particle sizes to reach a few nanometer surface roughness (rms). This process allows to shape optically polished spheres of diameter $D = 3$ mm to 10 mm as shown in Fig. 2.8.

The polished sphere once ready is stuck oriented on a goniometer head along a principal axis of the dielectric frame. As for the slab, the orientation between this frame and the crystallographic frame is determined. Then the sphere is oriented thanks to the crystallographic axes with an accuracy better than 0.1° using the polychromatic X-ray Laue technique. Several of them mounted on a HUBER goniometric head are shown in Fig. 2.8.

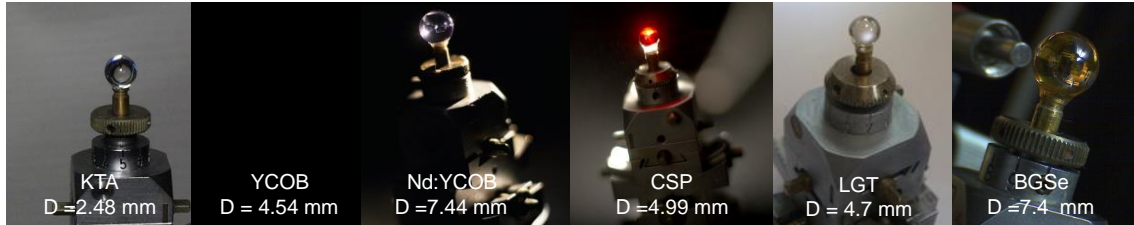


Figure 2.8: Examples of polished spheres mounted on goniometric heads.

2.3.2 SPHERE method

The SPHERE method gives a direct access to the angular distribution of any optical property as a function of wavelength in the dielectric frame. It is accessible in the full dielectric frame with a sphere and limited to a principal dielectric plane with a cylinder. The only limitation is the transparency range of the crystal.

The crystals studied in chapter 3 are transparent up to $7.4 \mu\text{m}$, and BGSe studied in chapter 4 is transparent up to $18 \mu\text{m}$, then we combined the SPHERE method with an optical parametric generator-difference frequency generation OPG-DFG in the picosecond regime which emission is continuously tunable between 0.4 to $11 \mu\text{m}$.

2.3.2.1 OPG-DFG in the picosecond regime

The scheme of the multi-stages OPG-DFG commercialized by Excel Technology and Light Conversion companies is shown in Figure 2.9.

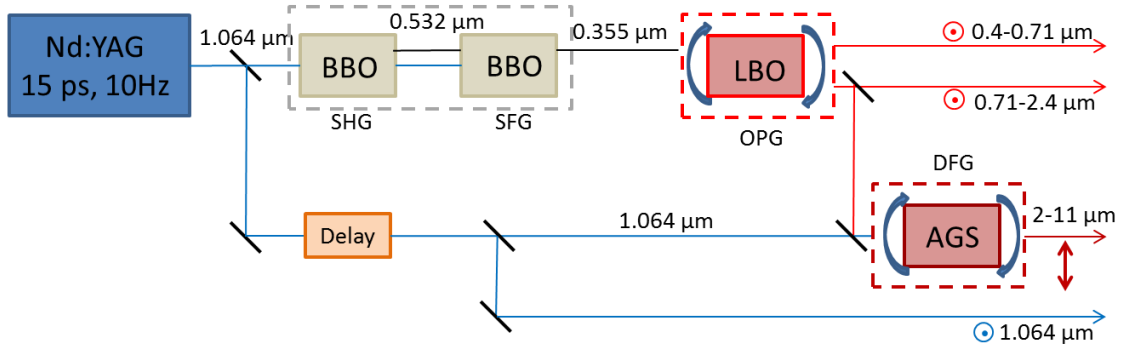


Figure 2.9: Scheme of the optical parametric generator - difference frequency generation (OPG-DFG) in the picosecond regime.

The pump beam is also Nd:YAG pulsed laser emitting at the wavelength of 1.064 μm with 10-Hz repetition rate but with a pulsewidth of 15 ps FWHM. The energy per pulse of about 40 mJ is divided into two parts:

- The first part is 75% of the Nd:YAG energy that is sent through two β -BBO nonlinear crystals properly oriented for phase-matched frequency conversion. A beam at 0.532 μm is generated from SHG in the first β -BBO crystal. Then a beam is generated at 0.355 μm in the second β -BBO crystal from collinear SFG between the incoming 1.064 μm and 0.532 μm beams. The beam generated at 0.355 μm is pumping the OPG based on a rotating LiB_3O_5 (LBO) nonlinear crystal. A phase-matched emission of a 0.4-0.71 μm signal beam and a 0.71-2.4 μm idler beam is generating in the OPG, with an energy per pulse ranging between 80 μJ and 500 μJ.
- The second part is 25% of the energy of the pulsed Nd:YAG laser. It is sent through an optical delay for a direct use. Otherwise it is combined after the delay with the OPG idler beam in a rotating AgGaS_2 (AGS) nonlinear crystal. Thus a non-collinear phase-matched DFG continuously tunable between 2.5 μm and 11 μm is generated.

All the OPG-DFG output beams that we used are linearly polarized as shown in Fig. 2.9.

Up to 4 μm, their energy is controlled independently by using a rotating half-wave plate associating with a Glan-Taylor polarizer; Achromatic plates were used for the tunable beams. For all our studies, the input energies were set below 200 μJ at the entrance of the sphere or the cylinder, to avoid any damage on the samples surface and for a propagation inside the samples in the undepleted pump approximation described in part 1.3.3 of chapter 1.

The OPG-DFG wavelengths are controlled using the protocol detailed in part 2.2.4.2.

2.3.2.2 Experimental setup

The scheme of the experimental setup implemented for the SPHERE method is shown in Fig. 2.10. Tunable incoming beams are sent at normal incidence on a sphere (or a cylinder) rotated on itself. It provides direct measurements as a function of wavelength of spatial walk-off angles, the dielectric frame orientation, phase-matching directions, the associated conversion efficiencies, the spectral and angular acceptances.

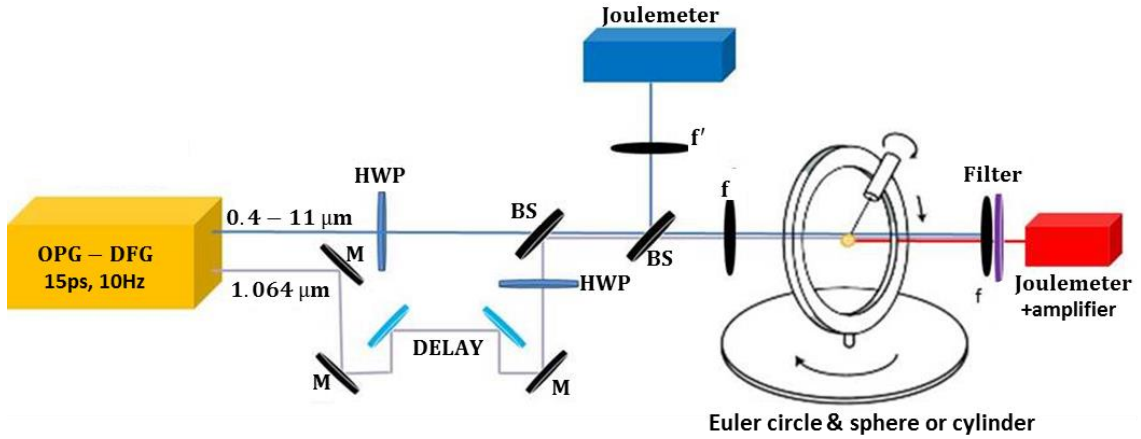


Figure 2.10: Scheme of the experimental setup implemented as the SPHERE method.

In the present work, second harmonic generation (SHG), sum-frequency generation (SFG) and difference-frequency generation (DFG) from quadratic processes are studied in the transparency range of nonlinear crystals cut as a sphere (or cylinder) [9]. One tunable incoming beam is necessary for SHG. It is combined collinearly with part of the 1.064 μm Nd:YAG beam in the sphere (or cylinder) for SFG and DFG. A delay line ensures the temporal overlap between the combined beams. It is built with mirrors as shown in Fig. 2.10. Up to 4 μm , achromatic half-wave-plates provide the configurations of polarization for type I, II and III of phase-matching condition. Above 4 μm , it is ensured by the sphere rotation in the plane perpendicular to the beams.

The incoming beams energies are measured using the J4-09 Molelectron pyroelectric joulemeter with a flat spectral response between 0.2 μm and 100 μm . It is located after a beam splitter and a CaF_2 lens with a focal length of $f'=50\text{ mm}$ as shown in Fig. 2.10. Filters remove the input beams after the sphere (or cylinder), so that the generated beam is detected by means of different photodetectors according to the associated phase-matching wavelength. The visible and near-IR until 1 μm ranges are covered by a Thorlabs Silicon photodiode, the range of 1-5.5 μm by a Hamamatsu Nitrogen-cooled InSb, and the far infrared until 12 μm by a PEM detector from VIGO based on a HgCdTe semi-conductor band gap. A J3-05 Molelectron joulemeter with a flat constant spectral response between 0.2 μm and 100 μm is combined with a PEM531 amplifier to

measure the energy of the generated beam. It is of particular interest when this energy is too low to be detected using the other detectors.

2.3.2.3 Euler circle

As shown in Figure 2.11, the sphere stuck oriented on a goniometric head is screwed at the centre of an Euler circle. The Euler circle uses three rotation axes marked by the angles α , β , and γ , giving a direct access to any direction of propagation inside the sphere. It allows a manual rotation of the sphere on itself with a precision of 0.1° .

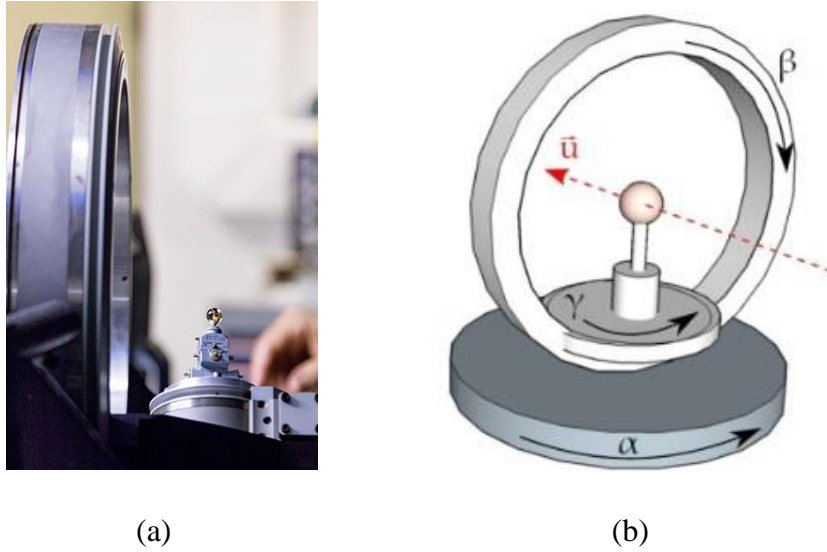


Figure 2.11: Euler circle picture (a) and scheme (b) showing the three rotation angles α , β , γ .

The relation between the Euler angles (α , β , γ) and the spherical angles (θ , φ) of the dielectric frame depends on the axis along which the sphere is stuck on the HUBER goniometric head. We describe below a possible situation enabling the sphere rotation in a dielectric principal plane.

As shown in Fig. 2.11(b), with the β -angle fixed, the sphere rotation axis remains vertical. Then if it is stuck along the y -axis of the dielectric frame, the rotation of the angles α or γ give access to all the directions of propagation of the (x, z) principal dielectric plane. If the angle α is also fixed, the angle θ is directly read by the variation of the angle γ with an accuracy of 0.001° .

Furthermore when the direction of propagation unit vector \vec{u} is along the x -axis of the dielectric frame, the relation between the spherical coordinates (θ , φ) in the dielectric frame and the angles (α , β , γ) of the Euler circle becomes [21]:

$$\begin{cases} \theta = \frac{\pi}{2} - (\alpha + \gamma) \\ \varphi = 0^\circ \end{cases} \quad (2.3)$$

2.3.2.4 Focusing inside the sphere or cylinder

The incoming beam must be focused properly inside the sphere (or the cylinder) in order to ensure a normal incidence and propagation along the diameter D of the sample. In the cylinder, a focusing is necessary only in the incident plane that is horizontal and perpendicular to the cylinder axis. It must be in the horizontal and vertical planes of the sphere that are parallel and perpendicular to the incident plane respectively [18, 21].

As an example, the focussing leading to beam propagation along the sphere diameter D is described. It is achieved by inserting a $f = 100$ -mm-focal CaF_2 lens in front of the sphere as shown in Fig. 2.12. A first crucial key point is the distance between the lens and the center of sphere: it must be adjusted very precisely in order to ensure a normal incidence on the sphere and propagation inside the sphere that is along the diameter D .

This distance can be calculated by using the Gaussian formalism in the paraxial approximation where each optical system is described by a ABCD matrix [21].

In fact, the crystal sphere behaves like two adjacent spherical lenses with the same two possible focal distances described by [18, 21]:

$$f^\pm(\lambda, \theta, \varphi) = \frac{n^\pm(\lambda, \theta, \varphi)R}{2[n^\pm(\lambda, \theta, \varphi) - 1]} \quad (2.4)$$

where $R = D/2$ is the radius of the sphere, λ is the incoming beam wavelength, (θ, φ) the spherical coordinates in the dielectric frame, and $n^\pm(\lambda, \theta, \varphi)$ the two possible refractive indices of the sphere along the propagation direction $\vec{u}(\theta, \varphi)$ that are given by Equations (1.11).

According to Eq. 2.4, if $n^\pm(\lambda, \theta, \varphi) < 2$ then the focal distances $f^\pm(\lambda, \theta, \varphi) > R$ and the focusing points F^\pm and F'^\pm of the sphere are outside the sample. It means that by setting the distance between the lens and the center of sphere so that the lens focal point corresponds to the sphere focal point F^\pm , as shown in Fig. 2.12(a), the incoming beam propagation inside the sphere is along its diameter D .

On the other hand, if $n^\pm(\lambda, \theta, \varphi) > 2$ then $f^\pm(\lambda, \theta, \varphi) < R$, so that the focusing points F^\pm and F'^\pm of the sphere are inside the sample. Consequently, the previous propagation scheme can damage the crystal. In that case we use the $2f - 2f$ propagation scheme shown in Fig. 2.12(b) in order to ensure a propagation of the incoming beam at normal incidence on the sphere and propagation inside the sphere that is along its diameter D .

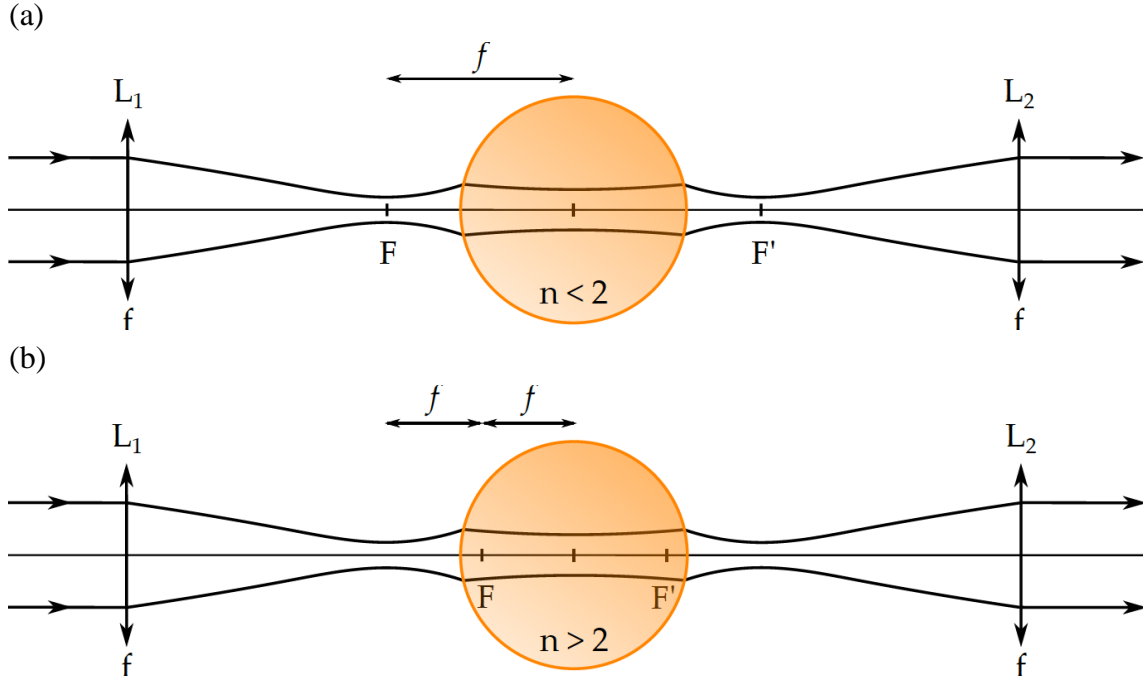


Figure 2.12: Propagation scheme around the sphere, showing the selected focusing scheme inside the sphere shaped in crystals with refractive indices $n^\pm(\lambda, \theta, \varphi) < 2$ (a) or $n^\pm(\lambda, \theta, \varphi) > 2$ (b).

A second crucial key point is that both propagation schemes of Fig. 2.12 are fulfilled only if the sphere diameter D is smaller than twice the Rayleigh $Z_R^\pm = \frac{\pi n^\pm(\lambda, \theta, \varphi) W_0^2}{\lambda M^2}$ length; W_0 is the beam waist radius at the beam wavelength λ that is located at the middle of the sphere. M^2 is the beam M-square factor [22]. Such a condition has been fulfilled before any studies reported in chapter 3 and 4.

$W_0(\lambda)$ is not accessible but can be calculated after measuring the beam-waist radius, $W(\lambda)$ at the focus point of a $f = 100$ -mm-focal CaF_2 lens located in front of the sphere. As an example, with the OPO-DFG beam wavelength set around $\lambda \approx 2 \mu\text{m}$, and using the knife method described in part 2.2.3, we found that $W = 45 \mu\text{m}$ [12]. Then a Gaussian formalism in the paraxial approximation described by ABCD matrices provides the calculation of the corresponding values of W_0 and Z_R^\pm [21].

The determination of W and W_0 values performed over to the full emission range of the tunable beam used in the SPHERE method provides the maximal value of the sphere or cylinder diameter D fulfilling $D \leq 2 Z_R^\pm$.

Using the SPHERE method, we performed direct measurements of the dielectric frame orientation, the phase-matching tuning curves in the principal planes and the relative signs between nonlinear coefficients by following the associated conversion efficiencies.

2.3.3 Direct measurements and analysis

2.3.3.1 Orientation of the dielectric frame

As already said, the determination of the orientation of the dielectric frame is easy in uniaxial crystals (hexagonal, tetragonal and trigonal) and in biaxial crystals belonging to the orthorhombic systems. In these crystals, the dielectric and the crystallographic frames are completely linked, their relative orientation being fixed and well-known [1].

But in the biaxial crystals belonging to the monoclinic system as crystals studied in chapter 3 and 4, it is much more complicated: the dielectric frame is linked to the crystallographic frame by the special crystallographic axis only. This axis is a 2-fold axis (point group 2) and/or the axis perpendicular to a mirror plane (point groups m and $2/m$). By convention, it is b -axis. Then the dielectric principal plane and the corresponding axes located in the plane perpendicular to b -axis can rotate as a function of wavelength [11].

The orientation of the dielectric frame can be found by studying the spatial walk-off angle in a principal plane (u, v) of birefringent crystals. As described in part 1.2.5, along any direction of propagation $\vec{u}(\omega, \theta, \varphi)$, two Poynting vectors $\vec{s}^{\pm}(\omega, \theta, \varphi)$ with the associated electric vectors $\vec{e}^{\pm}(\omega, \theta, \varphi)$, propagate oriented at spatial walk-off angles $\rho^{\pm}(\omega, \theta, \varphi)$ from the wave propagation directions vectors $\vec{k}^{\pm}(\omega, \theta, \varphi)$.

$\rho^+(\omega, \theta, \varphi)$ and $\rho^-(\omega, \theta, \varphi)$ are both equal to zero along principal axes and in the (x, y) dielectric plane of uniaxial crystals. Otherwise along all other directions of propagation in uniaxial and biaxial crystals, one spatial walk-off angle is not nil as $\rho^+(\omega, \theta, \varphi)$ shown in Fig. 2.13. Then the corresponding beam is refracted at the output surface of the sphere.

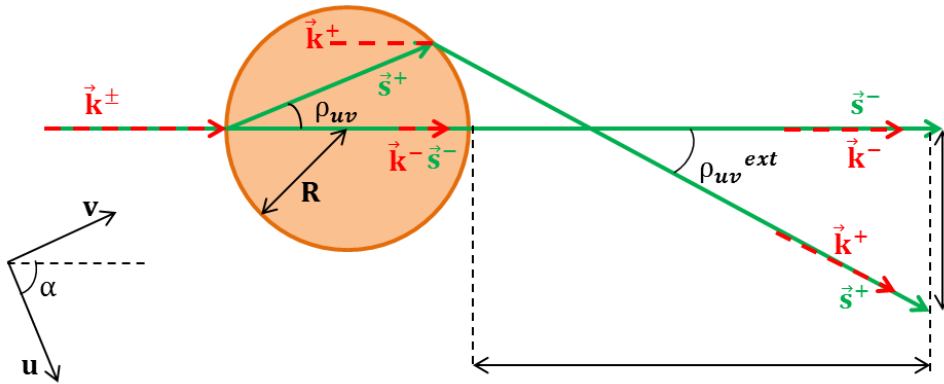


Figure 2.13: Propagation inside a sphere cut is a positive biaxial crystal as an example. The scheme of the sphere rotated in a principal plane $(u, v) = (y, z)$ of the dielectric frame, shows the spatial walk-off effect enhanced by the sphere.

The scheme of Fig. 2.13 can be observed by using for example an unpolarized He-Ne laser at the wavelength of $\lambda = 0.633 \mu\text{m}$ as the incoming laser beam at normal incidence at the entrance of the sphere. Let's consider for example the sphere rotated in the (y, z) principal plane of a positive biaxial crystal. By using the focusing scheme described in part 2.3.2.4 and Fig. 2.13, $\rho^+(\omega, \theta, \varphi)$ is not equal to zero contrary $\rho^-(\omega, \theta, \varphi)$ if the sphere is stopped out of principal axes. It leads to two output beams, which spots observed on a screen, are shown in Fig. 2.14(a). Note that they have perpendicular linear polarizations.

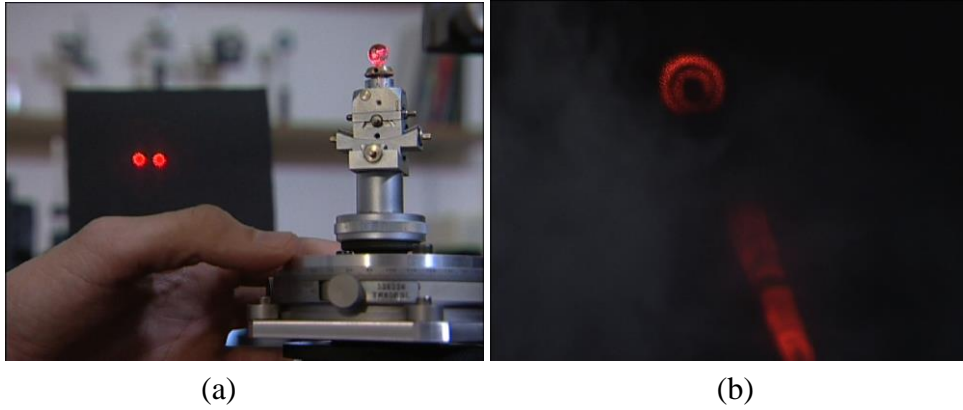


Figure 2.14: Observation of the propagating He-Ne laser beam at the output of a sphere shaped in a biaxial crystal when oriented out of the principal axes x , y or z (a), along one optical axis (OA) of the (x, z) plane (b).

On the contrary, along principal axes, both spatial angles $\rho^\pm(\omega, \theta, \varphi)$ are equal to zero, and the two Poynting unit vectors $\vec{s}^\pm(\omega, \theta, \varphi)$ coincide. Then when propagating a He-Ne laser beam along these axes, a single spot is observed at the output of the sphere.

Let's consider now the two optical axes (OA) located in the (x, z) principal plane of a biaxial crystal as explained in part 1.2.4.2. They are located symmetrically from each side of the z -axis and oriented at V_z angle from z -axis. By propagation a He-Ne laser beam along an optical axis (OA) using a sphere shaped in the (x, z) principal plane, shows a hollow cone caused by the different Poynting vectors, which is called the internal conical refraction phenomenon [23, 24]. It is enhanced by the output surface of the sphere that is equivalent to a lens with a very short focal length. It leads to double rings due to the divergence of the incoming beam as shown in Fig. 2.14(b), which are no longer observed out of the OA direction when the angle value from V_z is over 10 mrad.

Figure 2.15 gives an example of such data recorded over 360° in the (x, z) principal plane of the $\text{YCa}_4\text{O}(\text{BO}_3)_3$ (YCOB) positive biaxial crystal belonging to the point group m of the monoclinic system. It shows the mirror plane perpendicular to the special b -

axis and the goniometric position of a- and c-axis determined by using the Laue method from the X-ray diffraction.

By propagating the He-Ne laser at normal incidence at the entrance of the sphere rotated over 360° , four hollow cones are also observed as shown in Figure 2.14(b). They correspond by pairs to the two optical axes (OA). It means that in this crystal, the b-axis coincides with y-axis and the position of the symmetry axes correspond to the x-axis and z-axis. They are shown in Fig.2.15, as (a, z) , (c, x) and V_z angles values at $\lambda = 0.633 \mu\text{m}$ measured on the Euler circle with an accuracy of 0.1° .

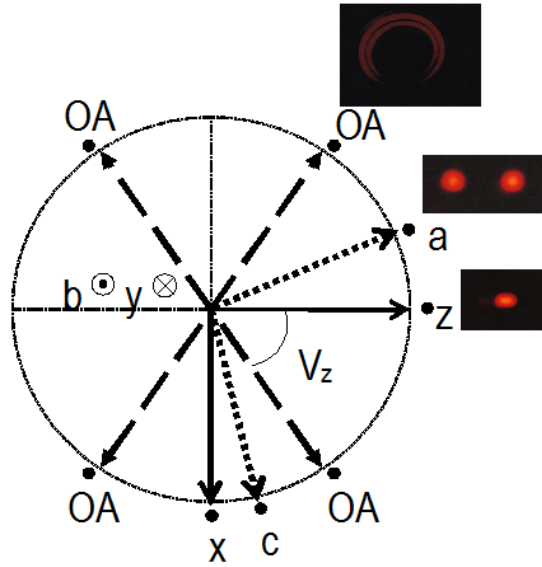


Figure 2.15: Orientation between the crystallographic frame (a, b, c) and the dielectric frame (x, y, z) , in a YCOB crystal where the special b-axis coincide with the y-axis. V_z is the angle between the z-axis and the optical axes (OA). The 3 pictures show the output beam observed on the screen with an unpolarized He-Ne laser propagating along the OA-, z-axis and a-axis.

By coupling the rotating sphere with the tunable OPG-DFG as the incoming beam and by following the protocol described in the previous parts and shown in Figure 2.15, it is possible to measure directly the orientation of the dielectric frame as a function of the wavelength, since the crystallographic attached to the atoms remains fixed.

One possibility is to follow the observation of the position of the output single spots as shown in Figure 2.15 as a function of the wavelength with the beam first propagating along a principal axis inside the sphere at $\lambda = 0.633 \mu\text{m}$. Instead of a screen, a CCD camera with a spectral sensitivity up to $1.1 \mu\text{m}$ and then a mid-IR sensor card up to $1.75 \mu\text{m}$ can be used. Despite the sphere is rotated using the Euler circle as described in part 2.3.2.3, the observation leads to the orientation of the dielectric frame as a function of wavelength with an accuracy of around 0.5° [25].

2.3.3.2 Phase-matching tuning curves in principal planes

The studied nonlinear crystal shaped as a sphere (or cylinder) is stuck along a principal dielectric axis and mounted at the center of the Euler circle. α and β Euler angles are fixed and set in order to rotate the sphere around its vertical axis as shown in Fig. 2.11(b). By this way, any fixed laser beam sent at normal incidence on the sphere, propagates in a principal plane of the dielectric frame.

For SHG tuning curves are directly measured, by using one incoming tunable beam delivered by the OPG-DFG source. Then phase-matched SHG can be studied for a fundamental wavelength ranging between 0.4 and 11 μm . Two collinear incoming beams are directly combined in the sphere for recording SFG and DFG tuning curves, one of them being tunable provided by the OPG-Signal- or OPG-Idler beam, and the other one provided by part of the 1.064 μm beam.

All possible configurations of polarization for types I, II and III of birefringent phase-matching condition associated with a non-zero conversion efficiency can be studied. Thus by studying SHG, SFG and DFG, between 0 and 8 different tuning curves can be recorded in the same principal plane, the only limitation being the transparency range of the studied crystal. However, among all possibilities, the tuning curves involving the principal refractive indices over the full transparency range of the studied crystal are selected i.e. n_o and n_e for a uniaxial crystal, n_x , n_y and n_z for a biaxial crystal.

A phase-matching direction θ_{PM} or φ_{PM} is directly read on the Euler Circle with the accuracy of $\pm 0.5^\circ$ after using the Euler angles as shown in part 2.3.2.3. Such a direction corresponds to a maximum value of the conversion efficiency according to Eq. (1.30) and Eq. (2.2).

Many examples of tuning curves recorded in principal planes of uniaxial and biaxial crystals cut as a sphere or a cylinder will be shown in Chapter 3. For example, for SHG, a tuning curve consists in the fundamental wavelength λ_ω plotted as a function of the phase-matching angle θ_{PM} or φ_{PM} . Let's explain the two possible strategies for recording SHG tuning curves:

- In the first one, the incoming fundamental wavelength λ_ω is fixed while changing the angles θ or φ using the Euler circle. The phase-matching angle θ_{PM} or φ_{PM} is read using the Euler angles, when the conversion efficiency $\eta_{\text{SHG}}(\lambda_{2\omega}, \theta_{\text{PM}}, \varphi_{\text{PM}}, D)$ defined by Eq. (2.2), reaches a maximal value. As in part 2.2.4.3, the phase-matching condition is confirmed for each point of the tuning curve if $\eta_{\text{SHG}}(\theta \text{ or } \varphi)$ shows the theoretical behavior of Fig. 1.7. For such a confirmation, the value of θ or φ is changed by rotating

the sphere around $(\theta_{PM}, \varphi_{PM})$ using the Euler circle, while the OPO-DFG wavelength is fixed at λ_{ω}^{PM} . This protocol is applied successively for all values of the angle θ or φ ranging between 0° and 90° in order to obtain the SHG tuning curve.

- In the second strategy, the angle θ or φ is fixed, and the incoming fundamental wavelength λ_{ω} is varied. Then λ_{ω} is read on the spectrometer and it can also be the phase-matching wavelength generated by SHG $\lambda_{2\omega}^{PM} = \lambda_{\omega}^{PM}/2$. In that case, this protocol is applied for all values of the spherical angles successively to obtain the SHG tuning curve. For that purpose, the OPO-DFG wavelength is tuned around λ_{ω}^{PM} in the sphere fixed in the direction $(\theta_{PM}, \varphi_{PM})$. This protocol is applied successively for all values of λ_{ω} covering the transparency range of the studied nonlinear crystal in order to obtain the SHG tuning curve.

According to chapter 1, the tuning curves are related with $n_o(\lambda)$ and $n_e(\lambda)$ in uniaxial crystals, and $n_x(\lambda)$, $n_y(\lambda)$ and $n_z(\lambda)$ in biaxial crystals that are modelled by Sellmeier equations. Then the fit of recorded tuning curves leads to the Sellmeier coefficients of these equations.

We can obtain the Sellmeier coefficients with the precision of the order of 10^{-4} by the simultaneous fit of all the experimental recorded tuning curves in all the principal planes for all studied types of SHG, SFG and DFG. We use the Levenberg-Macquardt algorithm encoded with Matlab, and many crystals have been studied already using this method in our group [26, 27]. Our Sellmeier equations are valid over the spectral range they have been involved in the different recorded tuning curves.

2.3.3.3 Conversion efficiencies associated to phase-matching conditions out of the principal planes

By using the SPHERE method and a crystal shaped as a sphere, it is possible to record the evolution of the conversion efficiency along phase-matching directions. Using Eq. (1.30) and (1.32), it is then possible to determine the effective coefficient d_{eff} and magnitude and relative sign of the involved nonlinear coefficients.

Let's consider as an example KTP that crystallizes in the mm2 orthorhombic point group. KTP has five non-zero and independent elements in its second-order electric susceptibility tensor that write under the Kleinman assumption and using the contracted notation, i.e. $d_{xzx} = d_{xxz} = d_{zxx}(= d_{15} = d_{31})$; $d_{yyz} = d_{zyy} = d_{zyy}(= d_{24} = d_{32})$; $d_{zzz}(= d_{33})$ [3].

The conversion efficiency along Type II SHG phase-matching directions has been measured out of the principal plane of the dielectric frame of KTP. The SPHERE

method was used with a laser beam providing the fundamental wavelength $\lambda_\omega = 1.064 \mu\text{m}$, and a rotating KTP sphere of diameter $D = 5.12 \text{ mm}$ [28]. The recorded data are shown in Figure 2.16(a).

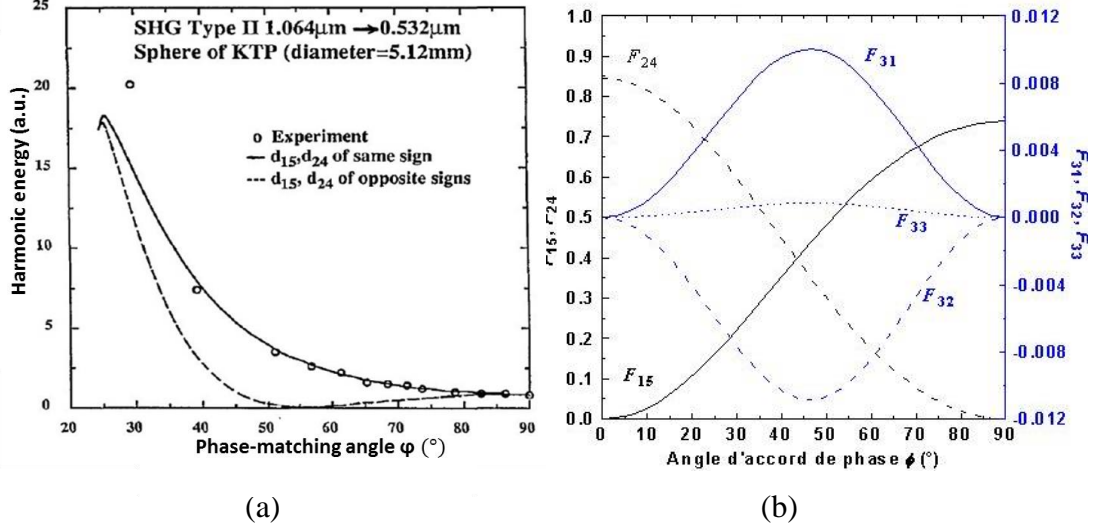


Figure 2.16: Type II SHG conversion efficiency as a function of the phase-matching angle ϕ out of the principal plane (a), calculations of the elements F_{ij} along type II SHG phase-matching curve (b). Dots stand for data recorded with the SPHERE method [28].

Since KTP is a positive biaxial crystal and using Eq. (1.32), the effective coefficient associated to the type II SHG out of the principal plane of KTP writes:

$$d_{eff} = F_{15} \cdot d_{15} + F_{24} \cdot d_{24} + F_{31} \cdot d_{31} + F_{32} \cdot d_{32} + F_{33} \cdot d_{33} \quad (2.5)$$

where the nonlinear coefficients d_{ij} depend on $\lambda_{2\omega}$ and the Field-factors F_{ij} on $(\lambda_\omega, \lambda_{2\omega}, \varphi_{PM})$.

Using Eq. (1.34) the five field factors $F_{ij}(\lambda_\omega, \lambda_{2\omega}, \varphi_{PM})$ of Eq. (2.5) can be calculated and according to their plot shown in Figure 2.16(b) we can consider that d_{eff} writes:

$$d_{eff} \approx F_{15} \cdot d_{15} + F_{24} \cdot d_{24} \quad (2.6)$$

Then Figure 2.16(a) shows that calculations using Eq. (2.6) are in agreement with experimental data when assuming d_{15} and d_{24} with the same relative sign (see solid line). On the contrary there is a big discrepancy between experimental data and calculations when assuming d_{15} and d_{24} of opposite relative sign (see dashed line). It means that d_{15} and d_{24} have the same sign [28].

2.4 Summary

We described in this chapter the experimental methods that we used at Néel Institute. They are devoted to the study of linear and nonlinear optical properties in crystals. We also detailed homemade shaping techniques used to shape crystals as slabs, spheres or cylinders that are cut oriented in the dielectric frame. The setups of all these methods were described as well as the measurements and analysis of data.

We reported methods using slabs for the recording of transmission spectra under polarized light, the determination of the optical damage threshold, and SHG studies under angular critical phase-matching (ACPM) condition.

Then we detailed the SPHERE method and explained how it allows the direct measurements as a function of wavelength of walk-off angles, the dielectric frame orientation and phase-matching condition: directions, associated conversion efficiencies, spectral and angular acceptances. We also explain the determination of the Sellmeier equations describing the dispersion of the principal refractive indices as a function of wavelength, and the magnitudes and relative signs of the non-zero elements of the second-order electric susceptibility from analysis of data.

Chapter 3 Phase-matching directions and Sellmeier equations of GdCOB, LGN and NaI₃O₈

3.1 Introduction

The studies reported in this chapter are in the framework of solid state and pulsed optical parametric generators (OPG) emission under phase-matching condition. Our interest is in high energy OPG emission with the broadest spectral bandwidth of the signal and idler generated beams covering band II (3-5 μm) of transmission of the atmosphere.

This so-called super-continuum condition of OPG emission is of prime importance for numerous civil and industrial high energy applications as the detection of gas, the dermatology or the study of the atmosphere. For the defence, the interest is for the optical countermeasure, the active multi-spectral imaging, or the detection and identification of dangerous molecules using infrared spectroscopy.

As discussed in Chapter 1, the super-continuum condition takes advantage of the type II difference frequency generation (DFG) when fulfilling the conservation energy $1/\lambda_1^+ = 1/\lambda_3^{*-} - 1/\lambda_2^+$ with the “magic” pump wavelength λ_3^* . When pumped at λ_3^* , the OPG tunability is provided with the broadest spectral bandwidth in a nonlinear crystal. However, it relies in the possibility of cutting the crystal at birefringence phase-matching angles that are solutions of Eq. (1.44), for a “magical” pump wavelength that is solution of Eq. (1.45).

An active research work is devoted to identify nonlinear crystals enabling such a condition but those that are currently used are not satisfactory. It is crucial that they have a large damage threshold and conversion efficiency. It is better that their transparency range not only covers band II but also includes half the “magic” pump wavelength, to avoid any risk of two-photon absorption. A magic pump wavelength corresponding to the emission of commercial Ti:Sa or Nd:YAG Lasers is an advantage. We identified three new crystals GdCa₄O(BO₃)₃ (GdCOB), La₃Ga_{5.5}Nb_{0.5}O₁₄ (LGN) and NaI₃O₈, as real a alternative for a phase-matched OPG super-continuum emission covering band II.

After a state of the art about useful linear and nonlinear optical properties already published, this chapter reports the studies that we performed in these three crystals successively. For each study, we specify the samples shapes and the methods from chapter 2 that we used. Then come measurements and analysis of data.

The data recorded in slabs concern in the dielectric frame orientation, the transmission spectra, damage threshold and recording SHG conversion efficiencies to determine the magnitude of nonlinear coefficients.

Then this chapter deals with phase-matching tuning curves, associated conversion efficiencies and the spectral and angular acceptances. These data are directly recorded in principal dielectric planes using spheres or cylinders and over the transparency range of crystals. All recorded data are analysed in this chapter using the theoretical elements of chapter 1. Then come the Sellmeier equations that are refined or determined from the fit of the tuning curves. All the reliable data are then used to calculate phase-matched OPG super-continuum emission with the broadest spectral bandwidth in order to evaluate the ability of the studied crystals to cover band II.

3.2 GdCOB

3.2.1 State of the art

In the past years, a new biaxial crystal belonging to the calcium-rare-earth Oxoborate family, $\text{GdCa}_4\text{O}(\text{BO}_3)_3$ (GdCOB), has been reported with good nonlinear coefficients and a high damage threshold [29, 30]. We studied one large size and good optical-quality sample. Note that GdCOB crystals have also the possibility to be doped with Nd^{3+} for laser emission and self-doubling [29, 30, 31].

Crystal growth and crystallographic frame

GdCOB crystals have been grown from a melt using the Czochralski pulling method [29]. The compound was prepared by classical solid-state reaction and X-ray diffraction patterns confirmed single phase compounds. Differential thermal analysis performed on the GdCOB compound has shown that the material melts congruently. Therefore crystals can be grown from a stoichiometric melt [29].

GdCOB crystals are colourless, with a good optical quality and not hygroscopic. Typically grown samples are 25 mm in diameter and 120 mm long. Bigger 50 mm in diameter and more than 100 mm long crystals were obtained with a larger iridium crucible as shown in Fig. 3.1 [29].

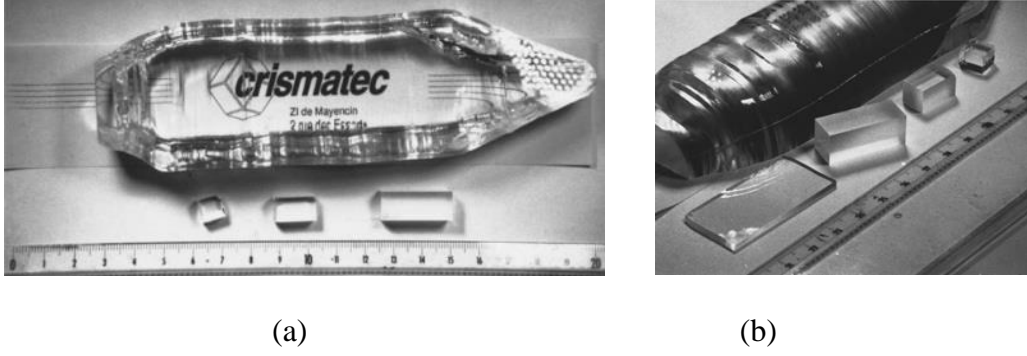


Figure 3.1: GdCOB single crystals grown by the Czochralski pulling method: (a) boule, (b) cut and polished samples [29].

GdCOB crystallizes in the monoclinic system and belongs to the point group m . Then the unit cell contains a mirror that is perpendicular to a special axis. By convention the special axis corresponds to b -axis of the crystallographic frame (a , b , c), a - and c - axes being in the mirror plane. But the crystallographic frame is not orthogonal since the angles between its axes are [29]: $\widehat{ab} = 90^\circ$, $\widehat{bc} = 90^\circ$ and $\widehat{ac} = 101.26^\circ$ as shown in Fig.3.2.

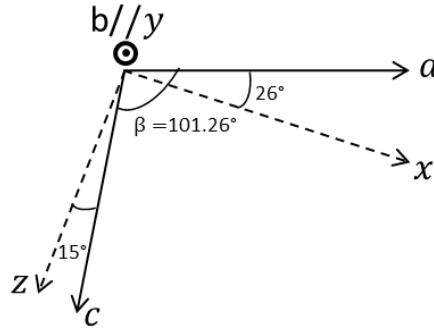


Figure 3.2: Orientation between the crystallographic frame (a , b , c) and the dielectric frame (x , y , z) at one wavelength from visible, in GdCOB from [29]. The international convention y -axis parallel to b -axis is used.

Orientation of the dielectric frame

The dielectric frame (x , y , z) that is orthonormal, cannot correspond to the axes of the crystallographic frame (a , b , c). In this case, as discussed in part 2.2.1, the two frames are linked by one axis only. In GdCOB, it was reported that y -principal dielectric axis corresponds to the special b -axis both remaining fixed. Then the two other dielectric axes, x - and z -, are in the mirror plane as the crystallographic a - and c - axes [29].

By combining X-ray diffraction and conoscopy, the tilt between the x - and z - axes from the a - c ones was found at one wavelength in the visible range [29]. It corresponds to the orientation between the crystallographic frame (a , b , c) and the dielectric frame (x , y , z)

shown in Fig. 3.2 where \hat{ax} to $= 26^\circ$ and $\hat{cz} = 15^\circ$, when using the international convention.

As shown in Fig. 3.2, none of the dielectric x- and z-axes corresponds to the crystallographic a- and c- axes in the visible range. Then the dielectric axes can rotate as a function of wavelength over the full transparency range of GdCOB crystal.

Transparency range

The unpolarized transmission spectra of GdCOB have been measured through the two parallel faces polished to optical quality of a 7 mm thick slab in the UV-range. A 2 mm thick slab was used over 2 μm [29]. They are shown in Figures 3.3(a) and 3.3(b) respectively.

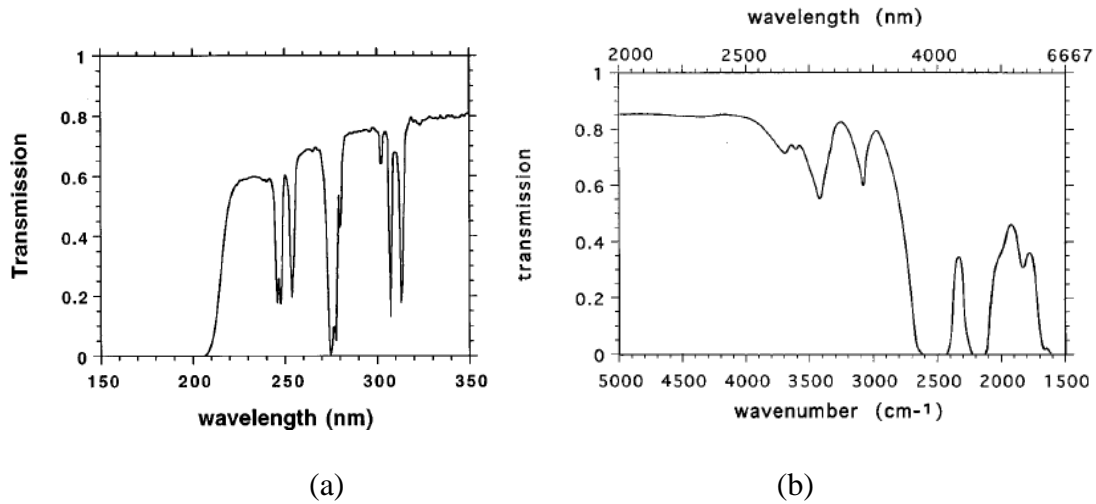


Figure 3.3: Unpolarized transmission spectra through (a) 7 mm- and (b) 2 mm-thick of GdCOB slab [29].

In Figure 3.3(a), a transmission range without absorptions bands is observed in GdCOB from 0.320 μm . It means no risk of two-photon absorption when pumping the GdCOB crystal by the wavelengths emission of Ti:Sa or Nd:YAG lasers.

Furthermore, the GdCOB crystal was found transparent between 0.32 and 4.17 μm . Then as shown in Fig. 3.3(b), the transparency window drops by a factor 2 and includes absorption bands between 4 and 6.6 μm . Taking into account these results, we can consider that GdCOB crystal well covers at least the lower wavelength range of the band II (3-5 μm) of transmission of the atmosphere.

Optical damage threshold

An optical damage threshold of the order of 1 GW/cm^2 has been reported from damage observation at the surface of the polished but uncoated input face of a GdCOB slab. It

was studied using the emission at 0.532- μm of the second-harmonic beam of a Q-switched Nd:YAG laser emitting pulses of 7 ns (FWHM) at 1.064 μm [29].

Optical class and Sellmeier equations of the principal refractive indices

The variation of three principal refractive indices as a function of wavelength, $n_x(\lambda)$, $n_y(\lambda)$ and $n_z(\lambda)$, have been reported over the wavelength range 0.35-1.12 μm . Different polarized tunable light sources and the minimum deviation technique in two prisms were used [32]. It is depicted in Fig. 3.4 showing that GdCOB is a positive biaxial crystal ($n_x < n_y < n_z$).

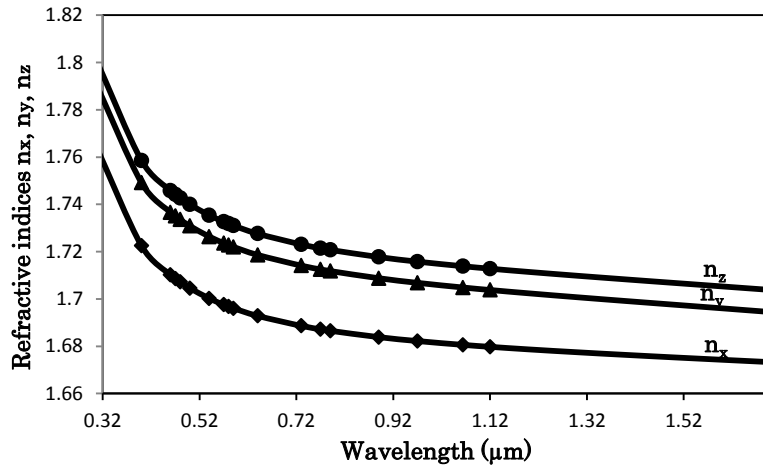


Figure 3.4: Values of the three principal refractive indices n_x , n_y and n_z of GdCOB as a function of wavelength. Dots stand for experimental data recorded with a prism method and lines for fit of data [32].

The following Sellmeier equation was proposed to fit the data shown in Fig. 3.4. Then $n_x(\lambda)$, $n_y(\lambda)$ and $n_z(\lambda)$ are expressed as [32]:

$$n_i^2(\lambda) = A_i + \frac{B_i}{\lambda^2 - C_i} - D_i \lambda^2 \quad (3.1)$$

where the wavelength λ is in μm , and i stands for x, y or z.

The best fit of data shown in Fig. 3.4 was obtained for the values of the coefficients A_i , B_i , C_i and D_i given in Table 3.1. Their accuracy is 10^{-4} but they are valid over the wavelength range 0.35-1.12 μm only.

coefficients	$i = x$	$i = y$	$i = z$
A_i	2.1685	2.2572	2.2587
B_i	0.6163	0.6169	0.6482
C_i	0.0341	0.0383	0.0409
D_i	107.0991	115.7501	148.8075

Table 3.1: Coefficients of the Sellmeier Eq. (3.1) for the best fit of GdCOB data shown in Fig. 3.4 [32].

The previous dispersion equations of the three principal refractive indices of GdCOB have been improved in the 0.4129–1.3382 μm wavelength range by recording SHG tuning curves in rotated slabs [33]. The corresponding data were still fitted by the single-pole Eq. (3.1). However, the best fit was found for new coefficients A_i, B_i, C_i and D_i given in Table 3.2 which accuracy is of about 10^{-5} .

coefficients	$i = x$	$i = y$	$i = z$
A_i	2.8063	2.8959	2.9248
B_i	0.02315	0.02398	0.02410
C_i	0.01378	0.01389	0.01406
D_i	0.00537	0.01132	0.01139

Table 3.2: Coefficients of the Sellmeier Eq. (3.1) for the best fit of GdCOB SHG data from [33].

Using both previous Sellmeier equations, phase-matching conditions types I, II or III SHG, SFG and DFG processes can be calculated in the full dielectric frame of GdCOB. In the following we are interested in recording directly the tuning curves in the three principal planes of the dielectric frame, using the SPHERE method. Our data will be compared to calculations using Eq. (3.1) and the coefficients from Table 3.1 or Table 3.2.

Second-order electric susceptibility tensor

GdCOB crystallizes in the point group m of the monoclinic system, and its crystallographic special b -axis is parallel to the dielectric y -axis. Then the second-order electric susceptibility tensor $\chi^{(2)}$ of the crystal has the following 14 non-zero and independent coefficients according to the Neumann principle. It writes [3]:

$$\chi^{(2)} = \begin{pmatrix} \chi_{xxx}^{(2)} & \chi_{xyy}^{(2)} & \chi_{xzz}^{(2)} & 0 & 0 & \chi_{xxz}^{(2)} & \chi_{xzx}^{(2)} & 0 & 0 \\ 0 & 0 & 0 & \chi_{yyz}^{(2)} & \chi_{yzy}^{(2)} & 0 & 0 & \chi_{yxy}^{(2)} & \chi_{yyx}^{(2)} \\ \chi_{zxx}^{(2)} & \chi_{zyy}^{(2)} & \chi_{zzz}^{(2)} & 0 & 0 & \chi_{zxz}^{(2)} & \chi_{zxx}^{(2)} & 0 & 0 \end{pmatrix} \quad (3.2)$$

Under the Kleinman assumption, it comes:

$$\begin{cases} \chi_{zxx}^{(2)} = \chi_{xxz}^{(2)} = \chi_{xzx}^{(2)}; \chi_{zyy}^{(2)} = \chi_{yyz}^{(2)} = \chi_{yzy}^{(2)} \\ \chi_{xyy}^{(2)} = \chi_{yxy}^{(2)} = \chi_{yyx}^{(2)}; \chi_{xzz}^{(2)} = \chi_{zzx}^{(2)} = \chi_{zzx}^{(2)} \end{cases} \quad (3.3)$$

Then the tensor $\chi^{(2)}$ becomes:

$$\chi^{(2)} = \begin{pmatrix} \chi_{xxx}^{(2)} & \chi_{xyy}^{(2)} & \chi_{xzz}^{(2)} & 0 & 0 & \chi_{zxx}^{(2)} & \chi_{zxx}^{(2)} & 0 & 0 \\ 0 & 0 & 0 & \chi_{zyy}^{(2)} & \chi_{zyy}^{(2)} & 0 & 0 & \chi_{xyy}^{(2)} & \chi_{xyy}^{(2)} \\ \chi_{zxx}^{(2)} & \chi_{zyy}^{(2)} & \chi_{zzz}^{(2)} & 0 & 0 & \chi_{xzz}^{(2)} & \chi_{xzz}^{(2)} & 0 & 0 \end{pmatrix} \quad (3.4)$$

Using the contracted notation, it also writes [3]:

$$\chi^{(2)} = \begin{pmatrix} \chi_{11}^{(2)} & \chi_{12}^{(2)} & \chi_{13}^{(2)} & 0 & \chi_{31}^{(2)} & 0 \\ 0 & 0 & 0 & \chi_{32}^{(2)} & 0 & \chi_{12}^{(2)} \\ \chi_{31}^{(2)} & \chi_{32}^{(2)} & \chi_{33}^{(2)} & 0 & \chi_{13}^{(2)} & 0 \end{pmatrix} \quad (3.5)$$

where:

$$\chi_{xxx}^{(2)} = \chi_{11}^{(2)}; \chi_{xyy}^{(2)} = \chi_{12}^{(2)}; \chi_{xzz}^{(2)} = \chi_{13}^{(2)}; \chi_{zxx}^{(2)} = \chi_{31}^{(2)}; \chi_{zyy}^{(2)} = \chi_{32}^{(2)}; \chi_{zzz}^{(2)} = \chi_{33}^{(2)} \quad (3.6)$$

The sign and magnitude of the six non-zero and independent elements of the second-order electric susceptibility tensor $d^{(2)} = \chi^{(2)}/2$ of GdCOB have been determined at the wavelength of 0.532 μm with an accuracy of 10^{-2} to 10^{-4} . They are given in Table 3.3. Three slabs cut along the three principal dielectric axes x, y and z and the separated-beam method from [34] were used.

Coefficients(pm/V)	Ref. [34]
d_{11}	0.28
d_{12}	0.22
d_{13}	-0.595
d_{31}	-0.34
d_{32}	1.665
d_{33}	-1.20

Table 3.3: Sign and magnitude at 0.532 μm of the six non-zero and independent elements of the electric susceptibility $d^{(2)} = \chi^{(2)}/2$ of GdCOB from [34].

Note that the magnitude of the six elements of Table 3.3 can be calculated at any other wavelength of the transparency range of GdCOB by using the Miller rules from Eq. (1.27) and Sellmeier equations.

In this part, Sellmeier equations are given by Eq. (3.1) and the coefficients from Table 3.1 or Table 3.2.

3.2.2 GdCOB sphere

There is no reason to study again the reliable data reported in GdCOB for the transmission spectra, the damage threshold and the magnitude and signs of the nonlinear coefficients. Then we decided to study the dielectric frame orientation as a function of wavelength and record tuning curves over the transparency range of GdCOB. For that purpose one crystal was shaped as a sphere using the *modus operandi* described in part 2.3.1.

GdCOB was cut as a sphere with a diameter of $D = 5.55$ mm and an asphericity $\Delta D/D$ better than 1%. The sphere surface is polished to optical quality and not coated. It is shown in Figure 3.5 when stuck and mounted on the HUBER goniometric head with the vertical rotation axis oriented along a principal axis of the dielectric frame (x, y, z).



Figure 3.5: GdCOB sphere of 5.55 mm diameter used for our experiments.

3.2.3 Orientation of the dielectric frame as a function of wavelength

We used the SPHERE method which setup is shown in Figure 2.10. Thus we were able to follow the orientation of the dielectric frame as a function of wavelength, by performing the measurements and analysis described in part 2.3.3.1 of chapter 2.

The sphere was stuck and mounted on the HUBER goniometric head with the vertical rotation axis oriented along the y-axis of the dielectric frame. It was oriented on the Euler circle as described in part 2.3.2.3 and shown in Fig. 2.11 to access the (x, z) principal dielectric plane.

The incoming tunable beam wavelength was first set at $0.65 \mu\text{m}$ and the sphere was oriented for the incoming beam propagation along the x-axis where there is no double refraction effect. In this condition, a single spot was observed at the output of the sphere as shown in the insert of Fig. 3.6. The observation of the single spot was followed for several wavelengths ranging between $0.4 \mu\text{m}$ to $1.75 \mu\text{m}$ using a CCD camera and a mid IR sensor card successively.

We found that the single spot stayed at the same position. According to part 2.3.3.1, it means that we did not observe a rotation of the dielectric frame over this wavelength range. Since the GdCOB sphere has been stuck oriented in the crystallographic frame, we determined that the angle between the a- and x-axes remains $(a, x) = 26^\circ \pm 0.5^\circ$, as shown in Fig. 3.6. Note that our data are in agreement with Fig. 3.2 recorded from [29].

According to the behaviour shown in Fig. 3.6, we expect that the dielectric frame of GdCOB does not rotate over its full transparency range.

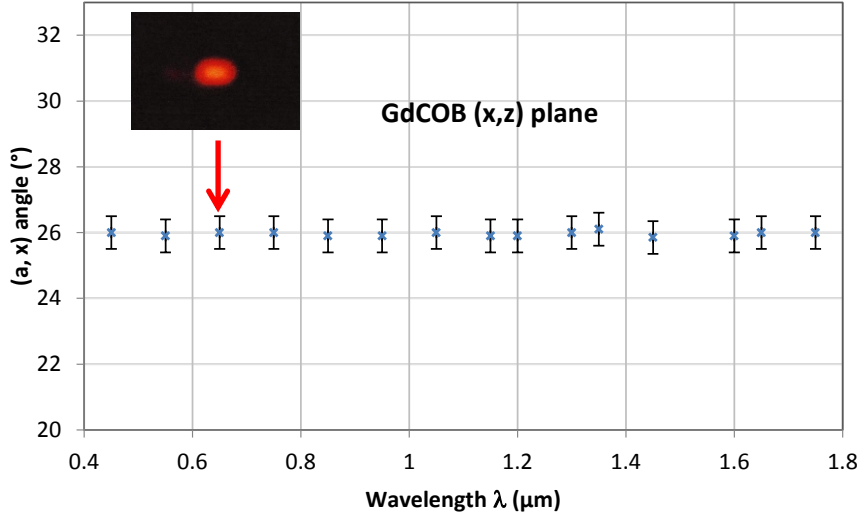


Figure 3.6: Angle (a, x) as a function of wavelength giving the orientation between the crystallographic (a, b, c) frame and the dielectric frame (x, y, z).

3.2.4 Recorded tuning curves

In this part, our objective was to record tuning curves in principal planes of the dielectric frame by using the SPHERE method. They are depicted as the birefringence phase-matching wavelength as a function of spherical phase-matching angles.

We can study all types (I, II or III) of SHG, SFG and DFG processes. However, we are especially interested in wavelengths over the transparency range of GdCOB that covers band II of transmission of the atmosphere. OPG-DFG source limited our studies to SHG and DFG(λ_1). However, according to Eq. 1.30, tuning curves can be recorded only in principal planes for which the associated effective coefficients d_{eff} do not remain equal to zero, and if birefringence phase-matching conditions is possible.

3.2.4.1 phase-matching conditions and associated effective coefficients

Using Eq. (3.4) and Eq. (1.33), we calculated the effective coefficients associated to all types of SHG and DFG(λ_1) tuning curves, in the three principal dielectric planes of the positive biaxial crystal GdCOB. They correspond to $\chi_{eff}(\lambda_{2\omega}, \theta_{PM}, \varphi_{PM})$ and $\chi_{eff}(\lambda_1, \theta_{PM}, \varphi_{PM})$ respectively. They have the advantage to write as the analytical expressions shown in Table 3.4 and Table 3.5 respectively. Note that $d_{eff} = \chi_{eff}/2$.

Type I SHG ($2\omega \ \omega \ \omega$)	Effective coefficient χ_{eff}
Plane y-z	$-\chi_{xyy}(\lambda_{2\omega})\cos[\theta_{\text{PM}}-\rho_{y,z}(\lambda_{\omega}, \theta_{\text{PM}})]^2$ $-\chi_{xzz}(\lambda_{2\omega})\sin[\theta_{\text{PM}}-\rho_{y,z}(\lambda_{\omega}, \theta_{\text{PM}})]^2$
Plane x-y	$-\chi_{xzz}(\lambda_{2\omega})\sin[\varphi_{\text{PM}}+\rho_{x,y}(\lambda_{2\omega}, \varphi_{\text{PM}})]$
Plane x-z ($\theta < V_z$)	$-\chi_{xyy}(\lambda_{2\omega})\cos[\theta_{\text{PM}}-\rho_{x,z}(\lambda_{2\omega}, \theta_{\text{PM}})]$ $+\chi_{zyy}(\lambda_{2\omega})\sin[\theta_{\text{PM}}-\rho_{x,z}(\lambda_{2\omega}, \theta_{\text{PM}})]$
Plane x-z ($\theta > V_z$)	0

Type II SHG ($2\omega \ \omega \ \omega$)	Effective coefficient χ_{eff}
Plane y-z	$\chi_{zxx}(\lambda_{2\omega})\sin[\theta_{\text{PM}}-\rho_{y,z}(\lambda_{\omega}, \theta_{\text{PM}})]$
Plane x-y	$\chi_{zxx}(\lambda_{2\omega})\sin[\varphi_{\text{PM}}+\rho_{x,y}(\lambda_{\omega}, \varphi_{\text{PM}})]\sin[\varphi_{\text{PM}}+\rho_{x,y}(\lambda_{2\omega}, \varphi_{\text{PM}})]$ $+\chi_{zyy}(\lambda_{2\omega})\cos[\varphi_{\text{PM}}+\rho_{x,y}(\lambda_{\omega}, \varphi_{\text{PM}})]\cos[\varphi_{\text{PM}}+\rho_{x,y}(\lambda_{2\omega}, \varphi_{\text{PM}})]$
Plane x-z ($\theta < V_z$)	0
Plane x-z ($\theta > V_z$)	$-\chi_{xyy}(\lambda_{2\omega})\cos[\theta_{\text{PM}}-\rho_{x,z}(\lambda_{\omega}, \theta_{\text{PM}})] +$ $\chi_{zyy}(\lambda_{2\omega})\sin[\theta_{\text{PM}}-\rho_{x,z}(\lambda_{\omega}, \theta_{\text{PM}})]$

Table 3.4: The effective coefficient $\chi_{\text{eff}}(\lambda_{2\omega}, \theta_{\text{PM}}, \varphi_{\text{PM}})$ of types I and II SHG in the three principal planes of the dielectric frame. $\rho_{l,m}(\lambda_i, \alpha)$ ($l, m = x, y$ or z ; $i = \omega$ or 2ω and $\alpha = \theta$ or φ) are the spatial walk-off angles given in Table (1.1). $(\theta_{\text{PM}}, \varphi_{\text{PM}})$ are phase-matching angles using spherical coordinates.

Type I DFG (λ_1)	Effective coefficient χ_{eff}
Plane y-z	$\chi_{zxx}(\lambda_1)\sin[\theta_{\text{PM}}-\rho_{y,z}(\lambda_1, \theta_{\text{PM}})]$
Plane x-y	$\chi_{zxx}(\lambda_1)\sin[\varphi_{\text{PM}}+\rho_{x,y}(\lambda_2, \varphi_{\text{PM}})]\sin[\varphi_{\text{PM}}+\rho_{x,y}(\lambda_3, \varphi_{\text{PM}})]$ $+\chi_{zyy}(\lambda_1)\cos[\varphi_{\text{PM}}+\rho_{x,y}(\lambda_2, \varphi_{\text{PM}})]\cos[\varphi_{\text{PM}}+\rho_{x,y}(\lambda_3, \varphi_{\text{PM}})]$
Plane x-z ($\theta < V_z$)	0
Plane x-z ($\theta > V_z$)	$-\chi_{xyy}(\lambda_1)\cos[\theta_{\text{PM}}-\rho_{x,z}(\lambda_1, \theta_{\text{PM}})] +$ $\chi_{zyy}(\lambda_1)\sin[\theta_{\text{PM}}-\rho_{x,z}(\lambda_1, \theta_{\text{PM}})]$

Type II DFG (λ_1)	Effective coefficient χ_{eff}
Plane y-z	$-\chi_{xyy}(\lambda_1)\cos[\theta_{\text{PM}}-\rho_{y,z}(\lambda_1, \theta_{\text{PM}})]\cos[\theta_{\text{PM}}-\rho_{y,z}(\lambda_2, \theta_{\text{PM}})] -$ $\chi_{xzz}(\lambda_1)\sin[\theta_{\text{PM}}-\rho_{y,z}(\lambda_1, \theta_{\text{PM}})]\sin[\theta_{\text{PM}}-\rho_{y,z}(\lambda_2, \theta_{\text{PM}})]$
Plane x-y	$-\chi_{xzz}(\lambda_1)\sin[\varphi_{\text{PM}}+\rho_{x,y}(\lambda_3, \varphi_{\text{PM}})]$
Plane x-z ($\theta < V_z$)	$-\chi_{xyy}(\lambda_1)\cos[\theta_{\text{PM}}-\rho_{x,z}(\lambda_3, \theta_{\text{PM}})]$ $+\chi_{zyy}(\lambda_1)\sin[\theta_{\text{PM}}-\rho_{x,z}(\lambda_3, \theta_{\text{PM}})]$
Plane x-z ($\theta > V_z$)	0

Type III DFG (λ_1)	Effective coefficient χ_{eff}
Plane y-z	$\chi_{zxx}(\lambda_1) \sin[\theta_{\text{PM}} - \rho_{y,z}(\lambda_2, \theta_{\text{PM}})]$
Plane x-y	$\chi_{zxx}(\lambda_1) \sin[\varphi_{\text{PM}} + \rho_{x,y}(\lambda_1, \varphi_{\text{PM}})] \sin[\varphi_{\text{PM}} + \rho_{x,y}(\lambda_3, \varphi_{\text{PM}})]$ $+ \chi_{zyy}(\lambda_1) \cos[\varphi_{\text{PM}} + \rho_{x,y}(\lambda_1, \varphi_{\text{PM}})] \cos[\varphi_{\text{PM}} + \rho_{x,y}(\lambda_3, \varphi_{\text{PM}})]$
Plane x-z ($\theta < V_z$)	0
Plane x-z ($\theta > V_z$)	$-\chi_{xyy}(\lambda_1) \cos[\theta_{\text{PM}} - \rho_{x,z}(\lambda_2, \theta_{\text{PM}})] +$ $\chi_{zyy}(\lambda_1) \sin[\theta_{\text{PM}} - \rho_{x,z}(\lambda_2, \theta_{\text{PM}})]$

Table 3.5: The effective coefficient $\chi_{\text{eff}}(\lambda_1, \theta_{\text{PM}}, \varphi_{\text{PM}})$ of types I, II and III DFG(λ_1), in the three principal planes of the dielectric frame. $\rho_{l,m}(\lambda_i, \alpha)$ ($l, m = x, y$ or z ; $i = 1, 2$, or 3 and $\alpha = \theta$ or φ) are the spatial walk-off angles given in Table (1.1). $(\theta_{\text{PM}}, \varphi_{\text{PM}})$ are phase-matching angles using spherical coordinates.

Using Eq (1.11) and Eq. (1.38), we give in Table 3.6 the equations verifying the corresponding phase-matching condition.

	Phase-matching condition
Type I SHG	$n^+(\lambda_\omega, \theta_{\text{PM}}, \varphi_{\text{PM}}) = n^-(\lambda_{2\omega}, \theta_{\text{PM}}, \varphi_{\text{PM}})$
Type II SHG	$n^+(\lambda_\omega, \theta_{\text{PM}}, \varphi_{\text{PM}}) + n^-(\lambda_\omega, \theta_{\text{PM}}, \varphi_{\text{PM}}) = 2n^-(\lambda_{2\omega}, \theta_{\text{PM}}, \varphi_{\text{PM}})$
Type I DFG (λ_1)	$n^+(\lambda_1, \theta_{\text{PM}}, \varphi_{\text{PM}})/\lambda_1 + n^-(\lambda_2, \theta_{\text{PM}}, \varphi_{\text{PM}})/\lambda_2 = n^-(\lambda_3, \theta_{\text{PM}}, \varphi_{\text{PM}})/\lambda_3$
Type II DFG (λ_1)	$n^+(\lambda_1, \theta_{\text{PM}}, \varphi_{\text{PM}})/\lambda_1 + n^+(\lambda_2, \theta_{\text{PM}}, \varphi_{\text{PM}})/\lambda_2 = n^-(\lambda_3, \theta_{\text{PM}}, \varphi_{\text{PM}})/\lambda_3$
Type III DFG (λ_1)	$n^-(\lambda_1, \theta_{\text{PM}}, \varphi_{\text{PM}})/\lambda_1 + n^+(\lambda_2, \theta_{\text{PM}}, \varphi_{\text{PM}})/\lambda_2 = n^-(\lambda_3, \theta_{\text{PM}}, \varphi_{\text{PM}})/\lambda_3$

Table 3.6: Phase-matching conditions for types I and II SHG and types I, II and III DFG(λ_1). $\lambda_{2\omega} = \lambda_\omega/2$ and λ_ω are the fundamental and SHG generated wavelengths respectively. λ_i with $i = 1, 2$, or 3 verify the relation of order $\lambda_3 < \lambda_2 < \lambda_1$. $(\theta_{\text{PM}}, \varphi_{\text{PM}})$ are phase-matching angles using spherical coordinates. n^+ and n^- are the refractive indices given by Eq. (1.11).

3.2.4.2 Type I and type II SHG

According to Table 3.4, it is no possible to record tuning curves for type I and II SHG in the (x, z) plane when $V_z < \theta < 90^\circ$ since the effective coefficient is equal to zero. It is the same for type II SHG in the (x, z) plane when $0^\circ < \theta < V_z$.

On the other hand, Table 3.6 shows that by studying type I SHG in the (x, z) plane and types I and II SHG in the (x, y) plane only, the Sellmeier equations of the three principal refractive indices of the positive biaxial GdCOB crystal can be involved over its full spectral range when using the tunability of our OPG-DFG.

The tuning curves were recorded by using the SPHERE method described in chapter 2 which experimental setup is shown in Figure 2.10. During our experiments, the sphere was stuck along the y -axis and the z -axis, successively. It was mounted at the center of

the Euler circle so that we were able to scan the whole (x, z) and (x, y) principal dielectric planes by rotating the sphere successively around the y - and z - axes. The incoming tunable beam was provided by the OPG-DFG (see chapter 2).

The recorded SHG tuning curves in the GdCOB sphere are shown by blue dots in Figures 3.7, 3.8 and 3.9, respectively (note that o and e stand for + and - in the (x, z) principal plane, while o and e stand for - and + in the (x, y) principal plane according to Table 1.1). These figures also give the two theoretical curves calculated by using the Sellmeier equation from Eq. (3.1) and the coefficients of Table 3.1 from F. Mougel *et al.* [32], and the coefficients of Table 3.2 from N. Numemura *et al.* [33]. They are depicted as a back dashed line and a green dashed line respectively.

Figures 3.7, 3.8 and 3.9 clearly highlight some disagreements between our experimental data and the calculations using the Sellmeier equations from F. Mougel *et al.* [32] or from N. Numemura *et al.* [33], especially above to $1.4 \mu\text{m}$. It is probably due to the fact that the Sellmeier equations previously published by Mougel *et al.* [32] and N. Numemura *et al.* [33] are just reasonable in the visible and near-infrared domain, up to $1.12 \mu\text{m}$.

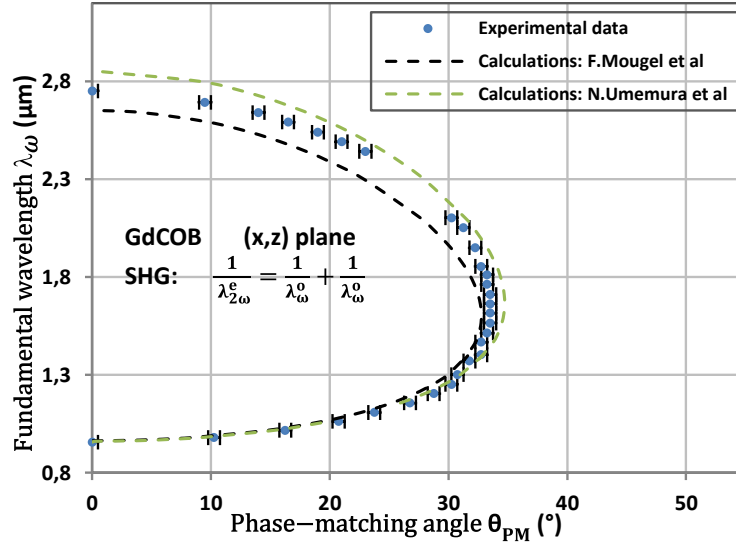


Figure 3.7: Type I SHG tuning curve in the (x, z) principal plane, the fundamental wavelength λ_ω is given as a function of phase-matching angle θ_{PM} . The blue dots correspond to our experimental data. The black and green dashed lines are calculations using the Sellmeier equations of [32] and [33], respectively.

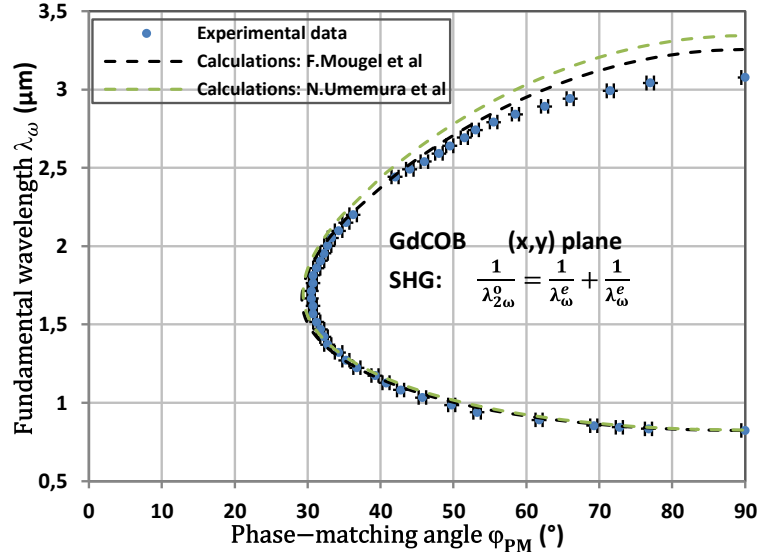


Figure 3.8: Type I SHG tuning curve in the (x,y) principal plane, the fundamental wavelength λ_ω is given as a function of phase-matching angle ϕ_{PM} . The blue dots correspond to our experimental data. The black and green dashed lines are calculations using the Sellmeier equations of [32] and [33], respectively.

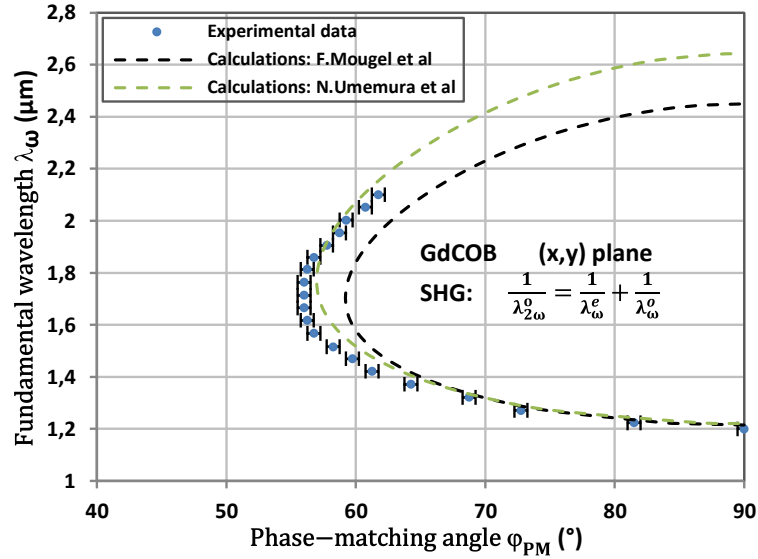


Figure 3.9: Type II SHG tuning curve in the (x,y) principal plane, the fundamental wavelength λ_ω is given as a function of phase-matching angle ϕ_{PM} . The blue dots correspond to the experimental data. The black and green dashed lines are calculations using the Sellmeier equations of [32] and [33], respectively.

Figures 3.8 and 3.9 show that SHG phase-matching condition is possible in GdCOB for fundamental wavelengths ranging between 0.8 and 3.2 μm . It is very important to note that all our recorded tuning curves can be used *per se* for the future use of GdCOB as a doubling crystal in devices in the same wavelength range that we studied.

3.2.4.3 Type II DFG

Dealing with the same strategy as that discussed in the previous part, Table 3.5 shows

that the effective coefficient of Type I and III DFG(λ_1) is always nil in the (x, z) plane. Furthermore, according to Table 3.6, we found sufficient to study type II DFG(λ_1) in the (x, z) plane since compared to SHG studies, we expect to extend the involved wavelength range of the Sellmeier equations, $n_x(\lambda)$, $n_y(\lambda)$ and $n_z(\lambda)$, of GdCOB crystal.

We used the SPHERE method described in chapter 2 which experimental setup is shown in Figure 2.10. The sphere was stuck along the y -axis and mounted at the center of the Euler circle and rotated in order to scan the whole (x, z) principal plane. For the two incoming beams: one has a tunable wavelength λ_3 , and the wavelength of the other one λ_2 , was fixed at $1.064 \mu\text{m}$. They are provided by our source described in part 2.3.2.1.

Dealing with DFG recorded data can be directly used for OPG devices then we propose:

- the pump wavelength λ_p which stands for the wavelength λ_3 ;
- the signal wavelength λ_s which stands for the wavelength $\lambda_s = \lambda_2 = 1.064 \mu\text{m}$;
- the Idler wavelength λ_i which stands for the wavelength λ_1 ;

Furthermore, according Eq. (1.24), $\lambda_p < \lambda_s \leq \lambda_i$ and $\lambda_p^{-1} = \lambda_s^{-1} + \lambda_i^{-1}$.

Type II DFG(λ_i) tuning curve recorded in the (x, z) plane of GdCOB is shown in Figure 3.10 from the variation of the pump and idler phase-matching wavelengths as a function of the phase-matching (PM) angle θ_{PM} . Figure 3.10 also shows the theoretical curves calculated by using the Sellmeier equation from Eq. (3.1) and the Coefficients given in Table 3.1 (from F. Mougel *et al* [32]) and in Table 3.2. (from N. Umemura *et al* [33]). They are depicted as a back dashed line and a green dashed line respectively.

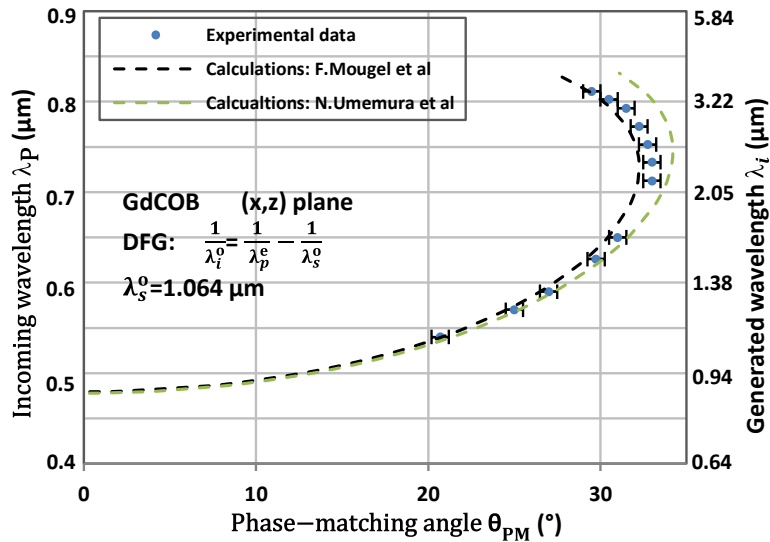


Figure 3.10: Type II DFG(λ_i) tuning curve in the (x, z) principal plane. The generated wavelength λ_i and the tunable incoming wavelength λ_p are given as a function of phase-matching angle θ_{PM} . The other incoming wavelength $\lambda_s = 1.064 \mu\text{m}$. The blue dots correspond to our experimental data. The black and green dashed lines are calculations using the Sellmeier equations of [32] and [33], respectively.

Figure 3.10 shows that type II DFG (λ_i) allows phase-matching conditions for wavelengths ranging from 0.48 to 0.81 μm . The corresponding range for λ_i is between 0.87 and 3.42 μm , the maximum wavelength of 3.42 μm is limited by the infrared cut-off of GdCOB. We also find a discrepancy especially the infrared range between our experimental data and the calculated tuning curves using the Sellmeier equations from F. Mougel *et al* [32] and N. Umemura *et al* [33]. All our recorded tuning curves can be used *per se* for the future use of GdCOB in OPG devices in the same wavelength range that we studied.

3.2.5 Refined Sellmeier equations of the three principal refractive indices

Because of discrepancies between our experimental data and calculations using [32] and [33], the Sellmeier equations of GdCOB need to be refined. As explained in chapter 2, it can be done with the precision of the order of 10^{-4} by the simultaneous fit of all the experimental recorded tuning curves. We use the Levenberg-Macquardt algorithm encoded with Matlab.

For GdCOB we fitted simultaneously the recorded tuning curves in the (x, z) and (x, y) planes for all studied types of SHG and DFG. We tried different forms of analytical Sellmeier equations to describe the dispersion equations of the three principal refractive indices. The best result was obtained with a dual oscillator form as follows:

$$n_i^2(\lambda) = A_i + \frac{B_i\lambda^2}{\lambda^2 - C_i} + \frac{D_i\lambda^2}{\lambda^2 - E_i} \quad (3.7)$$

λ is in μm , and i stands for x, y and z. The corresponding coefficients A_i, B_i, C_i, D_i and E_i are given in Table 3.7.

coefficients	$i = x$	$i = y$	$i = z$
A_i	2.1685	2.2572	2.2587
B_i	0.6163	0.6169	0.6482
C_i	0.0341	0.0383	0.0409
D_i	0.5773	1.3245	1.8922
E_i	107.0991	115.7501	148.8075

Table 3.7: Coefficients of Eq. (3.7) refining the dispersion equations $n_x(\lambda)$, $n_y(\lambda)$ and $n_z(\lambda)$ of GdCOB.

The results of our simultaneous fit are depicted as red lines in Figures 3.11 to 3.14.

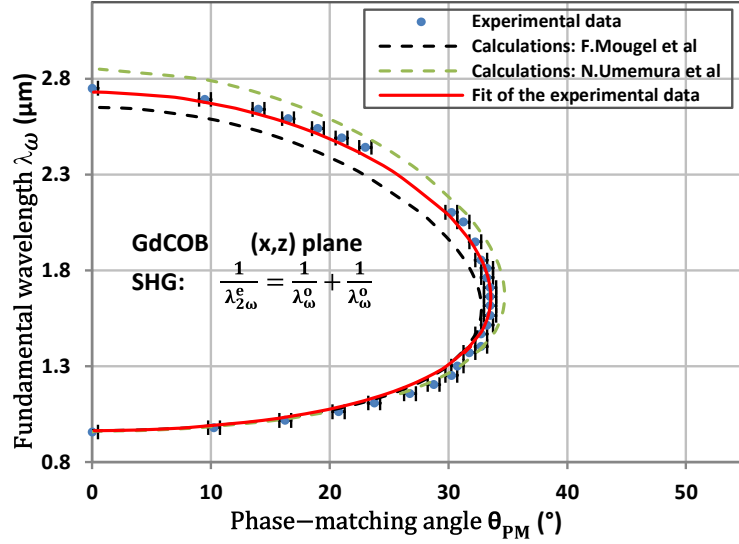


Figure 3.11: Type I SHG tuning curve, the fundamental wavelength λ_ω is given as a function of phase-matching angle θ_{PM} . The blue dots are the experimental data, the dashed lines are calculations using the Sellmeier equations of [32, 33] and the red solid line is our fit of the experimental data.

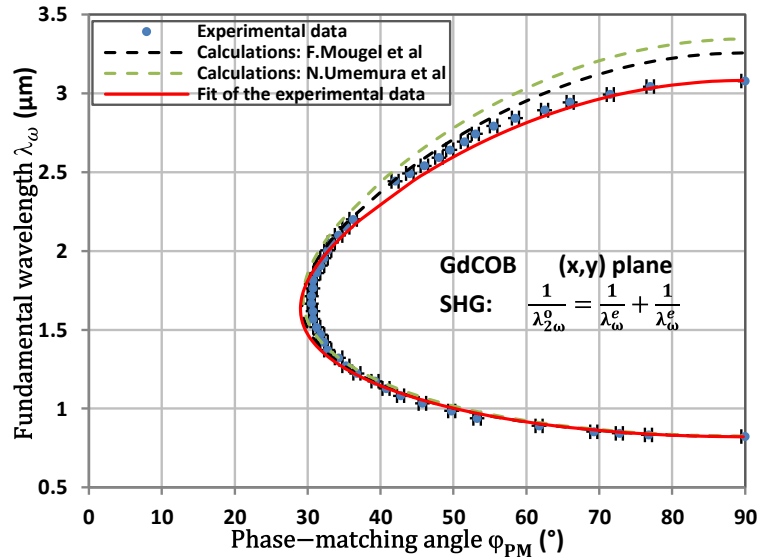


Figure 3.12: Type I SHG tuning curve in the (x,y) principal plane, the fundamental wavelength λ_ω is given as a function of phase-matching angle ϕ_{PM} . The blue dots correspond to the experimental data, the dashed lines are calculations using the Sellmeier equations of [32, 33] and the red solid line is our fit of the experimental data.

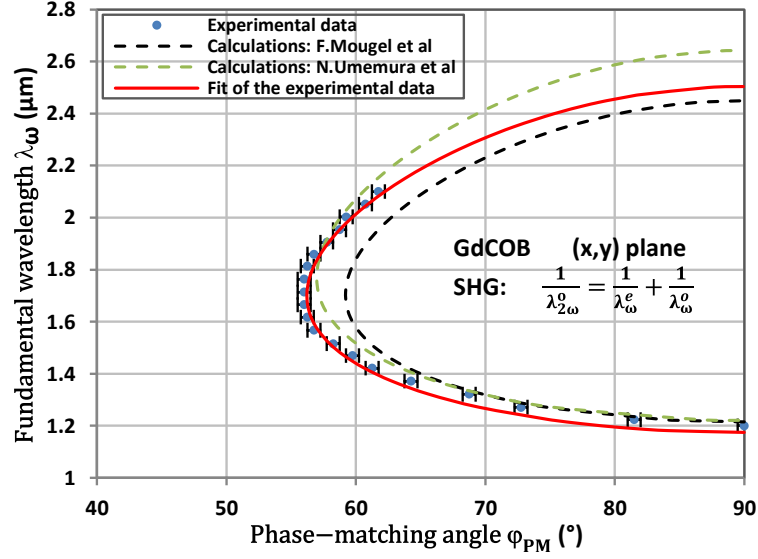


Figure 3.13: Type II SHG tuning curve in the (x,y) principal plane, λ_ω is given as a function of phase-matching angle ϕ_{PM} . The blue dots correspond to the experimental data, the dashed lines are calculated by the Sellmeier equations of [32, 33] and the red solid line is our fit of the experimental data.

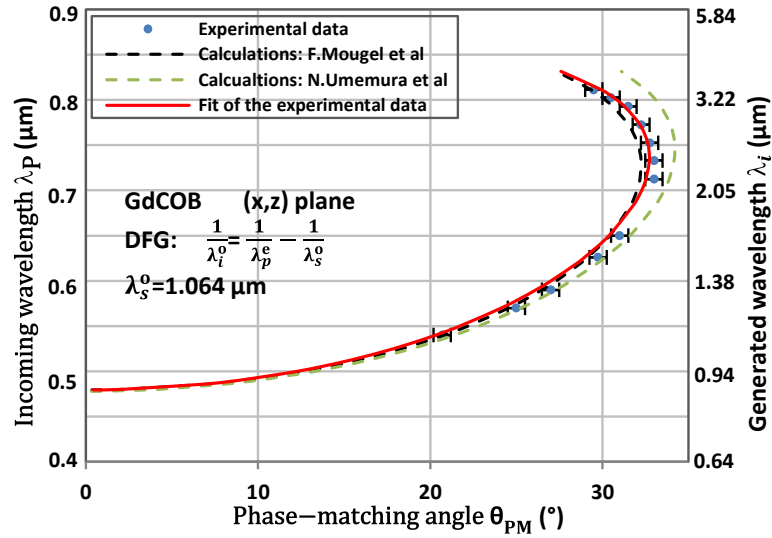


Figure 3.14: Type II DFG(λ_i) tuning curve in the (x,z) principal plane. The generated wavelength λ_i and the tunable incoming wavelength λ_p are given as a function of phase-matching angle θ_{PM} . The other incoming wavelength $\lambda_s = 1.064 \mu m$. The blue dots correspond to the experimental data. The dashed lines are calculations using the Sellmeier equations of [32, 33]. The red solid line is our fit of the experimental data.

Obviously, the results of our simultaneous fit shown in Figures 3.11 to 3.14, are in a much better agreement with our experimental data than calculations using Sellmeier equations from [32,33], especially at high wavelengths values.

Firstly, it is because the precision of our angular measurements is around $\pm 0.5^\circ$, leading

to a relative precision of the principal refractive indices $\Delta n_i/n_i$ better than 10^{-4} , (where i represents x, y and z). Secondly, the wavelength range of our measurements is much wider in our case than in [32,33].

Figure 3.15 shows that our measurements of the studied SHG and DFG(λ_i) cover the wavelength range of 0.41-2.1 μm for n_x , 0.41-3.4 μm for n_y and 0.48-3.1 μm for n_z , which nearly enables the calculation of the phase-matching directions over the entire transparent window of the crystal (red lines). In comparison, the previously published Sellmeier equations from [32] (black dashed lines) and [33] (green dashed lines) just cover the wavelength range of around 0.35–1.34 μm from the visible and near-infrared region.

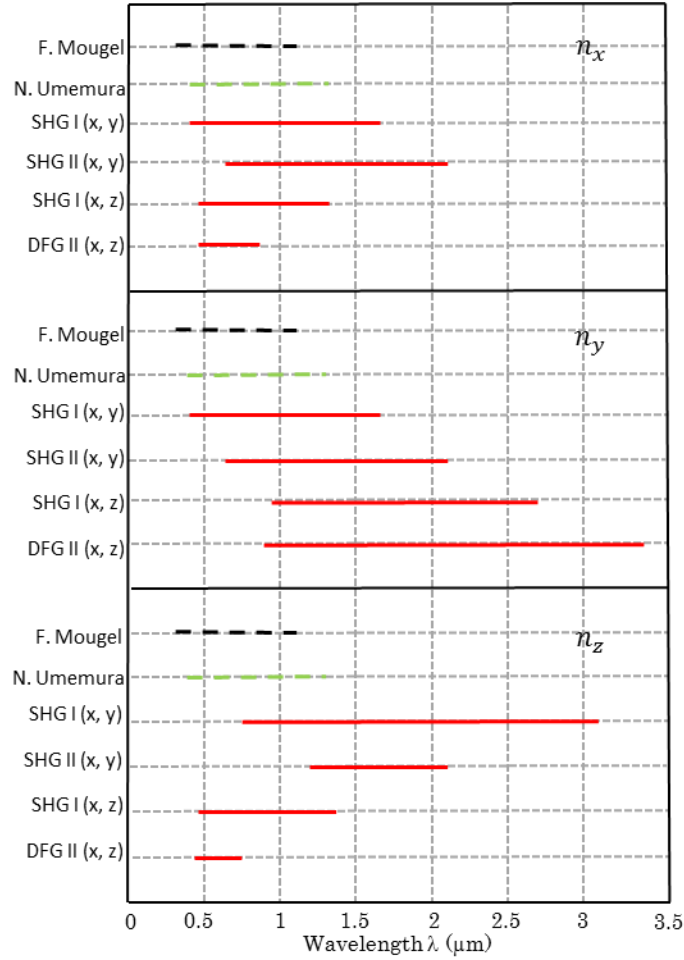


Figure 3.15: Wavelength ranges of solicitation of the three principal refractive indices of GdCOB by our experimental data (red continuous lines), the prism method from F. Mougel *et al.* [32] (black dashed lines), and the phase-matched method from N. Umemura *et al.* [33] (green dashed lines).

3.2.6 Determination of SHG spectral and angular acceptances

We determined spectral and angular acceptances of GdCOB from the recorded type I SHG tuning curve in the (x,z) plane using the sphere. The spectral acceptance was determined from recording the associated SHG conversion efficiency η_{SHG} as a function of the fundamental wavelength λ ; similarly, the angular acceptance was determined from recording η_{SHG} as a function of the spherical angle θ . The wavelength λ and the spherical angle θ were located on each side of the phase-matching wavelength λ_{PM} and angle θ_{PM} , respectively.

Figure 3.16 gives as an example the result we obtained from tuning the wavelength around the phase-matching wavelength $\lambda_{\omega}^{PM} = 1.6 \mu\text{m}$ with the orientation of the sphere set at the phase-matching angle $\theta_{PM} = 33.5^\circ$ ($\varphi_{PM} = 0^\circ$). Another example is shown in Figure 3.17 when rotating the sphere around the phase-matching angle $\theta_{PM} = 0^\circ$ ($\varphi_{PM} = 0^\circ$) with the incoming wavelength set at the phase-matching wavelength $\lambda_{\omega}^{PM} = 0.956 \mu\text{m}$.

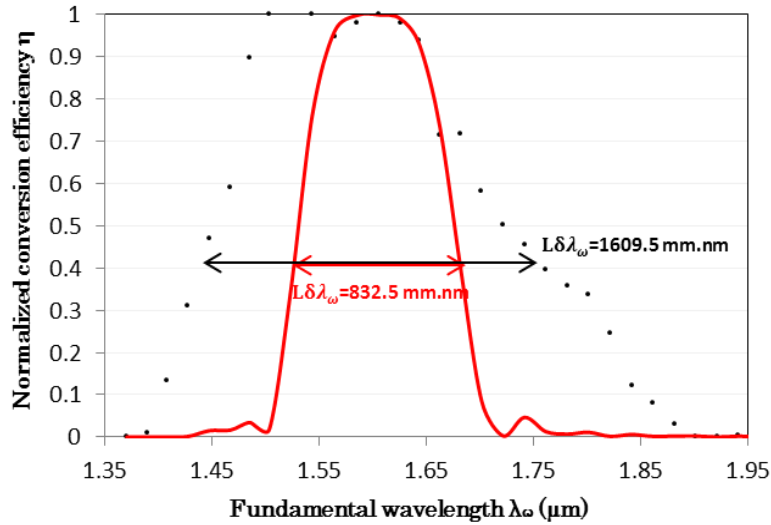


Figure 3.16: Measured (dots) and calculated (continuous line) variation of the normalized conversion efficiency η_{SHG} of type I SHG as a function of the wavelength around the phase-matching wavelength $\lambda_{\omega}^{PM} = 1.6 \mu\text{m}$. Data were recorded in the 5.55 mm diameter GdCOB sphere oriented at the phase-matching angle ($\theta_{PM} = 33.5^\circ, \varphi_{PM} = 0^\circ$) of the (x,z) principal plane. Calculations were performed using our refined Sellmeier Eq. (3.7) with coefficients of Table (3.7).

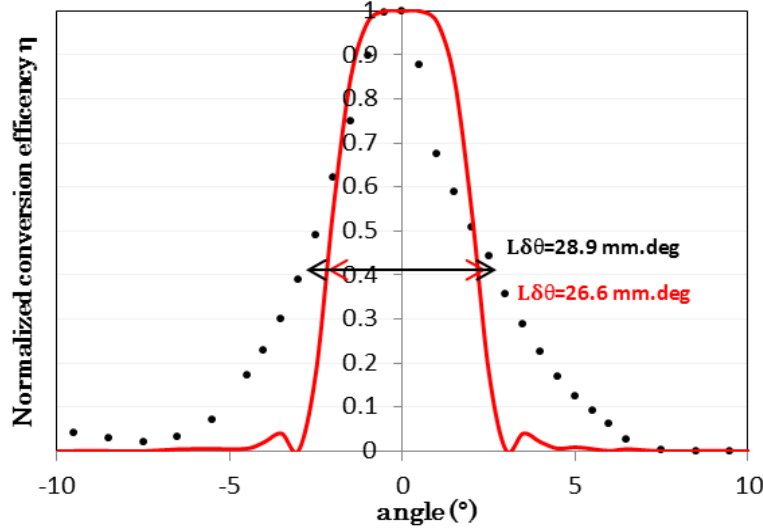


Figure 3.17: Measured (dots) and calculated (continuous line) variation of the normalized conversion efficiency η as a function of the angle for type I SHG at the phase-matching wavelength $\lambda_{\omega}^{PM} = 0.956 \mu m$. Data were recorded in the 5.55 mm diameter GdCOB sphere rotated in the (x, z) principal plane. Calculations were performed using our refined Sellmeier Eq. (3.7) with coefficients of Table (3.7).

Note that data of Fig. 3.17 are recorded along to z -axis and correspond to Angular Non-Critical Phase-matching (ANCPM).

Calculations using our refined Sellmeier equations from Eq. (3.7) and our refined coefficients from Table 3.7, are also depicted in Figures 3.16 and 3.17. They are in good agreement with our recorded data. However, the measured spectral acceptance is $\delta\lambda_{\omega} = 290 \text{ nm}$, which is much larger by around a factor 2 compared with the calculated $\delta\lambda_{\omega} = 150 \text{ nm}$. Such a difference is due to the fact that the sphere was a little damaged during prior measurements along this direction of propagation, which decreases the interaction diameter along this direction. It means that, nearly half of the diameter of the sphere contributes to the SHG conversion efficiency along this direction.

3.2.7 Condition of supercontinuum generation

Using our refined Sellmeier equations, we studied the potentiality of GdCOB for the supercontinuum generation by OPG with the broadest spectral bandwidth under phase-matching condition. As already said, it takes advantage of the type II DFG ($1/\lambda_i^+ = 1/\lambda_p^{*-} - 1/\lambda_s^+$) where $\lambda_p^* = \lambda_3^*$ is the “magic” pump wavelength.

According to Table 3.6, type II DFG tuning curves can be recorded in the three principal planes of the dielectric frame when using a positive biaxial crystal: in the (x, z) principal plane with $0 < \theta < V_z$ and in the (x, y) and (y, z) planes. However, only in the

(x,z) principal plane with $0 < \theta < V_z$ and in the (x,y) planes, the external index n^+ corresponds to a principal refractive index and then an inflection point can be found as discussed in part 1.3.8 of chapter 1.

We calculated the corresponding “magic” pump wavelengths by the solution of Eq. (1.45). It is possible taking into account the index surface of the positive biaxial class shown in Fig. 1.3(a), In the (x,z) plane with $0 < \theta < V_z$ and $n^+ = n_y$, we found that the “magic” pump wavelength $\lambda_p^* = 0.772 \mu\text{m}$. In the (x,y) principal plane where $n^+ = n_z$ then the “magic” pump wavelength $\lambda_p^* = 0.779 \mu\text{m}$.

Then using Table 3.7, we were able to calculate in the two previous planes, the type II DFG tuning curves with the broadest spectral bandwidth when using the calculated “magic” pump wavelength λ_p^* . They are depicted in Figure 3.18. We also chose the following pump wavelengths $\lambda_p = 0.750 \mu\text{m}$, $0.808 \mu\text{m}$ and $0.964 \mu\text{m}$. Their values are close to λ_p^* but they have the advantage to be emitted by a femtosecond Ti: Sapphire laser. They are depicted in Figure 3.19 and Figure 3.20 showing that they enable to generate up to $3.4 \mu\text{m}$ both in the (x,z) and (x,y) principal planes of the dielectric frame of GdCOB. The corresponding spectral bandwidths remain very broad extending to the maximal wavelength range between $1 \mu\text{m}$ $3.4 \mu\text{m}$ when GdCOB is pumped at $\lambda_p = 0.750 \mu\text{m}$ and oriented at the phase-matching direction $\theta_{PM} = 32.5^\circ$, $\varphi_{PM} = 0^\circ$ of the (x,z) plane.

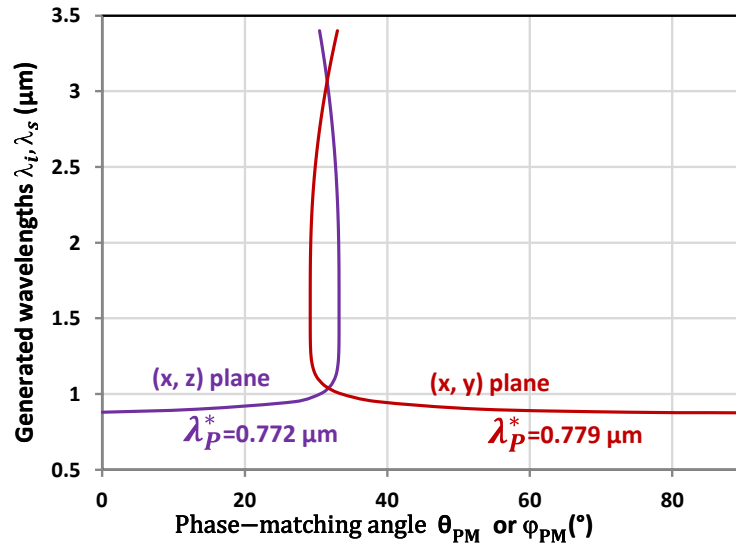


Figure 3.18: Calculated type II DFG ($1/\lambda_p^* = 1/\lambda_i^+ + 1/\lambda_s^+$) tuning curves in the (x,z) and (x,y) principal planes of GdCOB when using the magic pump wavelength λ_p^* . The generated wavelengths λ_i and λ_s are the idler and signal wavelengths, respectively.

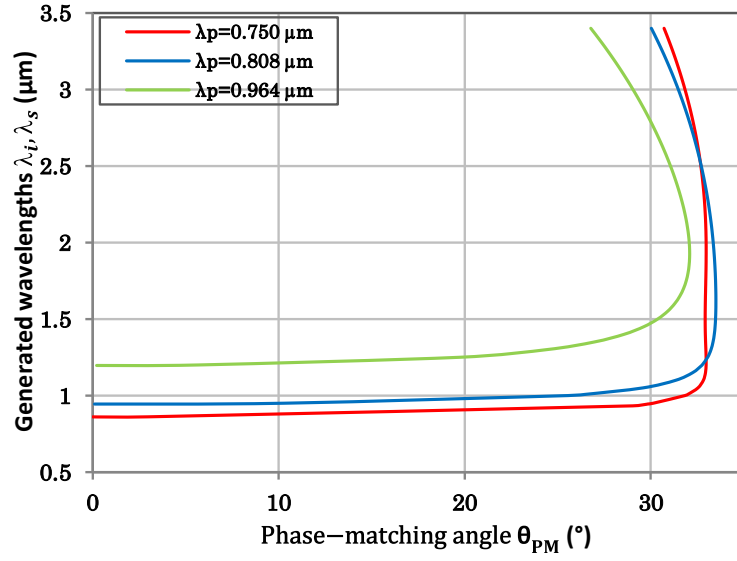


Figure 3.19: Calculated type II DFG ($1/\lambda_p^- = 1/\lambda_i^+ + 1/\lambda_s^+$) tuning curves in the (x,z) principal plane of GdCOB with a pump wavelength λ_p of 0.750, 0.808 and 0.964 μm . The generated wavelengths λ_i and λ_s are the idler and signal, respectively.

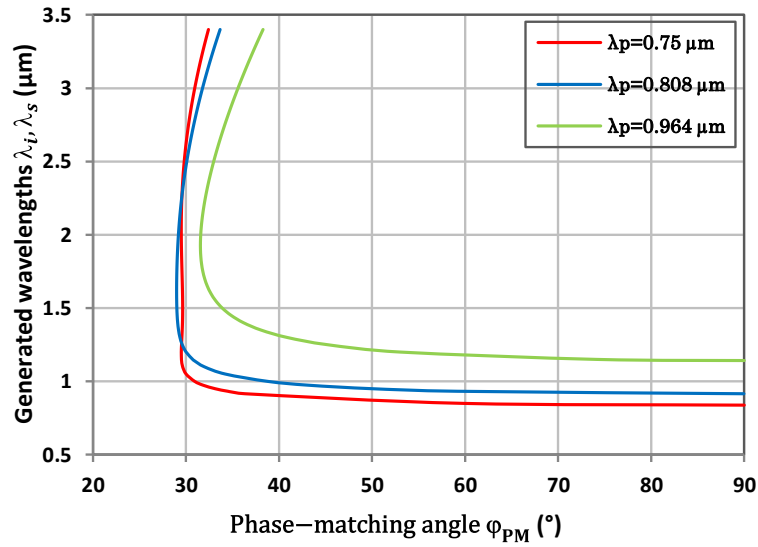


Figure 3.20: Calculated type II DFG ($1/\lambda_p^- = 1/\lambda_i^+ + 1/\lambda_s^+$) tuning curves in the (x,y) principal plane of GdCOB with a pump wavelength λ_p of 0.750, 0.808 and 0.964 μm . The generated wavelengths λ_i and λ_s are the idler and signal, respectively.

3.3 LGN

3.3.1 State of the art

In our group, we directly measured SHG, SFG and DFG tuning curves in the Langatate $\text{La}_3\text{Ga}_{5.5}\text{Ta}_{0.5}\text{O}_{14}$ (LGT) that is a positive uniaxial crystal. Thus we refined the Sellmeier equations of the ordinary and extraordinary principal refractive indices over the entire transparency range of the crystal. We also found from calculations the possibility to generate a supercontinuum from phase-matched OPG using LGT [35]. Then we confirmed the validity of our refined Sellmeier equations, by recording the phase-matching DFG tuning curves tunable between 1.2 and 4.7 μm in the femtosecond regime [36].

Recently our research group identified the Langanate $\text{La}_3\text{Ga}_{5.5}\text{Nb}_{0.5}\text{O}_{14}$ (LGN) belonging to the same family as a serious alternative of LGT that we wanted to study [37].

Crystal growth and crystallographic frame

A LGN single crystal weighting 410 g, with 45 mm in diameter and 100 mm in length is shown in Figure 3.21. It was grown using the Czochralski method [37].



Figure 3.21: LGN single crystal grown by using the Czochralski method.

LGN belongs to the 32 trigonal point group, then the c -axis of the crystallographic frame is perpendicular to the two other axis, *i.e.* a and b , with an angle of $(a, b)=120^\circ$. It means that the crystallographic frame (a, b, c) does not correspond to the orthonormal dielectric frame (x, y, z) . We chose a parallel to x then $(b, y)=30^\circ$ as shown in Fig. 3.22(a). However x - and y -axes of the dielectric frame can be located every 30° of the (a, c) crystallographic plane as shown in Fig. 3.22(b).

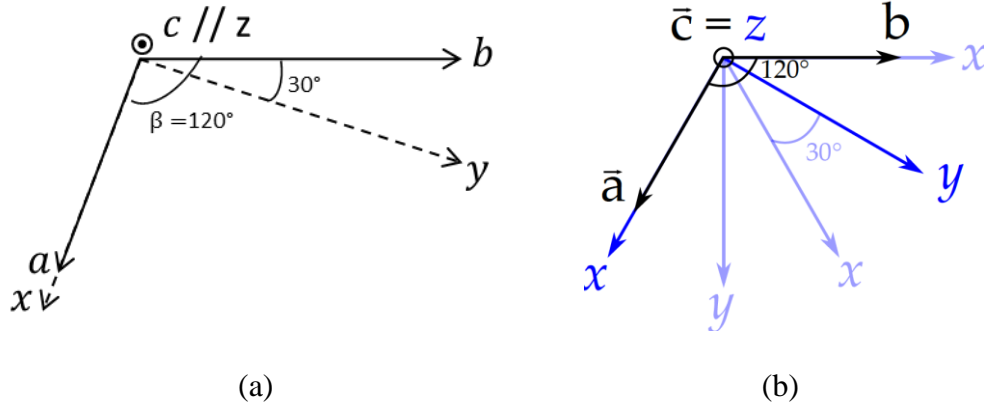


Figure 3.22: Orientation between the dielectric (x, y, z) and the crystallographic (a, b, c) frames of LGN.

Note that in uniaxial crystals the orientation between the dielectric frame (x, y, z) and the crystallographic frame (a, b, c) remains fixed as a function of wavelength.

Transmission spectra and optical damage threshold

Polarized and un-polarized transmission spectra as a function of wavelength were measured through a 2-mm-thick and y-cut LGN slab. As shown in Figure 3.23, LGN is transparent between 0.28 and 7.4 μm , despite a strong and narrow polarized absorption peak located at 1.85 μm due to oxygen defects during crystal growth. A smaller absorption peak exists at 3 μm because of Ga-O bonds [37]. The transparency range is suitable for the optical parametric generation (OPG) covering band II of transmission of the atmosphere when pumped with Ti: Sapphire or Nd: YAG lasers, and that without any risk of two photon absorption of the pump [37].

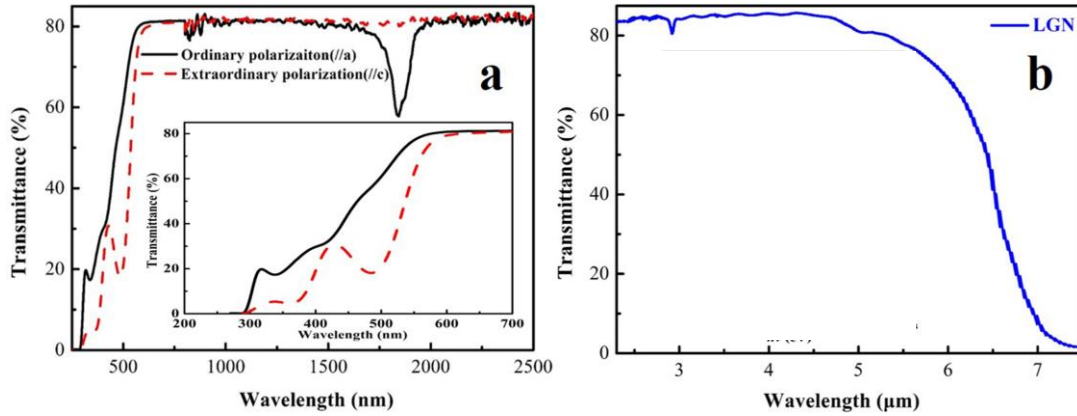


Figure 3.23: Polarized (a) and unpolarized (b) transmission spectra as a function of wavelength through a 2-mm-thick and y-cut LGN slab from [37]. The insert of (a) corresponds to a zoom of the ultraviolet edge.

The damage threshold of 1.41 GW/cm^2 was determined at 1.064 μm , using an input energy per pulse of 40 mJ, in the nanosecond regime [37].

Principal refractive indices

LGN is a positive uniaxial crystal since it was found that the ordinary principal refractive index (n_o) is smaller than the extraordinary one (n_e) ($n_o < n_e$) [38]. Both indices were previously measured as a function of the wavelength using an oriented prism with an accuracy of 10^{-4} . It enabled to determine Sellmeier equations describing the variation of the principal refractive indices as a function of wavelength that are valid between 0.36 and 2.32 μm . They are expressed as follows [38]:

$$n_i^2(\lambda) = A_i + \frac{B_i}{\lambda^2 - C_i} - D_i \lambda^2 \quad (3.8)$$

λ is in μm , and i stands for o and e . The corresponding coefficients A_i, B_i, C_i and D_i are given in Table 3.8.

coefficients	$i = o$	$i = e$
A_i	3.6842	3.7947
B_i	0.0466	0.0508
C_i	0.0297	0.0325
D_i	0.0096	0.0104

Table 3.8: Coefficients of Eq. (3.8) describing the dispersion equations of the ordinary and extraordinary principal refractive indices n_o and n_e of LGN over the wavelength range 0.36–2.32 μm from [38].

Recently, an alternative set of equations valid between 0.43 and 2.3 μm with an accuracy of 10^{-5} was reported. They were determined by placing a LGN prism in a high precision automatic spectrometer goniometer (HR Spectro Master from Trioptics) [37].

The dispersion equations of the two principal refractive indices of LGN, were described by the same Sellmeier equation given by Eq. (3.8) but new coefficients A_i, B_i, C_i and D_i were found from the fit of recorded data [37]. They are given in Table 3.9.

coefficients	$i = o$	$i = e$
A_i	3.79511	3.68270
B_i	0.05000	0.04640
C_i	0.03405	0.02980
D_i	0.00964	0.00870

Table 3.9: Coefficients of Eq. (3.8) describing the dispersion equations of the ordinary and extraordinary principal refractive indices n_o and n_e of LGN over the wavelength range 0.43–2.3 μm from [37].

Second-order electric susceptibility tensor

LGN crystallizes in the point group 32 of the trigonal system with a crystallographic special c-axis parallel to the z-dielectric axis. Then according to the Neumann principle, the second order susceptibility tensor $\chi^{(2)}$ writes at a given circular frequency [3]:

$$\chi^{(2)} = \begin{pmatrix} \chi_{xxx}^{(2)} & \chi_{xyy}^{(2)} & 0 & 0 & 0 & 0 & 0 & 0 & 0 & 0 \\ 0 & 0 & 0 & 0 & 0 & 0 & 0 & \chi_{yyx}^{(2)} & \chi_{yxx}^{(2)} & 0 \\ 0 & 0 & 0 & 0 & 0 & 0 & 0 & 0 & 0 & 0 \end{pmatrix} \quad (3.9)$$

Under the Kleinman symmetry approximation, the following relations are fulfilled:

$$\chi_{xxx}^{(2)} = -\chi_{xyy}^{(2)} = -\chi_{yyx}^{(2)} = -\chi_{yxx}^{(2)} \quad (3.10)$$

Then the second-order susceptibility tensor writes with one independent coefficient, as:

$$\chi^{(2)} = \begin{pmatrix} \chi_{xxx}^{(2)} & -\chi_{xxx}^{(2)} & 0 & 0 & 0 & 0 & 0 & 0 & 0 & 0 \\ 0 & 0 & 0 & 0 & 0 & 0 & 0 & -\chi_{xxx}^{(2)} & -\chi_{xxx}^{(2)} & 0 \\ 0 & 0 & 0 & 0 & 0 & 0 & 0 & 0 & 0 & 0 \end{pmatrix} \quad (3.11)$$

Under the contracted notation, it becomes [3]:

$$\chi^{(2)} = \begin{pmatrix} \chi_{11}^{(2)} & -\chi_{11}^{(2)} & 0 & 0 & 0 & 0 \\ 0 & 0 & 0 & 0 & 0 & -\chi_{11}^{(2)} \\ 0 & 0 & 0 & 0 & 0 & 0 \end{pmatrix} \quad (3.12)$$

where: $\chi_{xxx}^{(2)} = \chi_{11}^{(2)} \quad (3.13)$

Under Kleinman assumption, it was reported that the coefficient $d_{11} = \chi_{11}^{(2)}/2 = 3.0 \pm 0.1$ pm/V at $0.532 \mu\text{m}$ using the Maker Fringe technique [37].

3.3.2 Determination of the optical damage threshold

Using the experimental setup described in part 2.2.3, we determined the surface damage threshold of LGN and KTP slabs with the same thickness $L = 0.52$ mm. Both crystals were illuminated at $1.064 \mu\text{m}$ and located at the beam-waist $W_0 = 30 \mu\text{m}$ of the Nd: YAG laser (5 ns –FWHM and 10 Hz repetition rate).

Using the *modus operandi* described in part 2.2.3, LGN was damaged at an incoming energy of $500 \pm 10 \mu\text{J}$, *i.e.* a peak power density of 2.8 ± 0.7 GW/cm². It is a little bit lower than that of KTP where it was observed at $760 \pm 10 \mu\text{J}$, *i.e.* 4.3 ± 1.1 GW/cm². Note that using the same setup and the same KTP crystal as a reference, the crystal from the same family that is LGT had been damaged for an input energy of $480 \pm 10 \mu\text{J}$, which corresponds to a peak power density of 2.7 ± 0.7 GW/cm².

3.3.3 Recorded tuning curves

In this part, our objective is to record SHG and DFG(λ_i) tuning curves in principal dielectric planes of LGN by using the SPHERE method. As in the previous part, our interest is for birefringence phase-matching condition from types I and II SHG, and for types I, II and III DFG(λ_i), over the full transparency range of LGN. According to Eq. 1.30, SHG and DFG(λ_i) tuning curves can be recorded only if the associated effective coefficients d_{eff} do not remain nil and if phase-matching condition is possible.

3.3.3.1 Phase-matching condition and associated effective coefficients

Using Eq. 1.21, Eq. 1.22 and Eq. 1.32, we calculated the effective coefficients associated to all types of SHG and DFG(λ_i) tuning curves. Since LGN is a positive uniaxial crystal, they correspond to $\chi_{eff}(\lambda_{2\omega}, \theta_{PM}, \varphi_{PM})$ and $\chi_{eff}(\lambda_i, \theta_{PM}, \varphi_{PM})$ respectively and their analytical expressions can be written in the full dielectric frame as shown in Table 3.10. Note that $d_{eff} = \chi_{eff}/2$.

Types	Effective coefficient χ_{eff}
Type I SHG	$-\chi_{xxx}(\lambda_{2\omega}) \cos^2[\theta_{PM} - \rho(\lambda_{\omega}, \theta_{PM})] \sin 3\varphi_{PM}$
Type II SHG	$\chi_{xxx}(\lambda_{2\omega}) \cos[\theta_{PM} - \rho(\lambda_{\omega}, \theta_{PM})] \cos 3\varphi_{PM}$
Type I DFG(λ_i)	$\chi_{xxx}(\lambda_i) \cos[\theta_{PM} - \rho(\lambda_i, \theta_{PM})] \cos 3\varphi_{PM}$
Type II DFG(λ_i)	$-\chi_{xxx}(\lambda_i) \cos[\theta_{PM} - \rho(\lambda_i, \theta_{PM})] \cos[\theta_{PM} - \rho(\lambda_2, \theta_{PM})] \sin 3\varphi_{PM}$
Type III DFG(λ_i)	$\chi_{xxx}(\lambda_i) \cos[\theta_{PM} - \rho(\lambda_s, \theta_{PM})] \cos 3\varphi_{PM}$

Table 3.10: Effective coefficients $\chi_{eff}(\lambda_{2\omega}, \theta_{PM}, \varphi_{PM})$ and $\chi_{eff}(\lambda_i, \theta_{PM}, \varphi_{PM})$ associated to SHG and DFG(λ_i) tuning curves respectively, in the dielectric frame of the positive uniaxial crystal LGN. $\rho(\lambda_i, \theta_{PM})$ ($i = \omega$ or i) are spatial walk-off angles from part 1.2.5. $(\theta_{PM}, \varphi_{PM})$ are phase-matching angles.

Since LGN belongs to the uniaxial optical class, birefringence phase-matching conditions are solutions of Eq. 1.38 in the $(z, x) = (z, y)$ principal plane and the tuning curves given in Table 3.11 depend on the spherical phase-matching angle θ_{PM} only.

	Phase-matching condition
Type I SHG	$n^e(\lambda_{\omega}, \theta_{PM}) = n_o(\lambda_{2\omega})$
Type II SHG	$n_o(\lambda_{\omega}) + n^e(\lambda_{\omega}, \theta_{PM}) = 2n_o(\lambda_{2\omega})$
Type I DFG (λ_i)	$n^e(\lambda_i, \theta_{PM})/\lambda_i + n_o(\lambda_s)/\lambda_s = n_o(\lambda_p)/\lambda_p$
Type II DFG (λ_i)	$n^e(\lambda_i, \theta_{PM})/\lambda_i + n^e(\lambda_s, \theta_{PM})/\lambda_s = n_o(\lambda_p)/\lambda_p$
Type III DFG (λ_i)	$n_o(\lambda_i)/\lambda_i + n^e(\lambda_s, \theta_{PM})/\lambda_s = n_o(\lambda_p)/\lambda_p$

Table 3.11: Phase-matching conditions in LGN for type I and II SHG and for type I, II and III DFG(λ_i). $\lambda_{2\omega} = \lambda_{\omega}/2$ and λ_{ω} are the fundamental and SHG generated wavelengths respectively. θ_{PM} is the phase-matching angle in spherical coordinate, and the relation of order $\lambda_p < \lambda_s \leq \lambda_i$. $n_o = n^-$ is the ordinary principal refractive index and $n^e = n^+$ is given in part 1.2.4.1.

From Tables 3.10, we obtain that the effective coefficients are always nil in the (x, z) principal plane of the dielectric frame for type I SHG and type II DFG(λ_i) since $\varphi_{PM} = 0$ but they are maximal in the (y,z) principal plane where $\varphi_{PM} = 90^\circ$.

It is the contrary for type II SHG and type I and III DFG(λ_i): the effective coefficients are always nil in the (y, z) plane but maximal in the (x,z) plane.

Our experiment must take into account the restrictions imposed by the values of the effective coefficients. Among all tuning curves still possible to study, our strategy is to limit their number by using Table 3.11. With our OPG-DFG source used with the SPHERE method, the dispersion equations of the two principal refractive indices of the positive uniaxial LGN crystal should be well involved over its whole transparency range by studying only:

- type I SHG in the principal (y, z) plane of the dielectric frame
- type III DFG(λ_i) in the principal (x, z) plane of the dielectric frame
- type II DFG(λ_i) in the principal (y, z) plane of the dielectric frame.

3.3.3.2 LGN sphere

We cut and polished a LGN crystal as a sphere with a diameter of 10.8 mm and an asphericity below 1%. The sphere was stuck first along the x-axis on the HUBER goniometric head in order to access the (y, z) plane when rotated. Then it was stuck along the y-axis in order to access the (x, z) plane. It is shown in Figure 3.24.



Figure 3.24: Picture of the sphere of the LGN crystal stuck along x-axis on the HUBER goniometric head.

3.3.3.3 Type I SHG

As already said, we just considered type I SHG in the (y, z) principal plane of LGN. We used the experimental setup of the SPHERE method shown in Figure 2.10 and with the rotated sphere stuck along the x- axis. The recorded type I SHG tuning curve is shown

in Figure 3.25 i.e. the fundamental wavelengths λ_ω as a function of the phase-matching angle θ_{PM} . The second harmonic wavelength is $\lambda_{2\omega} = \lambda_\omega / 2$.

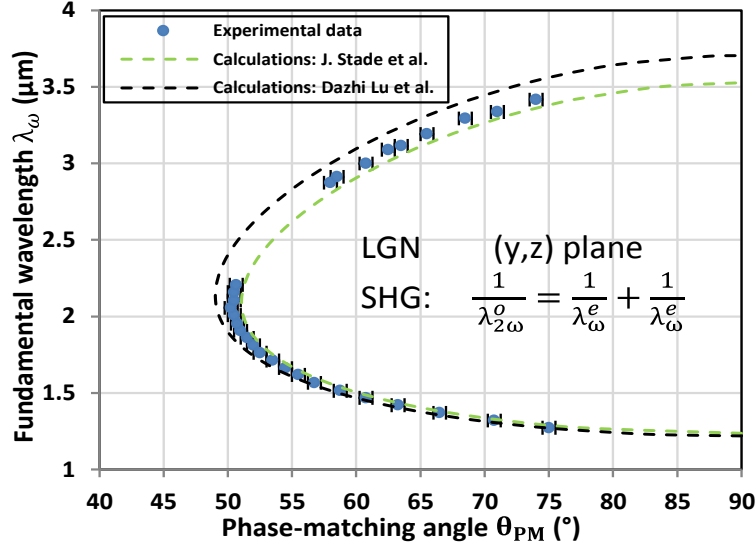


Figure 3.25: Type I SHG tuning curve in the (y, z) principal plane, the fundamental wavelength λ_ω is given as a function of phase-matching angle θ_{PM} . The blue dots correspond to our experimental data. The black and green dashed lines are calculations using the Sellmeier equations of [37, 38], respectively.

The calculated tuning curves using the Sellmeier equations from J. Stade *et al.* [37] and from Dazhi Lu *et al.* [38] are also shown in Figure 3.25 for comparison. They correspond respectively to a green dashed line and to the black dashed line. They both highlight discrepancies with our data.

3.3.3.4 Type II and type III DFG(λ_i)

In order to study DFG(λ_i) in two principal planes of LGN, the sphere was stuck along the principal y- and x-axis, successively to rotate in the (x, z) and (y, z) principal planes of the dielectric frame successively. The two incoming beams were the signal beam at the fixed wavelength $\lambda_s = 1.064 \mu\text{m}$, and the tunable pump wavelength λ_p . They are provided by the OPG-DFG source described in part 2.3.2.1. Figures 3.26 and 3.27 show the recorded the tuning curves of type III DFG ($1/\lambda_i^o = 1/\lambda_p^o - 1/\lambda_s^e$) in the (x, z) principal plane and type II DFG ($1/\lambda_i^e = 1/\lambda_p^o - 1/\lambda_s^e$) in the (y, z) principal plane, respectively.

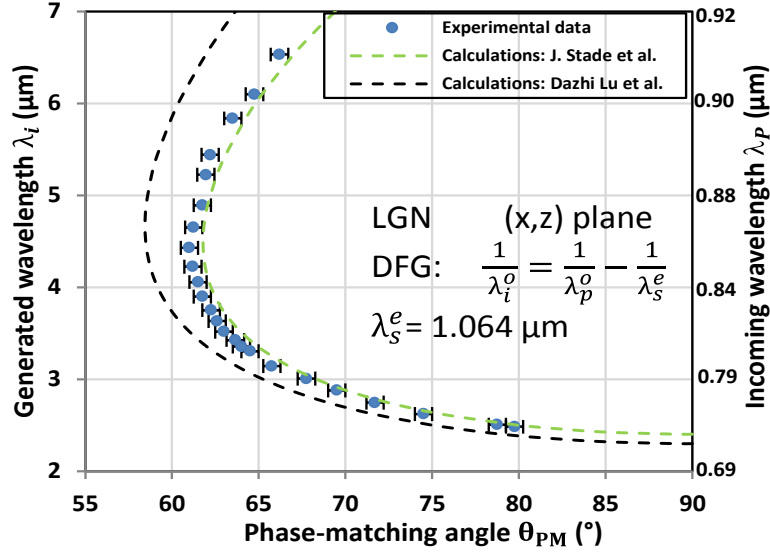


Figure 3.26: Type III DFG(λ_i) tuning curve in the (x,z) plane. The blue dots stand for our experimental data. The black and green dashed lines are calculations using the Sellmeier equations of [37, 38], respectively.

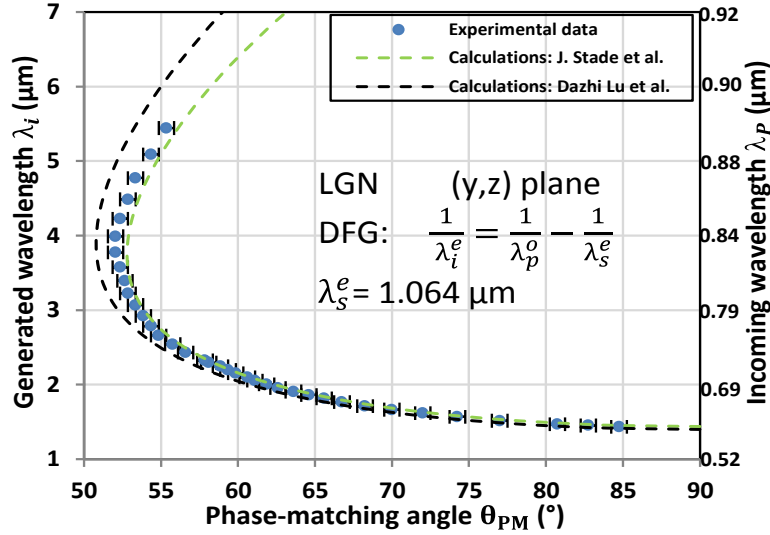


Figure 3.27: Type II DFG(λ_i) tuning curve in the (y,z) plane. The blue dots stand for our experimental data. The black and green dashed lines are calculations using the Sellmeier equations of [37, 38], respectively.

Since LGN is a positive uniaxial crystal, superscripts (o) and (e) stand for (-) and (+) and for the ordinary and extraordinary waves, respectively. λ_p , λ_s and λ_i are respectively the pump, signal and idler wavelengths verifying $\lambda_p < \lambda_s \leq \lambda_i$.

Figures 3.26 and 3.27 also show the calculated tuning curves using the Sellmeier equations from refs. [37, 38]. It highlights discrepancies between our recorded data especially above $2 \mu\text{m}$ even if calculations using [38] are closer to our data.

3.3.4 Refined Sellmeier equations of the two principal refractive indices

The discrepancies between our experimental data and the calculations using the Sellmeier equations from [37, 38] that are shown in Figures 3.25, 3.26 and 3.27, imply to refine the Sellmeier equations of LGN crystal.

For that purpose, we fitted simultaneously all our SHG and DFG(λ_i) tuning curves recorded in the principal planes of LGN. We used the Levenberg-Marquardt algorithm encoded with Matlab. Among the several possible forms of Sellmeier equations used to fit our recorded tuning curves, the best one was that used in refs. [37, 38], *i.e.*:

$$n_i^2(\lambda) = A_i + \frac{B_i}{\lambda^2 - C_i} - D_i \lambda^2 \quad (3.14)$$

λ is in μm , and i stands for o and e . The corresponding dispersive coefficients A_i, B_i, C_i and D_i are given in Table 3.12.

coefficients	$i = o$	$i = e$
A_i	3.6836	3.7952
B_i	0.0460	0.0483
C_i	0.0296	0.0314
D_i	0.0094	0.0102

Table 3.12: Coefficients of Eq. (3.14) refining the dispersion equations of the ordinary and extraordinary principal refractive indices n_o and n_e of LGN

The results of our simultaneous fit are depicted as red lines in Figures 3.28 to 3.30.

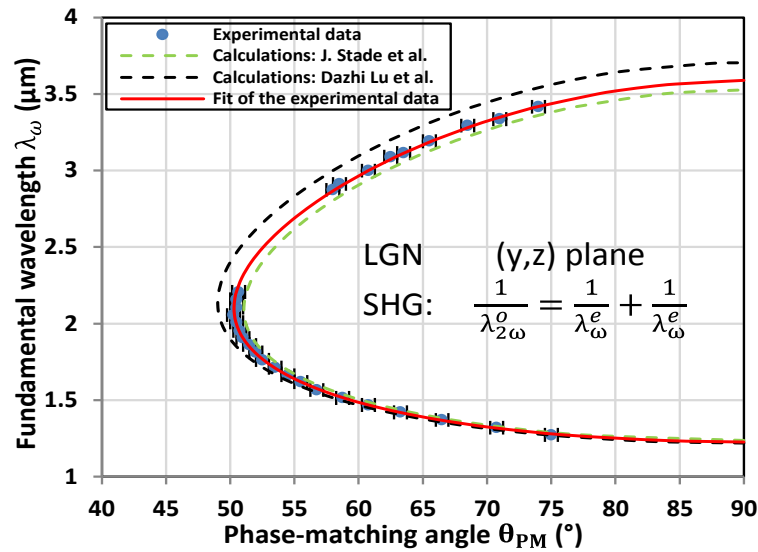


Figure 3.28: Type I SHG tuning curve, the fundamental wavelength λ_ω is given as a function of phase-

matching angle θ_{PM} . The dots correspond to the experimental data, the dashed lines are calculations using the Sellmeier equations of [37, 38] and the red solid line is our fit of the experimental data.

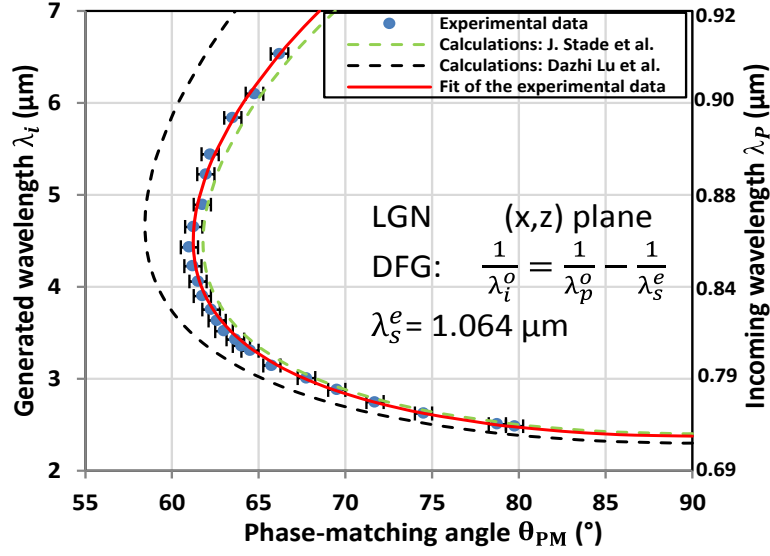


Figure 3.29: Type III DFG(λ_i) tuning curve in the (x, z) principal plane, the incoming wavelength λ_p and the generated wavelength λ_i are given as a function of phase-matching angle θ_{PM} . The signal incoming wavelength $\lambda_s=1.064 \mu\text{m}$. The dots correspond to the experimental data, the dashed lines are calculated by the Sellmeier equations of [37, 38] and the red solid line is our fit of the experimental data.

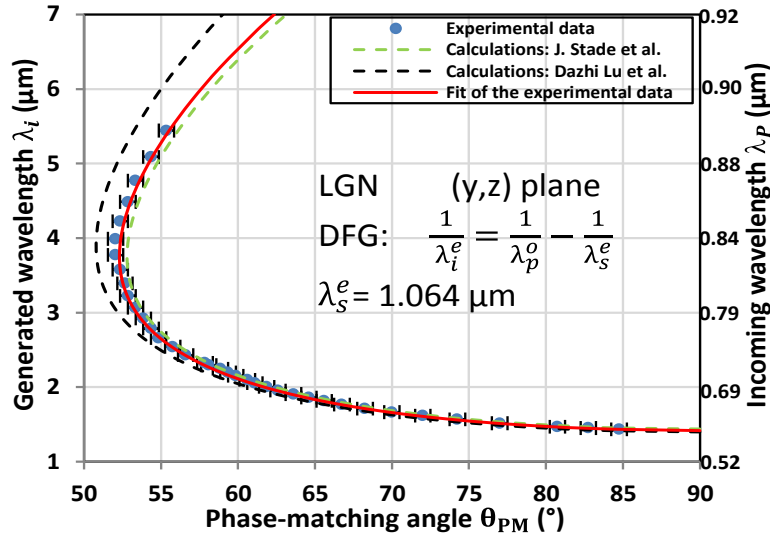


Figure 3.30: Type II DFG(λ_i) tuning curve in the (y, z) principal plane, the incoming wavelength λ_p and the generated wavelength λ_i are given as a function of phase-matching angle θ_{PM} . The signal incoming wavelength $\lambda_s=1.064 \mu\text{m}$. The dots correspond to the experimental data, the dashed lines are calculated by the Sellmeier equations of [37, 38] and the red solid line is our fit of the experimental data.

We refined the Sellmeier equations of LGN thanks to two advantages of our method:

- The precision of our angular measurements is around $\pm 0.5^\circ$, leading to a relative precision of the principal refractive indices $\Delta n_i/n_i$ better than 10^{-4} , (where i represents o and e). The accuracy of the prism method is between $10^{-3} - 10^{-4}$.

- Secondly, the wavelength range over which the principal refractive indices are involved is much wider in our case. Data from [37, 38] are valid up to 2.32 μm .

As shown in Figure 3.31, by performing our measurements up to 6.5 μm , we widely extended the wavelength range where the two principal refractive indices of LGN are valid, compared to studies from references [37, 38].

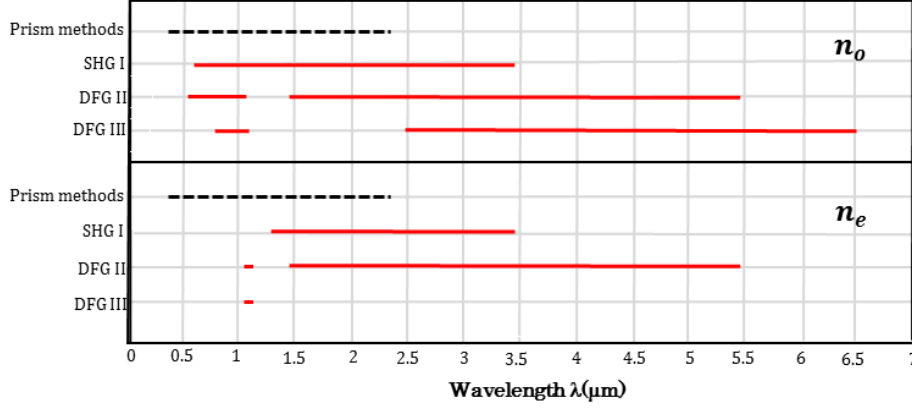


Figure 3.31: Spectral ranges where the principal refractive indices of LGN, n_o and n_e , are valid using the sphere method (red lines), and the prism methods from [37, 38] (black dashed lines).

3.3.5 Determination of the nonlinear coefficient from phase-matched SHG

The absolute value of $d_{11} = d_{xxx} = \frac{\chi_{xxx}^{(2)}}{2}$ was determined through a LGN slab cut with two faces parallel, polished to optical quality and cut perpendicular to an angularly critical phase-matching (ACPM) SHG. We chose a data from the type I SHG tuning curve recorded in the (y, z) principal plane that is shown for example in Figure 3.28 [39]. We chose the experimental setup described in detail in 2.2.4.

The corresponding effective coefficient is:

$$d_{\text{eff}}^{\text{LGN}} = d_{11}^{\text{LGN}} (\lambda_{2\omega_1}^{\text{PM}}) \cos^2 [\theta_{\text{PM}_1} - \rho^e(\theta_{\text{PM}_1}, \lambda_{\omega_1}^{\text{PM}})] \quad (3.15)$$

where $\rho^e(\theta_{\text{PM}_1}, \lambda_{\omega_1}^{\text{PM}})$ stands for the spatial walk-off angle.

We chose the nonlinear coefficient of KTP: $d_{24}^{\text{KTP}}(\lambda_{2\omega_2}^{\text{PM}} = 0.66 \mu\text{m}) = 2.37 \pm 0.17 \text{ pm/V}$ as a reference [19] for the determination of d_{11} of LGN.

The coefficient d_{24}^{KTP} governs type II SHG ($1/\lambda_{\omega_2}^e + 1/\lambda_{\omega_2}^o = 1/\lambda_{2\omega_2}^o$) in the (x, z) principal plane of KTP, the corresponding effective coefficient being $d_{\text{eff}}^{\text{KTP}} =$

$d_{24}^{\text{KTP}}(\lambda_{2\omega_2}^{\text{PM}}) \sin[\theta_{\text{PM}_2} - \rho^e(\theta_{\text{PM}_2}, \lambda_{\omega_2}^{\text{PM}})]$ with $\theta_{\text{PM}_2} = 58.5^\circ$ and $\rho^e(\theta_{\text{PM}_2}, \lambda_{\omega_2}^{\text{PM}}) = 2.57^\circ$ at the fundamental wavelength $\lambda_{\omega_2}^{\text{PM}} = 1.32 \mu\text{m}$.

A LGN slab was then cut at $(\theta_{\text{PM}_1} = 70.4^\circ, \varphi_{\text{PM}_1} = 90^\circ)$ according to our refined Sellmeier equations. As discussed in part 2.2.4, the goal is to study SHG in LGN at a fundamental wavelength the closest as possible to that of KTP in order to get rid of the spectral response of the experimental setup.

LGN and KTP slabs were cut with the same small thickness $L = 0.52 \text{ mm}$. The fundamental beam emitted by the OPG was focused with a 100-mm-focal length CaF_2 lens. Then the beam waist diameter was $w_0 = 120 \mu\text{m}$ on the two slabs surface, with a Rayleigh length of 30 mm that is much longer than L . Thus parallel beam propagation was ensured, and the spatial walk-off attenuation is minimized.

With the fundamental beam energy determined in front of the slab and the SHG energy measured at the exit the slab, we determined the corresponding SHG conversion efficiency of type I SHG in LGN ($\eta_{\text{I}}^{\text{LGN}}$), and that of type II SHG in KTP ($\eta_{\text{II}}^{\text{KTP}}$).

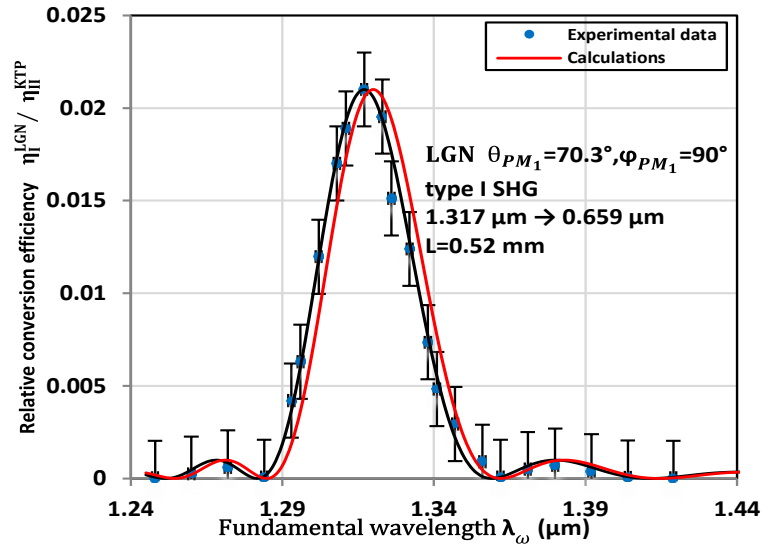


Figure 3.32: Calculated (red line) and measured (dots linked with black line) SHG conversion efficiency measured in LGN relatively to KTP, as a function of the fundamental wavelength λ_ω . Wavelengths accuracy is within dots size.

Figure 3.32 shows the ratio $\eta_{\text{I}}^{\text{LGN}} / \eta_{\text{II}}^{\text{KTP}}$ recorded as a function of the fundamental wavelength λ_ω . The peak wavelength is $\lambda_{\omega_1}^{\text{PM}} = 1.317 \mu\text{m}$ for LGN, which is very close to the targeted value $\lambda_{\omega_2}^{\text{PM}}$. The spectral acceptance $L \cdot \delta\lambda_{\omega_1}$ is equal to 19.8 mm.nm. It is in very good agreement with the calculation using our refined Sellmeier equations.

In these conditions, we can calculate $d_{\text{eff}}^{\text{LGN}}$ relative to $d_{\text{eff}}^{\text{KTP}}$ as follows:

$$(d_{\text{eff}}^{\text{LGN}})^2 = \frac{\eta_I^{\text{LGN}} L_{\text{KTP}}^2 G_{II}^{\text{KTP}} A_{II}^{\text{KTP}}}{\eta_{II}^{\text{KTP}} L_{\text{LGN}}^2 G_I^{\text{LGN}} A_I^{\text{LGN}}} (d_{\text{eff}}^{\text{KTP}})^2 \quad (3.16)$$

with

$$\begin{cases} A_I^{\text{LGN}} = \frac{T_o^{\text{LGN}}(\lambda_{2\omega_1}, \theta_{PM_1})}{n_o^{\text{LGN}}(\lambda_{2\omega_1}, \theta_{PM_1})} \left[\frac{T_e^{\text{LGN}}(\lambda_{\omega_1})}{n_e^{\text{LGN}}(\lambda_{\omega_1})} \right]^2 \\ A_{II}^{\text{KTP}} = \frac{T_o^{\text{KTP}}(\lambda_{2\omega_2}) T_e^{\text{KTP}}(\lambda_{\omega_2}, \theta_{PM_2}) T_o^{\text{KTP}}(\lambda_{\omega_2})}{n_o^{\text{KTP}}(\lambda_{2\omega_2}) n_e^{\text{KTP}}(\lambda_{\omega_2}, \theta_{PM_2}) n_o^{\text{KTP}}(\lambda_{\omega_2})} \end{cases} \quad (3.17)$$

n_o and n_e are the ordinary and extraordinary refractive indices. They were calculated at $\lambda_{\omega_1}^{\text{PM}} = 1.317 \mu\text{m}$ for LGN, and at $\lambda_{\omega_2}^{\text{PM}} = 1.32 \mu\text{m}$ for KTP using respectively the phase-matching angles θ_{PM_1} and θ_{PM_2} defined above and [19]. T_o and T_e are the corresponding Fresnel transmission coefficients. For LGN, the spatial walk-off angle $\rho^e(\theta_{PM_1}, \lambda_{\omega_1}^{\text{PM}}) = 0.55^\circ$ and the spatial walk-off attenuation $G_I^{\text{LGN}} = 0.999$. $G_{II}^{\text{KTP}} = 0.987$ for KTP [3, 19]. Note that the fact that Figure 3.32 shows a conversion efficiency of KTP that is two orders of magnitude higher than that of LGN, is due to the relative value of their trigonometric function that weights differently the nonlinear coefficients at the considered phase-matching angles.

Using Eq. (3.15), we found for LGN $|d_{11}(0.659 \mu\text{m})| = 2.9 \pm 0.5 \text{ pm/V}$ and a Miller index $\delta_{11} = 0.284 \pm 0.049 \text{ pm/V}$ [5]. It corroborates the data using the Maker fringes technique of [37]. Then it is very close to $|d_{24}(0.660 \mu\text{m})| = 2.37 \pm 0.17 \text{ pm/V}$ of KTP [19] but a little bit larger than $|d_{11}(0.659 \mu\text{m})| = 2.4 \pm 0.4 \text{ pm/V}$ of LGT [35].

3.3.6 Condition of supercontinuum generation

We studied the potentiality of LGN for a supercontinuum generation by OPG with the broadest spectral bandwidth under phase-matching conditions. According to Eq. (1.45), we calculated the “magic” pump wavelength $\lambda_p^* = \lambda_3^*$ of type II DFG i.e. $1/\lambda_p^* \rightarrow 1/\lambda_s^e + 1/\lambda_i^e$ in the (y, z) principal plane of LGN, while in the (x, z) principal plane, the corresponding effective coefficient is always zero as shown in Table 3.10. We used our refined Sellmeier equations from Eq (3.14) and the refined coefficients from Table 3.12.

Our calculations show that using a LGN crystal cut at the phase-matching direction ($\theta_{PM} = 52^\circ, \varphi_{PM} = 90^\circ$) and pumped with the “magic” wavelength $\lambda_p^* = \lambda_3^* = 0.982 \mu\text{m}$, the OPG achieves the broadest spectral bandwidth ranging between 1.4 and 3.45 μm . It is shown in Fig. 3.33. According to the value of d_{11} we found, the

associated figure of merit $\frac{(d_{\text{eff}}^{\text{yz}})^2}{n_o(\lambda_p)n_e(\lambda_i)n_e(\lambda_s)} = 0.15 \frac{\text{pm}^2}{\text{V}^2}$.

Figure 3.33 also shows calculated tuning curves still very broad when LGN is pumped at $\lambda_p = 1.064 \mu\text{m}$ and $\lambda_p = 0.8 \mu\text{m}$. These wavelengths, close to λ_p^* are very interesting since they correspond to the emission of Nd:YAG and Ti:Sa lasers respectively.

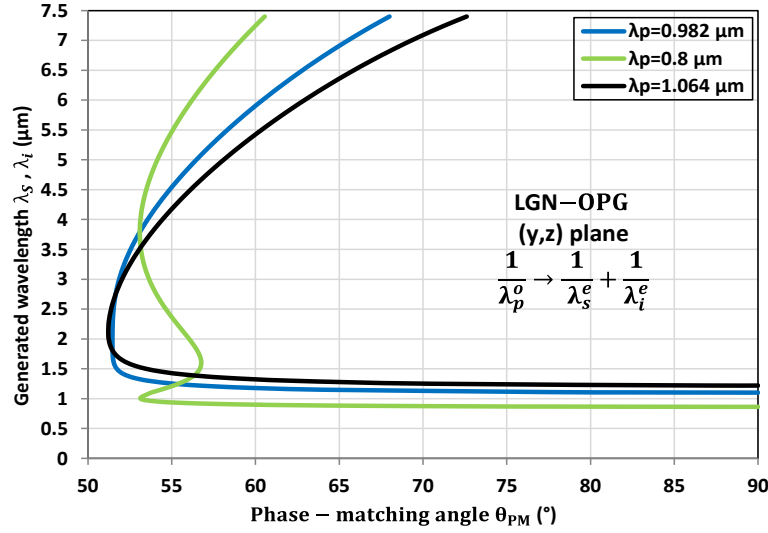


Figure 3.33: Calculated type II OPG tuning curves in the (y, z) principal plane of LGN at different pump wavelengths values λ_p . λ_i and λ_s are the generated idler and signal wavelength respectively.

3.4 NaI₃O₈

3.4.1 State of the art

In 2007, we synthesized and studied the crystal structure of the new acentric crystal NaI₃O₈ in our research group [40]. Three years later, another group showed that this material is a negative uniaxial crystal with potential nonlinear optical properties from powder SHG measurements and calculations based on the density functional theory (DFT) [41].

Crystal growth and crystallographic frame

In 2007, our group synthesized and studied the crystal structure of the new acentric crystal NaI₃O₈ [40]. Recent advances in crystal growth allowed our research group to get single crystals of very high quality suited for the first exhaustive study of the linear and nonlinear optical properties reported in this part.

NaI₃O₈ single crystals were grown by slow evaporation of Nitric Acid aqueous solutions (7M) at fixed temperature ranging between 60 and 70 °C. Samples of several millimeter dimensions were obtained as the one shown in Fig.3.34. While NaI₃O₈ displays a significant solubility in acidic solutions of lower molarity, such solutions were proved

to be unstable toward the reduction of the iodate species into iodine. The later gets incorporated in the growing crystals giving them a yellow tint.

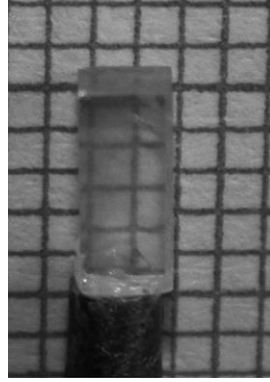


Figure 3.34: NaI₃O₈ single crystal (2×2×5 mm²) grown in our research group.

NaI₃O₈ belongs to the S4($\bar{4}$) tetragonal point group, and its crystallographic frame (a, b, c) is orthonormal and fully coincide with the dielectric frame (x, y, z) [41].

Second-order electric susceptibility tensor

Since NaI₃O₈ belongs to the S4($\bar{4}$) tetragonal point group, then according to the Neumann principle, the second order susceptibility tensor $\chi^{(2)}$ writes at a given circular frequency [3]:

$$\chi^{(2)} = \begin{pmatrix} 0 & 0 & 0 & \chi_{xyz}^{(2)} & \chi_{xzy}^{(2)} & \chi_{xxz}^{(2)} & \chi_{xzx}^{(2)} & 0 & 0 \\ 0 & 0 & 0 & \chi_{yyz}^{(2)} & \chi_{yzy}^{(2)} & \chi_{yxz}^{(2)} & \chi_{yzx}^{(2)} & 0 & 0 \\ \chi_{zxx}^{(2)} & \chi_{zyy}^{(2)} & 0 & 0 & 0 & 0 & 0 & \chi_{zxy}^{(2)} & \chi_{zyx}^{(2)} \end{pmatrix} \quad (3.18)$$

Under the Kleimman symmetry assumption, the following relations are fulfilled:

$$\begin{cases} \chi_{xyz}^{(2)} = \chi_{xzy}^{(2)} = \chi_{yzx}^{(2)} = \chi_{yxz}^{(2)} = \chi_{zxy}^{(2)} = \chi_{zyx}^{(2)} \\ \chi_{xzx}^{(2)} = \chi_{xxz}^{(2)} = \chi_{zxx}^{(2)} = -\chi_{yzy}^{(2)} = -\chi_{yyz}^{(2)} = -\chi_{zyy}^{(2)} \end{cases} \quad (3.19)$$

Then the second-order susceptibility tensor writes with two independent coefficients, as:

$$\chi^{(2)} = \begin{pmatrix} 0 & 0 & 0 & \chi_{xyz}^{(2)} & \chi_{xyz}^{(2)} & \chi_{xzx}^{(2)} & \chi_{xzx}^{(2)} & 0 & 0 \\ 0 & 0 & 0 & -\chi_{xzx}^{(2)} & -\chi_{xzx}^{(2)} & \chi_{xyz}^{(2)} & \chi_{xyz}^{(2)} & 0 & 0 \\ \chi_{xzx}^{(2)} & -\chi_{xzx}^{(2)} & 0 & 0 & 0 & 0 & 0 & \chi_{xyz}^{(2)} & \chi_{xyz}^{(2)} \end{pmatrix} \quad (3.20)$$

Using the contracted notation, it becomes [3]:

$$\chi^{(2)} = \begin{pmatrix} 0 & 0 & 0 & \chi_{14}^{(2)} & \chi_{15}^{(2)} & 0 \\ 0 & 0 & 0 & -\chi_{15}^{(2)} & \chi_{14}^{(2)} & 0 \\ \chi_{15}^{(2)} & -\chi_{15}^{(2)} & 0 & 0 & 0 & \chi_{14}^{(2)} \end{pmatrix} \quad (3.21)$$

where: $\chi_{xyz}^{(2)} = \chi_{14}^{(2)}; \chi_{xzx}^{(2)} = \chi_{15}^{(2)}$ (3.22)

Under the Kleimman assumption, there are only two independent nonzero coefficients of the second-order electric susceptibility tensor: $d_{14} = \frac{\chi_{14}^{(2)}}{2}; d_{15} = \frac{\chi_{15}^{(2)}}{2}$.

3.4.2 Determination of transmission spectra and optical damage threshold

The transmission spectra were recorded in polarized light through a polished and uncoated 3-mm-thick slab with the two faces cut perpendicularly to the x-axis. It is shown in the insert of Figure 3.35.

The linear polarization of light oriented successively perpendicularly and collinear with the z-axis, led to the ordinary and extraordinary transmission coefficients respectively. As described in part 2.2.2, we used a Perkin-Elmer Lambda 900 spectrometer to record spectra as a function of the wavelength between 0.175–3.300 μm , and a Bruker FT-IR above 3.3 μm . The transmission spectra depicted in Figure 3.35 show that NaI₃O₈ is transparent between 0.32 μm and to 6 μm despite strong absorption bands above 4 μm .

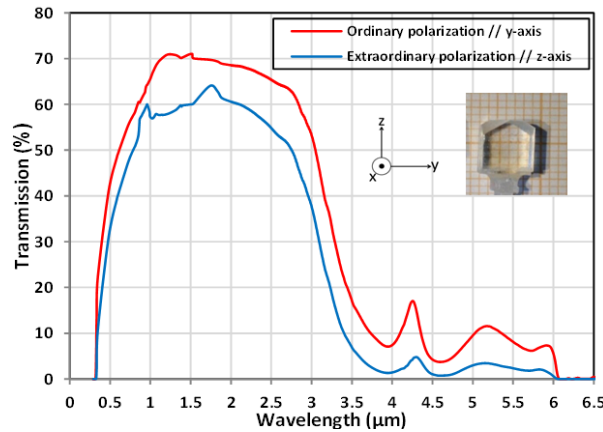


Figure 3.35: Transmission spectra of the 3-mm-thick NaI₃O₈ slab shown in insert.

Using the same experimental setup described in part 2.2.3, we measured the surface damage threshold of a NaI₃O₈ slab illuminated at 1.064 μm and located at the beam-waist $W_0 = 30 \mu\text{m}$ of the Nd: YAG laser (5 ns –FWHM and 10 Hz repetition rate).

Using the *modus operandi* described in part 2.2.3, NaI₃O₈ was damaged at an incoming

energy of $420 \pm 10 \mu\text{J}$, *i.e.* a peak power density of $2.4 \pm 0.6 \text{ GW/cm}^2$. It is much lower than that of KTP where it was observed at $760 \pm 10 \mu\text{J}$, *i.e.* $4.3 \pm 1.1 \text{ GW/cm}^2$.

3.4.3 Determination of the magnitude of a principal refractive index

Since we perform in the next part, the first exhaustive study of the nonlinear optical properties of NaI₃O₈ crystal, the magnitude of one principal refractive index at one wavelength is requested.

It will be simultaneously fitted with the tuning curves recorded in principal planes with the SPHERE method, in order to determine the Sellmeier equations describing $n_o(\lambda)$ and $n_e(\lambda)$ of NaI₃O₈. The reason is that phase-matching angles of tuning curves that are solutions of Eq. 1.38, depend only on ratios $n_o(\lambda_i)/n_e(\lambda_i)$ where $i = 1, 2, 3$ or ω or 2ω .

One possibility to determine the value of a principal refractive index at one wavelength is provided by Brewster angle measured in a rotated slab.

3.4.3.1 Brewster angle

Brewster angle is accessible by measuring the reflection coefficient of the reflected power over the incident power of a beam in polarized light at the input surface of a slab polished. The transmission coefficients T and the reflexion coefficients R at the surface of a slab vary as a function of the tilt θ between the incoming beam and the axis normal to the input surface of the slab. θ is also called the angle of incidence. Both T and R coefficients fulfil the Fresnel equations when recorded in polarized light [2].

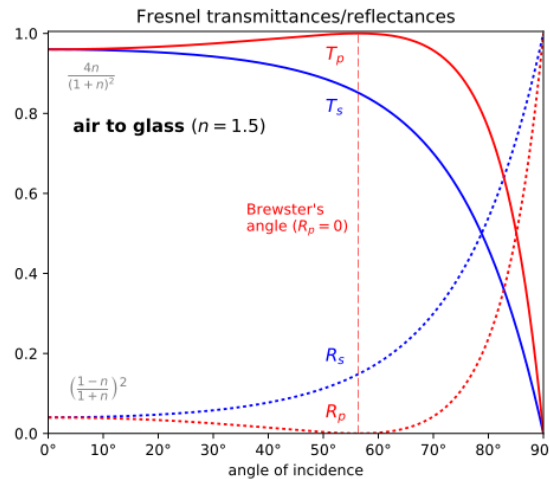


Figure 3.36: Variation of the transmission coefficients T_i and reflexion R_i coefficients at the surface of a rotated slab. They are depicted as a function of the tilt θ between the incoming beam and the axis normal to the surface of the slab, also called the angle of incidence. The subscript $i = p$ when the polarization of the incoming beam is parallel to the incident plane otherwise $i = s$.

According to the polarization state of the incoming beam is parallel or perpendicular to

the incident plane, the reflexion coefficients are $R_p(\theta)$ and $R_s(\theta)$ respectively. Using Fresnel equations, it can be shown that they follow the different behaviours shown in Figures 3.36 at the reflexion of an isotropic medium (glass). Note that the behaviour is complementary for $T_p(\theta)$ and $T_s(\theta)$ as shown in Fig. 3.36, since the following equalities must be fulfilled in a transparent medium: $T_p(\theta) + R_p(\theta) = 1$ and $T_s(\theta) + R_s(\theta) = 1$ [2].

Figure 3.36 shows a special value of the angle of incidence called the Brewster angle θ_B for which the incoming beam with its polarization state parallel to the incident plane is perfectly transmitted ($T_p = 1$) through the input surface of the slab, *i.e* the reflexion coefficient is nil ($R_p = 0$). Using Fresnel's equations, it can be shown that Brewster angle writes:

$$\theta_B = \text{Arctan}[n(\lambda)] \quad (3.23)$$

where n is the refractive index of the medium and λ the wavelength of the incident beam.

3.4.3.2 Our experimental setup

A scheme of the experimental setup we implemented is shown in Figure 3.37. We used a CW laser emitting at the wavelength of $0.671 \mu\text{m}$. The power of the incident beam was controlled using a half-wave plate (HWP) combined with a Glan polarizer. The orientation of the polarization state of the incident beam was controlled using another achromatic half-wave plate inserted before the rotated slab. A f-focal lens focused the input beam at the input surface of the slab providing a propagation in the plane wave approximation.

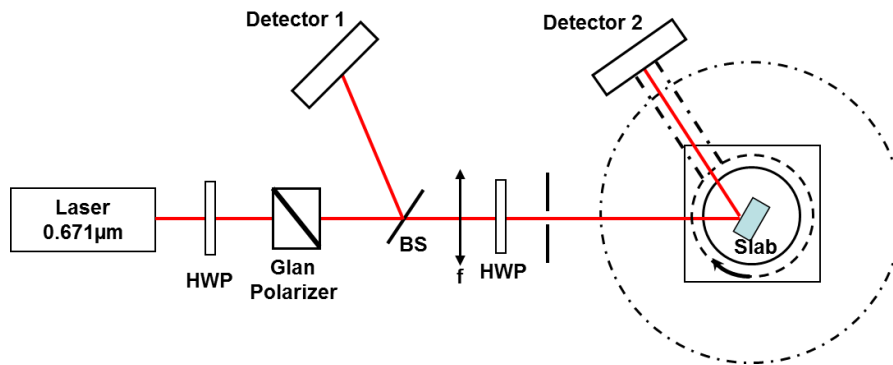


Figure 3.37: Our experimental setup measuring the Brewster angle at the input surface of a slab using the reflection of an incident beam at the wavelength of $0.671 \mu\text{m}$.

The power of the incident and reflected beams were measured simultaneously using two OPHIR powermeters simultaneously. The slab rotation was provided with an accuracy of 0.5° by motors controlled by a homemade software that also allowed an automatic

recording of data on a screen as shown in Fig. 3.38.

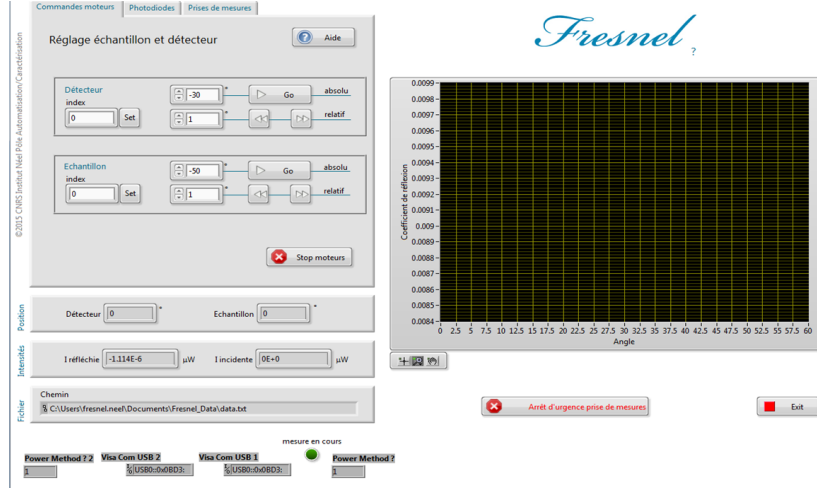


Figure 3.38: Homemade Software Screen.

3.4.3.3 Measurements and analysis

In order to validate our setup, we used this method to measure the value of a principal refractive index of the positive biaxial KTP crystal as a reference. We shaped a slab with two parallel faces cut perpendicular to x-axis of the dielectric frame in order to access the (x, y) principal plane when rotated.

Figures 3.39 show our recorded data obtained in KTP crystal for the polarization state of the incident beam oriented parallel to the incidence plane. Note that because of the mechanical reason, the data included in the red frame cannot be measured as shown in Figure 3.39(a). Data shown in Figure 3.39(b) is a zoom of data shown in Figure 3.39(a) when the incident angle is around 60.5° .

By fitting data shown in Figure 3.39(b), we found that the Brewster angle $\theta_B = 60.5^\circ \pm 0.5^\circ$. Then according to Eq. (3.23) it corresponds to a refractive index value of 1.77 ± 0.03 at $0.671 \mu\text{m}$.

According to Figure 1.3, the principal refractive that is sollicitated is index $n^-(\lambda, \theta_B) = \left[\frac{\cos^2(\theta_B)}{n_y^2(\lambda)} + \frac{\sin^2(\theta_B)}{n_x^2(\lambda)} \right]^{-1/2}$ of KTP. Then using θ_B value and the Sellmeier equations of KTP from [19], we found that $n^-(\lambda, \theta_B) = 1.761$ corroborating our analysis of data.

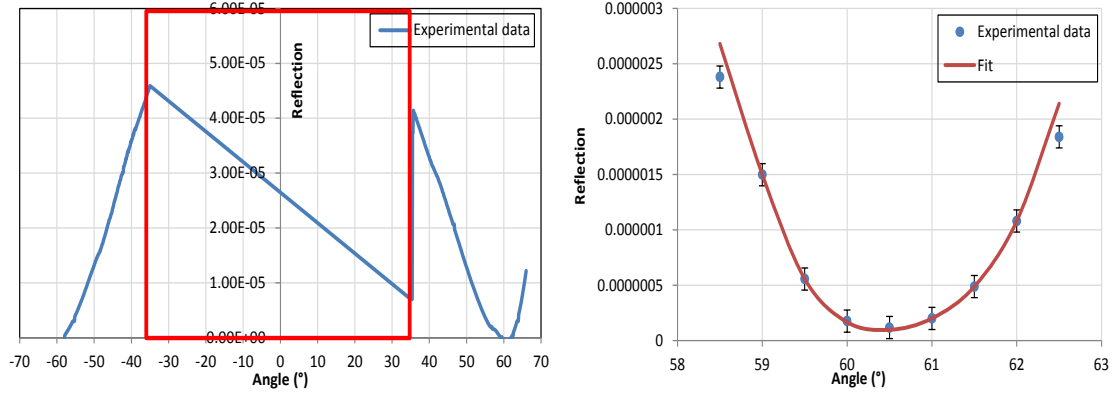


Figure 3.39: (a) Reflexion coefficient at the input surface of a KTP rotated slab, as a function of the angle of incidence. The polarization state is parallel to the incidence plane that corresponds to the (x,y) principal plane and the wavelength is $0.671 \mu\text{m}$. (b) Fit of zoom of data between 58.5° and 62.5° in order to determine the Brewster angle value.

Similarly, one principal refractive index of NaI₃O₈ was studied in order to determine the Brewster angle with a slab rotated in the incidence plane. For that purpose, the slab was shaped with two parallel faces cut perpendicular to x -axis of the dielectric frame. Then the incidence plane corresponds to the (x,y) principal plane. The polarization of the input beam was parallel to that plane. Note that in this case, according to Figure 1.2, at the Brewster angle the principal refractive index $n^+(\lambda, \theta_B) = n_o(\lambda)$ is sollicitated.

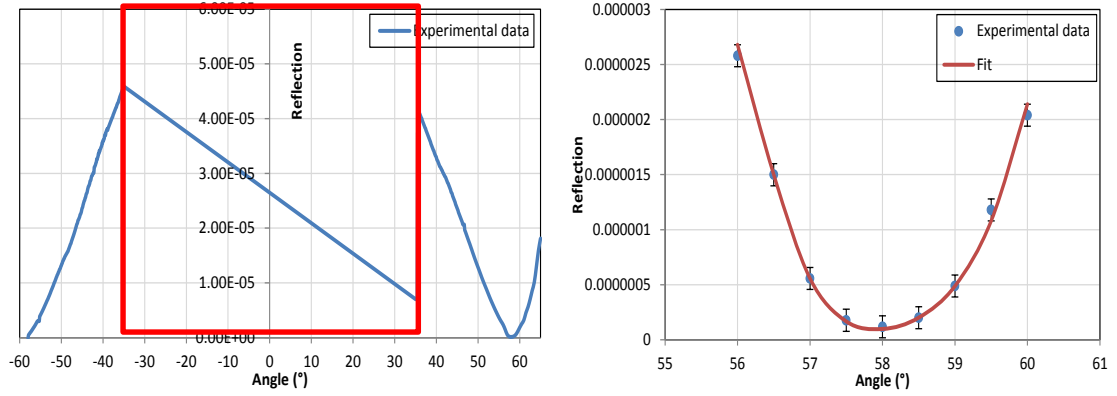


Figure 3.40: (a) Reflexion coefficient at the input surface of a KTP rotated slab, as a function of the angle of incidence. The polarization state is parallel to the incidence plane that corresponds to the (x,y) principal plane and the wavelength is $0.671 \mu\text{m}$. (b) Fit of zoom of data between 56° and 60° in order to determine the Brewster angle value.

As shown in Figure 3.40(b), our measurements led to a value of the Brewster angle $\theta_B = 58^\circ \pm 0.5^\circ$ and according to Eq. 3.23, we found that the corresponding principal refractive index of NaI₃O₈ is $n_o(0.671 \mu\text{m}) = 1.6 \pm 0.03$.

3.4.4 Recorded tuning curves

In this part, our objective was to record the SHG and DFG(λ_i) tuning curves in the principal planes of the dielectric frame of NaI₃O₈ by using the SPHERE method. As in GdCOB and LGN, we consider the birefringence phase-matching condition from all types I and II SHG, and types I, II and III DFG(λ_i) over the full transparency range of NaI₃O₈.

According to Eq. 1.30, SHG and DFG(λ_i) tuning curves can be recorded in principal dielectric planes only if the associated effective coefficients d_{eff} do not remain nil and if phase-matching conditions are possible.

3.4.4.1 Phase-matching conditions and associated effective coefficients

Using Eq. 1.21, Eq. 1.22 and Eq. 1.32, we calculated the effective coefficients associated to all types of SHG and DFG(λ_i) tuning curves. Since NaI₃O₈ is a negative uniaxial crystal, they correspond to $\chi_{eff}(\lambda_{2\omega}, \theta_{PM}, \varphi_{PM})$ and $\chi_{eff}(\lambda_i, \theta_{PM}, \varphi_{PM})$ respectively and their analytical expressions can be written in the full dielectric frame as shown in Table 3.13. Note that $d_{eff} = \chi_{eff}/2$.

Types	Effective coefficient χ_{eff}
Type I SHG	$-\chi_{xxz}(\lambda_{2\omega}) \sin[\theta_{PM} + \rho(\lambda_{2\omega}, \theta_{PM})] \cos 2\varphi_{PM} - \chi_{xyz}(\lambda_{2\omega}) \sin[\theta_{PM} + \rho(\lambda_{2\omega}, \theta_{PM})] \sin 2\varphi_{PM}$
Type II SHG	$[\chi_{xxz}(\lambda_{2\omega}) \sin 2\varphi_{PM} - \chi_{xyz}(\lambda_{2\omega}) \cos 2\varphi_{PM}] \left\{ \begin{array}{l} \sin[\theta_{PM} + \rho(\lambda_{\omega}, \theta_{PM})] \cos[\theta_{PM} + \rho(\lambda_{2\omega}, \theta_{PM})] \\ + \cos[\theta_{PM} + \rho(\lambda_{\omega}, \theta_{PM})] \sin[\theta_{PM} + \rho(\lambda_{2\omega}, \theta_{PM})] \end{array} \right\}$
Type I DFG(λ_i)	$[\chi_{xxz}(\lambda_i) \sin 2\varphi_{PM} - \chi_{xyz}(\lambda_i) \cos 2\varphi_{PM}] \left\{ \begin{array}{l} \sin[\theta_{PM} + \rho(\lambda_s, \theta_{PM})] \cos[\theta_{PM} + \rho(\lambda_p, \theta_{PM})] \\ + \cos[\theta_{PM} + \rho(\lambda_s, \theta_{PM})] \sin[\theta_{PM} + \rho(\lambda_p, \theta_{PM})] \end{array} \right\}$
Type II DFG(λ_i)	$-\chi_{xxz}(\lambda_i) \sin[\theta_{PM} + \rho(\lambda_p, \theta_{PM})] \cos 2\varphi_{PM} - \chi_{xyz}(\lambda_i) \sin[\theta_{PM} + \rho(\lambda_p, \theta_{PM})] \sin 2\varphi_{PM}$
Type III DFG(λ_i)	$[\chi_{xxz}(\lambda_i) \sin 2\varphi_{PM} - \chi_{xyz}(\lambda_i) \cos 2\varphi_{PM}] \left\{ \begin{array}{l} \sin[\theta_{PM} + \rho(\lambda_i, \theta_{PM})] \cos[\theta_{PM} + \rho(\lambda_p, \theta_{PM})] \\ + \cos[\theta_{PM} + \rho(\lambda_i, \theta_{PM})] \sin[\theta_{PM} + \rho(\lambda_p, \theta_{PM})] \end{array} \right\}$

Table 3.13: The effective coefficients $\chi_{eff}(\lambda_{2\omega}, \theta_{PM}, \varphi_{PM})$ and $\chi_{eff}(\lambda_i, \theta_{PM}, \varphi_{PM})$ associated respectively to SHG and DFG(λ_i) tuning curves in the full dielectric frame of the negative uniaxial crystal NaI₃O₈. $\lambda_{2\omega}$ and λ_i are the corresponding generated wavelengths. The spatial walk-off angles are given in part 1.2.5. $(\theta_{PM}, \varphi_{PM})$ are the phase-matching angles in spherical coordinates.

Since NaI₃O₈ belongs to the uniaxial optical class, birefringence phase-matching condition is given by solving Eq. 1.38 in the $(x, z) = (y, z)$ principal plane only. Then the tuning curves given in Table 3.14 only depend on the spherical phase-matching angle θ_{PM} .

	Phase-matching condition
Type I SHG	$n_o(\lambda_\omega) = n^e(\lambda_{2\omega}, \theta_{PM})$
Type II DFG (λ_i)	$n_o(\lambda_i)/\lambda_i + n_o(\lambda_s)/\lambda_s = n^e(\lambda_p, \theta_{PM})/\lambda_p$
Type II SHG	$n_o(\lambda_\omega) + n^e(\lambda_\omega, \theta_{PM}) = 2n^e(\lambda_{2\omega}, \theta_{PM})$
Type III DFG (λ_i)	$n^e(\lambda_i, \theta_{PM})/\lambda_i + n_o(\lambda_s)/\lambda_s = n^e(\lambda_p, \theta_{PM})/\lambda_p$
Type I DFG (λ_i)	$n_o(\lambda_i)/\lambda_i + n^e(\lambda_s, \theta_{PM})/\lambda_s = n^e(\lambda_p, \theta_{PM})/\lambda_p$

Table 3.14: Phase-matching conditions for type I and II SHG and type I, II and III DFG(λ_i) in NaI₃O₈. $\lambda_{2\omega} = \lambda_\omega/2$ and λ_ω are the fundamental and SHG generated wavelengths respectively. θ_{PM} is the phase-matching angle using the spherical coordinate. λ_i with $i = 1, 2$, or 3 verify the relation of order $\lambda_p < \lambda_s \leq \lambda_i$. $n_o = n^+$ is the ordinary principal refractive index and $n^e = n^-$ is given in part 1.2.4.1.

From Tables 3.13, we obtain that the same effective coefficient is involved in the (x, z) and (y, z) principal planes of the dielectric frame where $\varphi_{PM} = 0^\circ$ and $\varphi_{PM} = 90^\circ$ respectively. It is true for all types of SHG and DFG(λ_i). Since the tuning curves are also same in these two principal planes, our strategy is to measure the tuning curves in the (x, z) = (y, z) principal plane by shaping NaI₃O₈ crystal as a cylinder.

3.4.4.2 NaI₃O₈ cylinder

Using the Laue Method, NaI₃O₈ crystal was shaped as a cylinder with its rotation axis oriented perpendicular to ($c = z$)-axis (along the $y = x$ -axis) with a precision better than 0.5° . Its diameter is $D = 4.13$ mm with an acylindricity $\Delta D/D$ below 1%, and it is polished to optical quality as shown in Figure 3.41. Thus the cylinder gives access to all directions of the (x, z) = (y, z) principal plane when stuck on a Hubber goniometric head and placed at the center of an Euler circle.



Figure 3.41: The NaI₃O₈ cylinder with its rotation axis oriented perpendicular to ($c = z$)-axis.

3.4.4.3 Type I and type II SHG

According to Table 3.13, the effective coefficients for type I and type II SHG in the $(x, z) = (y, z)$ principal plane are not always equal to zero. Then we recorded both tuning curves using the SPHERE method which experimental setup is shown in Figure 2.10. They are shown in Figures 3.42 and 3.43, respectively.

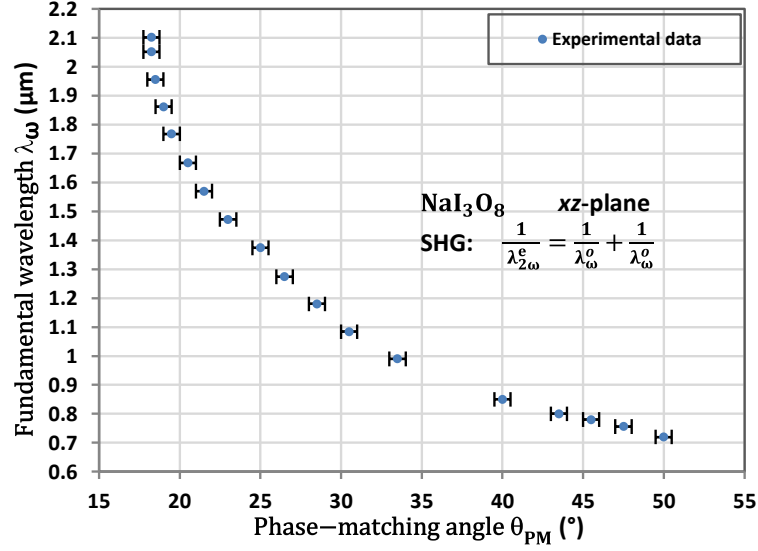


Figure 3.42: Type I SHG tuning curve in the (x, z) principal plane, the fundamental wavelength λ_ω is given as a function of phase-matching angle θ_{PM} . The dots correspond to our experimental data.

It was not possible to record data for fundamental wavelengths λ_ω lower than $0.7 \mu\text{m}$ because the SHG wavelengths $\lambda_{2\omega}$ were below the ultraviolet cut-off of NaI₃O₈.

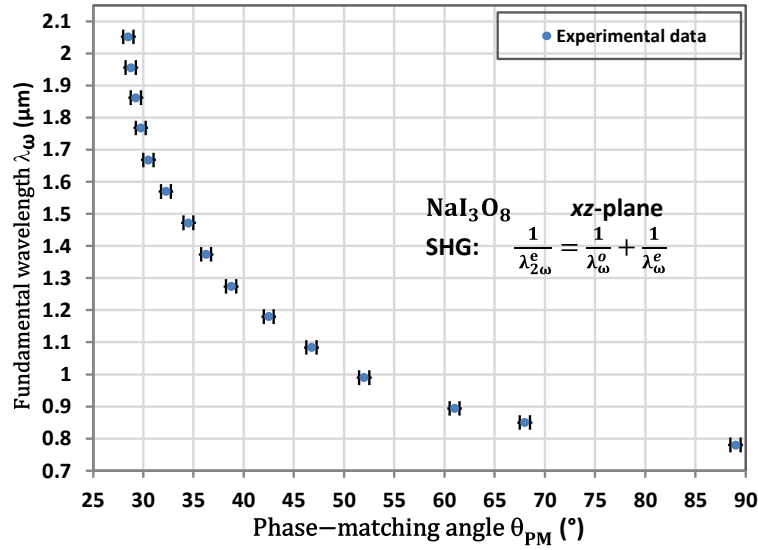


Figure 3.43: Type II SHG tuning curve in the (x, z) plane i.e. the fundamental wavelength λ_ω as a function of phase-matching angle θ_{PM} . The dots stand for our experimental data.

3.4.4.4 Type II and type III DFG

In the case of NaI₃O₈, DFG(λ_i) can be studied in the $(x, z) = (y, z)$ principal plane. In this case, the signal incoming beam at the fixed wavelength is $\lambda_s = 1.064 \mu\text{m}$, while the pump wavelength λ_p is tunable and provided by the OPG-DFG source. Figures 3.44 and 3.45 show the recorded the tuning curves of type II ($1/\lambda_i^o = 1/\lambda_p^e - 1/\lambda_s^o$) and type III DFG ($1/\lambda_i^e = 1/\lambda_p^e - 1/\lambda_s^o$) in the $(x, z) = (y, z)$ principal plane.

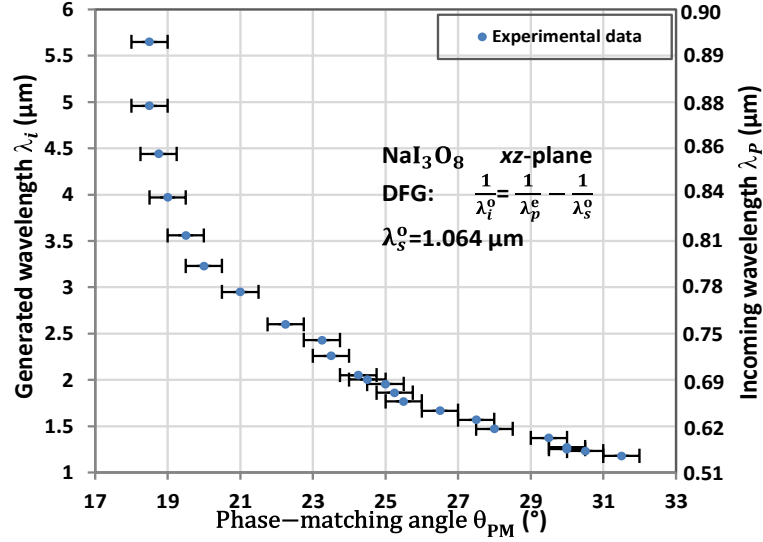


Figure 3.44: Type II DFG (λ_i) tuning curve in the (x, z) plane i.e. the incoming and generated wavelengths λ_p and λ_i as a function of the phase-matching angle θ_{PM} . The dots stand for our experimental data.

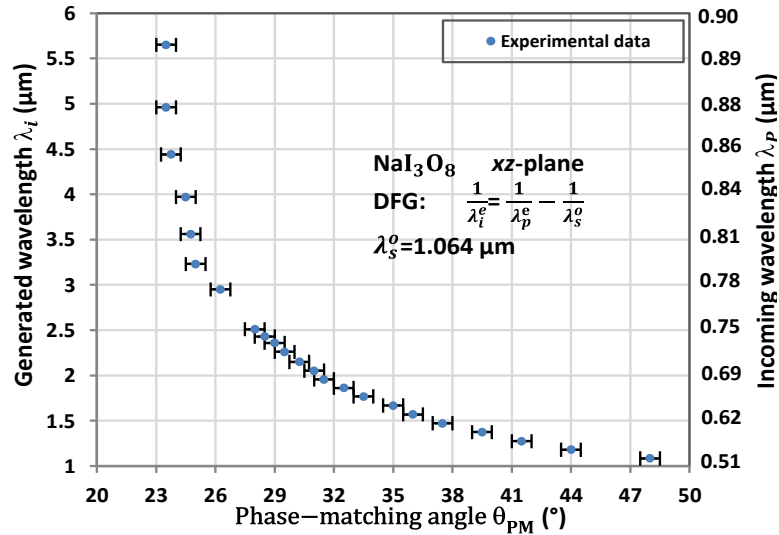


Figure 3.45: Type III DFG (λ_i) tuning curve in the (x, z) plane i.e. the incoming and generated wavelengths λ_p and λ_i as a function of phase-matching angle θ_{PM} . The dots stand for our experimental data.

Since NaI₃O₈ is a negative uniaxial crystal, superscripts (o) and (e) stand for (+) and (-) and for the ordinary and extraordinary waves, respectively. λ_p , λ_s and λ_i are respectively the pump, signal and idler wavelengths verifying $\lambda_p < \lambda_s \leq \lambda_i$.

As shown in Figure 3.44 and 3.45, type II and type III DFG(λ_i) with $\lambda_s=1.064 \mu\text{m}$, allow phase-matching condition when the incoming tunable pump wavelength is ranging from around 0.51 to 0.90 μm . The corresponding generated wavelength ranges for λ_i are between around 1 and 5.7 μm , the maximum wavelength is limited by the infrared cut-off of NaI₃O₈.

The above SHG and DFG(λ_i) tuning curves show that NaI₃O₈ allows phase-matched generation over its entire transparency range. These data can be used directly to cut the crystal at a phase-matching angle corresponding to the targeted parametric process and phase-matching wavelength.

3.4.5 First Sellmeier equations of the two principal refractive indices

We determined the Sellmeier equations of NaI₃O₈ crystal by fitting simultaneously all our SHG and DFG (λ_i) phase-matching data combined with a Brewster angle measurement. For that purpose, we used the Levenberg-Marquardt algorithm encoded with Matlab. We tried different types of dispersion equations, the best result being obtained with the following dual oscillator model:

$$n_i^2(\lambda) = A_i + \frac{B_i\lambda^2}{\lambda^2 - C_i} + \frac{D_i\lambda^2}{\lambda^2 - E_i} \quad (3.24)$$

λ is in μm , and i stands for o or e . The corresponding coefficients A_i, B_i, C_i, D_i and E_i are given in Table 3.15.

coefficients	$i = o$	$i = e$
A_i	1.7953	1.6942
B_i	0.7344	0.7101
C_i	0.0182	0.0162
D_i	0.5314	2.5841
E_i	412.9779	375.2799

Table 3.15: Coefficients of the Sellmeier Eq. (3.24) describing the variation of the ordinary (n_o) and extraordinary (n_e) principal refractive indices of NaI₃O₈ as a function of wavelength.

The relative accuracy $\Delta n_i/n_i$ is better than 10^{-4} ($i=o, e$) due to phase-matching angles recorded with a precision of $\pm 0.5^\circ$. Figures 3.46 to 3.49 show our experimental data

and fit using our Sellmeier equations.

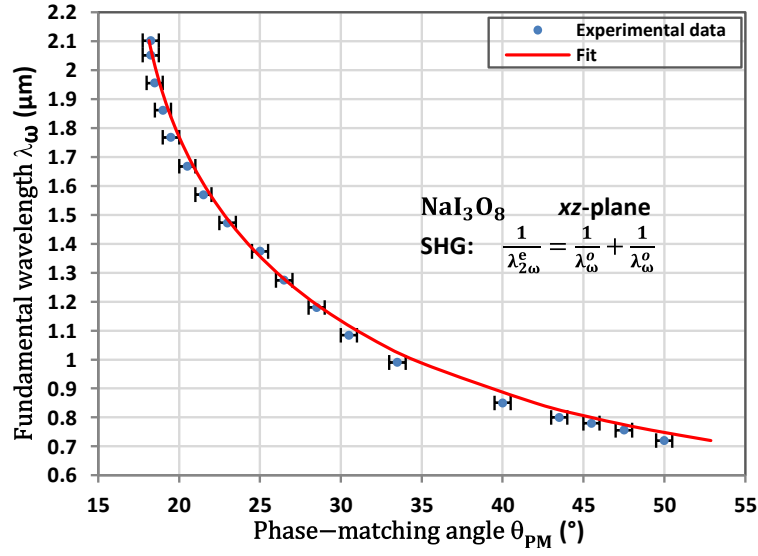


Figure 3.46: Type I SHG tuning curve, the fundamental wavelength λ_ω is given as a function of phase-matching angle θ_{PM} . The dots correspond to the experimental data and the red solid line is our fit of the experimental data.

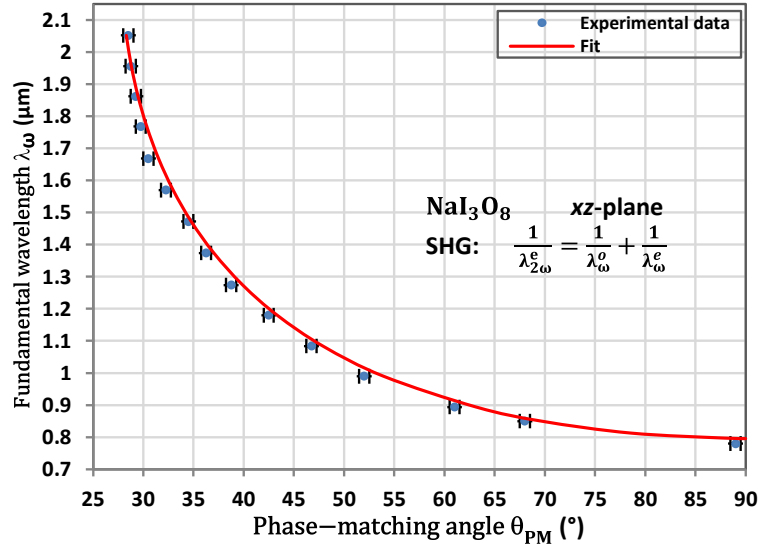


Figure 3.47: Type II SHG tuning curve, the fundamental wavelength λ_ω is given as a function of phase-matching angle θ_{PM} . The dots correspond to the experimental data and the red solid line is our fit of the experimental data.

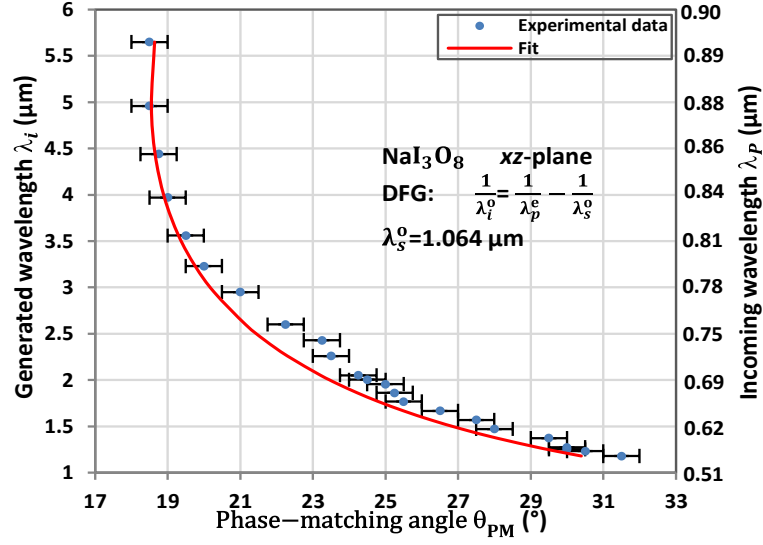


Figure 3.48: Type II DFG(λ_i) tuning curve in the (x, z) principal plane, the incoming wavelength λ_p and the generated wavelength λ_i are given as a function of phase-matching angle θ_{PM} . The dots correspond to the experimental data and the red solid line is our fit of the experimental data.

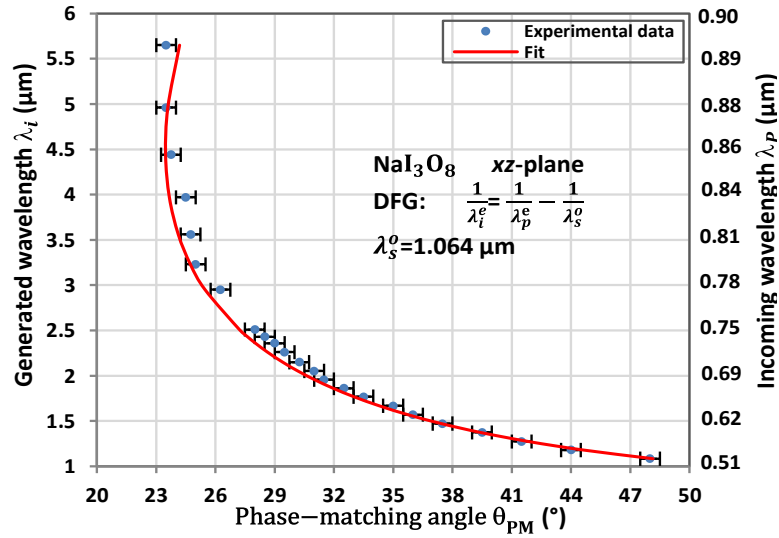


Figure 3.49: Type III DFG(λ_i) tuning curve in the (x, z) principal plane, the incoming wavelength λ_p and the generated wavelength λ_i are given as a function of phase-matching angle θ_{PM} . The dots correspond to the experimental data and the red solid line is our fit of the experimental data.

3.4.6 Determination of the nonlinear coefficients from phase-matched SHG

The magnitudes in absolute values of $d_{14} = d_{xyz} = \frac{\chi_{xyz}^{(2)}}{2}$; $d_{15} = d_{xxz} = \frac{\chi_{xxz}^{(2)}}{2}$ were determined through two NaI₃O₈ slabs with two parallel faces polished to optical quality

cut perpendicular to an angle critical phase-matching (ACPM) angle for SHG. We chose two data from the type I and type II SHG tuning curves recorded in the (x, z) = (y, z) principal plane that are shown in Figure 3.46 and 3.47, respectively. We used the experimental setup described in detail in 2.2.4.

The corresponding effective coefficients are:

$$d_{eff,I}^{NaI_3O_8} = -d_{15}^{NaI_3O_8}(\lambda_{2\omega}^{PM}) \sin[\theta_{PM} + \rho^+(\theta_{PM}, \lambda_{2\omega}^{PM})] \quad (3.25)$$

$$d_{eff,II}^{NaI_3O_8} = -d_{14}^{NaI_3O_8}(\lambda_{2\omega}^{PM}) \{ \sin[\theta_{PM} + \rho^+(\theta_{PM}, \lambda_{2\omega}^{PM})] \cos[\theta_{PM} + \rho^+(\theta_{PM}, \lambda_{2\omega}^{PM})] + \cos[\theta_{PM} + \rho^+(\theta_{PM}, \lambda_{2\omega}^{PM})] \sin[\theta_{PM} + \rho^+(\theta_{PM}, \lambda_{2\omega}^{PM})] \} \quad (3.26)$$

where ρ^+ is the spatial walk-off angle.

We chose type II SHG ($1/\lambda_{\omega}^e + 1/\lambda_{\omega}^o = 1/\lambda_{2\omega}^o$) in the (x, y) principal plane of KTiOPO₄(KTP) as a reference. The absolute value of the associated effective coefficient is $|d_{eff}^{KTP}(0.532\mu m)| = 2.43 \text{ pm/V}$, the corresponding phase-matching angle being equal to $\varphi_{PM} = 23.1^\circ$ [19].

In order to get rid of the spectral response of the experimental setup, we considered the fundamental wavelengths as near as possible for this set of measurements, and we chose the fundamental wavelength at $\lambda_{\omega}^{PM} = 1.064 \mu m$ for NaI₃O₈. Using the Sellmeier Eq. (3.24), we calculated that the corresponding phase-matching angles are $\theta_{PM} = 32.1^\circ$ for type I SHG, and $\theta_{PM} = 49.0^\circ$ in the case of type II SHG.

We cut two NaI₃O₈ slabs ($L_{NaI_3O_8,I} = 800 \mu m$, $L_{NaI_3O_8,II} = 680 \mu m$) and one KTP slab ($L_{KTP} = 800 \mu m$) at the corresponding phase-matching angles given above. We took such a small interacting length in order to avoid any spatial walk-off attenuation. The incoming fundamental beam was focused through a 100-mm focal length CaF₂ lens. The corresponding beam waist diameter was around $w_0 = 120 \mu m$, leading to a Rayleigh length $2 \times Z_R = 22 \text{ mm}$, which is much longer than the thickness of the slabs. Then the parallel beam propagation is ensured inside the three crystals.

Types I and II SHG conversion efficiencies of NaI₃O₈ were registered relatively to KTP as a function of the fundamental wavelength around $1.064 \mu m$ as shown in Figure 3.50 and Figure 3.51 where $\eta_I^{NaI_3O_8}$ and $\eta_{II}^{NaI_3O_8}$ correspond to types I and II SHG conversion efficiencies respectively, and η_{II}^{KTP} stands for the type II SHG conversion efficiency of KTP.

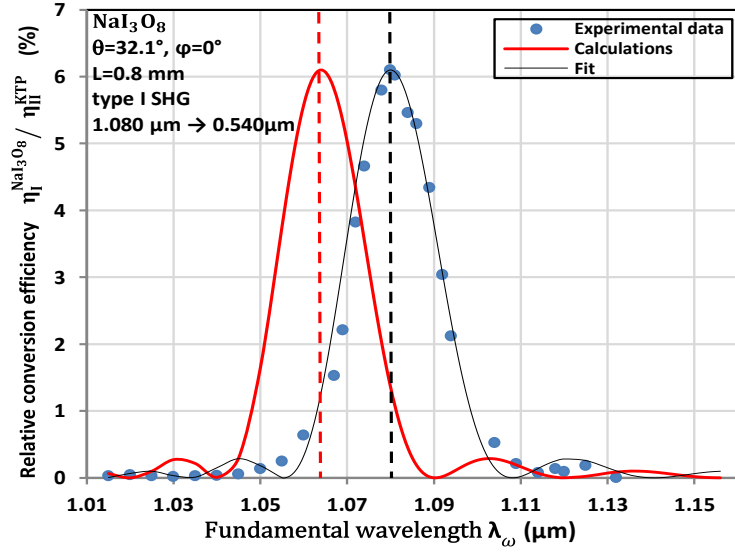


Figure 3.50: Calculated and measured Type I SHG conversion efficiency of NaI₃O₈. The dashed lines indicate the phase-matching wavelengths.

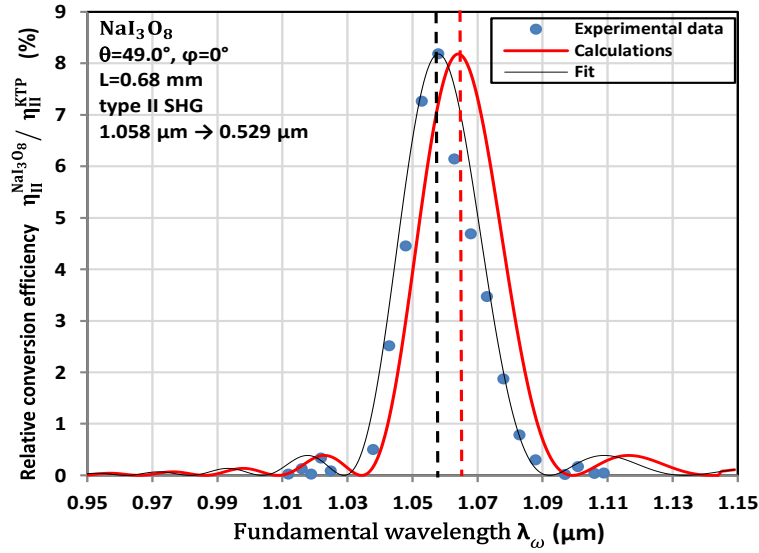


Figure 3.51: Calculated and measured Type II SHG conversion efficiency of NaI₃O₈. The dashed lines indicate the phase-matching wavelengths.

The maximum of each curve corresponds to phase-matching from which can be determined the absolute value of the effective nonlinear coefficient $d_{\text{eff}}^{\text{NaI}_3\text{O}_8}$ relatively to that of KTP, i.e. $d_{\text{eff}}^{\text{KTP}}$. The theoretical expression of $d_{\text{eff}}^{\text{NaI}_3\text{O}_8}$ is given hereafter:

$$(d_{\text{eff},I,II}^{\text{NaI}_3\text{O}_8})^2 = \frac{A_{II}^{\text{KTP}}}{A_{I,II}^{\text{NaI}_3\text{O}_8}} \frac{\eta_{I,II}^{\text{NaI}_3\text{O}_8}}{\eta_{II}^{\text{KTP}}} \frac{L_{\text{KTP}}^2}{L_{\text{NaI}_3\text{O}_8,I,II}^2} (d_{\text{eff}}^{\text{KTP}})^2 \quad (3.27)$$

with

$$A_I^{\text{NaI}_3\text{O}_8} = \frac{T_e^{\text{NaI}_3\text{O}_8}(\lambda_{2\omega}^{\text{PM}}, \theta_{\text{PM}})}{n_e^{\text{NaI}_3\text{O}_8}(\lambda_{2\omega}^{\text{PM}}, \theta_{\text{PM}})} \left[\frac{T_o^{\text{NaI}_3\text{O}_8}(\lambda_{\omega}^{\text{PM}})}{n_o^{\text{NaI}_3\text{O}_8}(\lambda_{\omega}^{\text{PM}})} \right]^2 \quad (3.28)$$

$$A_{II}^{NaI_3O_8} = \frac{T_e^{NaI_3O_8}(\lambda_{2\omega}^{PM}, \theta_{PM})}{n_e^{NaI_3O_8}(\lambda_{2\omega}^{PM}, \theta_{PM})} \frac{T_e^{NaI_3O_8}(\lambda_{\omega}^{PM})}{n_e^{NaI_3O_8}(\lambda_{\omega}^{PM}, \theta_{PM})} \frac{T_o^{NaI_3O_8}(\lambda_{\omega}^{PM})}{n_o^{NaI_3O_8}(\lambda_{\omega}^{PM})} \quad (3.29)$$

$$A_{II}^{KTP} = \frac{T_o^{KTP}(\lambda_{2\omega}^{PM}, \varphi_{PM})}{n_o^{KTP}(\lambda_{2\omega}^{PM}, \varphi_{PM})} \frac{T_e^{KTP}(\lambda_{\omega}^{PM})}{n_e^{KTP}(\lambda_{\omega}^{PM})} \frac{T_o^{KTP}(\lambda_{\omega}^{PM}, \varphi_{PM})}{n_o^{KTP}(\lambda_{\omega}^{PM}, \varphi_{PM})} \quad (3.30)$$

$n_{o,e}^{NaI_3O_8}(\lambda_{\omega}^{PM})$ are the ordinary and extraordinary principal refractive indices of NaI₃O₈. $n_{o,e}^{NaI_3O_8}(\lambda_{a\omega}^{PM}, \theta_{PM})$ and $n_{o,e}^{KTP}(\lambda_{a\omega}^{PM}, \varphi_{PM})$ are the ordinary and extraordinary refractive indices of NaI₃O₈ and KTP respectively. They are involved at the fundamental (a=1) or second harmonic (a=2) wavelengths, and at the phase-matching angle θ_{PM} or φ_{PM} . T_o and T_e are the associated Fresnel coefficients.

We found from Figs 3.50 and 3.51 that $\lambda_{\omega}^{PM} = 1.080 \mu\text{m}$ for type I SHG and $\lambda_{\omega}^{PM} = 1.058 \mu\text{m}$ for type II SHG in NaI₃O₈. It is slightly different from $1.064 \mu\text{m}$ and calculation using our Sellmeier equations, showing the difficulty of cutting very thin oriented slabs at the targeted orientation.

From the maximum values of the curves shown in Figure 3.50 and 3.51, we found that $|d_{\text{eff I}}^{NaI_3O_8}(\lambda_{2\omega}^{PM} = 0.540 \mu\text{m})| = 0.22 \pm 0.02 \text{ pm/V}$ and $|d_{\text{eff II}}^{NaI_3O_8}(\lambda_{2\omega}^{PM} = 0.529 \mu\text{m})| = 0.53 \pm 0.05 \text{ pm/V}$. Using Eq. (3.25) and (3.26), it comes: $|d_{14}^{NaI_3O_8}(0.529 \mu\text{m})| = 0.54 \pm 0.08 \text{ pm/V}$ and $|d_{15}^{NaI_3O_8}(0.540 \mu\text{m})| = 0.85 \pm 0.13 \text{ pm/V}$. The corresponding Miller indices determined using Eqs. (1.26) are: $\delta_{14}^{NaI_3O_8} = 0.32 \pm 0.05 \text{ pm/V}$ and $\delta_{15}^{NaI_3O_8} = 0.50 \pm 0.07 \text{ pm/V}$. They are close to $\delta_{15}^{KTP} = 0.25 \pm 0.04 \text{ pm/V}$, $\delta_{24}^{KTP} = 0.47 \pm 0.07 \text{ pm/V}$ and $\delta_{33}^{KTP} = 1.51 \pm 0.22 \text{ pm/V}$ of KTP [19].

3.4.7 Condition of supercontinuum generation

We studied the potentiality of NaI₃O₈ for a supercontinuum generation by OPG with the broadest spectral bandwidth under phase-matching conditions. According to Eq. (1.45), we calculated the “magic” pump wavelength $\lambda_p^* = \lambda_3^*$ of type II DFG i.e. $1/\lambda_p^* \rightarrow 1/\lambda_s^* + 1/\lambda_i^*$ in the (x, z) = (y, z) principal plane of NaI₃O₈. We used the Sellmeier equations from Eq. (3.24) and the coefficients from Table 3.15.

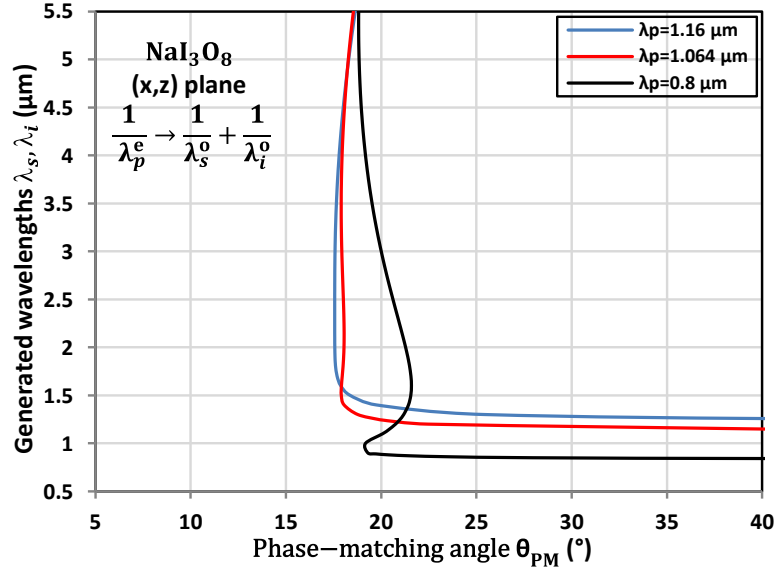


Figure 3.52: Calculated type II OPG($1/\lambda_p^e = 1/\lambda_i^o + 1/\lambda_s^o$) tuning curve in the $(x, z) = (y, z)$ plane of NaI_3O_8 at different pump wavelength λ_p of 1.16, 1.064 and 0.8 μm . λ_i and λ_s are the generated idler and signal wavelength respectively.

Our calculations show that NaI_3O_8 crystal cut at the phase-matching angle ($\theta_{\text{PM}} = 18^\circ$, $\varphi_{\text{PM}} = 0$ or 90°) and pumped with $\lambda_p^* = \lambda_3^* = 1.16 \mu\text{m}$, leads to an OPG emission with the broadest spectral bandwidth between 1.5 and 5.3 μm . It is shown in Figure 3.52. Calculated tuning curves are still very broad when NaI_3O_8 is pumped at $\lambda_p = 1.064 \mu\text{m}$ and $\lambda_p = 0.8 \mu\text{m}$ as shown in Fig. 3.52, these two wavelengths being interesting since corresponding to the emission Nd:YAG and Ti:Sa lasers, respectively.

3.5 Comparison between studied crystals

Using our Sellmeier equations, calculations led to different values of the “magic” pump wavelength, the corresponding phase-matching angles and the broadest spectral bandwidth for the phase-matched OPG supercontinuum generation in the GdCOB, LGN, NaI_3O_8 nonlinear crystals.

They are summarized in Table 3.16 with the corresponding values in LGT crystal for comparison.

Crystal	"magic" pump wavelength(μm)	Angle ($^\circ$)	Broadest spectral bandwidth (μm)
GdCOB	0.772	$\theta=32.5^\circ$, $\varphi=0^\circ$	1-2.95
LGN	0.982	$\theta=52^\circ$, $\varphi=90^\circ$	1.4-3.45
NaI_3O_8	1.16	$\theta=18^\circ$, $\varphi=0^\circ$ or 90°	1.5-5.3
LGT	0.964	$\theta=56^\circ$, $\varphi=90^\circ$	1.5-3.5

Table 3.16: Comparison of values of the “magic” pump wavelength, the corresponding phase-matching angles and the broadest spectral bandwidth for the phase-matched type II OPG($1/\lambda_p^e = 1/\lambda_i^+ + 1/\lambda_s^+$) in GdCOB, LGN, NaI_3O_8 and LGT. Our Sellmeier equations were used.

Note that we did not find a value of the “magic” pump wavelength leading to an OPG supercontinuum generation in KTP crystal.

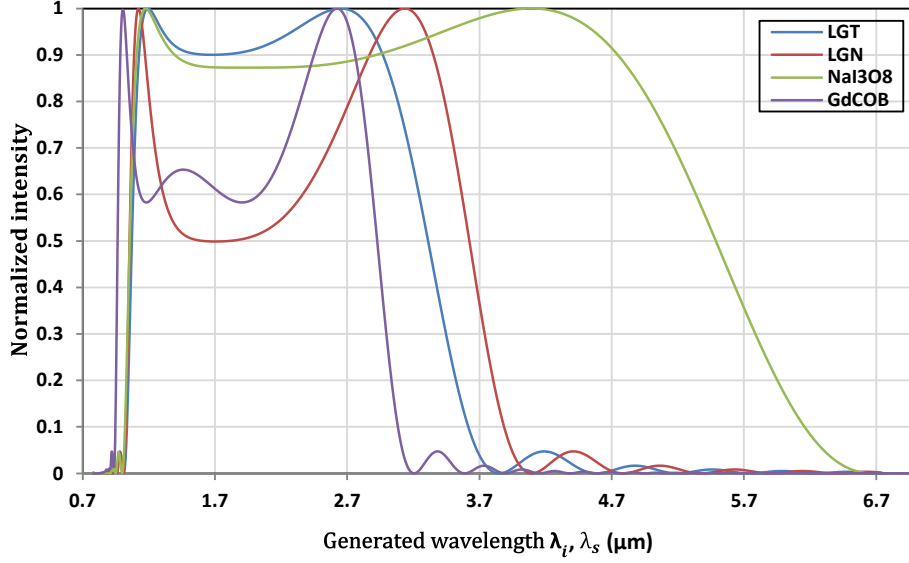


Figure 3.53: Normalized spectrum of the mid-IR Type II supercontinuum that can be generated in 1 mm thick crystals cutting along the directions and using the pump wavelength expressed in Table 3.16.

Using Eq. (1.30), we calculated the normalized broadest spectral bandwidth generated in 1 mm thick previous crystals. They are shown in Fig. 3.53 for comparison.

Figure 3.53 shows that the supercontinuum range of GdCOB is narrow, LGN and LGT are a little wider, while NaI₃O₈ is the widest.

The associated effective coefficients of GdCOB, LGN, NaI₃O₈ and LGT of type II OPG ($1/\lambda_p^- = 1/\lambda_i^+ + 1/\lambda_s^+$) are given in Table 3.17. Taking into account the corresponding phase-matching angles given in Table 3.16, their square value are shown for GdCOB, LGN, NaI₃O₈ and LGT in Figure 3.54 for comparison. According to Eq. (1.30), it highlights that the energy of the generated supercontinuum in LGT- and LGN-OPG should be much higher than that of GdCOB- and NaI₃O₈ – OPG.

Crystals	Effective coefficient d_{eff}
GdCOB	$-d_{12}(\lambda_i)\cos[\theta_{\text{PM}} - \rho_{x,z}(\lambda_p, \theta_{\text{PM}})]$
LGN	$d_{11}(\lambda_i)\cos[\theta_{\text{PM}} - \rho(\lambda_i, \theta_{\text{PM}})]\cos[\theta_{\text{PM}} - \rho(\lambda_s, \theta_{\text{PM}})]$
NaI ₃ O ₈	$-d_{15}(\lambda_i)\sin[\theta_{\text{PM}} + \rho(\lambda_p, \theta_{\text{PM}})]$
LGT	$-d_{11}(\lambda_i)\cos[\theta_{\text{PM}} - \rho(\lambda_i, \theta_{\text{PM}})]\cos[\theta_{\text{PM}} - \rho(\lambda_s, \theta_{\text{PM}})]$

Table 3.17: The effective coefficients of type II OPG ($1/\lambda_p^- = 1/\lambda_i^+ + 1/\lambda_s^+$) along the phase-matching angles shown in Table 3.16, for GdCOB, LGN, NaI₃O₈ and LGT.

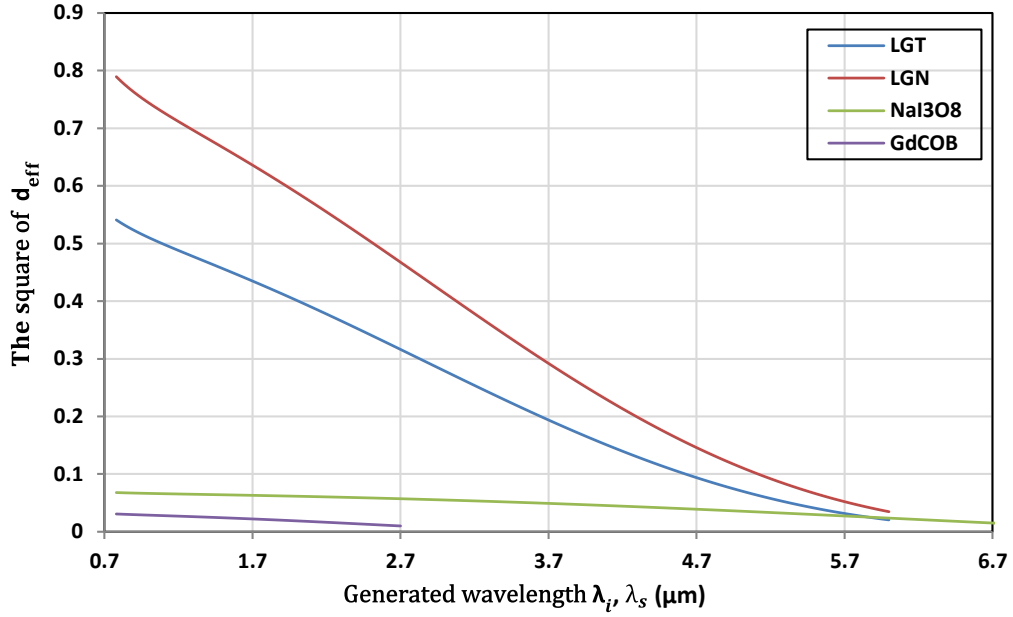


Figure 3.54: The square of the effective coefficients of GdCOB, LGN, NaI₃O₈ and LGT oriented along the directions shown in Table 3.16.

Note the damage thresholds of LGN, LGT and NaI₃O₈ determined under the same condition almost the same value: LGN ($2.8 \pm 0.7 \text{ GW/cm}^2$), LGT ($2.7 \pm 0.7 \text{ GW/cm}^2$) [42] and NaI₃O₈ ($2.4 \pm 0.6 \text{ GW/cm}^2$) [43]. An optical damage threshold higher than 1 GW/cm^2 was reported in GdCOB [29].

By combining all these previous crucial properties, we can conclude that:

- the performances of GdCOB crystals are much less attractive than the other nonlinear crystals. It is true as well for the broadest spectral bandwidth emitted and the efficiency.
- NaI₃O₈ crystal provides an OPG supercontinuum generation with the broadest spectral bandwidth compared with the other crystals; it is the only crystal to cover completely band II (3-5 μm) of transmission of the atmosphere. however the associated efficiency is very weak.
- LGT and LGN crystals are the most efficient crystals for the OPG supercontinuum generation, the performances of LGN crystals being better than that of LGT. But their maximal value of emitted wavelength does not exceed of about 4 μm .

Next step is to validate our calculations by recording experimental data on an implemented OPG using the scheme shown in Figure 3.55(a). For that purpose slabs of GdCOB and of LGN with the thickness of around 1 mm have been already cut at the phase-matching directions given in Table 3.16. They are shown in Figure 4.55(b). The

cutting of LGT and NaI_3O_8 slabs is in progress.

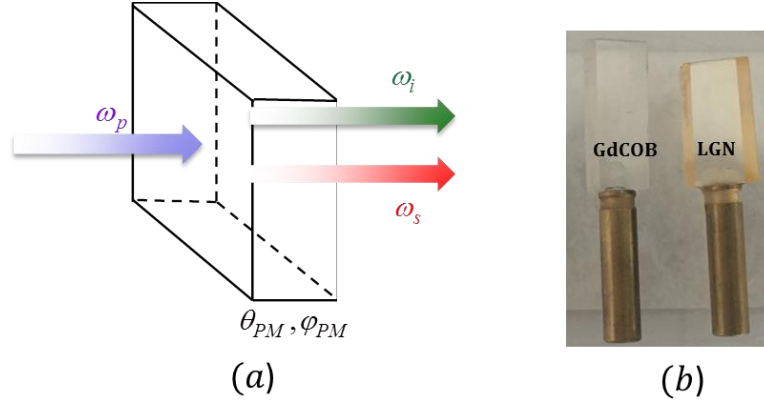


Figure 3.55: Scheme of the OPG supercontinuum emission (a) and the slabs cut in our lab (b) along the requested direction given in Table 3.16.

We will use the optical parametric oscillator (OPO) in the nanosecond regime shown in Figure 2.4 to provide the “magic” pump wavelengths, which are given in Table 3.16 according to the nonlinear crystal that will be investigated. The spectral bandwidth of the OPG supercontinuum generation will be characterized using a monochromator combined with detectors sensitive up to 5 μm .

3.6 Summary

We demonstrated that the dielectric frame does not rotate as a function of wavelength for the positive biaxial GdCOB crystal. For the positive uniaxial LGN crystal, we determined the damage threshold and the magnitude of its nonlinear coefficient from angular critical phase-matched SHG in comparison with KTP. We did the same studies for the negative uniaxial NaI_3O_8 crystal but we determined two second-order nonlinear coefficients. We also recorded transmission spectra in polarized light.

We directly recorded the tuning curves of SHG and DFG(λ_i) in principal dielectric planes of GdCOB, LGN and NaI_3O_8 using our SPHERE method. They can be directly used per se for devices. But they also allowed us to report the most reliable Sellmeier equations of these nonlinear crystals.

Using the previous data, our calculations show that type II OPG can generate a supercontinuum under phase-matching condition with the broadest spectral bandwidth in the three studied nonlinear crystals GdCOB, LGN and NaI_3O_8 . It requests the use of different “magic” pump wavelength values but all are located around 1 μm . Our

calculations provided a comparison of their performances and we expect that they will be soon validated by our experiments in progress dealing with phase-matched OPG supercontinuum generation using these crystals.

Chapter 4 Magnitude and relative sign of nonlinear coefficients of BGSe

4.1 Introduction

We recently performed the first exhaustive study to the best of our knowledge of the nonlinear optical properties of the new selenide BaGa₄Se₇ (BGSe) crystal. Since it was found transparent from 0.47 up to 18 μm [44], our objective was to evaluate its potentiality for a phase-matched OPG emission with the broadest bandwidth covering band II (3 – 5 μm) and band III (8–12 μm) of transmission of the atmosphere.

This crystal crystallizes in the point group *m* of the monoclinic system, however it was shown in our group that the dielectric frame does not rotate as a function of wavelength [45]. Furthermore, the second-harmonic generation (SHG) and difference-frequency generation (DFG) tuning curves were directly recorded in principal planes of this positive biaxial crystal using the SPHERE method. They can be used *per se*. They were also used to refine the Sellmeier equations over the transparency range of BGSe from the simultaneous fit of data [45].

Since BGSe belongs to the monoclinic point group *m*, with the crystallographic *b*-axis parallel to the dielectric *x*-axis, its second-order nonlinear susceptibility has six nonzero and independent nonlinear coefficients under Kleinman assumption. Using the contracted notation, and $d = \frac{\chi^{(2)}}{2}$, the coefficients write: d_{23} , d_{32} , d_{31} , d_{21} , d_{22} , and d_{33} . In our group, the magnitude of the coefficients d_{23} , d_{32} and d_{31} were determined from recording SHG conversion efficiencies under angular non-critical phase-matching (ANCPM) condition. Two slabs cut respectively along the principal *x*- and *y*-axes of the dielectric frame, were used [46].

In this chapter, we are interested in the magnitude of the three other coefficients d_{21} , d_{22} and d_{33} and in the relative sign of the six coefficients d_{23} , d_{32} , d_{31} , d_{21} , d_{22} , and d_{33} . We propose to determine these data from recording SHG conversion efficiencies.

4.2 State of the art

Crystal growth

Using the method of Bridgman-Stockbarger [44, 47, 48, 49], the synthesis of BGSe crystals was made possible in 2010 and samples of centimetric dimensions with a good optical quality were obtained as illustrated by Figure 4.1. The BGSe crystal does not contain oxygen in its chemical composition, which directly extends its transparent spectrum beyond 5 μm [47].

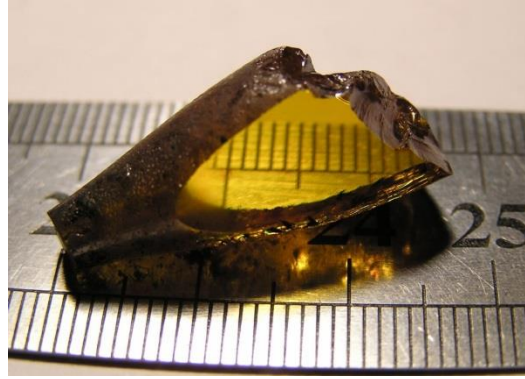


Figure 4.1: Picture of a 11.3-mm thick BGSe crystal obtained by the Bridgman-Stockbarger method with two faces polished to optical quality [47].

Relative orientation between the dielectric frame and the crystallographic frame

BGSe belongs to the monoclinic point group m , and the structure contains a mirror plane that is normal to a special axis labeled b -axis. Then the dielectric frame (x, y, z) of the monoclinic crystal does not correspond to the crystallographic frame (a, b, c) . For BGSe, the x -axis was found parallel to the b -axis and then remains fixed. The a -, c -crystallographic axes and y -, z -dielectric axes are all located in the mirror plan. The angle between the a - and c -axes is $(a, c) = 121.24^\circ$ [47].

Using the *modus operandi* described in detail in part 2.2.1, our group cut a slab with two parallel faces polished to optical quality and perpendicular to the b -(or x -) axis. Then they were able to locate all the other axes in the mirror plane of BGSe [46]. The crystallographic a - and c -axis were located by using the polychromatic X-rays diffraction in backscattered Laue geometry. The conoscopy transmission picture provided the location of the principal dielectric y - and z -axes and the following angles $(c, z) = 0^\circ$ and $(c, y) = 90^\circ$ were found at the wavelength of $0.6328 \mu\text{m}$ as shown in insert of Figure 4.2. It was also found that the dielectric frame of BGSe does not rotate as a function of wavelength [46].

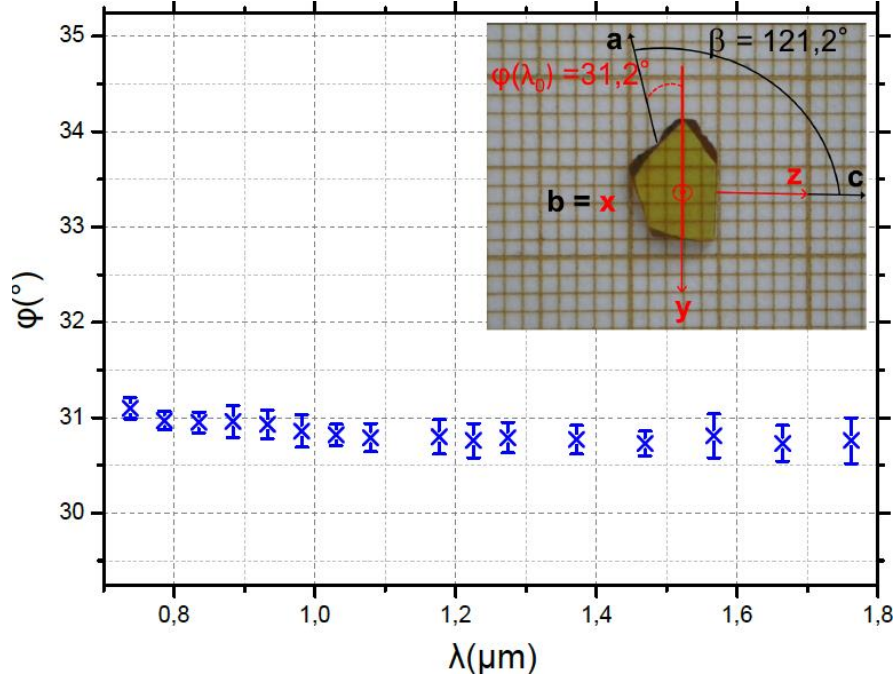


Figure 4.2: Orientation between the crystallographic frame (a, b, c) and the dielectric frame (x, y, z) as a function of the wavelength λ . The orientation at $\lambda = 0.628 \mu\text{m}$ is shown in insert through the BGSe slab [46].

Transmission spectrum

The transmission spectrum in un-polarized light had been studied by some groups [44, 47, 49, 50]. In our group, it was also measured through the 2-mm thick BGSe slab, cut along the y direction shown in Figure 4.2 [45]. All results showed that BGSe crystal is transparent between 0.47 and 18 μm as illustrated in Figure 4.3. In addition, the transmission is about 65% between 0.776 and 14.72 μm , and a strong absorption is observed around 15 μm as in [47, 49, 50]. Thus the BGSe transparency domain covers both band II (3-5 μm) and III (8-12 μm) transmission bands of the atmosphere.

The UV cut-off wavelength is around 0.47 μm , which explains the yellow color of the crystal shown in Figure 4.1 and in inset of Figure 4.2. It also ensures no risk of two photon absorption if the crystal is pumped around $\lambda_p = 1 \mu\text{m}$.

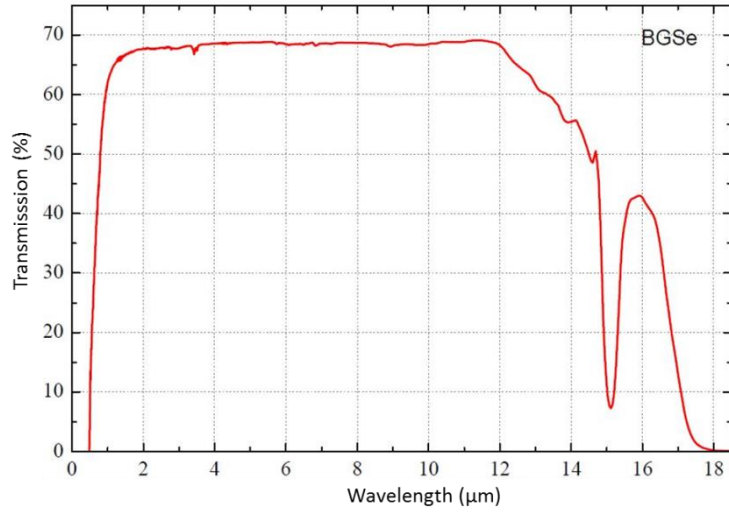


Figure 4.3: Transmission spectrum measured through the 11.3-mm thick slab cut in the y direction [45].

Optical damage threshold

The optical damage threshold of BGSe was determined in two different regimes [49, 50]. In the first regime, a Nd:YAG laser at the wavelength of 1.064 μm , with the pulse duration of 30 ps and the repetition frequency of 10 Hz, was used and the corresponding optical damage threshold was estimated at 3 GW/cm^2 [50].

The other regime was provided by a Nd:YAG laser emitting at 1.064 μm , with the pulse duration of 5 ns, the repetition frequency of 1 Hz and the beam diameter of 0.4 mm [49]. The energy values were increased little by little by radiating on the crystal surface with forty different positions. According to these measurements, the optical damage threshold of BGSe was around 557 MW/cm^2 and it is therefore higher than that of AGS which had been estimated at 150 MW/cm^2 under the same conditions [49].

Principal refractive indices

The three principal refractive indices n_x , n_y and n_z have been reported as a function of wavelength by [47] and [48]. They applied a minimum deviation technique in two prisms and their fit of data enabled to determine Sellmeier equations. It showed that BGSe is a positive biaxial crystal. The data were recorded between 0.48 and 10.4 μm in [47], but the accuracy was limited to typically of the order of 10^{-3} in the visible, and was worse in the infrared range. The accuracy has been improved up to 10^{-6} in [48], but data were recorded between 0.5 and 2.6 μm only. Then the Sellmeier equations from [47] and [48] did not correspond to the SHG and DFG(λ_i) tuning curves in principal planes of BGSe that were recorded in our group with the SPHERE method [45].

The simultaneous fit of SHG and DFG(λ_i) tuning curves recorded in principal planes

of the dielectric frame of BGSe by using a 7.55 mm diameter sphere, allowed our group to refine the Sellmeier equations describing the variation the three principal refractive indices n_x , n_y and n_z as a function of wavelength [45]. The refined Sellmeier equations of BGSe are expressed as follows:

$$n_i^2(\lambda) = A_i + \frac{B_i}{\lambda^2 - C_i} + \frac{D_i}{\lambda^2 - E_i} \quad (4.1)$$

λ is in μm , and i stands for x, y and z. They are valid between 0.48 and 11 μm .

The corresponding dispersive coefficients A_i, B_i, C_i, D_i and E_i are given in Table 4.1.

coefficients	$i = x$	$i = y$	$i = z$
A_i	7.405114	7.388458	7.622884
B_i	0.225316	0.224481	0.238018
C_i	0.051215	0.052725	0.069734
D_i	1782.091	1778.441	1885.307
E_i	1170.528	1238.145	1303.370

Table 4.1: Coefficients of Eq. 4.1 describing the dispersive equations of the three principal refractive indices n_x , n_y and n_z of BGSe over the wavelength range 0.48-11 μm [45].

The corresponding dispersion curves of the three principal refractive indices of BGSe are shown in Figure 4.4 over their domain of validity (0.48-11 μm). The relative accuracy $\Delta n_i/n_i$ (with $i = x, y$ or z) of the refined refractive indices is better than 10^{-4} .

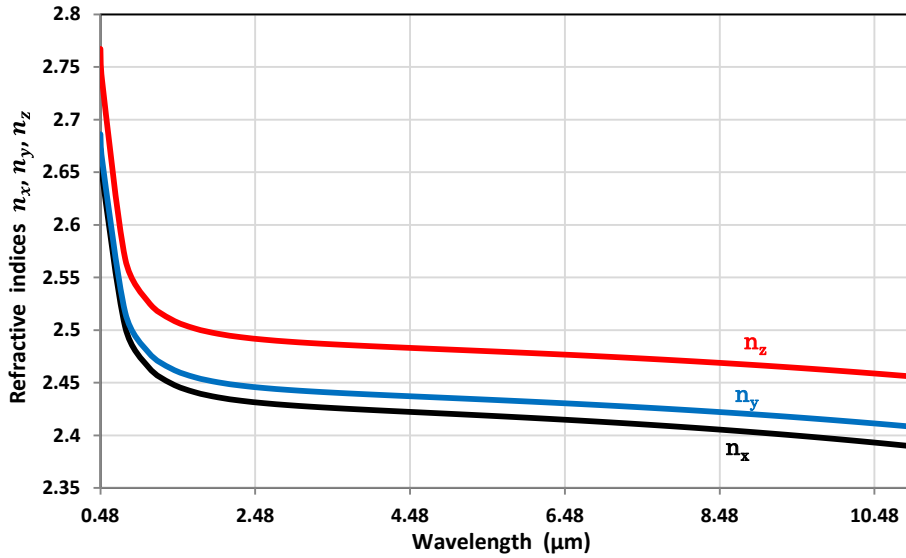


Figure 4.4: The three principal refractive indices n_x , n_y and n_z of BGSe as a function of wavelength [45].

Second-order electric susceptibility tensor

According to the Neumann principle, the second-order electrical susceptibility tensor of BGSe, $\chi^{(2)}$, is reduced to 14 non-zero and independent coefficients, and it writes [ref]:

$$\chi^{(2)} = \begin{pmatrix} 0 & 0 & 0 & 0 & 0 & \chi_{xxz}^{(2)} & \chi_{xzx}^{(2)} & \chi_{xxy}^{(2)} & \chi_{xyx}^{(2)} \\ \chi_{yxx}^{(2)} & \chi_{yyy}^{(2)} & \chi_{yzz}^{(2)} & \chi_{yyz}^{(2)} & \chi_{zyy}^{(2)} & 0 & 0 & 0 & 0 \\ \chi_{zxx}^{(2)} & \chi_{zyy}^{(2)} & \chi_{zzz}^{(2)} & \chi_{zyz}^{(2)} & \chi_{zzy}^{(2)} & 0 & 0 & 0 & 0 \end{pmatrix} \quad (4.2)$$

Under the Kleinman assumption, comes:

$$\begin{cases} \chi_{zxx}^{(2)} = \chi_{xxz}^{(2)} = \chi_{xzx}^{(2)}; \chi_{yxx}^{(2)} = \chi_{xxy}^{(2)} = \chi_{xyx}^{(2)} \\ \chi_{zyy}^{(2)} = \chi_{yzy}^{(2)} = \chi_{yyz}^{(2)}; \chi_{yzz}^{(2)} = \chi_{zyz}^{(2)} = \chi_{zzy}^{(2)} \end{cases} \quad (4.3)$$

Then the tensor $\chi^{(2)}$ becomes:

$$\chi^{(2)} = \begin{pmatrix} 0 & 0 & 0 & 0 & 0 & \chi_{zxx}^{(2)} & \chi_{zxx}^{(2)} & \chi_{yxx}^{(2)} & \chi_{yxx}^{(2)} \\ \chi_{yxx}^{(2)} & \chi_{yyy}^{(2)} & \chi_{yzz}^{(2)} & \chi_{zyy}^{(2)} & \chi_{zyy}^{(2)} & 0 & 0 & 0 & 0 \\ \chi_{zxx}^{(2)} & \chi_{zyy}^{(2)} & \chi_{zzz}^{(2)} & \chi_{yzz}^{(2)} & \chi_{yzz}^{(2)} & 0 & 0 & 0 & 0 \end{pmatrix} \quad (4.4)$$

Using the contracted notation, it also writes [ref]:

$$\chi^{(2)} = \begin{pmatrix} 0 & 0 & 0 & 0 & \chi_{31}^{(2)} & \chi_{21}^{(2)} \\ \chi_{21}^{(2)} & \chi_{22}^{(2)} & \chi_{23}^{(2)} & \chi_{32}^{(2)} & 0 & 0 \\ \chi_{31}^{(2)} & \chi_{32}^{(2)} & \chi_{33}^{(2)} & \chi_{23}^{(2)} & 0 & 0 \end{pmatrix} \quad (4.5)$$

where:

$$\chi_{yxx}^{(2)} = \chi_{21}^{(2)}; \chi_{yyy}^{(2)} = \chi_{22}^{(2)}; \chi_{yzz}^{(2)} = \chi_{23}^{(2)}; \chi_{zxx}^{(2)} = \chi_{31}^{(2)}; \chi_{zyy}^{(2)} = \chi_{32}^{(2)}; \chi_{zzz}^{(2)} = \chi_{33}^{(2)} \quad (4.6)$$

As shown in Table 4.2, on the basis a band structure modeling, the magnitude and the relative sign of the 6 nonlinear coefficients of BGSe were calculated at 0.532 μm [44]. The magnitude in absolute value of d_{22} and d_{23} were also determined at 0.532 μm , compared to d_{36} of the KDP crystal by recording SHG conversion efficiencies out-of phase-matching condition and the Maker fringes method [51]. They are also given in Table 4.2.

Coefficients(pm/V)	Ref. [44]	Ref. [51]
d_{21}	5.2	
d_{22}	18.2	$ 24.3 \pm 1.5 $
d_{23}	-20.6	$ 20.4 \pm 1.1 $
d_{31}	14.3	
d_{32}	-15.2	"weak"
d_{33}	-2.2	"weak"

Table 4.2: Nonlinear coefficients of BGSe at 0.532 μm written in the contracted notation from [44, 51].

Our group proposed to determine the nonlinear coefficients of BGSe by recording type-I and type-II SHG conversion efficiencies in principal planes. The calculated associated effective coefficients $d_{eff}(\lambda_{2\omega}, \theta_{PM}, \varphi_{PM})$ are given in Table 4.3 at the phase-matching angles $(\theta_{PM}, \varphi_{PM})$ and generated wavelength $\lambda_{2\omega} = \lambda_{\omega}/2$, for this positive biaxial crystal.

Principal plane	Types ($2\omega \ \omega \ \omega$)	Effective coefficient d_{eff}
x-z ($0 < \theta < V_z$)	Type I	$d_{32}(\lambda_{2\omega})\sin[\theta - \rho_{x,z}(\lambda_{2\omega}, \theta_{PM})]$
	Type II	$-d_{21}(\lambda_{2\omega})\cos[\theta - \rho_{x,z}(\lambda_{\omega}, \theta_{PM})]\cos[\theta_{PM} - \rho_{x,z}(\lambda_{2\omega}, \theta_{PM})] - d_{23}(\lambda_{2\omega})\sin[\theta_{PM} - \rho_{x,z}(\lambda_{\omega}, \theta_{PM})]\sin[\theta_{PM} - \rho_{x,z}(\lambda_{2\omega}, \theta_{PM})]$
x-z ($90^\circ > \theta > V_z$)	Type I	$d_{21}(\lambda_{2\omega})\cos^2[\theta_{PM} - \rho_{x,z}(\lambda_{\omega}, \theta_{PM})] + d_{23}(\lambda_{2\omega})\sin^2[\theta_{PM} - \rho_{x,z}(\lambda_{\omega}, \theta_{PM})]$
	Type II	$d_{32}(\lambda_{2\omega})\sin[\theta_{PM} - \rho_{x,z}(\lambda_{\omega}, \theta_{PM})]$
x-y	Type I	$d_{23}(\lambda_{2\omega})\cos[\varphi_{PM} + \rho_{x,y}(\lambda_{2\omega}, \varphi_{PM})]$
	Type II	$d_{31}(\lambda_{2\omega})\sin[\varphi_{PM} + \rho_{x,y}(\lambda_{\omega}, \varphi_{PM})]\sin[\varphi_{PM} + \rho_{x,y}(\lambda_{2\omega}, \varphi_{PM})] + d_{32}(\lambda_{2\omega})\cos[\varphi_{PM} + \rho_{x,y}(\lambda_{\omega}, \varphi_{PM})]\cos[\varphi_{PM} + \rho_{x,y}(\lambda_{2\omega}, \varphi_{PM})]$
y-z	Type I	0
	Type II	$d_{31}(\lambda_{2\omega})\sin[\theta_{PM} - \rho_{y,z}(\lambda_{\omega}, \theta_{PM})] - d_{21}(\lambda_{2\omega})\cos[\theta_{PM} - \rho_{y,z}(\lambda_{\omega}, \theta_{PM})]$

Table 4.3: Effective coefficients $d_{eff}(\lambda_{2\omega}, \theta, \varphi)$ associated to type I and II SHG in principal planes of a positive biaxial crystal as BGSe. $\rho_{l,m}(\lambda_{\omega}, \alpha)$ ($l, m = x, y$ or z and $\alpha = \theta_{PM}$ or φ_{PM}) are spatial walk-off angles given in Table 1.1. $(\theta_{PM}, \varphi_{PM})$ are phase-matching angles in spherical coordinates.

Table 4.3 shows that d_{23} , d_{32} and d_{31} are involved alone for type I or II phase-matched SHG along principal dielectric axes. It corresponds to angular non-critical phase-matching (ANCPM) conditions that have the advantage of a vanishing walk-off angle: d_{23} and d_{32} are accessible along x-axis from type I and II ANCPM SHG respectively, d_{31} along y-axis from type II ANCPM SHG.

Two slabs with two parallel and polished faces cut perpendicular to the principal x- and y-axes of the dielectric frame were used and the modulus operandi described in detail in part 2.2.4 of chapter 2 [46]. The magnitude of the nonlinear coefficients d_{23} , d_{32} and d_{31} are given in Table 4.4 at the studied phase-matching wavelength generated by SHG and also at $0.532 \mu\text{m}$ after using the Miller rules according to Eq. (1.26) and (1.27).

Coefficients (pm/V)	Ref. [46]	@ $0.532 \mu\text{m}$ [46]
d_{23}	$ 11.3 \pm 0.8 $ @ $0.9 \mu\text{m}$	$ 14.2 \pm 0.8 $
d_{31}	$ 1.4 \pm 0.3 $ @ $1.61 \mu\text{m}$	$ 2.1 \pm 0.3 $ 1.61
d_{32}	$ 3.7 \pm 0.4 $ @ $1.265 \mu\text{m}$	$ 5.0 \pm 0.4 $

Table 4.4: Nonlinear coefficients of BGSe determined at the experimental phase-matching wavelength generated by SHG and also at $0.532 \mu\text{m}$ after using the Miller rules [3].

In the present work, we are interested in determining the magnitude of the three other coefficients d_{21} d_{22} and d_{33} , as well as the relative sign of the 6 nonlinear coefficients d_{23} , d_{32} , d_{31} , d_{21} , d_{22} , and d_{33} of BGSe.

Table 4.3 shows the following information:

- d_{22} and d_{33} are never involved in any effective coefficient associated with SHG under phase-matching condition.
- d_{21} is always involved with d_{23} or d_{31} in the effective coefficients associated with phase-matched SHG. The magnitudes in absolute value of d_{23} and d_{31} are given in Table 4.4. However, without the relative sign between d_{21} and d_{23} or d_{21} and d_{31} , it is not possible to determine the magnitude and sign of d_{21} .
- Given the magnitude of two nonlinear coefficients in $d_{eff}(\lambda_{2\omega}, \theta_{PM}, \varphi_{PM})$ gives access to their relative sign. For example, it is the case between d_{21} and d_{23} from phase-matched type II SHG in the (x, y) principal plane of the dielectric frame (see Table 4.3).

4.3 Magnitudes of the nonlinear coefficients d_{21} d_{22} and d_{33}

As just said, the magnitudes of d_{21} , d_{22} and d_{33} cannot be determined from birefringence phase-matched SHG condition in the principal planes without knowing their relative sign. Then out of phase-matched SHG conditions can be considered.

From Eq. (1.30), the out of phase-matching SHG conversion efficiency η is proportional to:

$$\eta \propto 4 \frac{d_{eff}^2(\lambda_{2\omega}, \lambda_{\omega}, \theta, \varphi)}{[\Delta k(\lambda_{2\omega}, \lambda_{\omega}, \theta, \varphi)]^2} \sin^2 \left[\frac{\Delta k(\lambda_{2\omega}, \lambda_{\omega}, \theta, \varphi)L}{2} \right] \quad (4.7)$$

where $\Delta k(\lambda_{2\omega}, \lambda_{\omega}, \theta, \varphi) \neq 0$ stands for the out-of-phase-matching conditions that can be calculated by using Eq. (1.37) and L is the crystal length.

4.3.1 Maker fringes

With the value of the fundamental wavelength λ_{ω} fixed, sent in a L -thick slab cut perpendicular to a principal axis of the dielectric frame and rotated in the incidence plane, Maker fringes can be recorded. They can give access to the magnitude of any nonlinear coefficient, according to the 8 possible configurations of polarization of the three interacting waves that is used (see chapter 1). For this purpose, the incident plane corresponds to a principal plane of the dielectric plane.

For example, a BGSe slab cut along x-axis and rotated in the (x, z) ($V_z < \theta < 90^\circ$) principal

plane, with the linear polarization of the fundamental and harmonic beams oriented parallel to the (x, z) principal plane, d_{33} can be determined [51].

According to Table 1.1 and Eq.1.37, the corresponding $d_{eff}(\lambda_{2\omega})$ and Δk write:

$$\begin{cases} d_{eff}(\lambda_{2\omega}) = d_{33}(\lambda_{2\omega}) \sin^2[\theta - \rho_{x,z}(\lambda_{\omega}, \theta)] \\ \Delta k = \frac{4\pi}{\lambda_{\omega}} [n^e(\lambda_{2\omega}, \beta) - n^e(\lambda_{\omega}, \beta)] \end{cases} \quad (4.8)$$

With

$$n(\lambda_{i\omega}) = \left[\frac{\cos^2 \beta}{n_z^2(\lambda_{i\omega})} + \frac{\sin^2 \beta}{n_x^2(\lambda_{i\omega})} \right]^{-1/2} \quad (4.9)$$

where $i = 1$ for the fundamental beam and $i = 2$ for the harmonic one and $\lambda_{2\omega} = \lambda_{\omega}/2$. $\beta = \frac{\pi}{2} - \theta$ is the internal angle between the propagation direction \vec{u} and x-axis.

By inserting Eq. (4.8) and (4.9) in Eq. (4.7), we get the calculated curve standing for the out of phase-matching SHG conversion efficiency in the x-cut BGSe in order to determine d_{33} . It is shown as a function of the internal angle β over $\pm 30^\circ$. As an example, the fundamental wavelength is set at $\lambda_{\omega} = 3.1 \mu\text{m}$ and the thickness of the slab is $L = 510 \mu\text{m}$.

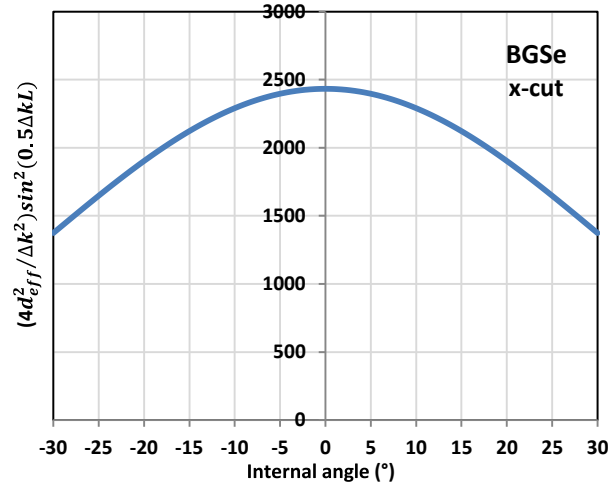


Figure 4.5: Calculated conversion efficiency as a function of the internal angle β in a $L = 510 \mu\text{m}$ and x-cut BGSe slab to access $d_{33}(\lambda_{2\omega})$. The slab is rotated in the (x, z) plane, with the polarizations of the fundamental and generated beams in this plane.

However Figure 4.5 shows no Maker fringes in a $L = 510 \mu\text{m}$ BGSe. In fact Maker fringes requires thick BGSe slabs as shown in Figure 4.6 when using a $L = 7.55 \text{ mm}$ sample. Another disadvantage of this method is the refraction of the input beam at the entrance of the slab that enhances the non-collinear propagation scheme inside the crystal. If not carefully modeled the analysis of data are not accurate.

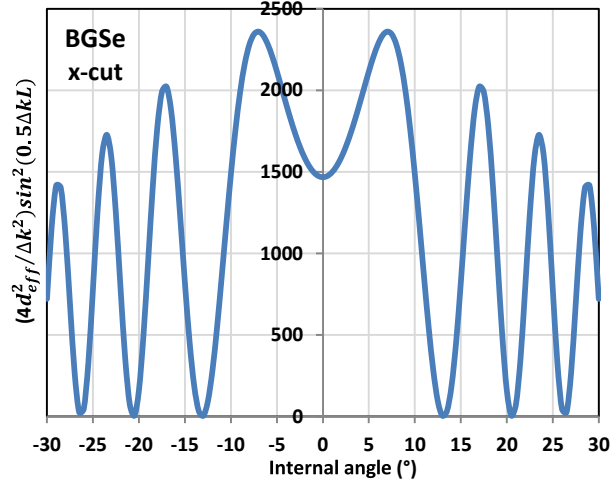


Figure 4.6: Calculated conversion efficiency as a function of internal angle β in a $L = 7.55$ mm and x-cut BGSe rotated slab to access $d_{33}(\lambda_{2\omega})$. β is in the (x, z) plane from x-axis, all polarizations are oriented in this plane.

Note that by rotating a 7.55 mm-diameter BGSe sphere, the incoming beams are not refracted at the input face, however spatial walk-off angles can attenuate the out-of-phase-matching conversion efficiency if all polarization states of the interacting waves are not parallel (see part 1.3.7).

Then we prefer to propose another method to overcome the disadvantages of Maker fringes.

4.3.2 Tunable fringes

We propose to use a slab cut along a principal dielectric axis that remains fixed (not rotated), and to record out-of-phase-matching SHG conversion efficiencies with an incoming fundamental wavelength λ_ω that can be tune over the transparency range of the crystal.

4.3.2.1 Calculations

We found that using two BGSe slabs cut oriented along x-axis and z-axis respectively, the coefficients d_{21} , d_{22} and d_{33} can be determined successively as follows:

- In the x-cut BGSe slab with the incident and generated beams polarized parallel to y-axis, the out of phase-matching condition $\Delta k(\lambda_{2\omega}, \lambda_\omega, \theta, \varphi)$ and the associated effective coefficient $d_{eff}(\lambda_{2\omega}, \lambda_\omega, \theta, \varphi)$ give access to $d_{yyy} = d_{22}$, since they write:

$$\begin{cases} d_{eff}(\lambda_{2\omega}) = d_{22}(\lambda_{2\omega}), \\ \Delta k = \frac{4\pi}{\lambda_\omega} [n_y(\lambda_\omega/2) - n_y(\lambda_\omega)] \end{cases} \quad (4.10)$$

If the polarizations are rotated to be parallel to z-axis, $d_{zzz} = d_{33}$ is accessible since $\Delta k(\lambda_{2\omega}, \lambda_{\omega}, \theta, \varphi)$ and $d_{eff}(\lambda_{2\omega}, \lambda_{\omega}, \theta, \varphi)$ write:

$$\begin{cases} d_{eff}(\lambda_{2\omega}) = d_{33}(\lambda_{2\omega}), \\ \Delta k = \frac{4\pi}{\lambda_{\omega}} [n_z(\lambda_{\omega}/2) - n_z(\lambda_{\omega})] \end{cases} \quad (4.11)$$

- In the z-cut BGSe slab with the incident beam polarized parallel to x-axis, and the generated beams polarized parallel to y-axis, the out-of-phase-matching conditions $\Delta k(\lambda_{2\omega}, \lambda_{\omega}, \theta, \varphi)$ and the associated effective coefficient $d_{eff}(\lambda_{2\omega}, \lambda_{\omega}, \theta, \varphi)$ give access to $d_{yxx} = d_{21}$, since they write:

$$\begin{cases} d_{eff}(\lambda_{2\omega}) = d_{21}(\lambda_{2\omega}), \\ \Delta k = \frac{4\pi}{\lambda_{\omega}} [n_y(\lambda_{\omega}/2) - n_x(\lambda_{\omega})] \end{cases} \quad (4.12)$$

- The nonlinear coefficient $d_{33} = d_{zzz}$ of KTP can be used as the reference. It is accessible in the x-cut slab with the incident and generated beams polarized parallel to z-axis, the out-of-phase-matching condition $\Delta k(\lambda_{2\omega}, \lambda_{\omega}, \theta, \varphi)$ and the associated effective coefficient $d_{eff}(\lambda_{2\omega}, \lambda_{\omega}, \theta, \varphi)$ write:

$$\begin{cases} d_{eff}(\lambda_{2\omega}) = d_{33}(\lambda_{2\omega}), \\ \Delta k = \frac{4\pi}{\lambda_{\omega}} [n_z(\lambda_{\omega}/2) - n_z(\lambda_{\omega})] \end{cases} \quad (4.13)$$

All the KTP and BGSe slabs can be cut with the same small thickness $L = 510 \mu\text{m}$.

KTP and BGSe labs must also be studied in the same wavelength range in order to get rid of the setup spectral response. In order to determine the most suitable spectral range, we calculated their out-of-phase-matching SHG conversion efficiency as a function of the fundamental wavelength λ_{ω} . The fundamental wavelength is ranging between 2.5 and 4.5 μm since our OPG-DFG still provides high energy in this range.

Our calculations are shown in Fig. 4.7 and Fig. 4.8 for x-cut BGSe, and in Fig. 4.9 for z-cut BGSe. They were performed by using the Sellmeier equations of BGSe from Eq. 4.1 [45] and the nonlinear coefficients from Table 4.1. We also applied the Miller rules from Eq. (1.26) and Eq. (1.27). We plotted Eq. (4.7) with:

- Eq. (4.10) in the x-cut BGSe with the incident and generated beams polarized parallel to y-axis; With Eq. (4.11) when all polarizations were rotated parallel to z-axis.
- Eq. (4.12) in the z-cut BGSe slab with the incident beam polarized parallel to x-axis, and the generated beam polarized parallel to y-axis.

We used d_{33} of KTP to validate our method and then as a reference for measurements in BGSe slabs. The Sellmeier equations of KTP are from [19] and $|d_{33}^{\text{KTP}}(0.532\mu\text{m})| = 11.3 \text{ pm/V}$ from [19]. We also applied the Miller rules from Eq. (1.26). The out-of-phase-matching SHG conversion efficiency in KTP as a function of the fundamental wavelength λ_ω was calculated using Eq. (4.7) and Eq. (4.13). It is shown in Fig. 4.10.

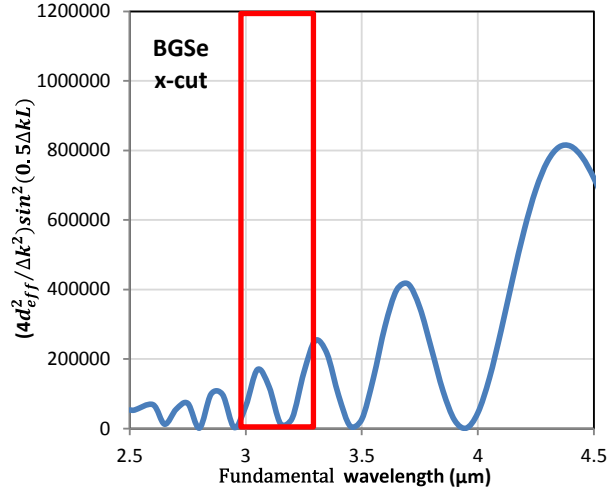


Figure 4.7: Calculated conversion efficiency for $d_{22}(\lambda_{2\omega})$ in BGSe, as a function of the fundamental wavelength.

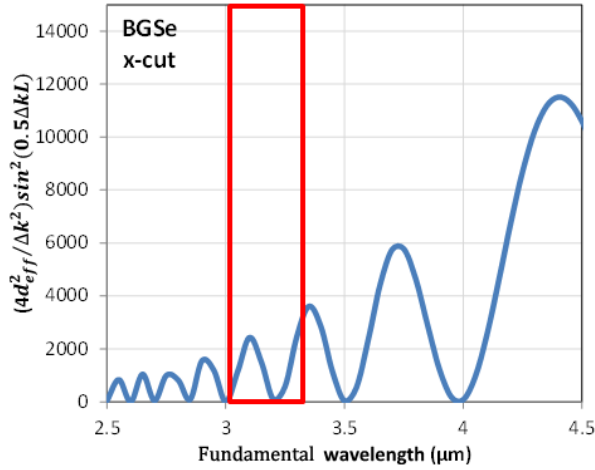


Figure 4.8: Calculated conversion efficiency for $d_{33}(\lambda_{2\omega})$ in BGSe, as a function of the fundamental wavelength.

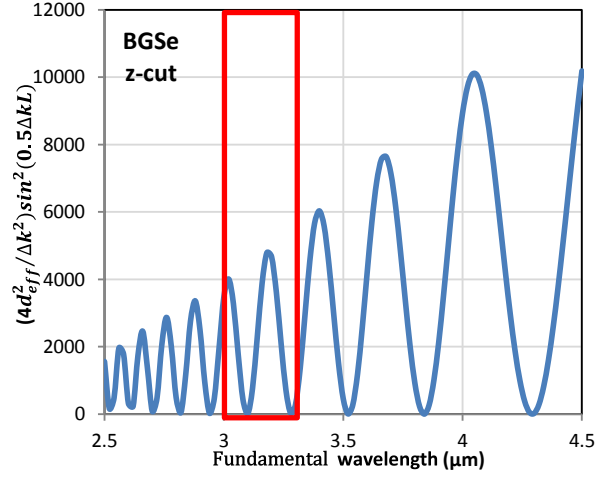


Figure 4.9: Calculated conversion efficiency for $d_{21}(\lambda_{2\omega})$ in BGSe, as a function of the fundamental wavelength.

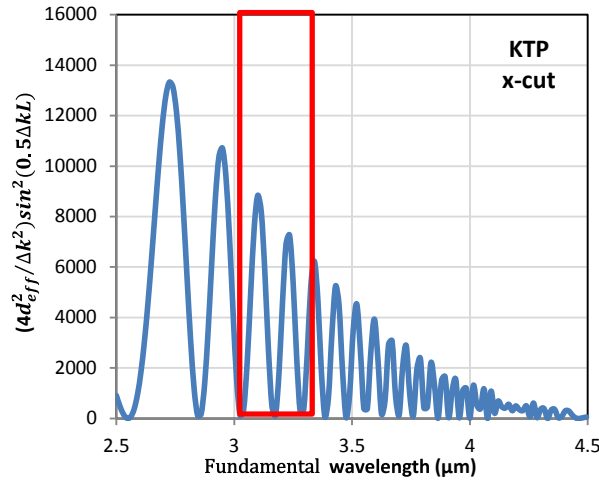


Figure 4.10: Calculated conversion efficiency for $d_{33}(\lambda_{2\omega})$ in KTP, as a function of the fundamental wavelength.

Figures 4.7 to 4.10 show that the conversion efficiency increases with the fundamental wavelength for BGSe, while it is the contrary for KTP. Then the best compromise is that the fundamental wavelength ranges between 3 and 3.3 μm . The corresponding expected tunable fringes are shown in the red windows depicted in Figures 4.7 to 4.10.

4.3.2.2 Experimental setup

The experimental setup is shown in Figure 4.11. The polarization of the fundamental beam was controlled by a half-wave plate, while using a Glan-Taylor polarizer to choose the polarization of the output beam. The energy of the input beam was measured using the J4-09 Molelectron pyroelectric joulemeter placed behind a beam splitter and a

lens with a focal length of 50 mm. The generated energy was measured at the exit of each slab by the J3-05 Molelectron pyroelectric joulemeter combined with a PEM531 amplifier, while a filter removed the input beam. With the fundamental and harmonic energies measured together, we calculated the corresponding conversion efficiency η on the fundamental wavelength.

The fundamental beam emitted by the OPG was focused with a 100-mm-focal length CaF_2 lens. Then the beam waist diameter was $w_0=120\text{ }\mu\text{m}$ on the two slabs surface, with a Rayleigh length of 30 mm that is much longer than L . Then the parallel beam propagation inside the slabs was ensured.

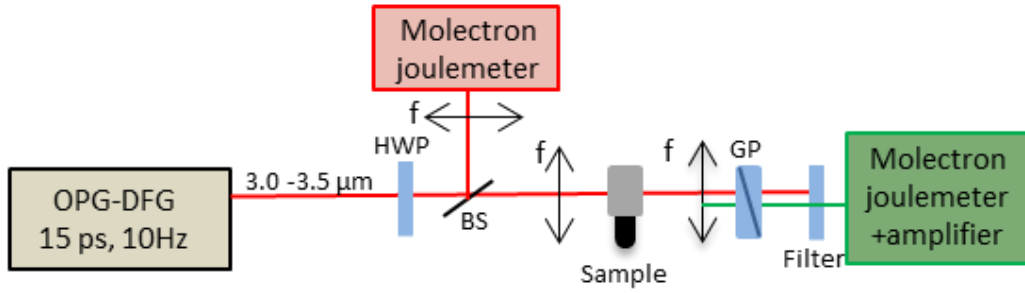


Figure 4.11: Experimental setup for the determination of the nonlinear coefficients magnitudes.

4.3.2.3 Experiments and analysis

As shown in Figure 4.12, the blue dots are the measurements of the normalized conversion efficiency η_{33}^{KTP} of KTP as a function of the wavelength between 3 and 3.3 μm . Using the Sellmeier equations [19], $|d_{33}^{KTP}(0.532\mu\text{m})| = 11.3\text{ pm/V}$ [19] and Miller's rule [5], we also calculated the normalized conversion efficiency η_{33}^{KTP} of KTP, independently. The calculations were in good agreement with the experimental results.

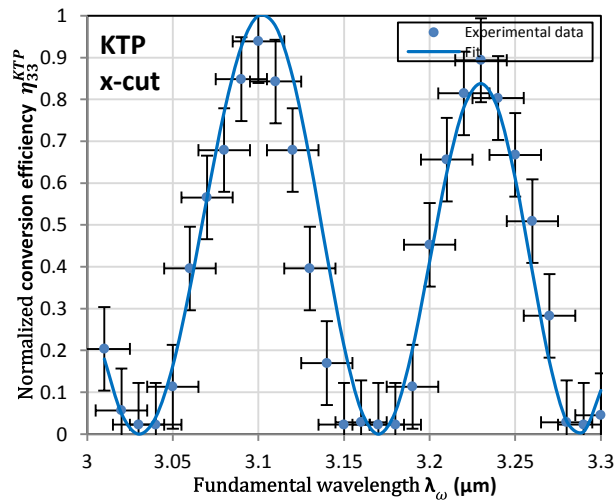


Figure 4.12: Calculated (blue line) and measured (blue dots) normalized conversion efficiency of KTP, as a function of the input beam wavelength.

Then, the conversion efficiencies η_{21}^{BGSe} and η_{22}^{BGSe} of BGSe relative to KTP as a function of the input wavelength between 3 and 3.3 μm are shown in Figure 4.13 and Figure 4.14. The red lines are the corresponding fit with the experimental results.

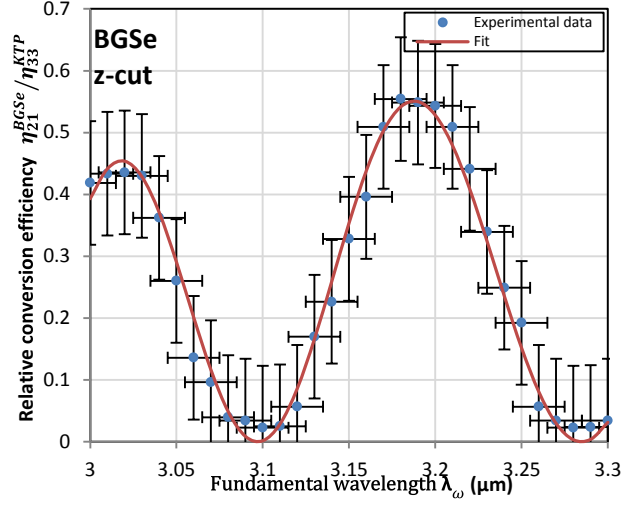


Figure 4.13: Fit (red line) and measured (blue dots) conversion efficiency of BGSe relative to KTP as a function of the input beam wavelength.

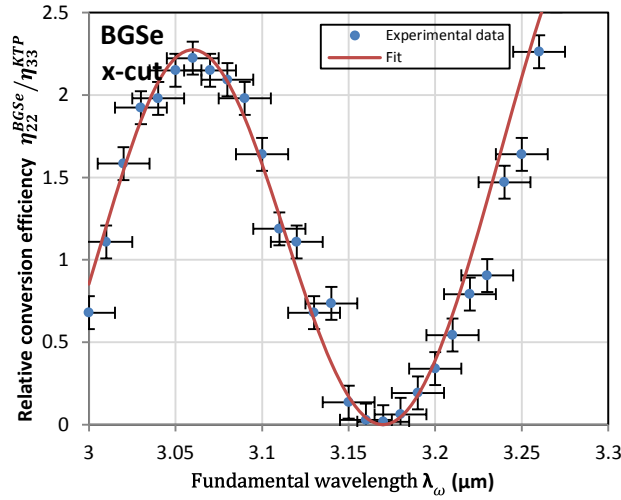


Figure 4.14: Fit (red line) and measured (blue dots) conversion efficiency of BGSe relative to KTP as a function of the input beam wavelength.

By combining Eq. (1.30) and Eq. (4.7), we can deduce the following relation:

$$(d_{\text{eff}}^{BGSe})^2 = \frac{\eta_{21,22}^{BGSe}}{\eta_{33}^{KTP}} \frac{A_{33}^{KTP}}{A_{21,22}^{BGSe}} \frac{G_{33}^{KTP}}{G_{21,22}^{BGSe}} \left(\frac{\Delta k_{21,22}^{BGSe}}{\Delta k_{33}^{KTP}} \right)^2 \frac{\sin^2(0.5 \Delta k_{33}^{KTP} L)}{\sin^2(0.5 \Delta k_{21,22}^{BGSe} L)} (d_{33}^{KTP})^2 \quad (4.14)$$

With

$$A_{21}^{BGSe} = \frac{T_y^{BGSe}(\lambda_{2\omega})}{n_y^{BGSe}(\lambda_{2\omega})} \frac{T_x^{BGSe}(\lambda_{\omega})}{n_x^{BGSe}(\lambda_{\omega})} \frac{T_x^{BGSe}(\lambda_{\omega})}{n_x^{BGSe}(\lambda_{\omega})} \quad (4.15)$$

$$A_{22}^{BGSe} = \frac{T_y^{BGSe}(\lambda_{2\omega})}{n_y^{BGSe}(\lambda_{2\omega})} \frac{T_y^{BGSe}(\lambda_\omega)}{n_y^{BGSe}(\lambda_\omega)} \frac{T_y^{BGSe}(\lambda_\omega)}{n_y^{BGSe}(\lambda_\omega)} \quad (4.16)$$

$$A_{33}^{KTP} = \frac{T_z^{KTP}(\lambda_{2\omega})}{n_z^{KTP}(\lambda_{2\omega})} \frac{T_z^{KTP}(\lambda_\omega)}{n_z^{KTP}(\lambda_\omega)} \frac{T_z^{KTP}(\lambda_\omega)}{n_z^{KTP}(\lambda_\omega)} \quad (4.17)$$

n_y^{BGSe} and n_x^{BGSe} are the principal refractive indices of BGSe. n_z^{KTP} is the principal refractive indices of KTP. T_x , T_y and T_z are the associated Fresnel coefficients.

We tried different values of $|d_{21}^{BGSe}(0.532\mu m)|$ and $|d_{22}^{BGSe}(0.532\mu m)|$ with Miller's rule [5] to fit the experimental data. Then we got $|d_{21}^{BGSe}(1.575 \mu m)| = 4.17 \text{ pm/V}$ and $|d_{22}^{BGSe}(1.575 \mu m)| = 4.88 \text{ pm/V}$. With the Miller's rule of Eq. (1.26), we found that $|d_{21}^{BGSe}(0.532\mu m)| = 5.3 \text{ pm/V}$ and $|d_{22}^{BGSe}(0.532\mu m)| = 6.2 \text{ pm/V}$. All these data are summarized in Table 4.5.

Coefficients (pm/V)	@ 1.575 μm	@ 0.532 μm
d_{21}	4.17	5.3
d_{22}	4.88	6.2

Table 4.5: Nonlinear coefficients of BGSe determined at the experimental wavelength and at 0.532 μm after using the Miller rules.

We were not able to measure the magnitude of the coefficient d_{33} , because the corresponding harmonic energy is lower compared with d_{21} and d_{22} as shown in Figure 4.8. Then we guess that, the magnitude of the coefficient d_{33} may be lower than 2.2 pm/V [44].

4.4 Relative sign between nonlinear coefficients

As explained in part 2.3.3.3 for KTP, the relative sign between two nonlinear coefficients involved in the same effective coefficient d_{eff} can be determined provided their magnitude have been already found. For that purpose $d_{eff}(\lambda_{2\omega}, \theta_{PM}, \varphi_{PM})$ was studied along SHG phase-matching conditions.

The fundamental wavelength λ_ω is fixed and the phase-matching angles θ_{PM} and φ_{PM} are the solutions of Eq. (1.38) provided the SHG phase-matching loci in the dielectric frame as illustrated in Fig. 2.16.

Another possibility is that one phase-matching angle θ_{PM} or φ_{PM} is varied only, with the fundamental wavelength λ_ω while fulfilling Eq. (1.38) to provide tuning curves in principal planes of the dielectric frame.

In that case, type I or II SHG tuning curves can be recorded in the three principal planes and the associated effective coefficients $d_{eff}(\lambda_{2\omega} = \lambda_{\omega}/2, \theta_{PM}, \varphi_{PM})$ summarized in Table 4.3 show that they involve by pairs the nonlinear coefficients d_{23} , d_{32} , d_{31} and d_{21} of BGSe.

In the (x, z) ($V_z < \theta < 90^\circ$) principal plane, the type I SHG tuning curve involves d_{21} and d_{23} since the associated effective coefficient writes:

$$d_{eff} = |d_{21}(\lambda_{2\omega})| \cos^2[\theta_{PM} - \rho_{x,z}(\omega, \theta_{PM})] \pm |d_{23}(\lambda_{2\omega})| \sin^2[\theta_{PM} - \rho_{x,z}(\omega, \theta_{PM})] \quad (4.18)$$

In the (y, z) principal plane, the type II SHG tuning curve involves d_{31} and d_{21} since the associated effective coefficient writes:

$$d_{eff} = |d_{31}(\lambda_{2\omega})| \sin[\theta_{PM} - \rho_{y,z}(\omega, \theta_{PM})] \pm |d_{21}(\lambda_{2\omega})| \cos[\theta_{PM} - \rho_{y,z}(\omega, \theta_{PM})] \quad (4.19)$$

In the (x, y) principal plane, the type II SHG tuning curve involves d_{31} and d_{32} since the associated effective coefficient writes:

$$d_{eff} = |d_{31}(\lambda_{2\omega})| \sin[\varphi_{PM} + \rho_{x,y}(\omega, \varphi_{PM})] \sin[\varphi_{PM} + \rho_{x,y}(2\omega, \varphi_{PM})] \\ \pm |d_{32}(\lambda_{2\omega})| \cos[\varphi_{PM} + \rho_{x,y}(\omega, \varphi_{PM})] \cos[\varphi_{PM} + \rho_{x,y}(2\omega, \varphi_{PM})] \quad (4.20)$$

4.4.1 Calculations

We calculated the three previous tuning curves by solving Eq (1.38) using the refined Sellmeier equations from [2]. They are shown in Figure 4.15(a), for type I SHG in the (x, z) ($V_z < \theta < 90^\circ$) principal plane. Fig. 4.16(a) and 4.17(b) correspond to type II SHG in the (y, z) and (x, y) principal planes respectively. They are depicted as the fundamental wavelength λ_{ω} as a function of the phase-matching angle θ_{PM} or φ_{PM} .

Then comes the variation of the effective coefficients associated to the previous tuning curves. They were calculated by using the magnitudes of d_{23} , d_{32} , d_{31} and d_{21} given in Tables 4.4 and 4.5 at $0.532 \mu\text{m}$, by using the refined Sellmeier equations from [45] and applying Miller rules from Eq. (1.26) and (1.27). The square values of three effective coefficients are shown in Figures 4.15(b), 4.16(b) and 4.17(b) as a function of the phase-matching angles θ_{PM} or φ_{PM} . Two calculations are depicted according to it is assumed that the magnitudes of two involved nonlinear coefficients have the same relative sign (see solid line) or have an opposite sign (see dashed line).

Then a comparison between the two possible calculations and recorded data will give their real relative sign without ambiguity. It is the relative sign between d_{21} and d_{23} from type I SHG in the (x, z) ($V_z < \theta < 90^\circ$) plane (see Figure 4.15(b)), the relative sign between d_{31} and d_{21} from type II SHG in the (y, z) plane (see Figure 4.16(b)), the

relative sign between d_{31} and d_{32} from type II SHG in the (x,y) plane (see Figure 4.17(b)).

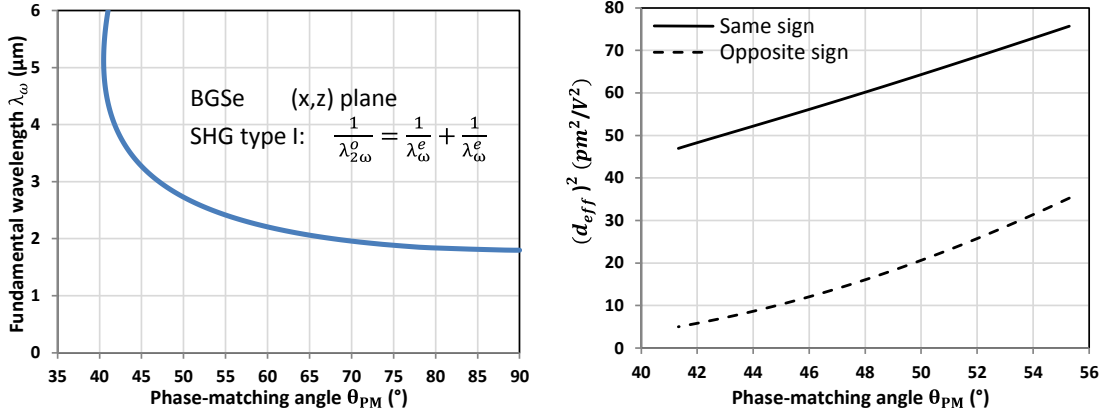


Figure 4.15: Type I SHG in the (x,z) plane ($V_z < \theta < 90^\circ$) of BGSe. (a) tuning curve, (b) square of the associated effective coefficient.

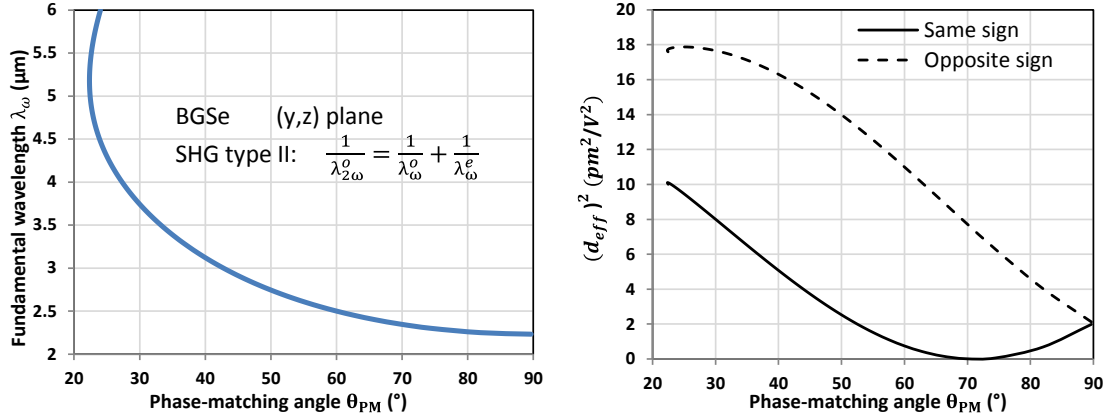


Figure 4.16: (a) Type II SHG in the (y,z) plane of BGSe. (a) tuning curve, (b) square of the associated effective coefficient.

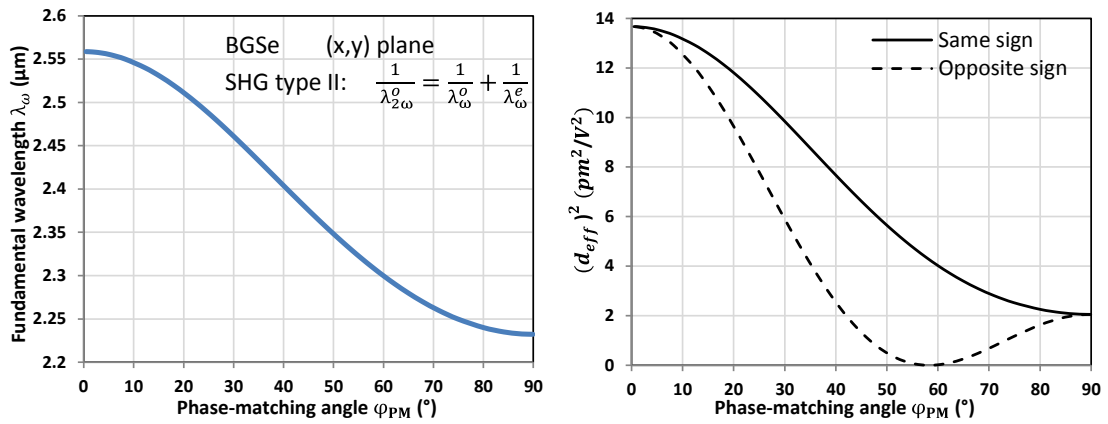


Figure 4.17: Type II SHG in the (x,y) plane of BGSe. (a) tuning curve, (b) square of the associated effective coefficient.

4.4.2 Measurement and analysis of data

In order to perform the experiments in three principal planes, we cut and polish BGSe as a sphere with a diameter of 7.55 mm as shown in Figure 4.18. The asphericity $\Delta D/D$ is better than 1% (D is the diameter of the sphere).

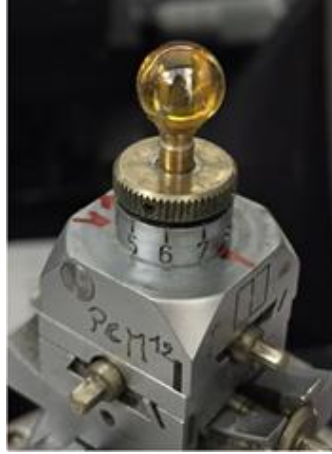


Figure 4.18: Picture of the sphere of BGSe of the diameter 7.55 mm shaped for our studies of the relative sign between nonlinear coefficients.

By stuck the sphere along the y - , x - and z -axes of the dielectric frame, successively, we measured the relative data of the conversion efficiency of type I SHG in the (x, z) ($V_z < \theta < 90^\circ$) principal plane, type II SHG in the (y, z) principal plane and type II SHG in the (x, y) principal plane, respectively.

The phase-matched condition and the corresponding conversion efficiency were studied in each configuration by using the experimental setup shown in Figure 2.10. Only one tunable incoming beam was necessary for the SHG experiments.

The square of the effective coefficient is ratio to the conversion efficiency. Then by measuring the conversion efficiency, we could get the related ratio of the square of the effective coefficient. Figures 4.19-4.21 show the corresponding experimental data as blue dots. They also show calculations of the square of the effective coefficient of type I SHG in the (x, z) ($V_z < \theta < 90^\circ$) principal plane, type II SHG in the (y, z) principal plane and type II SHG in the (x, y) principal plane, respectively. These calculations were performed assuming the magnitude of the two involved nonlinear coefficients of the same sign (see solid lines) and the opposite sign (see dashed lines).

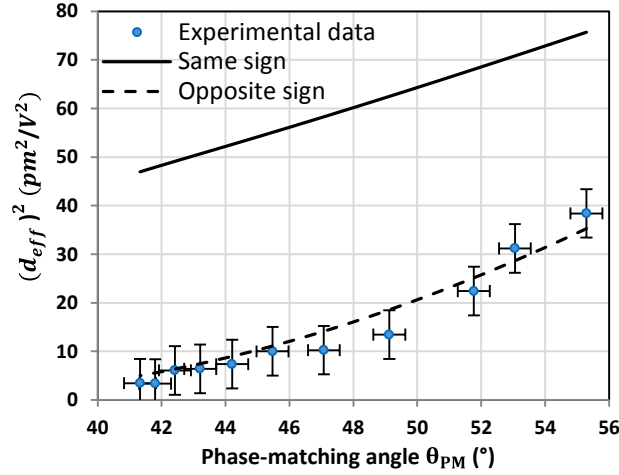


Figure 4.19: The square of the effective coefficient of type I SHG in the (x, z) ($V_z < \theta < 90^\circ$) principal plane of BGSe: measurements (dots) and calculations with the same sign of the two involved coefficients (solid line) and the opposite sign (dashed line).

The comparison of the calculations and experimental data shows that the experimental data is in good agreement with the dashed line. So we determined that the coefficients d_{21} and d_{23} have the opposite sign.

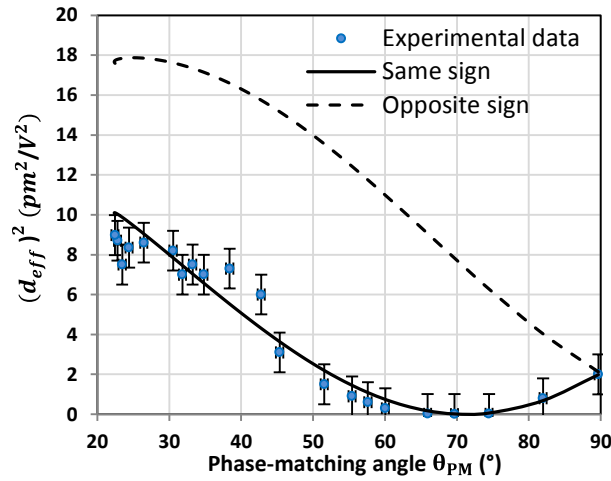


Figure 4.20: The square of the effective coefficient of type II SHG in the (y, z) principal plane of BGSe: measurements (dots) and calculations with the same sign of the two involved coefficients (solid line) and the opposite sign (dashed line).

The comparison of the calculations and experimental data shows that the experimental data is in good agreement with the solid line. What's more, the experimental data decrease slowly until zero at the angle of around 70° , then it increase again with the phase-matching angle. So we determined that the coefficients d_{31} and d_{21} have the same sign.

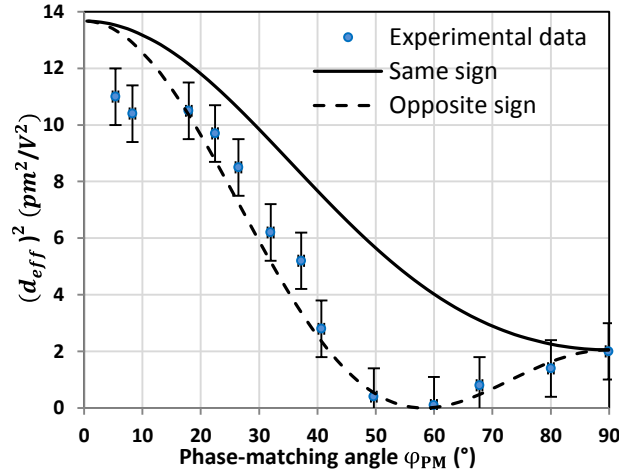


Figure 4.21: The square of the effective coefficient of type II SHG in the (x,y) principal plane of BGSe: measurements (dots) and calculations with the same sign of the two involved coefficients (solid line) and the opposite sign (dashed line).

The same comparison shows that the experimental data is in good agreement with the dashed line. And, the experimental data vanishes to zero at the angle of around 58° . Thus we determined that the coefficients d_{31} and d_{32} have an opposite sign.

4.4.3 Calculation out of the principal planes

Since it is not possible to determine the relative sign of d_{22} and d_{33} by studying SHG tuning curves in the principal planes of BGSe as shown in Table 4.3, we investigated if any possibility by studying type II SHG at the fundamental wavelength of $3 \mu\text{m}$ out of the principal planes. For that purpose we calculated the corresponding non-zero and independent elements of the field factor according to Eq. (1.36). They are shown in Figure 4.22 as a function of the phase matching angle φ_{PM} .

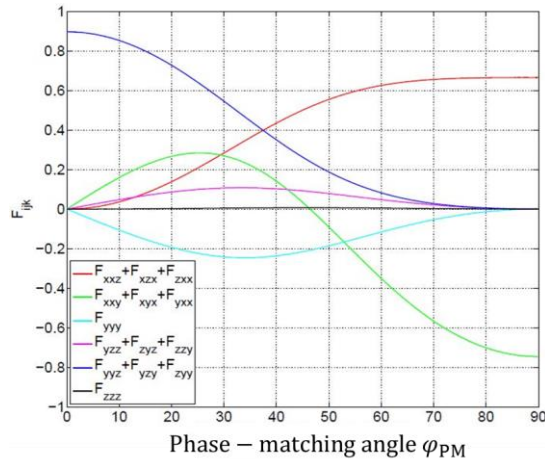


Figure 4.22: Field factors F_{ijk} along Type II SHG tuning curve in Kleinman approximation.

It highlights that it is not possible to isolate d_{22} and d_{33} from the other coefficients so that the determination of their relative sign might be complicated even if the magnitude

of d_{33} had been determined.

4.5 Condition of supercontinuum generation

Using the refined Sellmeier equations, we studied the potentiality of BGSe for the generation of a supercontinuum by phase-matched type II OPG. Since BGSe is a positive biaxial crystal, we considered type II DFG ($1/\lambda_i^+ = 1/\lambda_p^- - 1/\lambda_s^+$) where ($\lambda_p < \lambda_s < \lambda_i$) and $\lambda_s^{-1} + \lambda_i^{-1} = \lambda_p^{-1}$ in the principal planes where the associated effective coefficient is not equal to zero.

It is the case in the (x,y) principal plane, according to Eq. (1.45) with $n^+ = n_z$, then the magic pump wavelength is $\lambda_p = \frac{\lambda_{ZDW}}{2} = 2.45 \mu\text{m}$. But there is no optimum corresponding to a supercontinuum spectrum using this magic pump wavelength.

In the (x,z) principal plane, the magic pump wavelength is $2.37 \mu\text{m}$ [45] and the corresponding effective coefficient is:

$$d_{eff}(\lambda_i) = d_{21}(\lambda_i) \cos[\theta_{PM} - \rho_{x,z}(\omega_i, \theta_{PM})] \cos[\theta_{PM} - \rho_{x,z}(\omega_s, \theta_{PM})] + d_{23}(\lambda_i) \sin[\theta_{PM} - \rho_{x,z}(\omega_i, \theta_{PM})] \sin[\theta_{PM} - \rho_{x,z}(\omega_s, \theta_{PM})] \quad (4.21)$$

d_{21} was measured in part 4.4.3, while d_{23} had been measured using the phase-matching SHG method [46], and we have already determined the relative sign between d_{21} and d_{23} using the type II SHG in the (x,z) principal plane.

Figure 4.23 gives the theoretical type II DFG curves calculated by using our refined Sellmeier equations in the (x,z) principal plane of BGSe. The magic pump wavelength of $2.37 \mu\text{m}$ can be offered by the laser $\text{Cr}^{2+}:\text{ZnSe}$ [8]. As shown in Figure 4.23, the corresponding supercontinuum can be generated in a slab cut in the direction ($\theta_{PM} = 40.6^\circ, \varphi_{PM} = 0^\circ$) and the extension is between 3 and $11 \mu\text{m}$. We also chose $\lambda = 2.09 \mu\text{m}$ (Ho:YAG laser), $1.645 \mu\text{m}$ (diode-pumped Er-laser) and $1.064 \mu\text{m}$ (Nd:YAG laser) as the pump wavelengths.

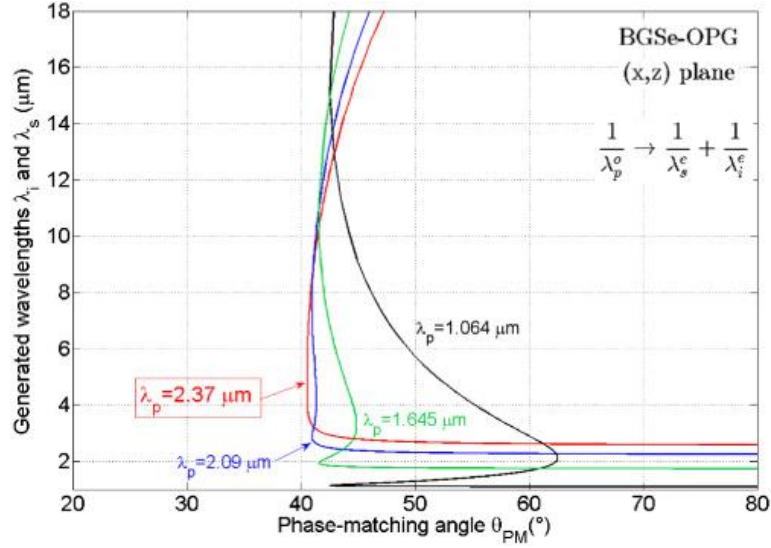


Figure 4.23: Calculated type II OPG tuning curves in the (x, z) principal plane of BGSe at different values of the pump wavelength λ_p . The generated wavelengths λ_i and λ_s are the idler and signal, respectively.

With a slab cut along $(\theta_{PM} = 40.6^\circ, \phi_{PM} = 0^\circ)$ and the pump wavelength set at $2.37 \mu\text{m}$ (“magic” pump wavelength), we calculated the corresponding normalized spectral bandwidth of Type II OPG super continuum generated in a 1 cm thick BGSe crystal according to Eq. (1.30). It is shown in Figure 4.24.

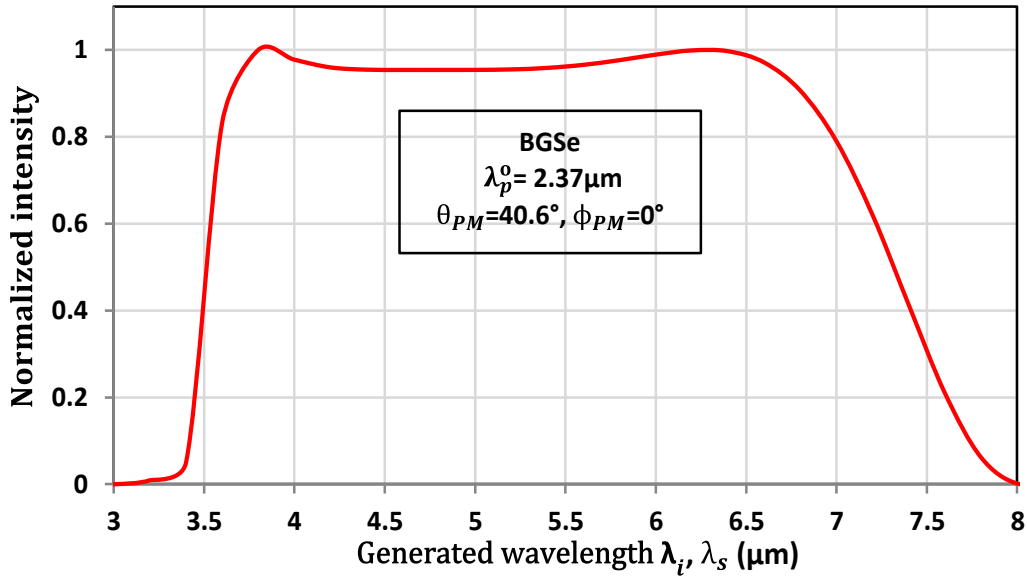


Figure 4.24: Normalized spectrum of the mid-IR Type II supercontinuum that can be generated in a 1 cm long BGSe crystal oriented at $\theta_{PM} = 40.6^\circ, \phi_{PM} = 0^\circ$. When using the magic pump wavelength $\lambda_p = 2.37 \mu\text{m}$.

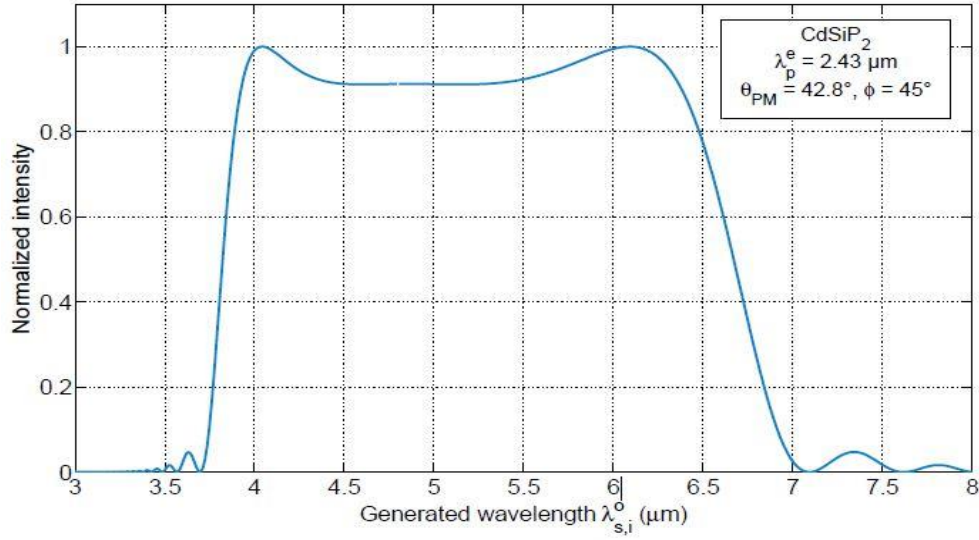


Figure 4.25: Normalized spectrum of the mid-IR Type II supercontinuum that can be generated in a 1 cm long CdSiP₂ crystal oriented at $\theta_{PM} = 42.8^\circ$, $\varphi_{PM} = 45^\circ$. When using the magic pump wavelength $\lambda_p = 2.43 \mu m$ [8].

The supercontinuum of a 1 cm thick CdSiP₂ is shown in Figure 4.25, by using the laser Cr²⁺:ZnSe at the wavelength of $2.43 \mu m$ as the pump wavelength [8]. Thus we can compare the mid-IR Type II supercontinuum for these two nonlinear crystals. From Figure 4.24 and 4.25, we found that under the same condition, the supercontinuum range of BGSe is a little wider than CdSiP₂.

However the corresponding effective coefficient of CdSiP₂ is:

$$d_{eff}(\lambda_i) = d_{36}(\lambda_i) \sin[\theta_{PM} - \rho(\lambda_p, \theta_{PM})] \quad (4.22)$$

$d_{36}(\lambda_i)$ can be offered by [8] and $\theta_{PM} = 42.8^\circ$, $\rho(\lambda_p, \theta_{PM})$ can be calculated using Eq. (1.18).

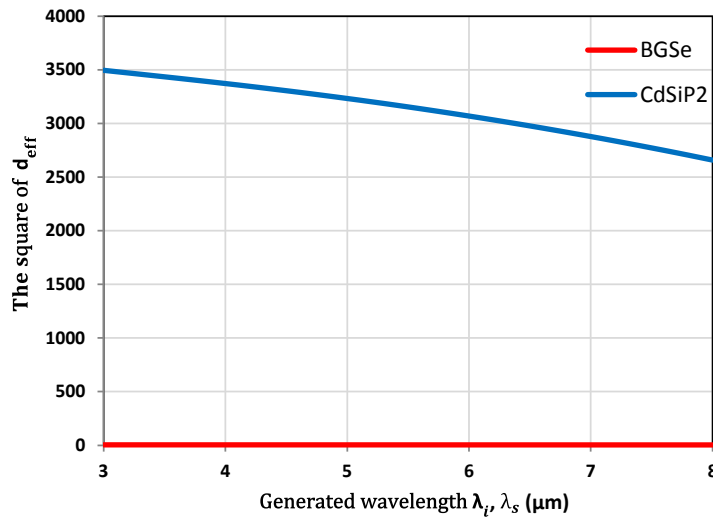


Figure 4.26: The square of the effective coefficients of BGSe and CdSiP₂, BGSe crystal oriented at $\theta_{PM} = 40.6^\circ$, $\varphi_{PM} = 0^\circ$; CdSiP₂ crystal oriented at $\theta_{PM} = 42.8^\circ$, $\varphi_{PM} = 45^\circ$.

Figure 4.26 shows that the effective of BGSe from Eq (4.21) is very weak compared with CSP. However, it can be improved by using a much thicker BGSe slab which has the advantage to enlarge the spectral bandwidth.

4.6 Summary

We reported for the first time to our knowledge, an exhaustive study providing the magnitude and the relative sign of the six nonlinear coefficients of a monoclinic BGSe crystal. The recorded data combined phase-matched and out of phase-matched SHG conversion efficiencies. But in the later case we proposed a new method labelled the tunable fringes method that is more efficient and reliable than Maker fringes. It uses a tunable fundamental beam at normal incidence at the surface of a slab that is kept fixed. It was validated with a KTP slab that is used a reference for measurements performed at the same wavelength in BGSe slabs. With the tunable fringes method, we determined the magnitude of the d_{21} and d_{22} nonlinear coefficients of BGSe.

Conclusion

This PhD work has been devoted to the exhaustive study of four crystals for their use in optical parametric generators (OPG) with an efficient emission that covers band II (3–5 μm) or band III (8–12 μm) of transmission of the atmosphere. We were interested in such an emission in their transparency range, from quadratic nonlinear processes under birefringence phase-matching conditions (BPM).

We used the methods available at Néel Institute which setup and *modus operandi* for recording data are detailed in chapter 2. We also discussed the analysis of data using the theoretical elements of linear optics and nonlinear optics given in chapter 1.

About our main results reported in chapter 3,

We report the first exhaustive study, to the best of our knowledge of the nonlinear optical properties of $\text{GdCa}_4\text{O}(\text{BO}_3)_3$ (GdCOB) positive biaxial crystal, $\text{La}_3\text{Ga}_{5.5}\text{Nb}_{0.5}\text{O}_{14}$ (LGN) positive uniaxial crystal, and NaI_3O_8 negative uniaxial crystal. Their transparency range covers band II.

The main results of this chapter are the studies of second harmonic generation (SHG) and difference frequency generation (DFG) that we performed under birefringence phase-matching condition in GdCOB and LGN spheres and in a NaI_3O_8 cylinder.

From DFG tuning curves recorded in several principal planes, we found that the emission covers band II (3–5 μm) in the three crystals. A simultaneous fit of all the recorded tuning curves also allowed us to refine the Sellmeier equations of GdCOB and LGN. Thanks to our studies, their domains of validity were extended and well cover the full transparency range of the crystals. Such an extended domain of validity was also found for the first Sellmeier equations reported in NaI_3O_8 , to the best of our knowledge.

We also determined the magnitude of the nonlinear coefficients of LGN and NaI_3O_8 crystals by recording through slabs birefringence angular critical phase-matching (ACPM) SHG conversion efficiencies in comparison with KTP. We determined that the magnitude of the nonlinear coefficient of LGN $|d_{11}(0.659 \mu\text{m})| = 2.9 \pm 0.5 \text{ pm/V}$. NaI_3O_8 has two nonlinear coefficients and we found that $|d_{14}(0.529 \mu\text{m})| = 0.54 \pm 0.08 \text{ pm/V}$ and $|d_{15}^{\text{NaI}_3\text{O}_8}(0.540 \mu\text{m})| = 0.85 \pm 0.13 \text{ pm/V}$. LGN and NaI_3O_8 have nearly the same damage threshold since they are equal to $2.8 \pm 0.7 \text{ GW/cm}^2$ and $2.4 \pm 0.6 \text{ GW/cm}^2$, respectively.

Our calculations provided a comparison of these three crystals for their ability to cover band II from phase-matched type II OPG supercontinuum generation. It shows that the different “magic” pump wavelength values are located around 1 μm . For the three crystals, GdCOB crystal is the less attractive concerning both the spectral bandwidth and the efficiency. NaI_3O_8 crystal provides the broadest spectral bandwidth compared with the two other crystals. However it is much less efficient than LGN, which finally seems to offer the best compromise.

About our main results reported in chapter 4,

We studied the BaGa_4Se_7 positive biaxial crystal that is transparent in band II and band III. Our interest was for the determination of the magnitude and the relative sign of the six nonlinear coefficients of the monoclinic BGSe crystal. Three nonlinear coefficients d_{23} , d_{31} and d_{32} had already been determined from SHG birefringence angular non-critical phase-matching ANCPM condition. But for the magnitudes of d_{21} , d_{22} , d_{33} , a new method recording SHG conversions efficiencies out-of phase-matching conditions is requested. We showed the interest of a new method using a tunable fundamental beam sent in a slab that remains fixed (we called it the tunable fringes method), instead of the Maker fringes method. KTP was used as the reference. Then we determined $|d_{21}^{\text{BGSe}}(1.575 \mu\text{m})| = 4.17 \text{ pm/V}$ and $|d_{22}^{\text{BGSe}}(1.575 \mu\text{m})| = 4.88 \text{ pm/V}$. We were not able to detect d_{33} .

Given the magnitude of the nonlinear coefficients of BGSe associated to SHG tuning curves in principal planes, we determined the relative sign of the coefficients d_{21} , d_{23} , d_{31} and d_{32} , it was possible by following the variation of conversion efficiencies along the associated SHG tuning curves. Using these results, our calculations showed in BGSe a broadest spectral bandwidth emitted by phase-matched type II OPG supercontinuum which covers band III better than CSP despite a much weaker associated efficiency compared to CSP.

To conclude, all these results provide new reliable data for further use of oriented crystals as devices generating parametric light in the infrared range.

References

- [1] J. F. Nye. Physical properties of crystals: their representation by tensors and matrices. Oxford University Press, 1985.
- [2] A. Yariv and P. Yeh. Optical Waves in Crystals: Propagation and Control of Laser Radiation. New York: Wiley, 1984.
- [3] B. Boulanger and J. Zyss. Nonlinear optical properties: In International Tables of Crystallography, chapter D, pages 178–219. 2006.
- [4] J. A. Armstrong, N. Bloembergen, J. Ducuing, and P. S. Pershan. Interactions between light waves in a nonlinear dielectric, *Physical review*, 127(6):1918–1939, 1962.
- [5] R. C. Miller. Optical second harmonic generation in piezoelectric crystals. *Applied Physics Letters*, 5(1):17–19, 1964.
- [6] B. Boulanger and G. Marnier. Field factor calculation for the study of the relationships between all the three-wave nonlinear optical interactions in uniaxial and biaxial crystals, *Journal of Physics: Condensed Matter*, 3(43):8327–8350, 1991.
- [7] Mehendale. S. C. and Gupta. P. K. Effect of the double refraction on type II phase matched second harmonic generation. *Optics Comm*, 68:301-304, 1988.
- [8] V. Kemlin. Parametric infrared generation: from crystals to devices. PhD thesis: 89-91, 2013.
- [9] G. Marnier and B. Boulanger. The sphere method: a new technique in linear and non-linear crystalline optical studies. *Optics Communications*, 72(3):139–143, 1989.
- [10] G. S. Settles. Visualizing Phenomena in Transparent Media. *Schlieren and Shadowgraph Techniques*, S3 S47, 2001.
- [11] Y. Petit, S. Joly, P. Segonds, and B. Boulanger. Recent advances in monoclinic

- crystal optics. *Laser and Photonics Reviews*, 7(6):920–937, 2013.
- [12] E. Boursier. Génération paramétrique infrarouge dans les cristaux de $\text{La}_3\text{Ga}_{5.5}\text{Ta}_{0.5}\text{O}_{14}$ et BaGa_4Se_7 . PhD thesis, 2016.
- [13] A. N. Winchell. Elements of optical mineralogy. Part I: Principles and methods. John Wiley & Sons Inc., 5th edition, 1965.
- [14] C. Traum, P. L. Inácio, C. Félix, P. Segonds, A. Peña, J. Debray, B. Boulanger, Y. Petit, D. Rytz, G. Montemezzani, P. Goldner, and A. Ferrier. Direct measurement of the dielectric frame rotation of monoclinic crystals as a function of the wavelength. *Optical Materials Express*, 4(1):57–62, 2014.
- [15] ISO 11254-1. Determination of laser-induced threshold of optical surfaces —Part 1: 1-on-1 test, 2000.
- [16] ISO 11254-2. Determination of laser-induced threshold of optical surfaces —Part 2: S-on-1 test, 2001.
- [17] D. R. Skinner and R. E. Whitcher. Measurement of the radius of a high-power laser beam near the focus of a lens. *J. Phys. E: Sci. Instrum.*, 5:237–238, 1972.
- [18] M. Born and E. Wolf. Principles of Optics. Pergamon Press, Sixth Edition, 1980.
- [19] B. Boulanger, J. P. Fève, G. Marnier, C. Bonnin, P. Villeval, and J. J. Zondy. Absolute measurement of quadratic nonlinearities from phase-matched second-harmonic generation in a single KTP crystal cut as a sphere. *J. Opt. Soc. Am. B*, 14:1380–1386, 1997.
- [20] B. Ménaert, J. Debray, J. Zaccaro, P. Segonds, and B. Boulanger. Bulk cylinders and spheres: from shaping to use for linear and nonlinear optics. *Optical Materials Express*, 7(8):3017–3022, 2017.
- [21] P. Brand. Study of 5%MgO:PPLN and CdSiP₂ for infrared parametric generation. PhD thesis, 2010.

- [22] A. E. Siegman. Lasers. University Science Books, 1986.
- [23] D. L. Portigal and E. Burstein. Internal Conical Refraction. *Journal of the Optical Society of America*, 59(12):1567–1573, 1969.
- [24] J. P. Fève, B. Boulanger and G. Marnier. Experimental study of internal and external conical refractions in KTP. *Optics Communications*, 105(3-4):243–252, 1994.
- [25] Feng Guo, Patricia Segonds, Julien Zaccaro, Jérôme Debray, Isabelle Gautier-Luneau, and Benoît Boulanger. Frequency conversion in the acentric tetragonal nonlinear crystal NaI3O8. *Optical Materials Express*, 7(5):1672–1678, 2017.
- [26] V. Kemlin, P. Brand, B. Boulanger, P. Segonds, P. G. Schunemann, K. T. Zawilski, B. Ménaert, and J. Debray. Phase-matching properties and refined Sellmeier equations of the new nonlinear infrared crystal CdSiP₂. *Optics Letters*, 36(10):1800–1802, 2011.
- [27] P. Segonds, B. Boulanger, J. P. Fève, B. Ménaert, J. Zaccaro, G. Aka, and D. Pelenc. Linear and nonlinear optical properties of the monoclinic Ca₄YO(BO₃)₃ crystal. *Journal of the Optical Society of America B*, 21(4):765–769, 2004.
- [28] B. Boulanger, J. P. Fève, G. Marnier, B. Ménaert, X. Cabirol, P. Villeval, and C. Bonnin. Relative sign and absolute magnitude of d(2) nonlinear coefficients of KTP from second-harmonic-generation measurements. *Journal of the Optical Society of America B*, 11(5):750–757, 1994.
- [29] G. Aka, A. Kahn-Harari, F. Mougél, D. Vivien, F. Salin, P. Coguelin, P. Colin, D. Pelene, and J. P. Damelet. Linear- and nonlinear-optical properties of a new gadolinium calcium oxoborate crystal, Ca₄GdO(BO₃)₃. *J. Opt. Soc. Am. B* 14(9): 2238– 2247, 1997.
- [30] Z. C. Wu and W. M. Liu. Efficient intracavity second-harmonic generation at 1063nm in a GdCOB crystal. *Laser Physics* 21(12): 2049– 2052, 2011.

-
-
- [31] H. H. Yu, N. Zong, Z. B. Pan, H. J. Zhang, J. Y. Wang, Z. P. Wang, and Z. Y. Xu. Efficient high-power self-frequency-doubling Nd:GdCOB laser at 545 and 530nm. *Opt. Lett.* 36(19): 3852–3854, 2011.
- [32] F. Mougel, G. Aka, F. Salin, D. Pelenc, B. Ferrand, A. Kahn-Harari, and D. Vivien. Accurate second harmonic generation phase matching angles prediction and evaluation of nonlinear coefficients of $\text{Ca}_4\text{YO}(\text{BO}_3)_3$ (YCOB) crystal. *Advanced Solid State Lasers*, 1999(Optical Society of America, 1999), p. WB11.
- [33] N. Umemura, H. Nakao, H. Furuya, M. Yoshimura, Y. Mori, T Sasaki, K. Yoshida and K. Kato. 90° phase-matching properties of $\text{YCa}_4\text{O}(\text{BO}_3)_3$ and $\text{Gd}_x\text{Y}_{1-x}\text{Ca}_4\text{O}(\text{BO}_3)_3$. *Japanese Journal of Applied Physics* 40(1): 596-600, 2001.
- [34] M. V. Pack, D. J. Armstrong, A. V. Smith, G. Aka, B. Ferrand, and D. Pelenc. Measurements of the chi (2) tensor of $\text{GdCa}_4\text{O}(\text{BO}_3)_3$ and $\text{YCa}_4\text{O}(\text{BO}_3)_3$ crystals. *JOSA. B*, 22(2): 417-425, 2005.
- [35] E. Boursier, P. Segongds, B. Boulanger, C. Felix, J. Debray, D. Jegouso, B.Menaert, D.Roshchupkin, and I. Shoji. Phase-matching directions, refined Sellmeier equations, and second-order nonlinear coefficient of the infrared Langatate crystal $\text{La}_3\text{Ga}_{5.5}\text{Ta}_{0.5}\text{O}_{14}$. *Opt. Letters* 39(13): 4033-4036, 2014.
- [36] E. Boursier, G. M. Archipovaite, J. C. Delagnes, S. Petit, G. Ernotte, P. Lassonde, P. Segongds, B. Boulanger, Y. Petit, F. Legare, D. Roshchupkin, and E. Cormier. Study of middle infrared difference frequency generation using a femtosecond laser source in LGT. *Opt. Letters* 42(18): 3698-3701, 2017.
- [37] D. Z. Lu, T. X. Xu, H. H. Yu, Q. Fu, H. J. Zhang, P. Segonds, B. Boulanger, X. Y. Zhang, and J. Y. Wang. Acentric langanite $\text{La}_3\text{Ga}_{5.5}\text{Nb}_{0.5}\text{O}_{14}$ crystal: a new nonlinear crystal for the generation of mid-infrared parametric light. *Opt. Express* 24(16): 17603-17615, 2016.

- [38] J. Stade, L. Bohaty, M. Hengst, and R. B. Heimann. Electro-optic, piezoelectric and dielectric properties of Languisite ($\text{La}_3\text{Ga}_5\text{SiO}_{14}$), Langanite ($\text{La}_3\text{Ga}_{5.5}\text{Nb}_{0.5}\text{O}_{14}$) and Langataite ($\text{La}_3\text{Ga}_{5.5}\text{Ta}_{0.5}\text{O}_{14}$). *Cryst. Res. Technol* 37(10): 1113-1120, 2002.
- [39] I. Shoji, T. Kondo, A. Kitamoto, M. Shirane, and R. Ito. Absolute scale of second-order nonlinear-optical coefficients. *Journal of the Optical Society of America B*, 14(9): 2268-2294, 1997.
- [40] D. Phanon and I. Gautier-Luneau. Promising Material for Infrared Nonlinear Optics: NaI_3O_8 Salt Containing an Octaoxotriiodate (V) Anion Formed from Condensation of $[\text{IO}_3]^-$ Ions. *Angew. Chem. Int. ED* 46(44): 8488-8491, 2007.
- [41] X. Xu, C. L. Hu, B. X. Li, B. P. Yang and J. G. Mao. $\alpha\text{-AgI}_3\text{O}_8$ and $\beta\text{-AgI}_3\text{O}_8$ with Large SHG Responses: Polymerization of IO_3 Groups into the I_3O_8 Polyiodate Anion. *Chem. Mater*, 26(10): 3219-3230, 2014.
- [42] F. Guo, D. Z. Lu, P. Segonds, J. Debray, H. H. Yu, H. J. Zhang, J. Y. Wang, and B. Boulanger. Phase-matching properties and refined Sellmeier equations of $\text{La}_3\text{Ga}_{5.5}\text{Nb}_{0.5}\text{O}_{14}$. *Optical Materials Express*, 8(4): 858-864, 2018.
- [43] Feng Guo, Patricia Segonds, Julien Zaccaro, Jérôme Debray, Isabelle Gautier-Luneau, and Benoît Boulanger. Frequency conversion in the acentric tetragonal nonlinear crystal NaI_3O_8 . *Optical Materials Express*, 7(5): 1672-1678, 2017.
- [44] J. Yao, D. Mei, L. Bai, Z. Lin, W. Yin, P. Fu, and Y. Wu. BaGa_4Se_7 : A new congruentmelting IR nonlinear optical material. *Inorganic Chemistry*, 49(20):9212–9216, 2010.
- [45] E. Boursier, P. Segonds, B. Ménaert, V. Badikov, V. Panyutin, D. Badikov, V. Petrov, and B. Boulanger. Phase-matching directions and refined Sellmeier equations of the monoclinic acentric crystal BaGa_4Se_7 . *Optics Letters*, 41(12):2731–2734, 2016.
- [46] E. Boursier, P. Segonds, J. Debray, P. L. Inácio, V. Panyutin, V. Badikov, D.

- Badikov, V. Petrov, and B. Boulanger. Angle noncritical phase-matched second-harmonic generation in the monoclinic crystal BaGa_4Se_7 . *Optics Letters*, 40(20):4591–4594, 2015.
- [47] V. Badikov, D. Badikov, G. Shevyrdyaeva, A. Tyazhev, G. Marchev, V. Panyutin, V. Petrov, and A. Kwasniewski. Phase-matching properties of BaGa_4S_7 and BaGa_4Se_7 : Wide-bandgap nonlinear crystals for the mid-infrared. *Physica Status Solidi - Rapid Research Letters*, 5(1):31–33, 2011.
- [48] F. Yang, J. Yao, H. Xu, F. Zhang, N. Zhai, Z. Lin, N. Zong, Q. Peng, J. Zhang, D. Cui, Y. Wu, C. Chen, and Z. Xu. Mid infrared Optical Parametric Amplifier with 6.4–11 μm Range Based on BaGa_4Se_7 . *IEEE Photonics Technology Letters*, 27(10):1100–1103, 2015.
- [49] J. Yao, W. Yin, K. Feng, X. Li, D. Mei, Q. Lu, Y. Ni, Z. Zhang, Z. Hu, and Y. Wu. Growth and characterization of BaGa_4Se_7 crystal. *Journal of Crystal Growth*, 346(1):1–4, 2012.
- [50] F. Yang, J. Yao, H. Xu, K. Feng, W. Yin, F. Li, J. Yang, S. Du, Q. Peng, J. Zhang, D. Cui, Y. Wu, C. Chen, and Z. Xu. High efficiency and high peak power picosecond mid-infrared optical parametric amplifier based on BaGa_4Se_7 crystal. *Optics Letters*, 38(19):3903–3905, 2013.
- [51] X. Zhang, J. Yao, W. Yin, Y. Zhu, Y. Wu, and C. Chen. Determination of the nonlinear optical coefficients of the BaGa_4Se_7 crystal. *Optics Express*, 23(1):552–558, 2015.

Appendix

- F. Guo, P. Segonds, B. Ménaert, J. Debray, G. Aka, P. Loiseau, and B. Boulanger, “*Dielectric frame, Sellmeier equations, and phase-matching properties of the monoclinic acentric crystal $GdCa_4O(BO_3)_3$* ” Optics Letters 41 (22), 5290 (2016);
- F. Guo, P. Segonds, J. Zaccaro, J. Debray, I. Gautier-Luneau, and B. Boulanger, “*Frequency conversion in the acentric tetragonal nonlinear crystal NaI_3O_8* ”, Optical Materials Express 7(5), 1672 (2017);
- F. Guo, D. Lu, P. Segonds, J. Debray, H. Yu, H. Zhang, J. Wang, and B. Boulanger, “*Phase-matching properties and refined Sellmeier equations of $La_3Ga_{5.5}Nb_{0.5}O_{14}$* ”, Optical Materials Express 8(4), 858 (2018).

Optics Letters

Dielectric frame, Sellmeier equations, and phase-matching properties of the monoclinic acentric crystal $\text{GdCa}_4\text{O}(\text{BO}_3)_3$

FENG GUO,^{1,2} PATRICIA SEGONDS,^{1,2,*} BERTRAND MÉNAERT,^{1,2} JÉRÔME DEBRAY,^{1,2} GERARD AKA,³ PASCAL LOISEAU,³ AND BENOÎT BOULANGER^{1,2}

¹Université Grenoble Alpes, Institut Néel, F38402 Grenoble Cedex 9, France

²CNRS, Institut Néel, F38402 Grenoble Cedex 9, France

³Chimie ParisTech, PSL Research University, CNRS, Institut de Recherche de Chimie Paris, 75005 Paris, France

*Corresponding author: patricia.segons@neel.cnrs.fr

Received 28 September 2016; revised 18 October 2016; accepted 18 October 2016; posted 19 October 2016 (Doc. ID 277730); published 10 November 2016

We directly measured the phase-matching properties of the biaxial $\text{GdCa}_4\text{O}(\text{BO}_3)_3$ (GdCOB) crystal using the sphere method. We studied second-harmonic generation and difference frequency generation in two principal planes of the crystal. All these data allowed us to refine the Sellmeier equations of the three principal refractive indices. These equations are valid over the entire transparency range of GdCOB and then could be used to calculate the tuning curves of infrared optical parametric generation. © 2016 Optical Society of America

OCIS codes: (190.2620) Harmonic generation and mixing; (190.4400) Nonlinear optics, materials; (190.4975) Parametric processes.

<http://dx.doi.org/10.1364/OL.41.005290>

The generation of a broadband supercontinuum extending between 1.5 and 3.5 μm from frequency downconversion still requests new potential nonlinear crystals when pumped by the Ti:sapphire laser around 0.8 μm . We identified the calcium-rare-earth oxoborate crystal $\text{GdCa}_4\text{O}(\text{BO}_3)_3$ (GdCOB) as a real alternative in this context.

Large GdCOB samples with a very good optical quality can be grown using the Czochralski pulling technique [1]. GdCOB is transparent from 0.32 to 2.7 μm , and its highest nonlinear coefficient which can be excited in the (x, z) principal dielectric plane, was found equal to that of LiB_3O_5 , twice that of KD_2PO_4 , and half that of KTiOPO_4 nonlinear crystals [1]. Furthermore, the damage threshold measured at 0.532 μm using the second-harmonic beam of a 7 ns (FWHM) and a 10 Hz repetition rate Nd:YAG laser is higher than 1 GW/cm^2 [1]. Up to now, the main interest for this crystal has been essentially devoted to the second-harmonic generation (SHG) from a fundamental beam around 1 μm [2], in particular, by self-doubling using GdCOB doped with Nd^{3+} or Yb^{3+} [3]. A thermal direction has been also predicted [4].

GdCOB belongs to the monoclinic point group m . Then the orthonormal optical frame (x, y, z) does not correspond to the crystallographic frame (a, b, c) [5]. The b -axis is perpendicular to the mirror plane m where the a - and c -axes are located, the angle between these two axes being $(a, c) = 101.26^\circ$ [1]. The y -axis is taken parallel to the b -axis by convention, so that the x - and z -axes lie in the mirror plane m with the following orientation: $(a, z) = 26^\circ$, $(c, x) = 15^\circ$ when measured at 0.6328 μm [1], knowing that for any monoclinic crystal the orientation of the dielectric frame may rotate as a function of the wavelength [6]. Since GdCOB is monoclinic, it belongs to the biaxial optical class. The three principal refractive indices n_x , n_y , and n_z have been measured between 0.35 and 1.12 μm by using the minimum deviation technique in two oriented prisms [7], and improved by the SHG and sum frequency generation experiments performed in the visible and near infrared ranges [8]. It was shown that it is a positive biaxial crystal, i.e., $n_x < n_y < n_z$, and the phase-matching directions of SHG were calculated in the three principal planes of GdCOB [7,8]. Under the Kleinmann assumption, the magnitude and sign of the six non-zero and independent coefficients of the second-order electric susceptibility tensor had been determined from measurements using a separated beam method [9].

In this Letter, the crystal of GdCOB was studied using the sphere method [10]. We showed that the dielectric frame (x, y, z) does not rotate as a function of wavelength. We also performed the measurement of the full SHG and difference-frequency generation (DFG) phase-matching properties in the (x, z) and (y, z) planes. These angular data allowed us to refine the Sellmeier equations of GdCOB from which we calculated the tuning curves, in particular, for the generation of a super continuum in the infrared.

The crystal of GdCOB was cut and polished as a sphere with a diameter of 5.55 mm and an asphericity below 1%. It was stuck on a goniometric head along the $(b||y)$ -axis, as shown in Fig. 1. The precision of the crystallographic orientation

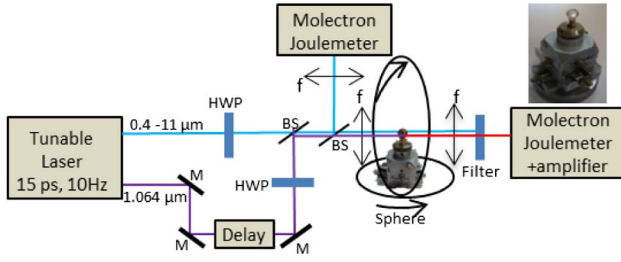


Fig. 1. Experimental setup used to measure directly the dielectric frame orientation and the phase-matching angles as a function of wavelength; the sphere of GdCOB is stuck on a goniometric head.

was better than 0.5° , thanks to the use of the x-ray backscattered Laue method. Then the sphere was placed at the center of a Euler circle in order to be rotated around the y -axis in any direction of the (x, z) plane.

The input beam was emitted by a 15 ps (FWHM) and a 10 Hz repetition rate optical parametric generator provided by Excel Technology and Light Conversion companies. The OPG is pumped at $1.064 \mu\text{m}$ and tunable between 0.4 and $2.4 \mu\text{m}$. The DFG between the pump and idler beams in an AgGaS_2 crystal extends the emission range up to $11 \mu\text{m}$. The wavelength was continuously controlled by an HR 4000 spectrometer and a NIRquest 512 Ocean Optics spectrometer, with an accuracy of around $\pm 1 \text{ nm}$.

A 75 mm focusing lens was placed at the entrance side of the sphere, as shown in Fig. 1, in order to ensure the normal incidence and quasi-parallel propagation along any diameter of the sphere [11].

For the determination of the orientation of the dielectric frame, the propagation was first achieved along the z -axis, where there is no double refraction effect. Thus, in that condition, a single output spot was observed. The observation of the spot was done using a CCD camera and a mid-IR sensor card with sensitivity that provided a spectral range from 0.4 to $1.75 \mu\text{m}$. First, we found in GdCOB that the spot remains at the same angle, which means that there is no rotation of the dielectric frame over this wavelength range and, second, we determined that the angle between the a - and z -axes is $(a, z) = 26^\circ \pm 0.5^\circ$, as shown in Fig. 2. We expect such a constant value at higher wavelengths.

According to the crystal symmetry of GdCOB and, by using previously published Sellmeier equations [7,8], we found that all possible quadratic processes that can be phase matched in

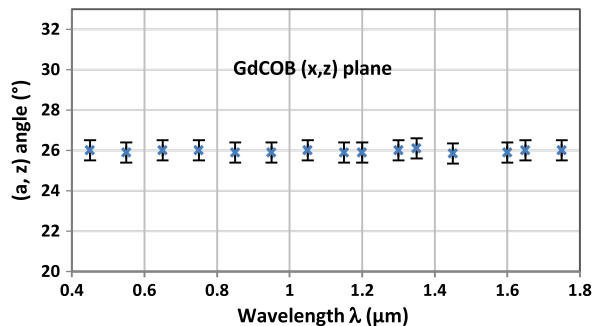


Fig. 2. Variation of the angle between the crystallographic and dielectric frames as a function of the wavelength.

the (x, z) plane with non-zero effective coefficients are type I SHG ($1/\lambda_{2\omega}^e = 1/\lambda_{\omega}^o + 1/\lambda_{\omega}^o$) and type II DFG ($1/\lambda_i^o = 1/\lambda_p^e - 1/\lambda_s^e$). In the (x, y) plane, they are type I SHG ($1/\lambda_{2\omega}^o = 1/\lambda_{\omega}^e + 1/\lambda_{\omega}^e$) and type II SHG ($1/\lambda_{2\omega}^o = 1/\lambda_{\omega}^e + 1/\lambda_{\omega}^o$). Superscripts o and e stand for the ordinary and extraordinary waves, respectively. λ_{ω}^k and $\lambda_{2\omega}^k$ (with k being o or e) are the fundamental and second-harmonic wavelengths, respectively. λ_p^k and λ_s^k are the pump and signal input wavelengths, and λ_i^k is the idler wavelength following the relation of order: $\lambda_p^k < \lambda_s^k \leq \lambda_i^k$.

The corresponding phase-matching conditions were studied by using the experimental setup shown in Fig. 1. The GdCOB sphere was stuck successively along the y - and z -axes to access the (x, z) and (x, y) principal planes, respectively. Only one tunable incoming beam is necessary for the SHG experiments, while two beams must be used for DFG. In the latter case, a delay line built with mirrors M was necessary to achieve a temporal overlap, as shown in Fig. 1. The input beams were linearly polarized, and different achromatic half-wave plates were used to change their polarization directions according to the different types of phase matching (see Fig. 1). The energies of the tunable incoming beams were simultaneously measured using a J4-09 Molelectron pyroelectric joulemeter with a beam splitter and a CaF_2 lens with a focal length of 50 mm . A Glan Taylor polarizer or filter allowed us to remove the input beams after the crystal, so that only the generated beams were measured. We used a J3-05 Molelectron joulemeter, combined with a PEM531 amplifier. The phase-matching angles were directly read on the Euler circle with an accuracy of about $\pm 0.5^\circ$ by detecting the maximum of the peak of conversion efficiency.

Figures 3 and 4 show type I SHG and type II DFG phase-matching curves recorded in the (x, z) plane of GdCOB. Types I and II SHG in the (x, y) plane are given in Figs. 5 and 6. Figures 3–6 also show black and green dashed lines corresponding to phase-matching curves calculated from previously published Sellmeier equations [7,8].

The wavelength range of solicitation of the three principal refractive indices is shown in Fig. 7: it corresponds to the range over which the phase-matching angles were measured. Note that even if the SHG measurements were performed at fundamental wavelengths up to $3.4 \mu\text{m}$, which is above the infrared cutoff of GdCOB, we did not observe any perturbation of the tuning curves.

We refined the Sellmeier equations of GdCOB by the simultaneous fit of all our experimental data. We tried different

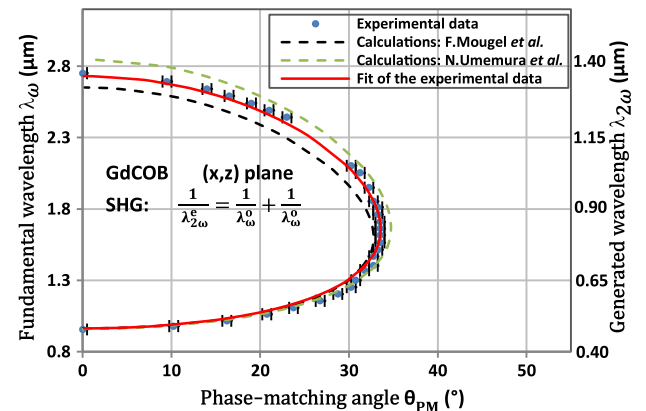


Fig. 3. Type I SHG tuning curve in the (x, z) plane of GdCOB.

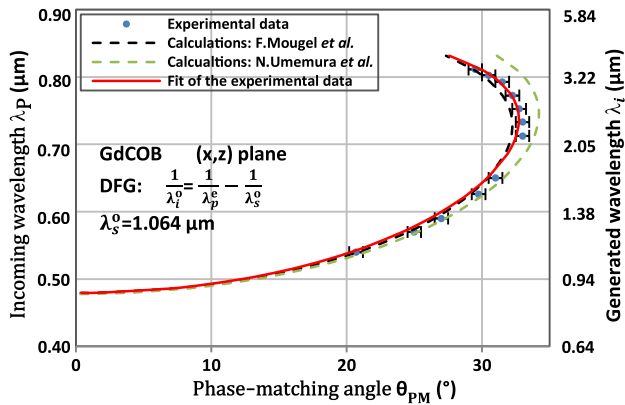


Fig. 4. Type II DFG tuning curve in the (x, z) plane of GdCOB.

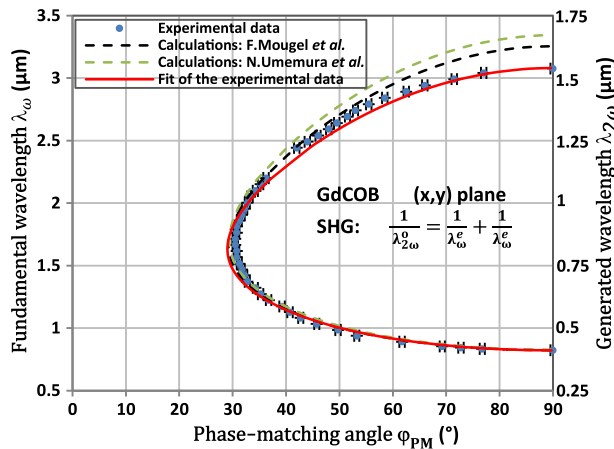


Fig. 5. Type I SHG tuning curve in the (x, y) plane of GdCOB.

dispersion equations using the Levenberg–Marquardt algorithm encoded with Matlab. The best result was obtained with a dual oscillator model, i.e.,

$$n_j^2(\lambda) = A_j + \frac{B_j \lambda^2}{\lambda^2 - C_j} + \frac{D_j \lambda^2}{\lambda^2 - E_j}, \quad (1)$$

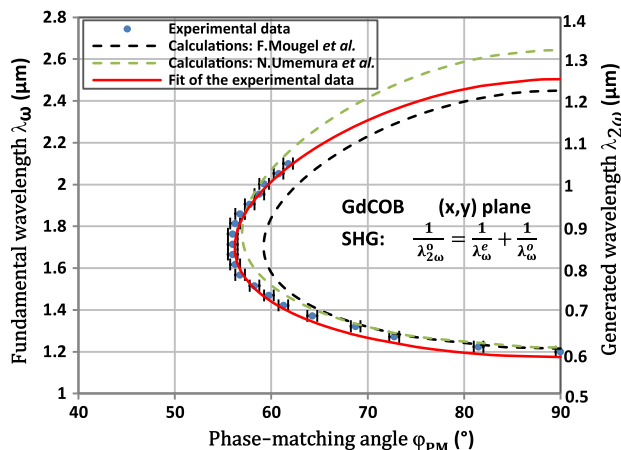


Fig. 6. Type II SHG tuning curve in the (x, y) plane of GdCOB.

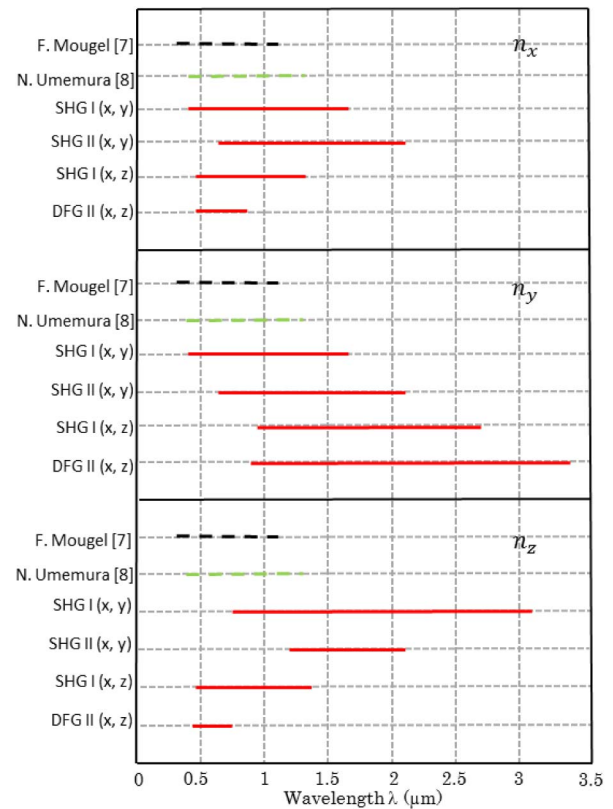


Fig. 7. Wavelength range of solicitation of the three principal refractive indices of GdCOB when determined using the sphere method (red continuous lines), the prism method from [7] (black dashed lines), and the phase-matched method from [8] (green dashed lines).

where λ is in μm , j stands for x, y or z ; and the corresponding dispersive coefficients A_j, B_j, C_j, D_j , and E_j are given in Table 1. Note that the Sellmeier coefficients follow the same relation of order as the corresponding refractive indices, i.e., $M_x < M_y < M_z$ with $M = A, B, C, D$, or E , which is relevant from the physical point of view.

The red continuous lines in Figs. 3–6 correspond to the phase-matching curves calculated with our refined Sellmeier equations. They clearly highlight a much better agreement with the experimental measurements, especially at long wavelengths, compared with calculations based on the previously published Sellmeier equations [7,8]. Such a discrepancy can be explained by two reasons. First, the precision of our angular measurements is around $\pm 0.5^\circ$, leading to a relative precision of the principal refractive indices $\Delta n_i/n_i$ better than 10^{-4} .

Table 1. Refined Sellmeier Coefficients of the Three Principal Refractive Indices n_x, n_y , and n_z of GdCOB Corresponding to Eq. (1)

Sellmeier Coefficients	$j = x$	$j = y$	$j = z$
A_j	2.1685	2.2572	2.2587
B_j	0.6163	0.6169	0.6482
C_j	0.0341	0.0383	0.0409
D_j	0.5773	1.3245	1.8922
E_j	107.0991	115.7501	148.8075

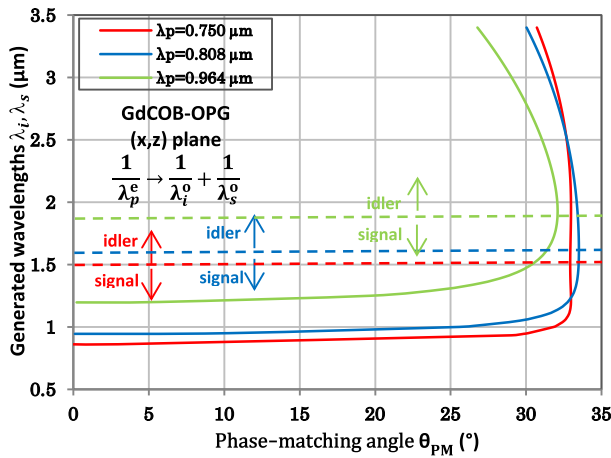


Fig. 8. Calculated OPG tuning curves in the (x, z) plane of GdCOB with pump wavelengths λ_p of 0.750, 0.808, and 0.964 μm . λ_i and λ_s are the idler and signal wavelengths, respectively.

(where i represents x , y , and z), while $\Delta n_i/n_i$ was of the order of 10^{-3} using the prism method. Second, the wavelength range of measurement is much wider in our case.

Using our refined Sellmeier equations, we identified GdCOB as a promising crystal for the optical parametric generation (OPG) of a supercontinuum pumped by the Ti:sapphire laser. The phase-matching type corresponds to that of type II DFG, i.e., $1/\lambda_p^e \rightarrow 1/\lambda_i^o + 1/\lambda_s^o$, and the propagation has to be performed in the (x, z) plane where the figure of merit $(d_{\text{eff}}^{xz})^2/n^e(\lambda_p)n^o(\lambda_i)n^o(\lambda_s)$ is maximal, of about $0.1 \text{ pm}^2/\text{V}^2$ using data from [9,12]. Figure 8 shows three tuning curves corresponding to three wavelengths well spread over the Ti:sapphire emission band: $\lambda_p = 0.750$, 0.808, and 0.964 μm . The broadest spectrum is 1–3.4 μm , corresponding to $\lambda_p = 0.750 \mu\text{m}$, the GdCOB crystal being cut at $(\theta_{\text{PM}} = 32.5^\circ, \varphi_{\text{PM}} = 0^\circ)$.

In conclusion, we reported for the first time, to the best of our knowledge, the full phase-matching tuning curves of SHG and DFG in the calcium-rare-earth oxoborate crystal GdCOB. We also demonstrated that the dielectric frame does not rotate as a function of wavelength. The measured phase-matching

angles can be used *per se* for designing any parametric devices, but they also allowed the Sellmeier equations to be refined. Based on these equations, we showed that a GdCOB-OPG could generate a super continuum extending from 1 to 3.4 μm when pumped at 0.750 μm . These good nonlinear optical properties of GdCOB are completed by a very high damage threshold, which is two orders of magnitude higher than that of potassium titanyl phosphate (KTP) [13].

Acknowledgment. The author thanks the China Scholarship Council (CSC) for the financial support of Feng Guo.

REFERENCES

- G. Aka, A. Kahn-Harari, F. Mougél, D. Vivien, F. Salin, P. Coguelin, P. Colin, D. Pelenc, and J. P. Damelet, *J. Opt. Soc. Am. B* **14**, 2238 (1997).
- Z. C. Wu and W. M. Liu, *Laser Phys.* **21**, 2049 (2011).
- H. H. Yu, N. Zong, Z. B. Pan, H. J. Zhang, J. Y. Wang, Z. P. Wang, and Z. Y. Xu, *Opt. Lett.* **36**, 3852 (2011).
- P. Loiko, X. Mateos, Y. C. Wang, Z. B. Pan, K. Yumashev, H. J. Zhang, U. Griebner, and V. Petrov, *Opt. Mater. Express* **5**, 1089 (2015).
- Y. Petit, S. Joly, P. Segonds, and B. Boulanger, *Laser Photon. Rev.* **7**, 920 (2013).
- C. Traum, P. L. Inacio, C. Felix, P. Segonds, A. Pena, J. Debray, B. Boulanger, Y. Petit, D. Rytz, G. Montemezzani, P. Goldner, and A. Ferrier, *Opt. Mater. Express* **4**, 57 (2014).
- F. Mougél, G. Aka, F. Salin, D. Pelenc, B. Ferrand, A. Kahn-Harari, and D. Vivien, in *Advanced Solid State Lasers* (Optical Society of America, 1999), paper WB11.
- N. Umemura, H. Nakao, H. Furuya, M. Yoshimura, Y. Mori, T. Sasaki, K. Yoshida, and K. Kato, *Jpn. J. Appl. Phys.* **40**, 596 (2001).
- M. V. Pack, D. J. Armstrong, A. V. Smith, G. Aka, B. Ferrand, and D. Pelenc, *J. Opt. Soc. Am. B* **22**, 417 (2005).
- G. Marnier and B. Boulanger, *Opt. Commun.* **72**, 139 (1989).
- J. P. Feve, B. Boulanger, O. Pacaud, I. Rousseau, B. Menaert, G. Marnier, P. Villeval, C. Bonnin, and G. M. Loiacono, *J. Opt. Soc. Am. B* **17**, 775 (2000).
- B. Boulanger and J. Zyss, in *International Tables for Crystallography*, A. Authier, ed., Vol. D of Physical Properties of Crystals (Academic, 2004), pp. 178–219.
- S. Zhang, Z. Cheng, J. Lu, G. Li, J. Lu, Z. Shao, and H. Chen, *J. Cryst. Growth* **205**, 453 (1999).

Frequency conversion in the acentric tetragonal nonlinear crystal NaI_3O_8

FENG GUO,^{1,2} PATRICIA SEGONDS,^{1,2} JULIEN ZACCARO,^{1,2} JÉRÔME DEBRAY,^{1,2} ISABELLE GAUTIER-LUNEAU,^{1,2} AND BENOÎT BOULANGER^{1,2,*}

¹Université Grenoble Alpes, Institut Néel, F38402 Grenoble Cedex 9, France

²CNRS, Institut Néel, F38402 Grenoble Cedex 9, France

*benoit.boulanger@neel.cnrs.fr

Abstract: We performed the first study of phase-matched second harmonic generation and difference frequency generation in the acentric nonlinear crystal NaI_3O_8 . By fitting all the recorded phase-matching tuning curves, we determined the Sellmeier equations describing the wavelength dispersion of the ordinary and extraordinary principal refractive indices. We also measured the absolute value of the quadratic nonlinear coefficients and we calculated the conditions of supercontinuum generation in NaI_3O_8 .

© 2017 Optical Society of America

OCIS codes: (190.2620) Harmonic generation and mixing; (190.4400) Nonlinear optics, materials; (190.4975) Parametric processes.

References and links

1. D. Phanon and I. Gautier-Luneau, "Promising material for infrared nonlinear optics: NaI_3O_8 salt containing an octaoxotriiodate(V) anion formed from condensation of $[\text{IO}_3^-]$ ions," *Angew. Chem. Int. Ed. Engl.* **46**(44), 8488–8491 (2007).
2. X. Xu, C. L. Hu, B. X. Li, B. P. Yang, and J. G. Mao, " $\alpha\text{-AgI}_3\text{O}_8$ and $\beta\text{-AgI}_3\text{O}_8$ with large SHG responses: polymerization of IO_3 groups into the I_3O_8 polyiodate anion," *Chem. Mater.* **26**(10), 3219–3230 (2014).
3. Y. Guillion, B. Ménaert, J. P. Fève, P. Segonds, J. Douady, B. Boulanger, and O. Pacaud, "Crystal growth and refined Sellmeier equations over the complete transparency range of RbTiOPO_4 ," *Opt. Mater.* **22**(2), 155–162 (2003).
4. I. Shoji, T. Kondo, A. Kitamoto, M. Shirane, and R. Ito, "Absolute scale of second-order nonlinear-optical coefficients," *J. Opt. Soc. Am. B* **14**(9), 2268–2294 (1997).
5. B. Boulanger and J. Zyss, in *International Tables for Crystallography*, A. Authier, ed., Vol. D of Physical Properties of Crystals (Kluwer Academic, 2004), pp. 178–219.
6. B. Boulanger, J. P. Fève, G. Marnier, B. Ménaert, X. Cabriol, P. Villeval, and C. Bonnin, "Relative sign and absolute magnitude of $d(2)$ nonlinear coefficients of KTP from second-harmonic-generation measurements," *J. Opt. Soc. Am. B* **11**(5), 750–757 (1994).
7. R. C. Miller, "Optical second harmonic generation in piezoelectric crystals," *Appl. Phys. Lett.* **5**(1), 17–19 (1964).

1. Introduction

In 2007, we synthesized and studied the crystal structure of the new acentric crystal NaI_3O_8 [1]. Three years later, another group showed that this material is a negative uniaxial crystal with potential nonlinear optical properties. They performed powder second harmonic generation (SHG) measurements and calculations based on the density functional theory (DFT) [2]. Recent advances in crystal growth allowed us to get single crystals of very high quality suited for the first exhaustive study of linear and nonlinear optical properties described in the present letter. We recorded the transmission spectra in polarized light and determined the damage threshold in NaI_3O_8 slabs polished to optical quality. We directly measured phase-matching tuning curves of SHG and difference frequency generation (DFG) by using a method where NaI_3O_8 was cut as a cylinder polished on its curved surface [3]. From these experimental data we determined accurate Sellmeier equations describing the dispersion of the ordinary and extraordinary principal refractive indices, n_o and n_e ($n_o > n_e$), as a function of the wavelength. We also determined the absolute values of the two independent nonlinear coefficients d_{14} and d_{15} using a phase-matching technique [4].

2. Crystal growth, transmission spectra and damage threshold

NaI_3O_8 single crystals were grown by slow evaporation of Nitric Acid aqueous solutions (7M) at fixed temperature ranging between 60 and 70 °C. We obtained samples of several millimeter dimensions as the one shown in the insert of Fig. 1(a). While NaI_3O_8 displays a significant solubility in acidic solutions of lower molarity, such solutions were proved to be unstable toward the reduction of the iodate species into iodine. The later gets incorporated in the growing crystals giving them a yellow tint. Since NaI_3O_8 belongs to the $S4(\bar{4})$ tetragonal point group, its crystallographic frame (a , b , c) is orthonormal and fully coincides with the dielectric frame (x , y , z) [1, 2].

The transmission spectra depicted in Fig. 1(a) were recorded in polarized light through a 3-mm-thick slab. The two faces were cut perpendicularly to the x -axis, polished but uncoated. The linear polarization of light oriented successively perpendicularly and collinear with the z -axis, led to the ordinary and extraordinary transmission coefficients respectively. We used a Perkin-Elmer Lambda 900 spectrometer to record spectra as a function of the wavelength between 0.175 and 3.300 μm , and a Bruker FT-IR above 3.3 μm . Figure 1(a) shows that NaI_3O_8 is transparent between 0.32 and 6 μm despite strong absorption bands above 4 μm .

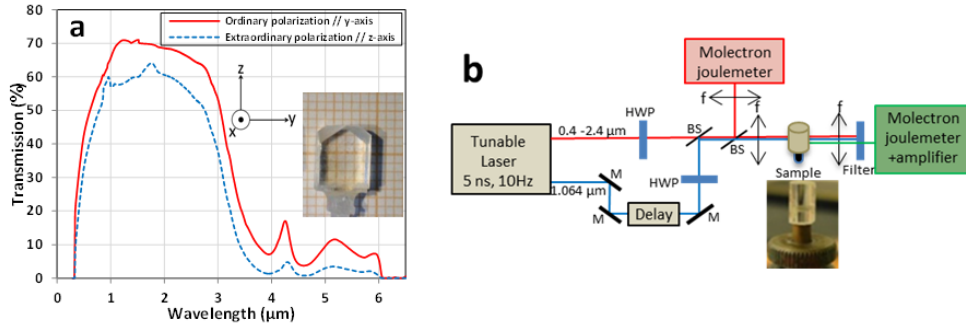


Fig. 1. NaI_3O_8 : (a) Transmission spectra of the 3-mm-thick slab shown in insert; (b) Setup used for phase-matching measurements in the 4.13-mm-cylinder shown in insert.

We determined the surface damage threshold of NaI_3O_8 compared with that of KTiOPO_4 (KTP). The two slabs were illuminated by a 1.064- μm laser with 5-ns FWHM, 10-Hz repetition rate and 30- μm beam waist radius. NaI_3O_8 was damaged at an input energy of 140 μJ , corresponding to a peak power density of 0.79 GW/cm^2 . It was only 5 times lower than the damage threshold in KTP, which has been observed at 760 μJ *i.e.* 4.29 GW/cm^2 .

3. Phase-matching properties, Sellmeier equations and nonlinear coefficients

Under Kleinman symmetry, the second-order electric susceptibility tensor of the NaI_3O_8 crystal has two independent nonzero coefficients, *i.e.* $d_{xyz} = d_{xzy} = d_{yxz} = d_{yzx} = d_{zxy} = d_{zyx} (= d_{14})$; $d_{xxz} = d_{xxz} = d_{xxz} = -d_{yzy} = -d_{yyz} = -d_{zyy} (= d_{15})$, where d_{14} and d_{15} stand for the contracted notation [5]. The five following types of SHG and DFG processes can be phase-matched with a nonzero effective coefficient identically in the xz - and yz -plane: type I SHG ($1/\lambda_\omega^o + 1/\lambda_\omega^e = 1/\lambda_{2\omega}^e$), type II SHG ($1/\lambda_\omega^o + 1/\lambda_\omega^e = 1/\lambda_{2\omega}^o$), type I DFG ($1/\lambda_p^e - 1/\lambda_s^e = 1/\lambda_i^o$), type II DFG ($1/\lambda_p^e - 1/\lambda_s^o = 1/\lambda_i^o$) and type III DFG ($1/\lambda_p^e - 1/\lambda_s^o = 1/\lambda_i^e$). Superscripts o and e stand for the ordinary and extraordinary waves, respectively. λ_ω^k and $\lambda_{2\omega}^k$ (with k being o or e) are the fundamental and second harmonic wavelengths, respectively. λ_p^k and λ_s^k are the pump and signal input wavelengths, and λ_i^k is the idler wavelength generated by DFG, with the following relation of order: $\lambda_p^k < \lambda_s^k \leq \lambda_i^k$.

The corresponding tuning curves were directly measured by using a method where the NaI_3O_8 crystal was cut as a cylinder with a diameter $D = 4.13$ mm and an acylindricity $\Delta D/D$ below 1%. The curved surface was polished to optical quality as shown in the insert of Fig. 1(b). We previously used this sample shape to study many nonlinear crystals, as RTP for example [3].

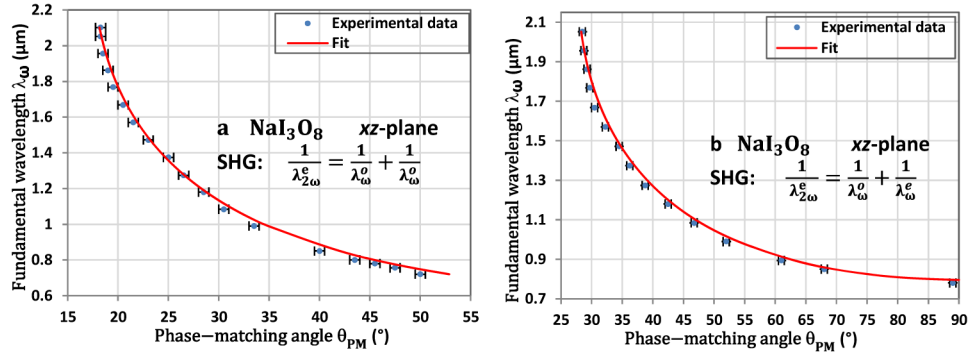


Fig. 2. Measured (dots) and fitted (line) (a) Type I- and (b) type II- SHG tuning curves in NaI_3O_8 .

Using an X-ray backscattered Laue method, the cylinder was cut with its rotation axis oriented along the y-axis with a precision better than 0.5° . Then it was stuck on a goniometric head along this axis. When placed at the center of an Euler circle, the cylinder can rotate on it-self to access any direction of the xz -plane. Note that this plane is equivalent to yz -plane, since NaI_3O_8 belongs to the $S4(\bar{4})$ tetragonal point group. Using a focusing 100-mm-focal length lens properly placed, an incoming beam remains in normal incidence and propagates parallel to the diameter of the rotating cylinder as shown in Fig. 1(a) [3].

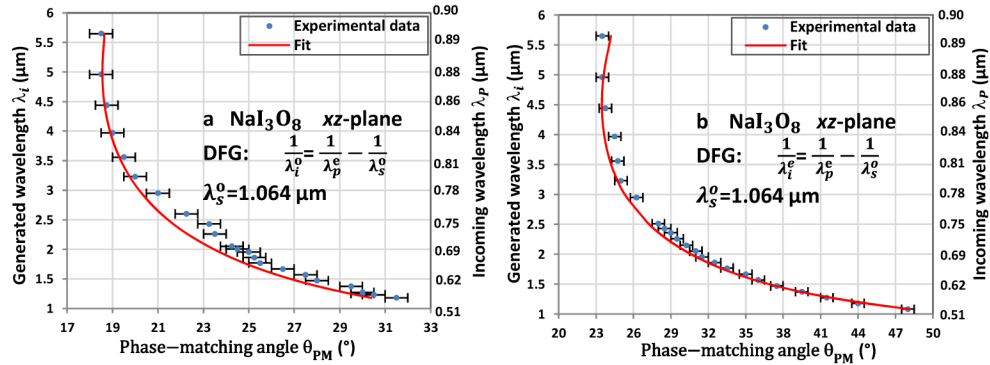


Fig. 3. Measured (dots) and fitted (line) (a) Type II- and (b) type III- DFG tuning curves in NaI_3O_8 .

One incoming tunable beam was necessary for SHG. It was emitted by a 5-ns (FWHM) and 10-Hz repetition rate optical parametric oscillator (OPO) from Continuum Company. The OPO was pumped at 1.064 μm and tunable between 0.4 μm and 2.4 μm . The OPO beam and part of the 1.064 - μm beam were collinearly combined for achieving DFG. They were put in spatial and temporal coincidence inside the cylinder using mirrors and the delay line shown in Fig. 1(b). All beams being linearly polarized, achromatic half-wave plates (HWP) provided their polarization rotation, in order to achieve the different types of phase-matching, i.e. type I, II and III. Input energies were measured at the entrance of the cylinder using a J4-09 Molelectron pyroelectric joulemeter coupled to a beam splitter and a 50-mm focal length CaF_2 lens. They were removed at the output of the cylinder by using a polarizer and a filter. Thus

only beams generated by SHG and DFG were measured on the J3-05 Molelectron joulemeter combined with a PEM531 amplifier. Phase-matching angles corresponding to maximum values of the conversion efficiency were directly read on the Euler circle with an accuracy of $\pm 0.5^\circ$. The corresponding phase-matching wavelengths were recorded with a precision of $\pm 1\text{nm}$ using a HR 4000 Ocean Optics spectrometer. Figures 2 show the measured types I and II SHG tuning curves, types II and III DFG being given in Figs. 3. For SHG, it was not possible to record phase-matching angles for fundamental wavelengths lower than $0.7\text{ }\mu\text{m}$ because the corresponding generated wavelengths were below the ultra-violet cut-off wavelength. Similarly, we did not study type I DFG tuning curve since the incoming tunable pump wavelength being below $0.5\text{ }\mu\text{m}$, it could damage the surface of the cylinder. The tuning curves of Figs. 2 and 3 indicate that NaI_3O_8 allows phase-matching conditions over its entire transparency range, which is also the spectral range of reliability of its two principal refractive indices. These data can be used directly to cut the crystal at a phase-matching angle corresponding to the targeted parametric process and phase-matching wavelength. But the combination of the simultaneous fit of all the phase-matching curves with the magnitude of the ordinary refractive index n_o at a given wavelength, can lead to the determination of the Sellmeier equations [3]. We used $n_o(\lambda = 0.671\text{ }\mu\text{m}) = 1.6$ that we determined from the direct measurement of a Brewster angle of 58° in the xy -plane of NaI_3O_8 cut as a slab, and the Levenberg-Marquardt algorithm encoded with Matlab. We tried different dispersion equations, the best result being obtained with the following dual oscillator model:

$$n_j^2(\lambda) = A_j + \frac{B_j\lambda^2}{\lambda^2 - C_j} + \frac{D_j\lambda^2}{\lambda^2 - E_j} \quad (1)$$

λ is in μm , and j stands for o or e . The Sellmeier coefficients A_j , B_j , C_j , D_j and E_j are given in Table 1. Since the precision of the measured phase-matching angles was of about $\pm 0.5^\circ$, the relative accuracy of the determined refractive indices $\Delta n_i / n_i$ is better than 10^{-4} . It is corroborated in Figs. 2 and 3 by the very good agreement between our data and calculations. On the contrary, the comparison of our refractive indices at $1.064\text{ }\mu\text{m}$ with calculations using the model of ref. [2] that is shown in Table 2 highlights a strong discrepancy. This feature is not so surprising since the modelling of the first order electric susceptibility is very complicated.

Table 1. Sellmeier Coefficients for the Two Principal Refractive Indices n_o and n_e of NaI_3O_8 .

Sellmeier coefficients	A_j	B_j	C_j	D_j	E_j
$j = o$	1.7953	0.7344	0.0182	0.5314	412.9779
$j = e$	1.6942	0.7101	0.0162	2.5841	375.2799

The following step was to determine the magnitude of the two independent nonlinear coefficients of NaI_3O_8 , d_{14} and d_{15} . For that purpose, we measured conversion efficiencies in NaI_3O_8 slabs cut at critical phase-matching angles for types I-SHG and type II-SHG, and for type II-SHG in KTP that was taken as a reference [4]. We chose all fundamental wavelengths as near as possible, to get rid of the experimental setup spectral response. With ρ^e as the spatial walk-off angle, the corresponding effective coefficients are in NaI_3O_8 [4,5]:

$$d_{\text{eff},I}^{\text{NaI}_3\text{O}_8} = -d_{15}^{\text{NaI}_3\text{O}_8}(\lambda_{2\omega}^{\text{PM}}) \sin[\theta_{\text{PM}} + \rho^e(\theta_{\text{PM}}, \lambda_{2\omega}^{\text{PM}})] \quad (2)$$

$$d_{\text{eff},II}^{\text{NaI}_3\text{O}_8} = -d_{14}^{\text{NaI}_3\text{O}_8}(\lambda_{2\omega}^{\text{PM}}) \left\{ \begin{aligned} &\sin[\theta_{\text{PM}} + \rho^e(\theta_{\text{PM}}, \lambda_{\omega}^{\text{PM}})] \cos[\theta_{\text{PM}} + \rho^e(\theta_{\text{PM}}, \lambda_{2\omega}^{\text{PM}})] \\ &+ \cos[\theta_{\text{PM}} + \rho^e(\theta_{\text{PM}}, \lambda_{\omega}^{\text{PM}})] \sin[\theta_{\text{PM}} + \rho^e(\theta_{\text{PM}}, \lambda_{2\omega}^{\text{PM}})] \end{aligned} \right\} \quad (3)$$

Using Eq. (1) and Tab. 2, we calculated the corresponding phase-matching and walk-off angles in NaI_3O_8 at the phase-matching wavelength $\lambda_{\omega}^{\text{PM}} = 1.064 \mu\text{m}$. We found for type I SHG that $\theta_{\text{PM}} = 32.1^\circ$ and $\rho^e(\theta_{\text{PM}}, \lambda_{\omega}^{\text{PM}}) = 1.38^\circ$; $\theta_{\text{PM}} = 49^\circ$, $\rho^e(\theta_{\text{PM}}, \lambda_{\omega}^{\text{PM}}) = 1.52^\circ$ and $\rho^e(\theta_{\text{PM}}, \lambda_{2\omega}^{\text{PM}}) = 1.51^\circ$ in the case of type II SHG. We chose type II SHG ($1/\lambda_{\omega}^e + 1/\lambda_{\omega}^o = 1/\lambda_{2\omega}^o$) in the xy -plane of KTP as a reference. The absolute value of the associated effective coefficient is $|d_{\text{eff}}^{\text{KTP}}| = 2.43 \text{ pm/V}$, the corresponding phase-matching and walk-off angles being $\varphi_{\text{PM}} = 23.1^\circ$, $\rho^e(\theta_{\text{PM}}, \lambda_{\omega}^{\text{PM}}) = 0.17^\circ$ and $\rho^e(\theta_{\text{PM}}, \lambda_{2\omega}^{\text{PM}}) = 0.29^\circ$ [6]. We cut two NaI_3O_8 slabs ($L_{\text{I}}^{\text{NaI}_3\text{O}_8} = 800 \mu\text{m}$, $L_{\text{II}}^{\text{NaI}_3\text{O}_8} = 680 \mu\text{m}$) and one KTP slab ($L^{\text{KTP}} = 800 \mu\text{m}$) at the phase-matching angles given above. We took such a small interacting length in order to avoid any spatial walk-off attenuation. Since the incoming fundamental beam was focused through a 100-mm focal length CaF_2 lens, the corresponding beam waist radius was around $w_0 = 60 \mu\text{m}$. It leads to a Rayleigh length $2xZ_R = 22 \text{ mm}$, which is much longer than the thickness of the slabs and ensures a parallel beam propagation. Types I and II SHG conversion efficiencies of NaI_3O_8 , recorded relatively to KTP as a function of the fundamental wavelength are shown in Fig. 4: $\eta_{\text{I}}^{\text{NaI}_3\text{O}_8}$ and $\eta_{\text{II}}^{\text{NaI}_3\text{O}_8}$ correspond to types I and II SHG conversion efficiencies of NaI_3O_8 respectively, and $\eta_{\text{II}}^{\text{KTP}}$ stands for type II SHG conversion efficiency of KTP.

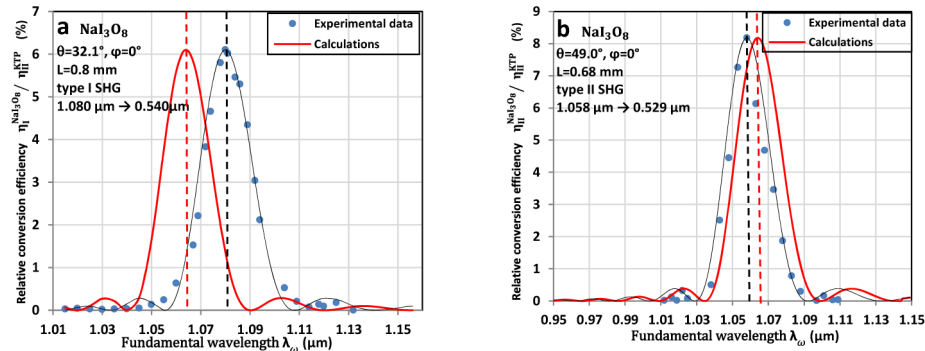


Fig. 4. Calculated (line) and measured (dots) conversion efficiencies in NaI_3O_8 of (a) type I SHG and (b) type II SHG as a function of the fundamental wavelength.

The absolute value of the effective nonlinear coefficient $d_{\text{eff}}^{\text{NaI}_3\text{O}_8}$ relatively to $d_{\text{eff}}^{\text{KTP}}$ of KTP can be determined from the maximum of each curve shown in Fig. 4 and by using:

$$(d_{\text{eff},I,II}^{\text{NaI}_3\text{O}_8})^2 = \frac{\eta_{\text{I,II}}^{\text{NaI}_3\text{O}_8}}{\eta_{\text{II}}^{\text{KTP}}} \frac{(L^{\text{KTP}})^2}{(L_{\text{I,II}}^{\text{NaI}_3\text{O}_8})^2} \frac{G_{\text{II}}^{\text{KTP}}}{G_{\text{I,II}}^{\text{NaI}_3\text{O}_8}} \frac{A_{\text{II}}^{\text{KTP}}}{A_{\text{I,II}}^{\text{NaI}_3\text{O}_8}} (d_{\text{eff}}^{\text{KTP}})^2 \quad (4)$$

With

$$A_I^{\text{NaI}_3\text{O}_8} = \frac{T_e^{\text{NaI}_3\text{O}_8}(\lambda_{2\omega}^{\text{PM}}, \theta_{\text{PM}})}{n_e^{\text{NaI}_3\text{O}_8}(\lambda_{2\omega}^{\text{PM}}, \theta_{\text{PM}})} \left[\frac{T_o^{\text{NaI}_3\text{O}_8}(\lambda_{\omega}^{\text{PM}})}{n_o^{\text{NaI}_3\text{O}_8}(\lambda_{\omega}^{\text{PM}})} \right]^2 \quad (5)$$

$$A_{II}^{NaI_3O_8} = \frac{T_e^{NaI_3O_8}(\lambda_{2\omega}^{PM}, \theta_{PM})}{n_e^{NaI_3O_8}(\lambda_{2\omega}^{PM}, \theta_{PM})} \frac{T_e^{NaI_3O_8}(\lambda_{\omega}^{PM}, \theta_{PM})}{n_e^{NaI_3O_8}(\lambda_{\omega}^{PM}, \theta_{PM})} \frac{T_o^{NaI_3O_8}(\lambda_{\omega}^{PM})}{n_o^{NaI_3O_8}(\lambda_{\omega}^{PM})} \quad (6)$$

$$A_{II}^{KTP} = \frac{T_o^{KTP}(\lambda_{2\omega}^{PM}, \varphi_{PM})}{n_o^{KTP}(\lambda_{2\omega}^{PM}, \varphi_{PM})} \frac{T_e^{KTP}(\lambda_{\omega}^{PM})}{n_e^{KTP}(\lambda_{\omega}^{PM})} \frac{T_o^{KTP}(\lambda_{\omega}^{PM}, \varphi_{PM})}{n_o^{KTP}(\lambda_{\omega}^{PM}, \varphi_{PM})} \quad (7)$$

$n_o^{NaI_3O_8}(\lambda_{\omega}^{PM})$ and $n_o^{KTP}(\lambda_{ao}^{PM}, \varphi_{PM})$ stand for the ordinary refractive indices of NaI_3O_8 and KTP respectively. $n_e^{NaI_3O_8}(\lambda_{ao}^{PM}, \theta_{PM})$ and $n_e^{KTP}(\lambda_{\omega}^{PM})$ are the extraordinary refractive indices. They are involved at the fundamental ($a = 1$) or second harmonic ($a = 2$) wavelengths, and at θ_{PM} or φ_{PM} phase-matching angles. T_o and T_e are the associated Fresnel coefficients. The spatial walk-off attenuations are negligible since we found: $G_I^{NaI_3O_8} = 0.999$ for type I SHG in NaI_3O_8 , $G_{II}^{NaI_3O_8} = 0.987$ for type II SHG, and $G_{II}^{KTP} = 0.999$ for type II SHG in KTP. The phase-matching wavelengths of NaI_3O_8 are $\lambda_{\omega}^{PM} = 1.080 \mu m$ for type I SHG and $\lambda_{\omega}^{PM} = 1.058 \mu m$ for type II SHG as shown in Figs. 4. They are slightly different from $1.064 \mu m$, showing the difficulty of cutting very thin oriented slabs. Note that they are just slightly different from the calculated ones using our Sellmeier Eq. (1) and Tab. 1, which give the very good order of magnitude reached with the equations from the present work. From the maximum value of the curves shown in Fig. 4 and using Eqs. (4)-(7), we found that $|d_{eff I}^{NaI_3O_8}(\lambda_{2\omega}^{PM} = 0.540 \mu m)| = 0.22 \pm 0.02 \text{ pm/V}$ and $|d_{eff II}^{NaI_3O_8}(\lambda_{2\omega}^{PM} = 0.529 \mu m)| = 0.53 \pm 0.05 \text{ pm/V}$. Then it comes from Eqs. (2) and (3): $|d_{14}(0.529 \mu m)| = 0.54 \pm 0.08 \text{ pm/V}$ and $|d_{15}^{NaI_3O_8}(0.540 \mu m)| = 0.85 \pm 0.13 \text{ pm/V}$. The discrepancy is strong when compared with calculations using the model of ref. [2] as shown in Tab. 2 since the modelling of the second-order electric susceptibility remains an open question. The corresponding Miller indices determined using Eq. (1) are [7]: $\delta_{14}^{NaI_3O_8} = 0.32 \pm 0.05 \text{ pm/V}$, $\delta_{15}^{NaI_3O_8} = 0.50 \pm 0.07 \text{ pm/V}$, $\delta_{15}^{KTP} = 0.25 \pm 0.04 \text{ pm/V}$, $\delta_{24}^{KTP} = 0.47 \pm 0.07 \text{ pm/V}$ and $\delta_{33}^{KTP} = 1.51 \pm 0.22 \text{ pm/V}$ [6].

Table 2. Refractive Indices and Nonlinear Coefficients of NaI_3O_8 : Comparison between our work and [2].

Parameters	Present work	From [2]	Parameters	Present work	From [2]
$n_o(1.064 \mu m)$	1.594	2.198	$d_{14} \text{ (pm/V)}$	0.54(@ 0.529 μm)	13.1 (λ not given)
$n_e(1.064 \mu m)$	1.551	1.973	$d_{15} \text{ (pm/V)}$	0.85(@ 0.540 μm)	1.5 (λ not given)
n_o/n_e	1.027	1.114	d_{14}/d_{15}	0.63	8.71

Reliable NaI_3O_8 -OPG tuning curves can be calculated using our Sellmeier equations. Thus, we found that a supercontinuum can be generated from type II OPG ($1/\lambda_p^e - 1/\lambda_s^o = 1/\lambda_i^o$) in the dielectric xz-plane of NaI_3O_8 . The supercontinuum is the broadest one, ranging between $2.55 \mu m$ and $4.65 \mu m$, when the pump wavelength is equal to $1.16 \mu m$ and the crystal oriented at $\theta = 18.5^\circ$ from the z-axis as shown in Fig. 5. A supercontinuum can also be generated when the crystal is pumped by the Ti:Sapphire at $0.8 \mu m$ and the Nd:YAG at $1.064 \mu m$, also shown in Fig. 5.

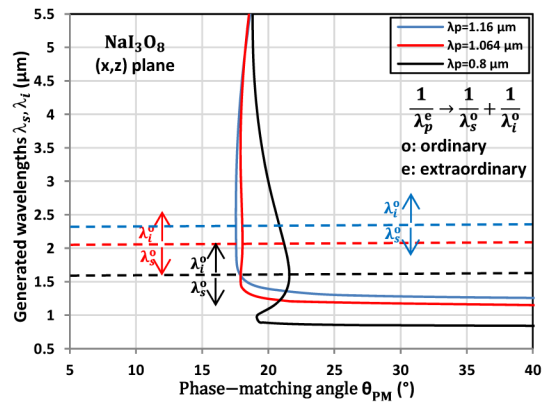


Fig. 5. Calculated OPG tuning curve in the xz plane of NaI_3O_8 with $\lambda_p = 1.16, 1.064$ and $0.8 \mu\text{m}$.

4. Conclusion

We measured for the first time to the best of our knowledge the transmission spectra in polarized light, the damage threshold, and the phase-matching conditions of SHG and DFG in the new acentric uniaxial NaI_3O_8 crystal. It allowed us to determine the Sellmeier equations and the absolute value of the two nonzero second-order nonlinear coefficients. Our data show that NaI_3O_8 is very attractive since using our Sellmeier's equations we showed that a NaI_3O_8 -based OPG can generate a supercontinuum in the mid-IR when pumped in the near-IR. We also bring a new input to refine the modelling of the second-order electric susceptibility in iodates compounds.

Funding

The authors thank the China Scholarship Council (CSC) for the financial support of Feng Guo.



Phase-matching properties and refined Sellmeier equations of $\text{La}_3\text{Ga}_{5.5}\text{Nb}_{0.5}\text{O}_{14}$

FENG GUO,^{1,3} DAZHI LU,^{1,2,3} PATRICIA SEGONDS,^{1,*} JÉRÔME DEBRAY,¹
HAOHAI YU,² HUAJIN ZHANG,² JIYANG WANG,² AND BENOÎT BOULANGER¹

¹Univ. Grenoble Alpes, CNRS, Grenoble INP, Institut Néel, 38000 Grenoble, France

²State Key Laboratory of Crystal Materials and Institute of Crystal Materials, Shandong University, Jinan 250100, China

³These authors contribute equally to this work.

*patricia.segonds@neel.cnrs.fr

Abstract: We directly measured the phase-matching angles of second-harmonic generation and difference-frequency generation up to $6.5\ \mu\text{m}$ in the Langanate crystal $\text{La}_3\text{Ga}_{5.5}\text{Nb}_{0.5}\text{O}_{14}$ (LGN). We also determined the nonlinear coefficient and damage threshold. We refined the Sellmeier equations of the ordinary and extraordinary principal refractive indices, and calculated the conditions of supercontinuum generation.

© 2018 Optical Society of America under the terms of the [OSA Open Access Publishing Agreement](#)

OCIS codes: (190.2620) Harmonic generation and mixing; (190.4400) Nonlinear optics, materials; (190.4975) Parametric processes.

References and links

1. E. Boursier, P. Segonds, B. Boulanger, C. Félix, J. Debray, D. Jegouso, B. Ménaert, D. Roshchupkin, and I. Shoji, "Phase-matching directions, refined Sellmeier equations, and second-order nonlinear coefficient of the infrared Langanate crystal $\text{La}_3\text{Ga}_{5.5}\text{Ta}_{0.5}\text{O}_{14}$," *Opt. Lett.* **39**(13), 4033–4036 (2014).
2. D. Z. Lu, T. X. Xu, H. H. Yu, Q. Fu, H. J. Zhang, P. Segonds, B. Boulanger, X. Y. Zhang, and J. Y. Wang, "Acentric Langanite $\text{La}_3\text{Ga}_5\text{SiO}_{14}$ crystal: a new nonlinear crystal for the generation of mid-infrared parametric light," *Opt. Express* **24**(16), 17603–17615 (2016).
3. J. Stadel, L. Bohaty, M. Hengst, and R. B. Heimann, "Electro-optic, piezoelectric and dielectric properties of Langanite ($\text{La}_3\text{Ga}_5\text{SiO}_{14}$), Langanite ($\text{La}_3\text{Ga}_{5.5}\text{Nb}_{0.5}\text{O}_{14}$) and Langatite ($\text{La}_3\text{Ga}_{5.5}\text{Ta}_{0.5}\text{O}_{14}$)," *Cryst. Res. Technol.* **37**(10), 1113–1120 (2002).
4. B. Boulanger, J. P. Fève, G. Marnier, C. Bonnin, P. Villeval, and J. J. Zondy, "Absolute measurement of quadratic nonlinearities from phase-matched second-harmonic generation in a single KTP crystal cut as a sphere," *J. Opt. Soc. Am. B* **14**(6), 1380–1386 (1997).
5. B. Boulanger and J. Zyss, in *International Tables for Crystallography*, A. Authier, ed., Vol. D of Physical Properties of Crystals (Kluwer Academic, 2004), pp. 178–219.
6. R. C. Miller, "Optical second harmonic generation in piezoelectric crystals," *Appl. Phys. Lett.* **5**(1), 17–19 (1964).
7. V. Petrov, M. Ghotbi, O. Kokabee, A. Esteban-Martin, F. Noack, A. Gaydardzhiev, I. Nikolov, P. Tzankov, I. Buchvarov, K. Miyata, A. Majchrowski, I. V. Kityk, F. Rotermund, E. Michalski, and M. Ebrahim-Zadeh, "Femtosecond nonlinear frequency conversion based on BiB_3O_6 ," *Laser Photonics Rev.* **4**(1), 53–98 (2010).

1. Introduction

We identified the Langanate $\text{La}_3\text{Ga}_{5.5}\text{Ta}_{0.5}\text{O}_{14}$ (LGT) as a serious candidate for the parametric generation between 3 and $6.5\ \mu\text{m}$ [1]. We then focused on a new compound of the same family, *i.e.* the Langanate $\text{La}_3\text{Ga}_{5.5}\text{Nb}_{0.5}\text{O}_{14}$ (LGN). We reported in a previous paper that when the transmittance is half its maximal value, the ultraviolet cut-off is down to $0.35\ \mu\text{m}$ and the infrared cut-off is up to $6.5\ \mu\text{m}$, in very high quality and large-size crystals grown with the Czochralski method [2]. Since LGN crystallizes in the 32 trigonal point group, there is only one nonzero element of its second-order electric susceptibility tensor under Kleinman symmetry, *i.e.* $d_{xxx} = -d_{yyy} = -d_{yyx} = -d_{xyx}$ ($=d_{11}$) where d_{11} stands for the contracted notation. We found that the absolute magnitude of d_{11} is equal to $3.0 \pm 0.1\ \text{pm/V}$ at $0.532\ \mu\text{m}$ using the Maker fringes method [2]. We also reported a damage threshold of $1.41\ \text{GW/cm}^2$ at $1.064\ \mu\text{m}$ in the nanosecond regime [2]. LGN is a positive uniaxial crystal, so that the ordinary principal refractive index (n_o) is smaller than the extraordinary one (n_e). Both indices

were previously measured as a function of the wavelength using an oriented prism, which enabled to determine Sellmeier equations valid between 0.36 and 2.32 μm [3]. Using the same method, we proposed an alternative set of equations valid between 0.43 and 2.3 μm [2].

Using sets of equations from [2] and [3], we did not find the same calculated phase-matching tuning curves in the principal dielectric planes of LGN for all the possible quadratic processes associated with a non-zero conversion efficiency [2]. Then we decided to directly record these curves, which is described in the present paper. We report for the first time to the best of our knowledge the direct measurement in LGN of the phase-matching tuning curves of second harmonic generation (SHG) and difference frequency generation (DFG). A simultaneous fit of all our data allowed us to refine the Sellmeier equations of the two principal refractive indices of LGN. We also determined the nonlinear coefficient d_{11} at another wavelength from [2] and the damage threshold. We could then calculate the conditions of supercontinuum generation.

2. Phase-matching angles and Sellmeier equations

The LGN crystal was cut and polished as a sphere with a diameter of 10.8 mm and asphericity below 1%. It was stuck on a goniometric head as shown in Fig. 1(a). It was successively oriented along the x - and y - dielectric axes with an accuracy better than 0.5° , using the X-ray backscattered Laue method. Then the LGN sphere was placed at the center of an Euler circle to be rotated in any direction. Thus any directions of the two (y, z) and (x, z) principal dielectric planes can be addressed successively in the same sample.

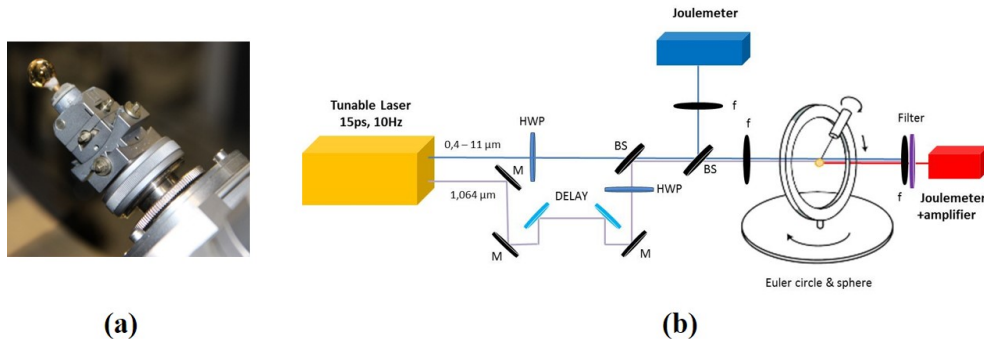


Fig. 1. (a) Picture of the LGN crystal sphere stuck on a goniometric head; (b) Setup used for the direct measurement of SHG and DFG phase-matching tuning curves.

Only one incoming beam tunable between 0.4 and 11 μm is used for studying SHG. It was emitted by a Light Conversion optical parametric generator (OPG) with 15-ps FWHM and 10-Hz repetition rate. The OPG is pumped by the third-harmonic of a beam at 1.064 μm emitted by a Excel Technology Nd:YAG laser. Thus for the study of DFG, we can combine the OPG beam with part of the 1.064 μm beam directly in the sphere as shown in Fig. 1(b).

A 100-mm-focusing lens (f) placed at the entrance side of the sphere ensured normal incidence and quasi-parallel propagation of all the input beams along any diameter of the sphere. The polarization was adjusted by using achromatic half-wave-plates (HWP).

The energy of the incoming beams was measured with a J4-09 Molelectron pyroelectric joulemeter placed behind a beam splitter (BS) and a lens with a focal length of 50 mm. The energy of the generated beam was measured simultaneously at the exit of the sphere by a J3-05 Molelectron pyroelectric joulemeter associated with a PEM531 amplifier. A filter removed all input beams. The phase-matching wavelengths were controlled by monitoring the wavelengths of the input beams between 0.4 and 1.7 μm with accuracy of ± 1 nm using HR 4000 and of ± 3 nm with NIRquest 512 Ocean Optics spectrometer. The phase-matching

angles were read on the Euler circle with an accuracy of $\pm 0.5^\circ$. A phase-matching direction is detected when the conversion efficiency reaches a maximal value.

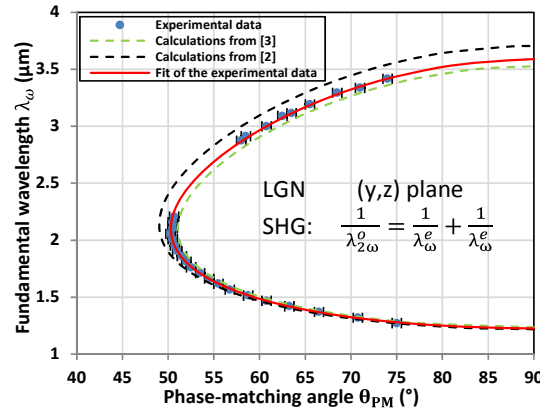


Fig. 2. SHG tuning curve in the (y, z) plane of LGN. Wavelengths accuracy is within dots size.

The recorded SHG and DFG phase-matching tuning curves are shown in Figs. 2 and 3, respectively. We studied type I SHG ($1/\lambda_{2\omega}^o = 1/\lambda_\omega^e + 1/\lambda_\omega^e$) and type II DFG ($1/\lambda_i^e = 1/\lambda_p^o - 1/\lambda_s^e$) in the (y, z) plane, and type III DFG ($1/\lambda_i^o = 1/\lambda_p^o - 1/\lambda_s^e$) in the (x, z) plane. Superscripts o and e stand for the ordinary and extraordinary waves, respectively. λ_ω and $\lambda_{2\omega}$ are the fundamental and second harmonic wavelengths. λ_p , λ_s and λ_i are respectively the pump, signal and idler wavelengths verifying $\lambda_p < \lambda_s \leq \lambda_i$.

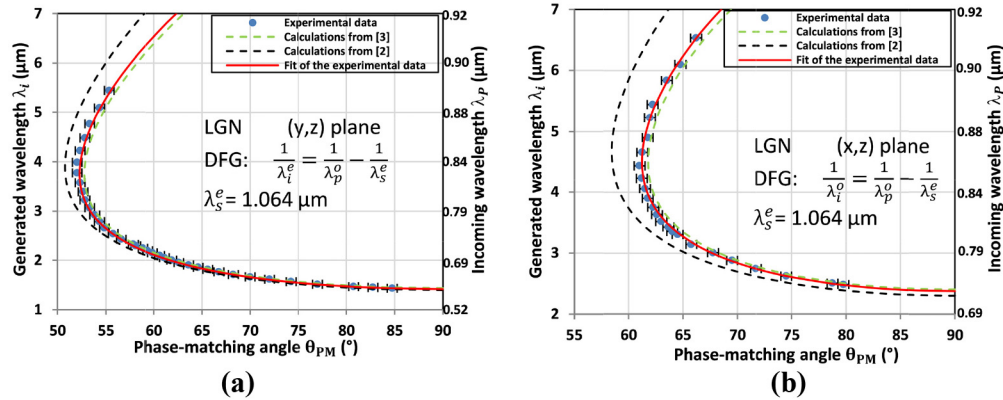


Fig. 3. DFG tuning curve (a) in the (y, z) and (b) in the (x, z) plane of LGN. Wavelengths accuracy is within dots size.

Figures 2 and 3 also show the calculated phase-matching curves using the Sellmeier equations from Refs [2]. and [3]. It highlights discrepancies between our experimental data and both sets of calculations, even if calculations using [3] are closer to our experimental data. It is true especially above $2.3 \mu\text{m}$ that corresponds to the limit of the spectral range over which the ordinary and extraordinary principal refractive indices were determined in Refs [2]. and [3]. As shown in Fig. 4, by performing our measurements up to $6.5 \mu\text{m}$, we widely extended the wavelength range where the two principal refractive indices of LGN are involved. Such a difference might explain the discrepancies shown in Fig. 2 and 3.

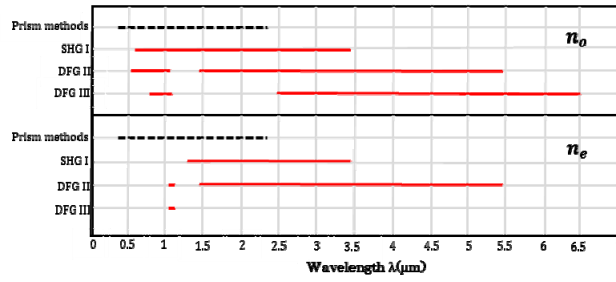


Fig. 4. Spectral ranges where the principal refractive indices of LGN, n_o and n_e , are involved, using the sphere method (red lines), and the prism technique from [2] and [3] (black dashed lines).

We refined the Sellmeier equations of LGN by the simultaneous fit of all our SHG and DFG experimental data shown in Fig. 2 and 3. We used the Levenberg-Marquardt algorithm encoded with Matlab. Among the several possible forms of Sellmeier equations to fit the ordinary and extraordinary refractive indices, the best one was that used in Refs [2, 3], *i.e.*:

$$n_j^2(\lambda) = A_j + \frac{B_j}{\lambda^2 - C_j} - D_j \lambda^2 \quad (1)$$

where λ is in μm and j stands for o or e . The precision of our angular measurements is $\pm 0.5^\circ$, leading to a relative accuracy $\Delta n_j / n_j$ better than 10^{-4} . The numerical values of the best fit parameters A_j , B_j , C_j and D_j are summarized in Table 1. Our interpolated tuning curves using the Sellmeier equations of the present work correspond to the continuous red lines shown Figs. 2 and 3. They clearly show a much better agreement with our experimental data than using the calculations from Refs [2]. and [3].

Table 1. Refined Sellmeier Coefficients of the Two Principal Refractive Indices n_o and n_e of LGN

Sellemeir coefficients	A_j	B_j	C_j	D_j
$j = o$	3.6836	0.0460	0.0296	0.0094
$j = e$	3.7952	0.0483	0.0314	0.0102

3. Nonlinear coefficient and damage threshold

The absolute value of d_{11} of LGN can be determined from angle critical phase-matched type I SHG in the (y, z) plane. The corresponding effective coefficient is expressed as:

$$d_{eff}^{LGN} = d_{11}^{LGN}(\lambda_{\omega_1}) \cos^2[\theta_{PM_1} - \rho^e(\theta_{PM_1}, \lambda_{\omega_1})] \quad (2)$$

where $\rho^e(\theta_{PM_1}, \lambda_{\omega_1})$ stands for the spatial walk-off.

We chose the nonlinear coefficient of KTP $d_{24}^{KTP}(\lambda_{2\omega_2} = 0.66 \mu\text{m}) = 2.37 \pm 0.17 \text{ pm/V}$ as a reference [4] for the determination of d_{11} of LGN. The coefficient d_{24}^{KTP} governs type II SHG ($1/\lambda_{\omega_2}^e + 1/\lambda_{\omega_2}^o = 1/\lambda_{2\omega_2}^o$) in the (x, z) plane of KTP, the corresponding effective coefficient being $d_{eff}^{KTP} = d_{24}^{KTP}(\lambda_{2\omega_2}) \sin[\theta_{PM_2} - \rho^e(\theta_{PM_2}, \lambda_{\omega_2})]$ with $\theta_{PM_2} = 58.5^\circ$ and $\rho^e(\theta_{PM_2}, \lambda_{\omega_2}) = 2.57^\circ$ at the fundamental wavelength $\lambda_{\omega_2} = 1.32 \mu\text{m}$. A LGN slab was then cut at $(\theta_{PM_1} = 70.4^\circ, \varphi_{PM_1} = 90^\circ)$ according to our refined Sellmeier equations, the goal being to study the SHG in LGN at a fundamental wavelength the closest as possible to that of KTP. It has the advantage that we could get rid of the spectral response of the experimental

setup. The LGN and KTP slabs were cut with the same small thickness $L = 0.52$ mm. The fundamental beam emitted by the OPG was focused with a 100-mm-focal length CaF_2 lens. Then the beam waist diameter was $w_o = 120$ μm on the two slabs surface, with a Rayleigh length of 30 mm that is much longer than L . Then parallel beam propagation was ensured, and the spatial walk-off attenuation is minimized.

The fundamental beam energy was measured with the J4-09 Molelectron pyroelectric joulemeter placed behind a beam splitter and a lens with a focal length of 50 mm. The SHG energy was measured at the exit of each slab by the J3-05 Molelectron pyroelectric joulemeter combined with a PEM531 amplifier, while a filter removed the input beam. Then we can determine the corresponding SHG conversion efficiency of type I SHG in LGN (η_I^{LGN}), and that of type II SHG in KTP (η_{II}^{KTP}).

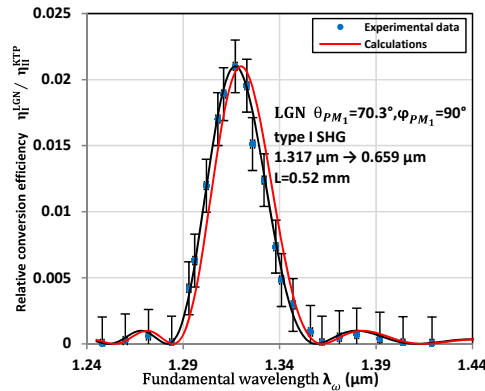


Fig. 5. Calculated (red line) and measured (dots linked with black line) conversion efficiency in LGN relatively to KTP, as a function of the fundamental wavelength. Wavelengths accuracy is within dots size.

Figure 5 shows the ratio $\eta_I^{\text{LGN}} / \eta_{II}^{\text{KTP}}$ recorded as a function of the fundamental wavelength λ_o . The peak wavelength is $\lambda_{o_1} = 1.317$ μm for LGN, which is very close to the targeted value λ_{o_2} . The spectral acceptance $L\delta\lambda_{o_1}$ is equal to 19.8 nm. It is in very good agreement with the calculation using our refined Sellmeier equations. In these conditions, we can calculate $d_{\text{eff}}^{\text{LGN}}$ relatively to $d_{\text{eff}}^{\text{KTP}}$ as follows:

$$(d_{\text{eff}}^{\text{LGN}})^2 = \frac{\eta_I^{\text{LGN}}}{\eta_{II}^{\text{KTP}}} \frac{L_{\text{KTP}}^2}{L_{\text{LGN}}^2} \frac{G_{II}^{\text{KTP}}}{G_I^{\text{LGN}}} \frac{A_{II}^{\text{KTP}}}{A_I^{\text{LGN}}} (d_{\text{eff}}^{\text{KTP}})^2 \quad (3)$$

with

$$A_I^{\text{LGN}} = \frac{T_o^{\text{LGN}}(\lambda_{2\omega_1}, \theta_{PM_1})}{n_o^{\text{LGN}}(\lambda_{2\omega_1}, \theta_{PM_1})} \left[\frac{T_e^{\text{LGN}}(\lambda_{\omega_1})}{n_e^{\text{LGN}}(\lambda_{\omega_1})} \right]^2 \quad (4)$$

and

$$A_{II}^{\text{KTP}} = \frac{T_o^{\text{KTP}}(\lambda_{2\omega_2}) T_e^{\text{KTP}}(\lambda_{\omega_2}, \theta_{PM_2}) T_o^{\text{KTP}}(\lambda_{\omega_2})}{n_o^{\text{KTP}}(\lambda_{2\omega_2}) n_e^{\text{KTP}}(\lambda_{\omega_2}, \theta_{PM_2}) n_o^{\text{KTP}}(\lambda_{\omega_2})} \quad (5)$$

n_o and n_e are the ordinary and extraordinary refractive indices. They were calculated at $\lambda_{\omega_1} = 1.317$ μm for LGN using Eq. (1) and Table 1, and at $\lambda_{\omega_2} = 1.320$ μm for KTP using

respectively the phase-matching angles θ_{PM_1} and θ_{PM_2} defined above and [4]. T_o and T_e are the corresponding Fresnel transmission coefficients. For LGN, the spatial walk-off angle $\rho^e(\theta_{PM_1}, \lambda_{o_1}) = 0.55^\circ$ and the spatial walk-off attenuation $G_I^{LGN} = 0.999$. $G_{II}^{KTP} = 0.987$ for KTP [4,5]. Note that Fig. 5 shows a conversion efficiency of KTP that is two orders of magnitude higher than that of LGN: it is due to the relative value of their trigonometric functions that weigh differently on the nonlinear coefficients at the considered phase-matching angles. According to Eq. (2), we found that $|d_{11}(0.659 \mu\text{m})| = 2.9 \pm 0.5 \text{ pm/V}$ and $\delta_{11} = 0.284 \pm 0.049 \text{ pm/V}$, the Miller index [6], which corroborates the result obtained using the Maker fringes technique [2]. Furthermore it is also very close to $|d_{24}(0.660 \mu\text{m})| = 2.37 \pm 0.17 \text{ pm/V}$ of KTP [4], and a little bit larger than $|d_{11}(0.659 \mu\text{m})| = 2.4 \pm 0.4 \text{ pm/V}$ of LGT [1].

We also determined the surface damage threshold of the same LGN and KTP slabs. Both crystals were illuminated by the same Nd:YAG laser at $1.064 \mu\text{m}$ with a very high beam quality, a pulse duration of 5 ns (FWHM) and repetition rate of 10 Hz. By using a 100-mm-focal BK7 lens, we measured a beam waist diameter of $60 \pm 3 \mu\text{m}$ at their input surface using the standard knife-method. In these conditions, LGN was damaged at an incoming energy of $500 \pm 10 \mu\text{J}$, corresponding to a peak power density of $2.8 \pm 0.7 \text{ GW/cm}^2$. It is a little bit lower than that of KTP where the damage was observed at $760 \pm 10 \mu\text{J}$, *i.e.* $4.3 \pm 1.1 \text{ GW/cm}^2$. Using the same setup and same KTP crystal as a reference, LGT had been damaged for an input energy of $480 \pm 10 \mu\text{J}$, which corresponds to a peak power density of $2.7 \pm 0.7 \text{ GW/cm}^2$ [3]. In our previous work, we reported a surface damage threshold of 1.41 GW/cm^2 in a 1-mm thick LGN slab using KDP as a reference [2]. They were illuminated by a Nd:YAG laser at $1.064 \mu\text{m}$ with a pulse duration of 10 ns (FWHM) and a repetition rate of 1 Hz. Moreover, the experimental protocol was different than the one we used here since the average power had been set at 20 mW and the beam waist diameter at the entrance surface of the slab was equal to $200 \mu\text{m}$. Furthermore, the slabs were moved toward the focal point until damage was observed at their input surface. All these differences could explain the different result.

4. Calculation of the supercontinuum generation by phase-matched OPG

Using our refined Sellmeier equations and the method described in ref [7], we showed that a supercontinuum can be generated using a type II phase-matched OPG *i.e.* $1/\lambda_p^o \rightarrow 1/\lambda_s^e + 1/\lambda_i^e$ when pumped at $\lambda_p = 0.982 \mu\text{m}$ in the (y, z) plane of LGN. Figure 6 shows that the emission could range between 1.4 and $3.45 \mu\text{m}$, the LGN crystal being cut at ($\theta_{PM} = 52^\circ$, $\phi_{PM} = 90^\circ$). According to the value of d_{11} determined above, the calculated corresponding figure of merit $(d_{eff}^{yz})^2 / n^o(\lambda_p)n^e(\lambda_i)n^e(\lambda_s)$ is equal to $0.15 \frac{\text{pm}^2}{V^2}$ in LGN,

which is a relatively low value. However, the supercontinuum range and the figure of merit are both larger in LGN compared with LGT [1]. Concerning the pump laser to use, Fig. 6 shows that the tuning curve of LGN exhibits a quasi-supercontinuum behavior when the crystal is pumped at $\lambda_p = 1.064 \mu\text{m}$, while it is not anymore the case at $\lambda_p = 0.8 \mu\text{m}$.

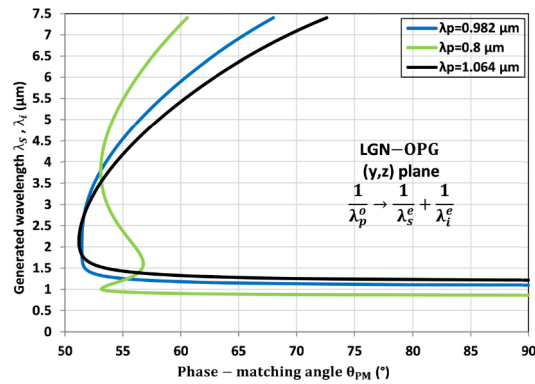


Fig. 6. Calculated OPG tuning curves in the (y, z) plane of LGN at different values of the pump wavelength λ_p .

5. Conclusion

We measured the SHG and DFG phase-matching tuning curves of LGN as well as the absolute magnitude of the associated nonlinear coefficient. These data can be used *per se* for designing any parametric device, but we also used them for refining the Sellmeier equations of the crystal. Using these equations, we found the possibility of generating a super continuum in the mid-IR by pumping LGN at the standard wavelength of emission of the Nd:YAG laser. This interesting feature combined with the ability of this crystal to be grown in large size and high optical quality put LGN in the category of the best nonlinear crystals for practical applications.

Acknowledgment

The authors thank the China Scholarship Council (CSC) for the financial supports of Feng Guo and Dazhi Lu.

Studies of new nonlinear crystals for infrared parametric generation

Nowadays, the optical parametric generators (OPG) with the broadest spectral bandwidth is a good alternative cover band II (3–5 μm) or band III (8–12 μm) of transmission range of the atmosphere. We were interested in such an emission from quadratic nonlinear processes under birefringence phase-matching conditions (BPM). It is performed in the transparency range of already identified nonlinear crystals, but they are not satisfying. Then this PhD work is devoted first to the study of $\text{GdCa}_4\text{O}(\text{BO}_3)_3$ (GdCOB) biaxial crystal, and $\text{La}_3\text{Ga}_{5.5}\text{Nb}_{0.5}\text{O}_{14}$ (LGN) and NaI_3O_8 uniaxial crystals. We recorded their tuning curves and conversion efficiencies for BPM. We selected second harmonic generation and difference frequency generation in slabs, spheres or cylinders. We refined the Sellmeier equations. We determined the magnitude of the nonlinear coefficients, spectral and angular acceptances in uniaxial crystals. We also determined the magnitude and sign of all the nonlinear coefficients of BaGa_4Se_7 biaxial crystal. All these results provide reliable data for further experimental evaluations of OPG broadest spectral bandwidth covering band II or III using these crystals.

Key words: nonlinear optics, parametric generation, phase-matching, nonlinear crystals

Etudes de nouveaux cristaux non linéaires pour la génération paramétrique dans l'infrarouge

De nos jours, la génération paramétrique optique (OPG) avec la plus grande largeur spectrale possible, est une bonne alternative pour couvrir les bandes II (3–5 μm) ou band III (8–12 μm) de transmission de l'atmosphère. Une telle émission à partir de processus non linéaires quadratiques en conditions d'accord de phase par biréfringence (BPM), nous a intéressés. Elle est réalisée sur le domaine de transparence de cristaux non linéaires déjà identifiés, mais ils ne sont pas satisfaisants. C'est pourquoi ce travail de thèse est consacré d'abord à l'étude du cristal biaxe $\text{GdCa}_4\text{O}(\text{BO}_3)_3$ (GdCOB), et des cristaux uniaxes $\text{La}_3\text{Ga}_{5.5}\text{Nb}_{0.5}\text{O}_{14}$ (LGN) et NaI_3O_8 . Nous avons enregistré leurs courbes d'accord de phase et les rendements de conversion associés en conditions de BPM. Nous avons sélectionné la génération de second harmonique et la différence de fréquence dans des lames, des sphères ou cylindres. Nous avons affiné les équations de Sellmeier. Nous avons déterminé la valeur absolue des coefficients non linéaires des cristaux uniaxes. Nous avons aussi déterminé la valeur absolue et le signe de tous les coefficients du cristal biaxe BaGa_4Se_7 . Tous ces résultats constituent une base fiable pour les évaluations expérimentales à venir de la plus grande largeur spectrale des OPG qui utilisent ces cristaux.

Mots-clés : optique non linéaire, génération paramétrique, accord de phase, cristaux non linéaires